478

HYPERCHARGE EXCHANGE REACTIONS IN A TRIGGERED BUBBLE CHAMBER

by

Jasbinder Singh Chima

A thesis submitted for the degree
of Doctor of Philosophy of the
University of London

Department of Physics
Imperial College
London SW7

November 1979

ABSTRACT

Results from the reactions

$$\pi^+ \; p \rightarrow k^+ \, \Sigma \, \pi \quad (\pi)$$

$$\pi^+ \; p \rightarrow k^+ \, \Lambda \, \pi \, \pi \; (\pi)$$

$$k^- \; p \rightarrow \pi^- \, \Sigma \, \pi \quad (\pi)$$

$$k^- \; p \rightarrow \pi^- \, \Lambda \, \pi \, \pi \; (\pi)$$

at 7.0. GeV/c are presented. Some comparisons are made with identical reactions at 11.5 GeV/c. Data at both momenta were taken in the SLAC 1m. Rapid Cycling Bubble Chamber, with the flash being triggered by fast forward going mesons with different hypercharge to that of the beam. In π^+p exposure trigger by fast forward proton was also allowed. Detailed description of resonance production both in the forward going meson system and target baryon system are presented.

CONTENTS

CONTENTS (CONTINUED)

CHAPTER 1

Data Acquistion

I.I INTRODUCTION

In this thesis results are presented of a study of hypercharge exchange reactions of the type

$$\pi^+ + p \rightarrow \text{Meson(s)} + \text{Hyperon}$$

$$k^- + p \rightarrow \text{Meson(s)} + \text{Hyperon}$$

where the description of the final state includes particles with weak and electromagnetic decays as well as strongly decaying resonances. A special feature of these reactions is that often the polarization of the final state baryon can be measured via the analysis of a weak decay in the hyperon decay chain.

The results are based on the data collected in a π^+p and k^-p triggered bubble chamber experiment which started in 1974.[1] A loose collaboration of the bubble chamber groups of Imperial College and Stanford Linear Accelerator Centre conducted the experiment. Imperial College took data at 7 Gev/c while the SLAC group ran at 11.5 Gev/c.[1] Although the two groups collaborated in setting up the SLAC Hybrid Facility and acquistion of the data at the two energies the data reduction was carried out independently.

Most high energy experiments can be characterised as studies of phenomena observed when two particles with specific quantum numbers are made to collide. Since the result of these collisions are governed by statisticl laws a large number of observations is usually necessary in order to obtain precise results. A specific experiment can be roughly divided into three stages:

(a) Data acquistion

(b) Reduction of data in order to obtain a complete description of the collisions

(c) Analysis of data aimed at an understanding of the particles produced and their reaction mechanisms.

In this chapter stage (a) will be described and chapter two will contain a description of stage (b). In chapter three , four and five will be presented results from the author's contribution to stage(c).

I.2 Motivation For The Experiment

The experiment was proposed primarily for four different types of studies.

(1) A high statistics study of Σ^+ and $\Sigma^{*+}(1385)$ production in the pairs of line reversed reactions I,II and III,IV.

$$\pi^+ p \rightarrow k^+ \Sigma^+ \qquad \text{(I)}$$
$$k^- p \rightarrow \pi^- \Sigma^+ \qquad \text{(II)}$$
$$\pi^+ p \rightarrow k^+ \Sigma^{*+}(1385) \qquad \text{(III)}$$
$$k^- p \rightarrow \pi^- \Sigma^{*+}(1385) \qquad \text{(IV)}$$

At high energy these reaction are thought to be dominated by $k^*(890)$ and $k^*(1420)$ Regge pole exchange.[27] Comparison of the pairs of line reversed reactions provides a simple test of the exchange degenerate properties of these two trajectories.

(2) Higher mass resonances particularly in the 1700 Mev region.

(3) Vector meson production.

(4) Baryon exchange processes.

At the time the experiment was proposed, in 1974 , previous bubble chamber experiments studying reactions of type (1) above 3 Gev/c incoming beam momentum had a typical sensitivity of 20 events/μb or less.The present experiment raised the sensitivity to 150 events/μb for reaction (I) and(III) and 100 events/μb for reactions (II) and (IV). To do such a high statistics experiment in a conventional bubble chamber would have required a prohibatively large exposure. The total cross-sections for π^+p and k^-p at 7 Gev/c are :

$$\sigma_{\pi^+p} = 27.8 \text{ mb}$$

$$\sigma_{k^-p} = 25. \text{ mb}$$

whereas the cross-section for hypercharge exchange reactions are only a few mb at 7 Gev/c and fall rapidly with increasing beam momentum. However the bubble chamber is an ideal detector for Σ and Λ decays. The 4π detection capability allows the parity violating decays of the Λ and Σ to be observed and hence good polarization measurement of these is possible.

Reactions of the type (1) in which a high energy peripheral interaction gives rise to a fast forward going particle, are very well suited to studies in a hybrid system; as the fast forward going particle can provide a trigger.

I.3 Experimental Setup[2]

The experiment was performed using the SLAC Hybrid Facility. The facility consists of a 1m. rapid cycling bubble chamber with electronic detectors upstream and downstream allowing identification of incoming beam and outgoing particles respectively. The electronic detectors thus allowed a trigger to be defined to flash the bubble chamber lamps.

The Beam[3]

The Stanford Linear Accelerator provides a primary beam of 21 Gev/c pulsed at up to 360 Hz with a pulse duration of 1.6μs. The primary beam is dumped into a 1.1 radiation length beryllium target from which SLAC beamline 14 emerges, cycling at 15 Hz. The secondary beam was designed to give an average of 6π's or 4 k's per pulse at 7 Gev/c. A single r.f. separator was used to achive separation in the k^- run. The p/$\bar{p}$ component in the secondary beam was small, 2% for k^- beam , while in the π^+beam contamination was 5%. The momentum bite was such that for π^+ beam $\delta p/p$ 0.7% and for the k^- $\delta p/p$ 1.5%. The $k/(\pi+\mu)$ ratio in the secondary k^- beam varied between 3and 4. Quadruple magnets were carefully adjusted to produce an extremely parallel beam which enabled a simplification of the software trigger discussed below. The beam entered the SHF at an angle of 4° to the horizontal.

The Slac Hybrid Facility [2]

Layout of the Hybrid Facility is shown in Figl.1 which also defines the coordinate system.

The upstream part of the SHF consists of two plastic scintillators S1 and S2 which defined a beam particle. Beam particle type was established by the threshold cerenkov C1 in which only π^+ or lighter particle emitted light. Hence there was contamination of the beam by μ's in the π^+ case and $\bar{p}$'s in the k^- case. The angle of entry of the beam particles was defined by the y and z coordinates from the beam multiwire proportional wire chambers (PWC'S) P1 and P2.

The hadron beam was injected into the liquid hydrogen rapid cycling bubble chamber,BC. This is a 1m chamber with a pulsing rate of 10 - 15 Hz. Three cameras recorded the events with bright field illumination. The magnetic field used at 7 Gev/c was 18 Kg.

The downstream system consists of: 3 PWC'S P3,P4 and P5 located in the fringe field of the bubble chamber magnet; a 10-cell pressurised cerenkov counter ,C2,and a hodoscope array S3. For the k^- run a muon detector was added downstream of S3 to elliminate false triggers from inflight beam decays $k^- \to \mu^- \nu$. The counter consisted of 1.0m of iron absorber followed by a multi-element scintillator plane S4, a further 0.1m of iron absorber and finally a second scintillator plane S5.

The position of the fast interaction product were recorded by P3,P4 and P5. These PWC'S contain three sub-planes which recorded hits in y,z and diagonally (u-plane) . Cerenkov C2 provided identification for most of the outgoing particles. For the π^+ run Freon 12 at 35 Psi was used giving pion threshold of 1.9 Gev/c. Thus the downstream system provided information on both the momenta and identity of the outgoing particles.

The Trigger [4]

The trigger was in two parts, a hardware trigger which took approsimately 20 nsec. and a second stage software algorithm which took 1.5 mSec to give a decision.

The triggering signature for the π^+ induced reaction was a fast (2.5 Gec/c) k^+ or p, while in the k^- case it was a π^-. A successful hardware trigger consisted of a coincidence between a beam signal and C2 indicating correct type of particle emerging from the interaction. For π^+ induced reactions the fast trigger was:

$$S1.C1.S2.\overline{C2}.S3$$

and for the k^- induced reaction was:

$$S1.\overline{C1}.S2.C2$$

where S1.C1.S2 signifies the passage of a good beam particle and $\overline{C2}$.S3 indicates a downstream k or p in the π^+ case. While in the k^- case S1.$\overline{C1}$.S2 indicates a good beam and C2 the passage of pion through the downstream system. Since C1 is a threshold cerenkov set to give light for π's there will be beam contamination by μ's in π^+ case and $\bar{p}$ in k^- case besides that due to upstream beam interactions.

A successful hardware trigger caused data from all PWC'S and the two cerenkovs to be read out and stored in a buffer from where it was read into a DGC 840 computer . Transfering of data into a buffer took approximately 180 ns. Hence a second hardware trigger could be recorded in the same beam spill. A maximum of two hardware triggers were possible for each beam which would typically contain 6 particles.

At the end of the beam spill or after a second hardware trigger, the data fromthe first trigger was transferred into the computer and the software algorithm was executed.

The object of the algorithm was to establish if there was a track in the downstream system with momentum above the cut-off value, originated from an interaction in the bubble chamber fiducial volume. The maximum time allowed to decide whether to flash the bubble chamber lamps was the bubble growth time of 3ms. Since the algorithm took 1.5ms a maximum of two hardware triggers could be processed in a single beam spill. The main steps in the excution of the algorithm were:

(1) For the k^- run a search was made for a pattern of hits in S4 and S5 which could correspond to a muon trajectory. If such a trajectory was found the trigger was immediately rejected.

(2) A multiplicity cut was applied to the beam PWC hits. A maximum of two beams was allowed within the PWC resolution time of 200 ns.

(3) Multiplicity cuts were applied to each of the individual plane in P3, P4 and P5.

(4) Pairs of associated (y,z) hits were found in P3, P4 and P5 and limits to the number of pairs found in each PWC.

(5) A pair of downstream PWCs (eg. P3, P5) was chosen for an attempt at vertex and momentum determination.

(6) Utilising the parallel nature of the beam, a search was made to reject non-interacting beam tracks in the downstream system by looking in P3 and P5 for hits predicted from P1 and P2.

(7) A search was made for a configuration of hits in the xz plane which could have originated from an interaction in the bubble chamber fiducial volume, multiple scattering being taken into account.

(8) A successful result then allowed a momentum calculation to be made using the y- values corresponding to the trajectory found in (7). For this computation, tables of magnetic field integrals and a calibrated mean trajectory for a nominal beam tracks were used.

(9) If the momentum determined in (8) was greater than the cut-off value a check was made that the predicted position matched an actual hit in at least one plane of the unused PWC, P4.

The above procedure was repeated for all combination of hits in the selected PWCs and, if necessary, for further pairs of PWCs. The first posotive result was sufficent to trigger the flash.

For each hardware trigger all counter data (PWC hits, scalers etc.) were written on a magnetic tape irrespective of whether a picture was taken. In the π^+ run one in 25 of the beam tracks gave a hardware trigger while in the k^- run it was one in 15. The overall trigger reduced the typical picture taking rate to one per 250 beam tracks, thus reducing the total number of pictures by an order of magnitude over a conventional bubble chamber exposure.

I.4 Data

Data taking was spread over 18 months from summer of 1976 to winter of 1977. A summary of the data taking is given in table 1.1.

	Beam	Period	Number of pictures taken/10000
1	π^+	Summer 1976	130
2	π^+	Winter 1976	96
3	π^+	Spring 1977	190
1	k^-	Spring 1977	217
2	K^-	Winter 1977	190

Table 1.1 Summary of Data for 7 Gev/c π^+, k^- exposures.

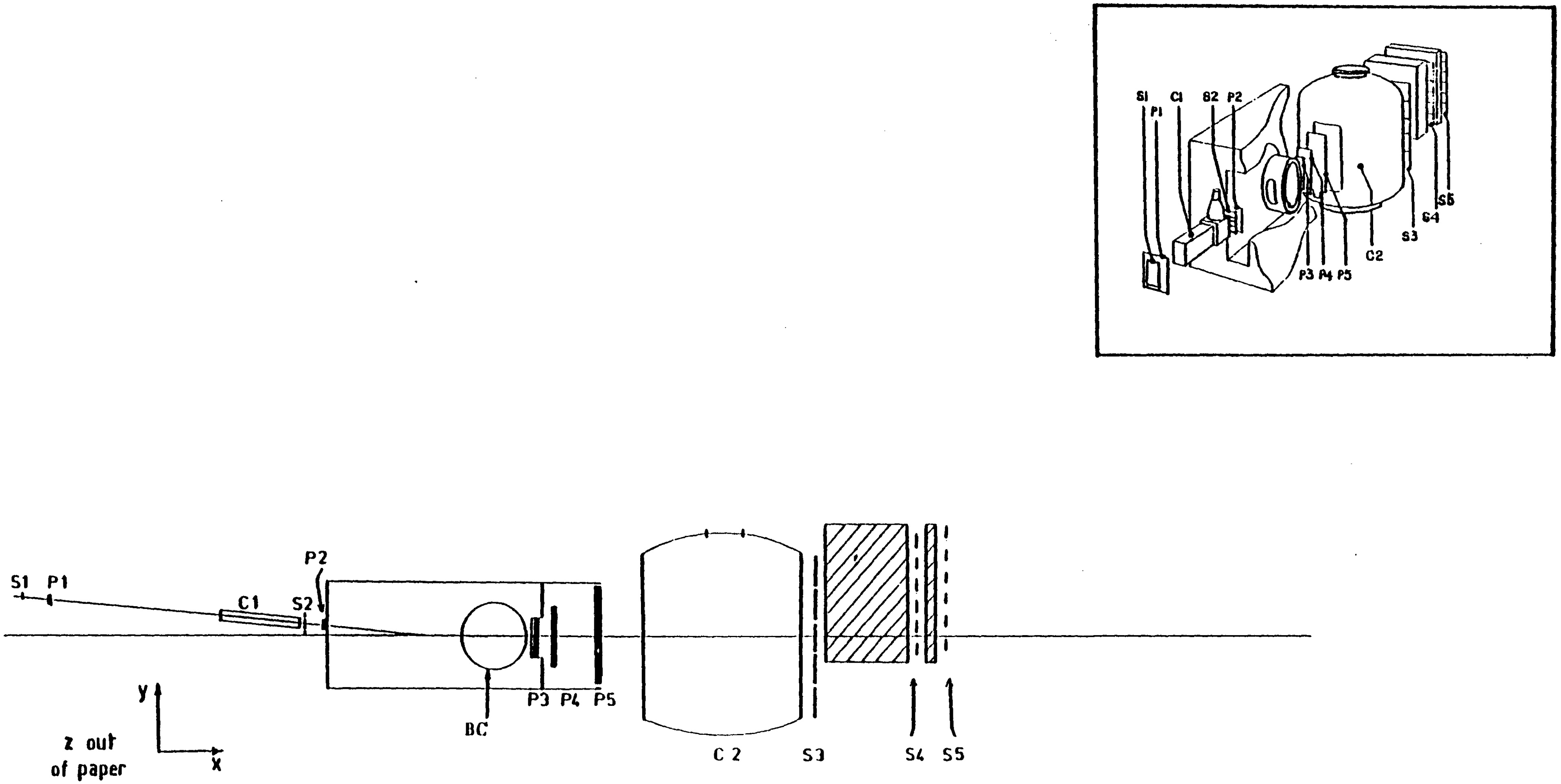

Fig.1.1 Schematic diagram of the SLAC Hybrid Facility. Inset shows a cut-away view of the SHF .

CHAPTER 2

Data Reduction and Corrections

2.1 Introduction

In this section the event processing chain will be described. In a typical analysis of bubble chamber film the following stages can be distinguished:

(1) Scanning

(2) Measurement

(3) Geometrical reconstruction

(4) Kinematical interpretation

(5) Selection of correct interpretation

(6) Compilation of data.

The term "Production Chain" is usually used to indicate the collection of operations required before physics analysis can be started, these are summarised in Fig 2.1.

2.1.1 Scan-Types

The events searched for on the bubble chamber pictures are usually divided into various scan-types corresponding to the different topological structure of the interactions. In this experiment these scan types were denoted by the code:

$N^T\ N^{Vch}\ N^{Vo}$

where: N^T is the number of outgoing tracks seen at the primary (collision) vertex.

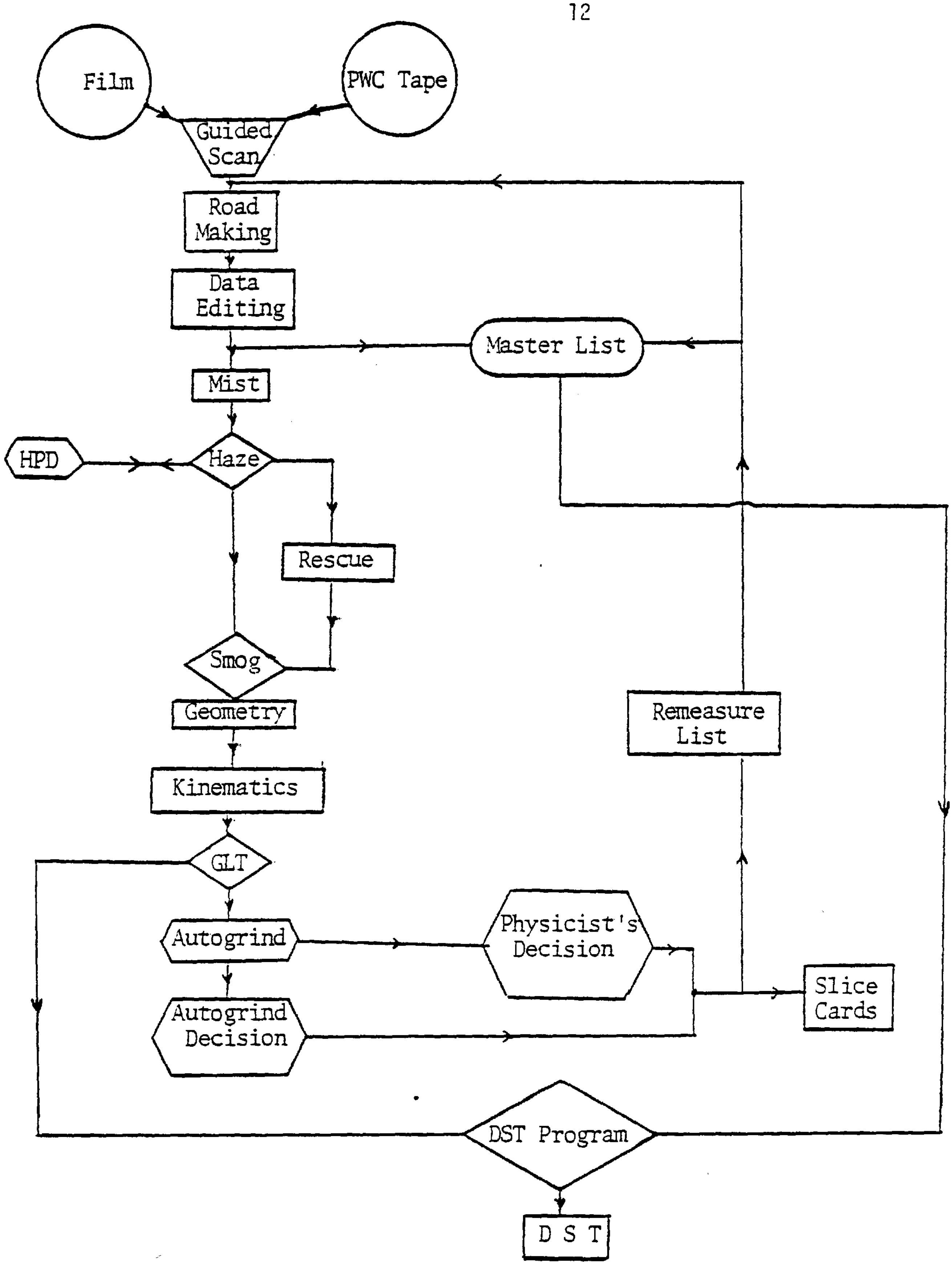

Fig 2.1 The Processing Chain

N^{vch} is the number of these tracks which have a kink, corresponding to a weak decay of a charged strange particle in the bubble chamber.

N^{Vo} is the number of neutral strange particles coming from the interaction vertex, and decaying visible in the bubble chamber.

The events used for analysis belong to one of the following scan-types:

201

210

401

410

The scan-types 200 and 400 were processed for only part of the total film sample. The production chain for the scan-type 400 differed from other topologies as will be discussed further on in this section.

2.1.2 Scanning and Measuring [5-6]

The film was scanned for events of the above mentioned scan-types. Events were selected for measurement only if information from the upstream PWC P2 indicated the event to be "good". By "good" we mean the event appeared on the beam track that caused the trigger. This was checked on the scan table by means of a template positioned with respect to two fiducial marks as illustrated in Fig. 2.2. Since the beam was almost parallel an approximate linear relationship existed between the P2 hit in the y - direction (the y2 number) and the y co-ordinate of the position of the entry of the beam particle into the bubble chamber. The scale on the template was normalised to the y hits in P2. The scanners were given

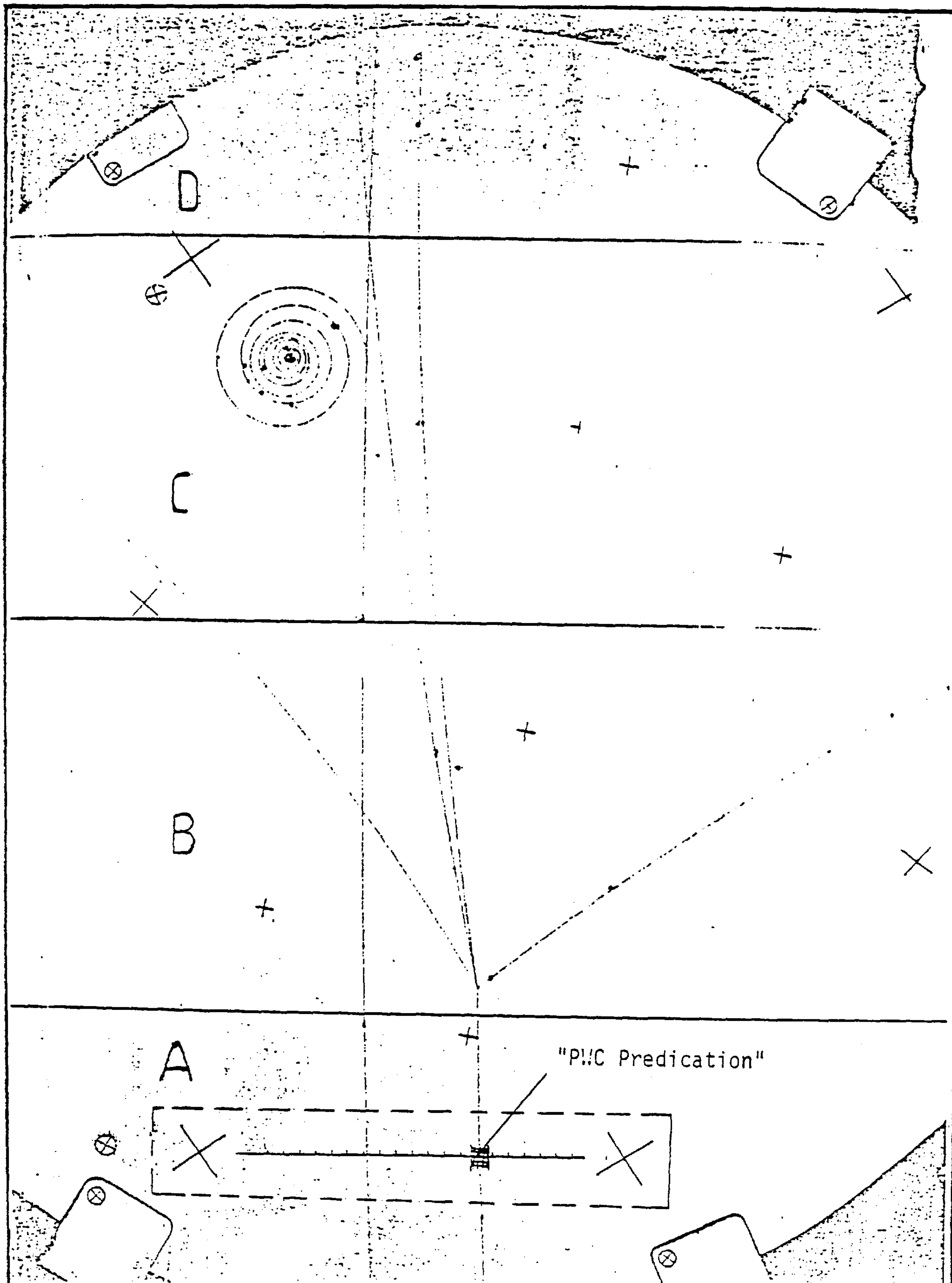

Fig 2.2 Event in the SHF Bubble Chamber(View 3).
The dotted rectangle represents the template(see text).

scan sheets containing for each frame the Y2 number and the tolerance within which to accept an event. This information came from the "PWC tape" produced at the data taking containing all counter information for each hardware trigger (see chapter 1). The guided scan reduced by approximately 35% the number of events measured. Events occuring in region D (see Fig 2.2) were also rejected since the outgoing tracks were not sufficiently long for good reconstruction of the event in geometry.

Initially all events satisfying the above condations were measured. In most of the film, however, only events with visible strange particle decays were measured while the rest were recorded.

After the scanning phase vertices and other points needed to measure the event on an automatic measuring device, the HPD (Hough Powell Device), were predigitised using an online program. This was done on scan tables which were equipped with a measurement system that allowed the predigitisation of coordinates.

Data from the scanning tables were recorded on magnetic tape via a minicomputer. This data was used as input to a program called MIST which assembled the three views for each event. Output from this program was used as input to the HPD controlling program, HAZE.

The HPD is attached to a dual processor PDP10 computer which operates in time-sharing mode. The program HAZE analyses data from the HPD as well as controlling it.

When the HPDs first came into operation it was thought that the HPD, apart from the measuring of events, could perform the event recognition,by the aid of computer programs. Such a performance never materialised however, and some kind of guidance was found to be necessary. At present three levels of guidance are recognised in the measurement of bubble chamber film.

(1) Road Guidance: In this method every track of the event to be measured by the HPD is roughly measured as indicated above. Coordinates of the middle and ends of tracks are measured to an accuracy of 50 - 100 μm on film. Also two well separated fiducials are measured in order to define the coordinate system. These measurements are then used to define roads of width 0.5 - 1mm on film whithin which digitisings of the tracks should lie. The analysis program, HAZE, then uses only those digitisings from the HPD, which lie within these roads for the measurement of the track.

(2) Vertex Guidance: Here pre-digitised information is reduced to a measurement of vertices of the event only and one fiducial mark. The analysis program finds the tracks emanating from the vertex. Having found the tracks it then adopts track following mode to follow and measure each track.

(3) Zero Guidance: In this method no pre-digitising information is given. The only information given is whether an event is present and its topology.

For all strange particle topologies road guidance was used. The HPD using a flying spot digitiser scanned through the film in two possible orthognal modes, for each view. The analysis program proceeds by dividing the track digitisations into equal length slices and calculates for each slice a master point and an ionisation measurement. If the HPD failed to produce these master points for a track due to confusion with overlapping tracks or due to a badly defined road the track was recovered by a program called RESCUE which was on line to a CRT device. An operator with a light pen redefined the road points of the track in question. The output from HAZE was a tape of measurements and a tape of digitisations for events to be rescued.

The measurements of the three views were merged together by a program called SMOG, output from which was used by the geometry program.

Measurement of 400s by Zero Guidance

An attempt was made at measuring the scan-type 400 in zero guidance mode. The processing chain in this case is as illustrated in Fig 2.3. Only the scanning and measuring part differs from the road guidance measurement. Film from the SHF is particularly suited to this kind of an attempt as the frames are relatively clean.

Information from PWC's P1 and P2 were used to locate the approximate position of entry into the bubble chamber of the beam which caused the trigger. Using the masterlist and the PWC tape a file was compiled containing the identity of the event and the y coordinate of the beam at approximately 1 cm into the chamber for each view (see Fig 2.4).

The flying spot produces digitisations of all bubble images on the frame. The object the is to keep the digitisations which represent the tracks and discard all others. In the case of road guidance the road filters the digitisations keeping mainly those corresponding to the tracks. In zero guidance this filtering procedure necessitates the finding of the tracks in order to keep their digitisations.

The zero guidance program used on the Imperial College HPD consists of three distinct parts:-

(1) Part of the HAZE program which controls the HPD.[6]

(2) Beam track following and vertex location package.[7]

(3) CERN Minimum Guidance program which finds and follows tracks from the vertex.

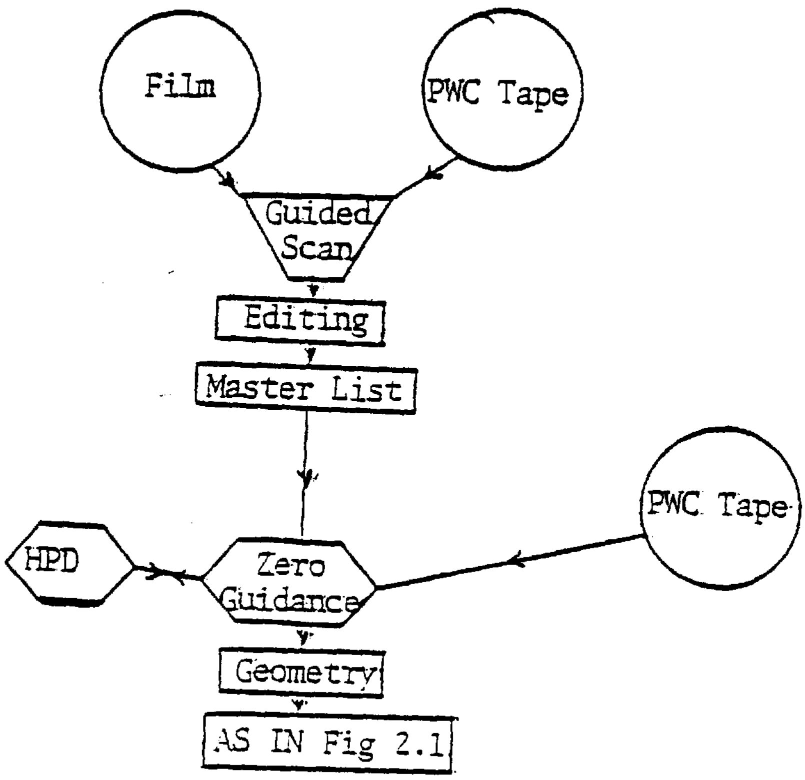

Fig. 2.3 Zero Guidance Processing Chain

After the digitisation for one view is complete in the normal (y) direction, the zero guidance program defines a window of 100y counts (1y count = 1.6 μm, 1 x count = 2μm) centred on the prediction from the PWC's mentioned above. The window is 200 scanlines in x (the Imperial College HPD has a scan line spacing of 60 μm) (see Fig. 2.4). The rectangle thus defined is further divided in y into smaller rectangles; the dividing lines of which have the curvature of the beam. The program tests each segment of the window for a track. When a track is found digitisings from 20 scanlines are connnected into a "string". A "displaced area" is then defined by projection from the found length of track in the current area.

In the case of the beam the projection is according to the equation.

$$\text{Tan } \Theta = A\,(x - B) + C$$

Where: Θ is the angle the beam track makes with the x-axis at position x.

A, B and C are constants found by fitting the beam track along the length of the bubble chamber.

In following a beam in this way the program is always trying to match up successive "strings". Only if it fails to do so, or the track being followed no longer satisfies the beam equation is a vertex suspected. Hence vertex finding in events with a fast forward going secondary track will

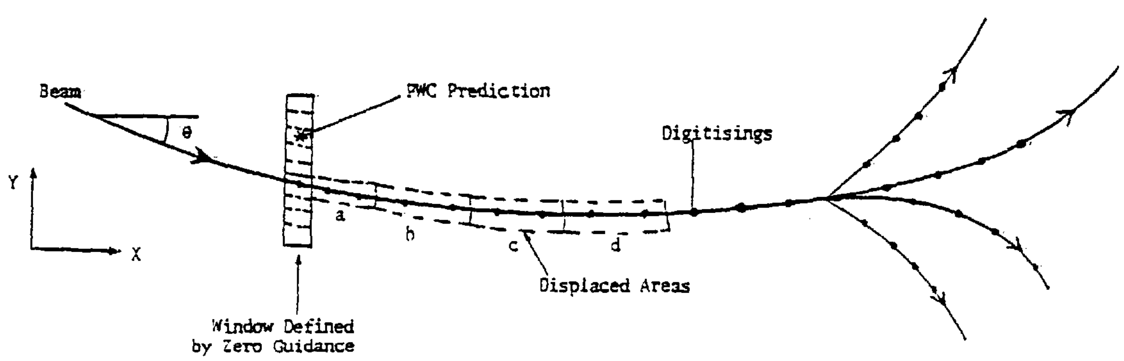

(a)

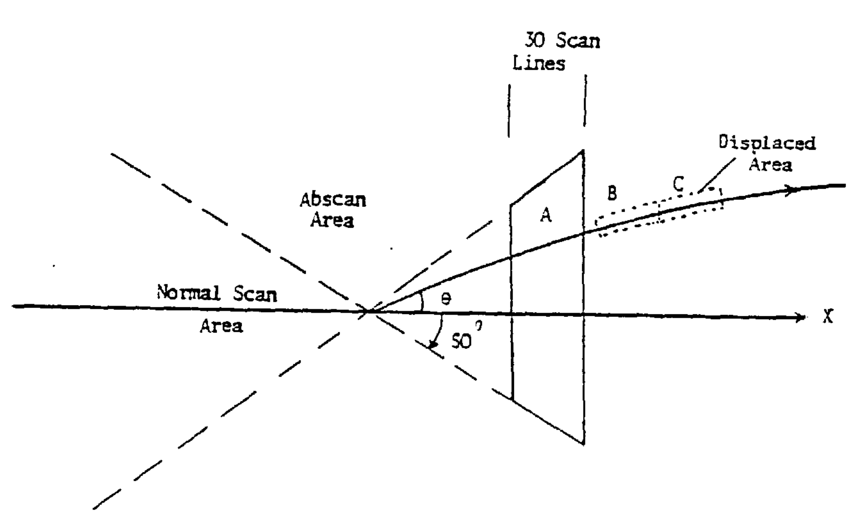

(b)

Fig 2.4 (a) Beam Track Following
(b) Secondary Track Finding

be intrinsically more difficult. A method adopted to counter this was to search for tracks on either side of the beam when a vertex was not found. If a vertex was not found on the current beam the next beam in the window was tested., and if no vertex was found on any of the beam tracks the window was widened to 200 y counts and the procedure repeated.

When a vertex was found the CERN Minimum Guidance (M.G.) program was employed to locate all the secondary tracks emanating from it. Briefly the program works as follows. The area around the vertex is divided into 4 sectors according to whether tracks should be picked up in the "normal digitisings" (scan along y) or the "abnormal digitisings" (Scan along x). M.G. then does a tanθ/y scatter plot of the digitising in region A (see Fig. 2.4 (b)). If this scatter plot indicates tracks, then each is followed in a similar manner to the beam following. The above procedure is repeated for other quadrants if all tracks are not found in the current area. The HPD does an abscan of the frame while tracks are being located in the normal scan digitisings. The measurements are output to a tape which is used for input to the geometry program as in road guidance.

Approximately 136 thousand frames were measured on the HPD in the zero guidance mode. The overall pass rate through the processing chain was approximately 50% of the pass rate through the HAZE processing chain.

2.1.3 Geometrical Reconstruction[8]

The geometric reconstruction of tracks in three dimensional space from the three two dimensional projections was done by the CERN HYDRA GEOMETRY program. The coefficients needed for the transformation from film space to bubble chamber space were determined using a conventional hand measuring machine. The geometry program calculated and wrote out an output tape containing the coordinates of all the vertices and end points of the stopping tracks and curvature, dip and azimuth angles of the tracks at the respective vertex with corresponding errors. The track errors calculated depends on the mass assignment to the corresponding particle. The geometry output contained residuals for all such successful mass assignments which were useful at hypothesis selection stage.

In the final stage of the geometry program an attempt was made at improving the parameters for the beam and fast outgoing tracks. This was done by combining ("Hybridisation")[9] the measured bubble chamber information and the PWC hits P1 to P5. Using the three momenta and vertex position from the bubble chamber measurements the fast forward and beam tracks were swum to the downstream and upstream PWC's respectively. The PWC's were searched for corresponding hits and if found an overall χ^2 fit to these hits and bubble chamber measurements was attempted. In the case of badly measured (small) beam tracks title values were used for the swimming of the beam to P2, P1. If the resulting "hybridised χ^2" value was good the new track parameters were kept. The hybridisation of the bubble chamber track measurements significantly improved the measurement of the fast outgoing tracks. Detailed results of the hybridisation can be found in |10| .

The output tape from the geometry was used as the input to the kinematics fitting program. The kinematic program GRIND was used to find the mass assignments "hypothesis" consistant with the measured data.

2.1.4 Kinematical Fits[11-12]

The mass assignments considered in GRIND depend on the topology of the event. For a given topology a complete set of possible mass permutation of the final state particles, satisfying the quantum number conservation laws, was compiled. The hypotheses considered made allowance for the presence of one or more, unseen, neutral particles which may have been produced. When no unseen neutral is present the conservation law of energy and momentun impose four constraints (4c) on the measured variables. A 4C - fit then determines the best estimate for the variables by means of a four-constraint least - squares method. When a single unseen neutral is present a 1C - fit determines the "missing" quantities. When more unseen neutrals are produced there are more unknowns than equations. The unseen neutral particles are then represented by a fictitious object with its mass and momentum being determined in the conservation laws. Although there is no real fit in this case the term 0C - fit is usually used.

A first criterion in deciding which hypothesis is to be tried in a particular event configuration is the missing - mass criterion. After having made a particular hypothesis about masses of each of the charged secondary tracks, the missing mass is derived from the measured data, and is given by:

$$MM^2 = (E_{inc} - \sum_i^n E_i)^2 - (\underline{P}_{inc} - \sum_i^n \underline{P}_i)^2$$

where E_{inc} = Total incoming energy

E_i = Energy of secondary particle i

P_{inc} = Beam momentum

P_i = Momentum of secondary particle i

n = Number of secondary particle i.

The MM^2 being understand within the measurement errors .

If MM^2	=	0	No unseen neutrals 4C - fit is attempted
MM^2	=	M_i^2	One useen neutral with mass M_i, 1C - fit is attempted
MM^2	$\geqslant$	$(M_k + M_{\pi^o})^2$	More than one unseen neutrals, OC -fit

M_i is the mass of a particle ,within the measurement error.

GRIND results list all hypotheses considered with the fitted momenta and their errors for the successful fits and the reason for failure in the case of rejected hypothesis.

Below are listed the kinematic constraint class of the important final states belong to the scan-type 201 in the k^- induced reactions :-

Reaction	Kinermatic Constranit at Primary Vertex
$k^- p \rightarrow \Lambda \pi^+ \pi^-$	4C
$\Sigma^o \pi^+ \pi^-$	2C
$\Lambda \pi^+ \pi^- \pi^o$	1C
$\Lambda \pi^+ \pi^-$ + neutrals	OC

The $\pi^+\pi^-\Sigma^0$ hypothesis is raised to a 2C - fit due to the $\Lambda\Upsilon$ being constrained to be a Σ^0.

The output from GRIND, called the Grind Library Tape (GLT), contained both the kinematic and geometry results. The ionization data was also transmitted through the chain to the GLT.

Each event on the GLT was in three possible situations.

(1) The event had a unique hypothesis.

(2) The event had a two or more ambiguous hypotheses.

(3) The event failed in geometry or kinematics.

2.1.5 Hypothesis Selection [13]

The purity of a final state can in general be affected by events belonging to the final state being misassigned or by events failing to yield any acceptable fit.

A selection stage is necessary to check the results of the kinematic program and to reduce the number of hypotheses assigned to an event. An important piece of information which facilitates this in bubble chamber experiments is the bubble density of the charged tracks which is related to the velocity and hence to the mass of the particles.

The GRIND output was subjected to an automatic hypothesis selection program called AUTOGRIND. This,apart from ionization information also utilises information from the external cerenkov CANUTE (C 2) .
In the π^{+} induced reactions no light in CANUTE implied that the fast, triggering, track could confidently be assumed to be a kaon or a proton. Only events which had a hybridised outgoing track and a hit in the hodoscope, s3, were used for physics analysis. In the k^{-} induced reactions a hodoscope hit was not demanded. The hybridisation requirement, CANUTE having light and a negative signal from themuon counter implied that the fast track was probably a pion. These pieces of information were important since at these high triggering momenta ionization cannot help in particle identification.

In approximately 35% of the cases automatic selection of hypothesis could be made by the program. The automatic selection being made only if the trigger track had a momentum greater than the set values and measurement of the event was considered acceptable through examination of mass-fit residuals.

The AUTOGRIND output contained a list of all decided and undecided events. The undecided events were checked on the scan table where the event was examined and the predicted track ionization was compared to the observed bubble density on the film.

Most of the ambiguities in the kink (Σ) events were due to uncertainty in the Σ decay mode, these could easily be resolved on the scan table by ionization of the decay track. The final state $\Lambda\pi\pi$ and $\Sigma^0\pi\pi$ are often ambiguous and usually both hypotheses have to be accepted. To further increase the purity of the sample we demanded a χ^2 probability of > 1% for 4C hypotheses and >5% for 2C and 1C fits. In the events where the ambiguities could not be resolved all kinematic fits consistant with the given information were accepted. A check on final state separation is shown in Fig 2.5. Contamination of the 2C channel by the 4C at a few per cent level is evident. Ambiguities being resolved by taking the highest constraint or the highest probability in the case of equal constraint fit. (More detailed information on processing final states containing Λ or Σ can be found in ref |14| and |10| respectively).

The result of the combination of physicist and Autogrind decisions was a file of 'Slice-Cards' which contained decisions for each event. Decision was always one of the following:

(1) One or more hypothesis assigned.

(2) Measurement quality inadequate (remeasure).

(3) Event rejected.

Events were rejected , if outside the fiducial volume, not properly measurable or failure to find any acceptable hypothesis.

The 'Slice-Card' file together with the GLT and the Masterlist file were then used to run the DST (Data Summary Tape) program which produced an output tape for physics analysis.

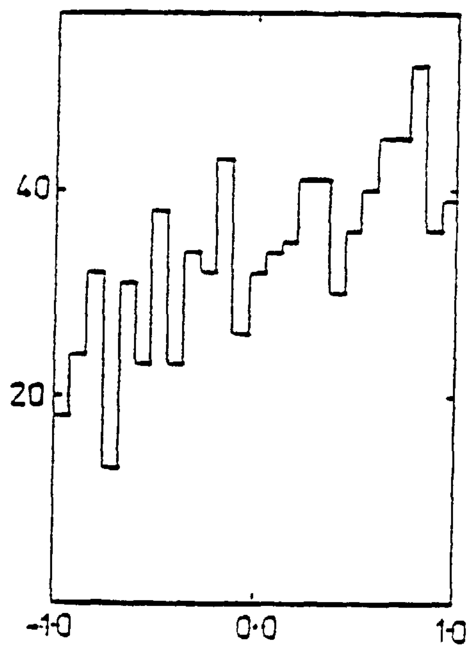

(a)

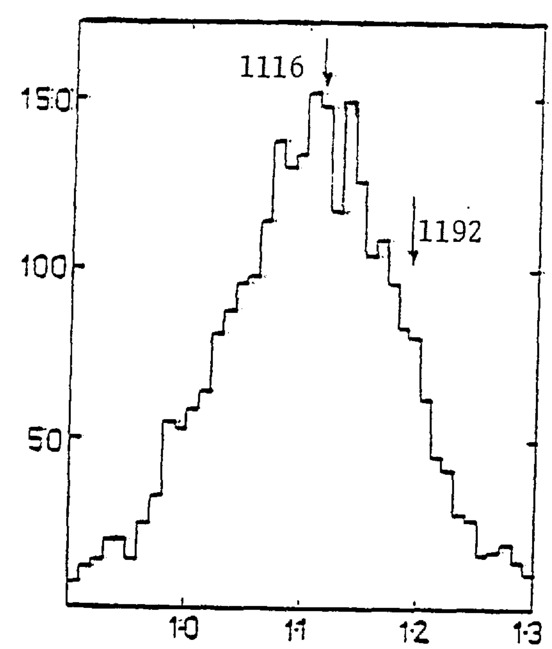

(b)

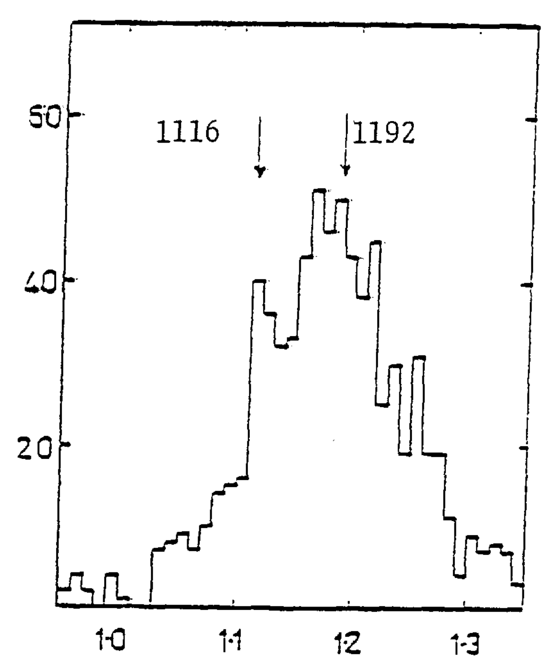

(c)

Fig 2.5 (a) Cosine of the angle between Λ direction in the Σ^o rest frame and Λ line of flight. $\Sigma^o \to \Lambda\gamma$ should have a flat distribution. Missing mass to the $\pi\pi$ (πK) system, calculated with unfitted momenta, for events assigned to final state $\Lambda\pi\pi$, $\Lambda\pi K$ (b) and $\Sigma\pi\pi$, $\Sigma\pi K$(c).

2.2.1 Corrections: Scanning Losses [10 14 15]

All the events used in this thesis have a scan-type involving the visible decay of a strange particle . Hence losses are expected to occur due to decays outside the visible region of the bubble chamber and for decays which for geometrical reasons are not recognised by the scanners. The main reasons that the scanner misses events are:

(1) the length of the track between the production vertex and the decay vertex of the lambda or sigma is very small.

(2) the track lenth of the lambda or sigma is such that it decays outside the illuminated volume of the chamber

(3) the decay angle between the track of the sigma and the track of its charged decay product is so small that the kink is not recognised.

Losses of type (1) will result in scan-type 201 events appearing as 400's and scan-type 210 appearing as 200's. Type (2) losses will be particularly severe for $\Sigma^+ \rightarrow p\ \pi^0$ decay. (1) and (2) give rise to the so-called length weight while (3) results in the small angle weight for the kink events.

The idea of weighting is to correct for the above losses by applying cuts to the data sample in such a way that the remaining data are in a region where the detection efficiency is known. The events in this data sample are then given a weight, which is the inverse of the detection probability . This then compensates for the data falling outside the cuts.

In order to correct for losses due to (1) and (2) above, one has to calculate the probability for the hyperon decay occuring between L_0 and L_1 ; where L_0 is the short length cut-off for decays near to the production vertex and L_1 is the length a hyperon can travel before leaving the illuminated volume of the chamber.

The probability that a particle will travel, without decaying, a distance greater than or equal to L_o is given by;

$$P_1 = \exp(-L_o / \eta c\tau)$$

where: $\eta = \frac{p}{m}$

P = Momentum

m = Particle mass

τ = Particle lifetime

The probability that the decay will take place between L_o and L_1 is therefore given by

$$P_2 = \exp(-L_o/\eta c\tau) - \exp(-L_1/\eta c\tau)$$

Since the scan is done using projections of the tracks it is more realistic to change the formulae accordingly and to use the projected distances.

The probability of having a decay between the projected distances l_o and l is:

$$P_2' = \exp(l_o/\eta c\tau \cos\lambda) - \exp(-l/\eta c\tau \cos\lambda)$$

where λ = dip angle of the hyperon tracks*

---

* The dip (λ) and azimuth ($\emptyset$) of a track are defined by:

dip : $\lambda = \text{arctg}\,(P_z / (P_x^2 + P_y^2)^{\frac{1}{2}})$

azimuth : $\emptyset = \arcsin(P_y/(P_x^2+P_y^2)^{\frac{1}{2}}) = \text{arcos}\,(P_x/(P_x^2+P_y^2)^{\frac{1}{2}})$

with P_x, P_y, P_z : the three components of the momentum vectors of the track.

The correction is then performed by cutting away all events where the projected length of the hyperon track is smaller than l_0 or greater than l, and weighting the remaining events with:

$$W_1 = \frac{1}{P_2'}$$

The cut-off values for the decay length are determined as follows. For various values of l_0, the total weighted number of events is plotted while l is held fixed and conversely l_0 is fixed and l varied. When the cut-off length enters the region where detection probability is unity the weighting procedure compensates exactly for the number of events cut away and the total weighted number reaches a plateu value. The cut-off values are chosen at the point where the weighted number of events reaches its plateau value. More details of this procedure for forward Λ prodcution can be found in chapter 5. Unless otherwise stated the lower cut for both the Σ^+ and Λ hyperons was chosen to be 8 mm while, the upper length cut was 15 cm for the Λ and 6 cm for the Σ^+.

The kink events give rise to a second weight usually referred to as the small angle weight. This arises due to the loss of events as a result of the opening angle between the Σ and the charged decay product being too small to discern the kink. There are three correction methods for the losses caused by small angle decays.

(1) A correction method which makes a cut on the space angle between the sigma track and its charged decay product.

(2) A correction method, which makes a cut on the projected angle between the sigma track and its charged decay product.

(3) A correction method using a detection efficiency function in the region below the cuts of methods (1) and (2).

In (1) each event remaining inside the cuts is given a weight

$$W_\theta = \frac{2}{\cos\theta^*_{MAX} - \cos\theta^*_{MIN}}$$

$\cos\theta^*$ is the cosine of the decay angle in the Σ rest-frame, the maximum and minimum values being determined in the same way as the length cuts.

In method (2) the projected laboratory decay angle is used as opposed to the space angle of (1). In the third method a parametrised efficiency function is used for the region where the detection efficincy is no longer 1, however it is usually difficult to make a priori predictions about the form of the efficiency function. In this experiment method (2) was adopted. Small-angle losses were found to be important only for the protonic decay of the Σ^+.[10] Where the data were small only neutron decay mode was used for cross-section estimates to avoid statistical fluctuations that can be caused by relatively high weights.

2.2.2 Geometric Losses

Since this was a triggered experiment a loss of events will occur due to the trigger particle failing to traverse the down stream counter due to the geometric acceptance of the SHF. This loss of events will obviously be a function of the kinematic variable t, the four momentum transfer to the target, and the position of the interaction in the bubble chamber.

For each event reaching the DST a geometric accentance weight was generated. This is just

$$G_W = \frac{1}{G_A}$$

where G_A is the geometric acceptance probability for an event G_A was estimated by swimming tracks with the parameters p, λ, ϕ, of the trigger track through the down stream system (see Fig 2.6).

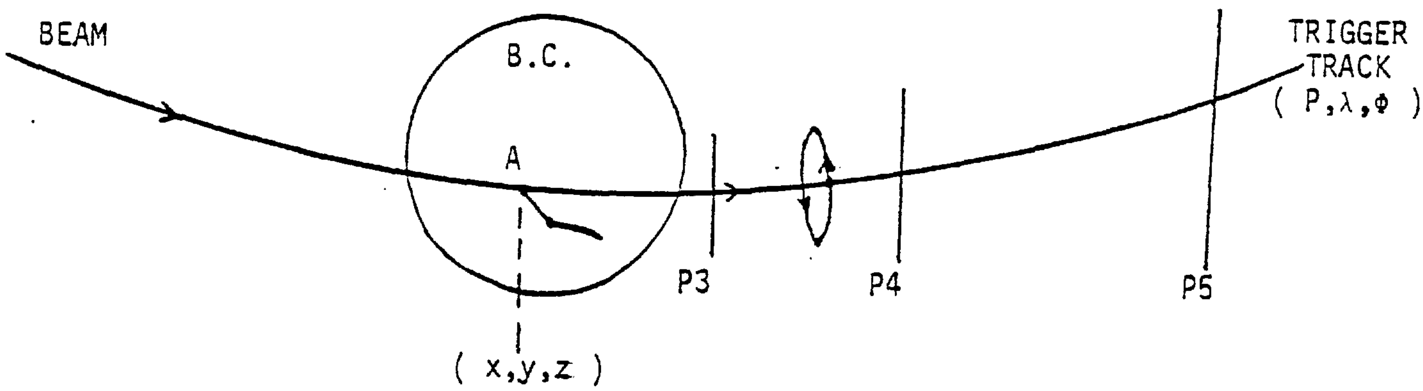

Fig 2.6 Geometrical weight estimation.

The interaction vertex (A in Fig 2.6) position was moved to various positions within the fiducial volume. The X, Y, Z co-ordinates were generated such that X was random within the fiducial volume, Y and Z were Gaussian as given by the beam profile. The outgoing track was randomly rotated about the beam direction while keeping the scattering angle constant for the given event. The angle Ø was computed for each x value since Ø changed with x due to the magnetic field. Trigger tracks were swum to the down-stream hodoscope in the π^+ exposure and the middle of CANUTE for the k^- exposure. A cut on $|t| < 1.0$ $(\mathrm{GeV}/c)^2$ was imposed on the data to keep the geometric acceptance weight low. G_A was then simply given by the ratio of the tries in which the fast track was swum successfully through the downstream system and the total number. The geometric acceptance of various reactions will be described in the following chapters.

2.2.3 Algorithm Losses

As described in chapter one the software algorithm was designed to act as a beam veto which moves with the position of each beam track. The veto was parametrised in terms of difference in hits between the trigger track and the would-be beam track at PWC P3 and P5. This veto thus rejected events occuring at very low |t|. The effect of the veto was studied in a similar manner to that described in 2.2.2 and an algorithm weight was assigned to each event. It was larger than one for events at $|t| < 0.01$ only.[10]

2.3.1 Overall Normalisation[10 16 55]

The channel cross-section is given by:

$$\sigma = \frac{1}{n\ \lambda}$$

λ = Mean free path for a particular final state

n = Number of nuclei per unit volume

$$\lambda = \frac{N_B . L}{N_e}$$

where N_B is the total number beam tracks passing through the chamber

N_e is corrected number of events in the final state being considered

L is the fiducial length which was chosen to be 65 cm with $-40 < x < 25$.

$$\sigma = \frac{N_e . t}{N_B . L} \quad \text{where } t = \frac{1}{n} = \frac{A}{N_A \rho}$$

A is the gramatomic weight.

ρ is the density of hydrogen

N_A is Avogadro's number.

In estimating N_B and N_e corrections are necessary which are normally associated with purely counter experiments. Besides the corrections mentioned in section 2.2, which are necessary for physics analysis, the following further corrections are required, to N_e, for channel cross-section estimation.

(1) Processing throughput efficiency

(2) Scanning correction

(3) Fast trigger losses

(4) Slow trigger losses.

The total number of beam tracks, N_B, to first approximation could be estimated from the S1 . C1 . S2 signal (see chapter 1). Corrections to this estimate were required for the following:

(a) Beam contamination

(b) Beam interaction or decay downstream of C1

(1) <u>Processing throughput efficiency</u>

A correction, to N_e, is required for events lost in the event processing chain. This loss would occur due to unmeasurable events or due to bad measurement in the HPD resulting in failure in geometrical reconstruction. This loss is expected to be random. The correction factor is

$$W_p = \frac{N + R}{N}$$

where N is the number of events of a particular scan-type

R is the number of unmeasurable or to be remeasured, events of the same scan-type.

(2) Scanning Correction

This is a correction for events lost at the scanning stage. A small sample of the film was scanned twice to estimate this correction. If the number of events for a given scan-type seen in each scan are n_1 and n_2 and the number seen in both the scans in n_{12} then assuming the scans to be independent the scanning efficiency is then given by

$$e_s = \frac{N_{12}\ (N_1 + N_2 - N_{12})}{N_1\ N_2}$$

the scanning weight is then

$$W_s = \frac{N_1\ N_2}{N_{12}\ (N_1 + N_2 - N_{12})}$$

(3) Fast Trigger losses

A fast trigger could be lost due to (a) the dead time of the electronics counters and (b) the fast outgoing track decaying or interacting (c) two or more in time beam particles.

(a) A dead time of 200 nSec was imposed to allow readout and storage of the counter data. Another fast trigger occuring within this time interval was rejected. Second cause of loss of fast triggers was that only a maximum of two fast triggers were allowed from each beam spill.

(b) In cases where the fast forward particle interacts or decays the fast trigger is lost. The loss due to interaction was estimated from the knowledge of the amount of material through which the particle had to pass. The loss due to decay was more important in the π^+ exposure where a fast forward k^+ could decay into a lighter particle which by giving light in CANUTE would veto the trigger.

(c) In the π^+ exposure, where no light was required in CANUTE,a fast trigger would have been rejected if one or more beam particles arrived in time with the beam that caused the trigger.

(4) Software Algorithm Losses

Losses in this section of the trigger occured as a result of (a) multiplicity cuts in the PWC's, (b) muon counter punch through (c) PWC inefficiencies

(a) Fast triggers with greater than two hits in the upstream PWC's were rejected. Any spill with greater than 12 beam particles was also rejected in the algorithm.

(b) In the k^- exposure the triggering π^- could punch through muon veto, see Fig. 1.1. This would lead to rejection of the trigger. To estimate the loss of triggers due to the punch through some π^- film was taken. Pictures were taken on a fast non beam particle passing through the downstream system (mostly elastic π^-s). For events where the triggering track hybridises the muon counter was examined and hence the punch through estimated. It was found to be approximately 6%

(c) A fast trigger was rejected if the algorithm failed to find a certain combination of hits in the PWC's.

An upstream space point was required in either P1 or P2, hence a hit was required in both the y and z planes. While downstream all three planes were required to be hit in two of the PWC's and at least one matching hit in one of the three planes of the third PWC. Thus PWC inefficiencies resulted in fast triggers being rejected. This loss was corrected for by estimating the PWC efficiencies as follows:

An offline program was used to search for track trajectories using the PWC data for each hardware trigger. Briefly the program worked as follows:[54]

(a) Combination of hits from the upstream PWC were used to define a beam trajectory.

(b) The downstream PWC's were used to construct a trajectory through the downstream PWC's.

(c) If trajectories were found in both (a) and (b) an overall trajectory was searched for by giving a variable interaction position and scattering angle, of the beam trajectory in (a), within the bubble chamber. An acceptable trajectory through the SHF was required to have a hit on at least 11 out of the possible 13 planes.

Procedure (a) - (c) was repeated if more than one trajectory was found in either the up or downstream PWC's. Inefficiencies thus showed up as missing hits in the planes. The plane efficiency was then given by

$$\frac{\text{hits}}{\text{hits} + \text{misses}}$$

Table 2.1 shows the individual plane and the combined PWC station efficiencies.

Fig 2.7 shows the PWC'S hit distribution reconstructed from the PWC effeciency program mentioned above.

From the PWC station (P1 - P5) efficiencies the upstream and downstream overall PWC efficiencies were calculated as follows:

in the upstream PWC's only one of the two PWC's was required to have a full complement of hits. Hence the upstream PWC efficiency is:

$$P1.P2 \;+\; P1.\,(1 - P2) \;+\; P2.\,(1 - P1).$$

The overall downstream PWC efficiency is:

$$P_3\,P_4\,P_5 + P_3\,P_4\,\overline{P}_5 + P_3\,\overline{P}_4\,P_5 + \overline{P}_3\,P_4\,P_5$$

$\overline{P}$ is the efficiency for having 1 or 2, but not 3, hits in a station and is given by:

$$\overline{P}_i = \sum_{\substack{yzu \\ \text{cyclic}}} P_y\,P_z\,P_u' \;+\; P_y\,P_z'\,P_u'$$

where $P_i' = (1 - P_i)$

The number of events were thus corrected for the combined inefficiency of the PWC's.

Corrections to the number of the beam tracks, N_B, as estimated from the upstream counter had to be corrected for contamination and beam perticle decay or interaction before reaching the bubble chamber.

(a) Beam Contamination

In the π^+ exposure signature for a good beam particle was

S1. C1. S2

where C1 gave light for π's and lighter particles. A lead filter removed electrons from the beam leaving muons as a source of contamination.

The muon contamination was estimated by a special π^+ run where the beam was allowed to punch through the muon veto. Knowing the punch through the contamination of the beam was estimated and was approximately 5%.

The $\overline{P}$ contamination of the k^- beam was estimated to be $\leq 2\%$.

(b) Beam interaction/decay

The number of beams N_B, had to be further corrected for interaction and decays upstream of the bubble chamber. The main sources of interaction being the beam hodoscope S2 and the entrance windows of the vacum-tank and the bubble chamber.

Summary

The channel cross-section is then given by:

$$\sigma = \frac{\prod_i W_i \cdot N_e \cdot t}{\prod_j W_j \; N_B \cdot L}$$

where $\prod_i W_i$, $\prod_j W_j$ are products of the weights for correction discussed above. Weights for various corrections are listed in table 2.2.

RUN	π^+				K^-			
WIRE PLANE / PWC	y	u	z	OVERALL	y	u	z	OVERALL
P1	90		90	81	89		88	78
P2	95		97	92	91		90	82
P3	97	93	95	86	85	94	93	83
P4	97	95	95	87	96	94	95	86
P5	94	92	95	83	94	96	95	86

Table 2.1 PWC efficiencies for π^+ and k^- runs.

(Statistical error $\leq$ 4%)

Type of Loss	$\pi^+ p \to K^+_{fwd}$ (%)	$K^- p \to \pi^-_{fwd}$ (%)
Beam PWCs inefficiency	7.4 ± 2.0	9.0 ± 2.0
Downstream PWCs inefficiency	6.0 ± 2.0	6.0 ± 2.0
Beam track interaction or decay	7.4 ± 2.0	15.5 ± 3.0
Trigger track interaction or decay	16.7 ± 4.0	12.3 ± 3.0
Beam contamination	5.5 ± 1.5	-
Hadron punch-through	-	5.7 ± 1.5
C2 resolution	3.0 ± 1.0	-
Multiplicity cuts	7.5 ± 1.0	8.4 ± 1.0
Scanning*	3.3 ± 1.5	4.6 ± 1.5
Measuring*	15.0 ± 3.0	15.0 ± 3.0

Table 2.2 Typical values used to correct the cross-sections.

* refers to the topology: 2-. r σ 1·0

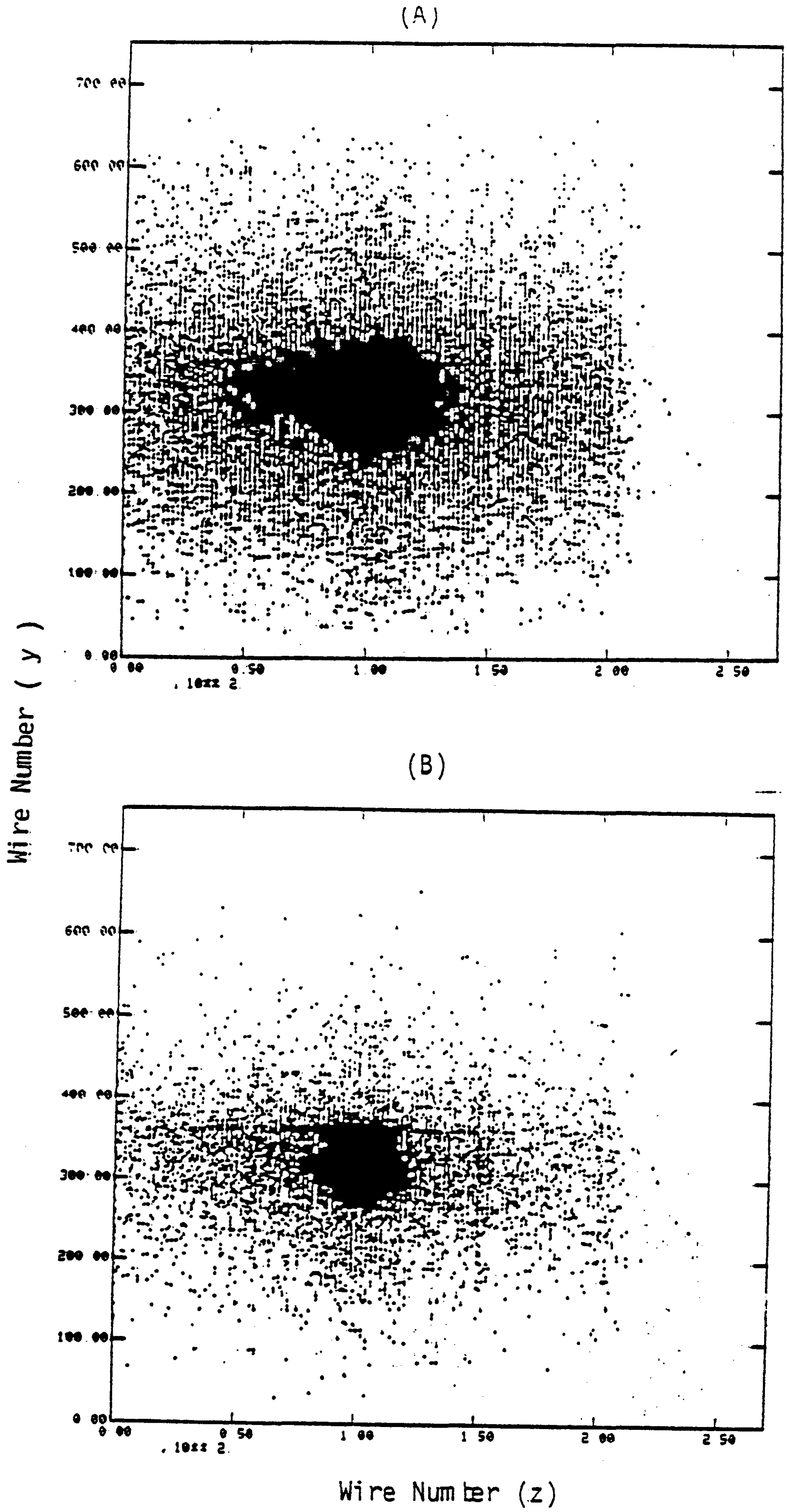

PWC P 3

Fig 2.7 (i) PWC hit distribution

(A) Hits found in all 3 subplanes

(B) Distribution of 'missing hits' (in one or more of the subplanes)

Dead wires and support wires(in P4 and P5 only) are clearly visible.

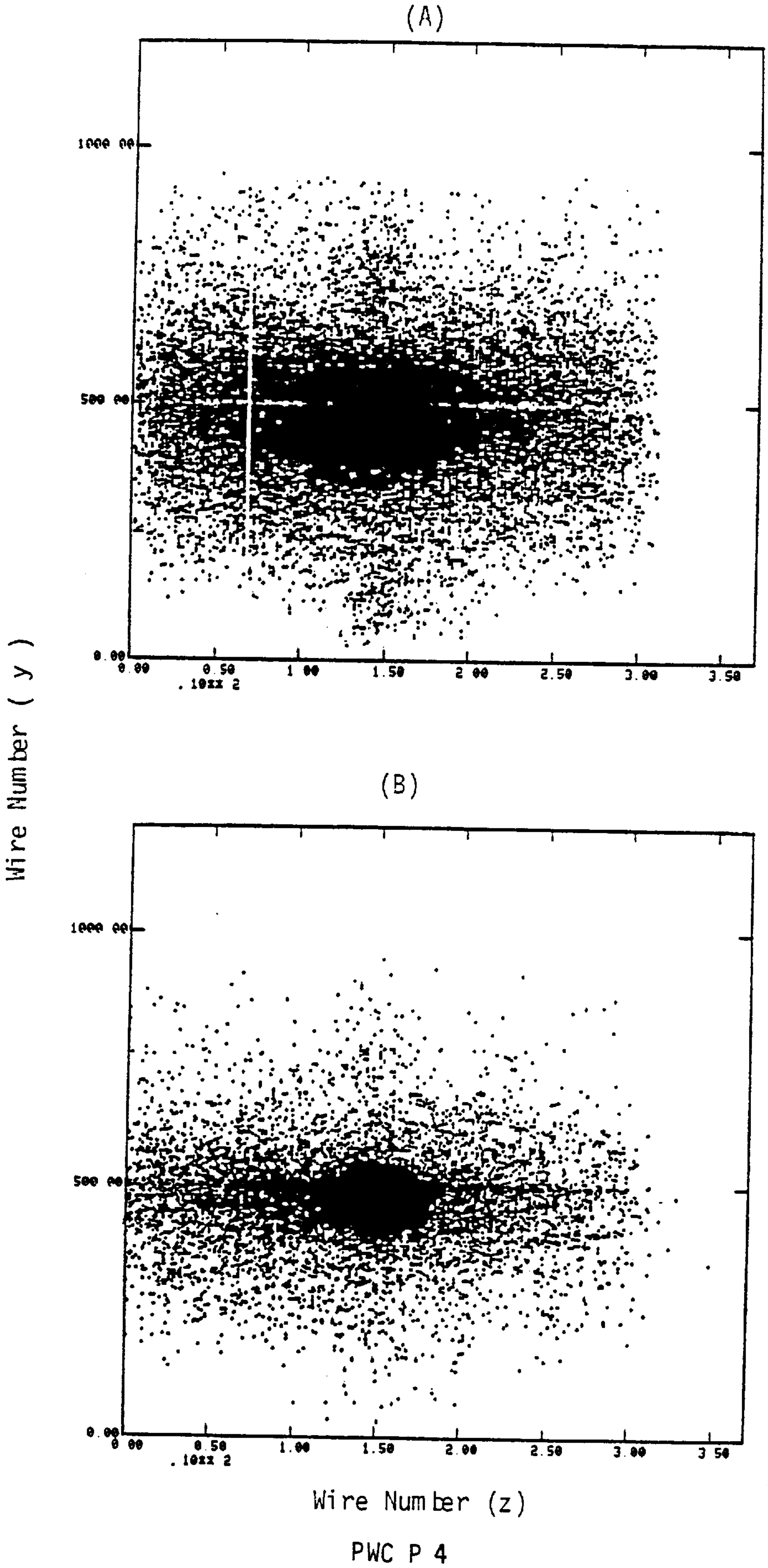
(A)
1000.00
500.00
0.00
0.00
0.50
.10xx 2
1.00
1.50
2.00
2.50
3.00
3.50
Wire Number (y)
(B)
1000.00
500.00
0.00
0.00
0.50
.10xx 2
1.00
1.50
2.00
2.50
3.00
3.50
Wire Number (z)
PWC P 4

Fig 2.7 (ii)

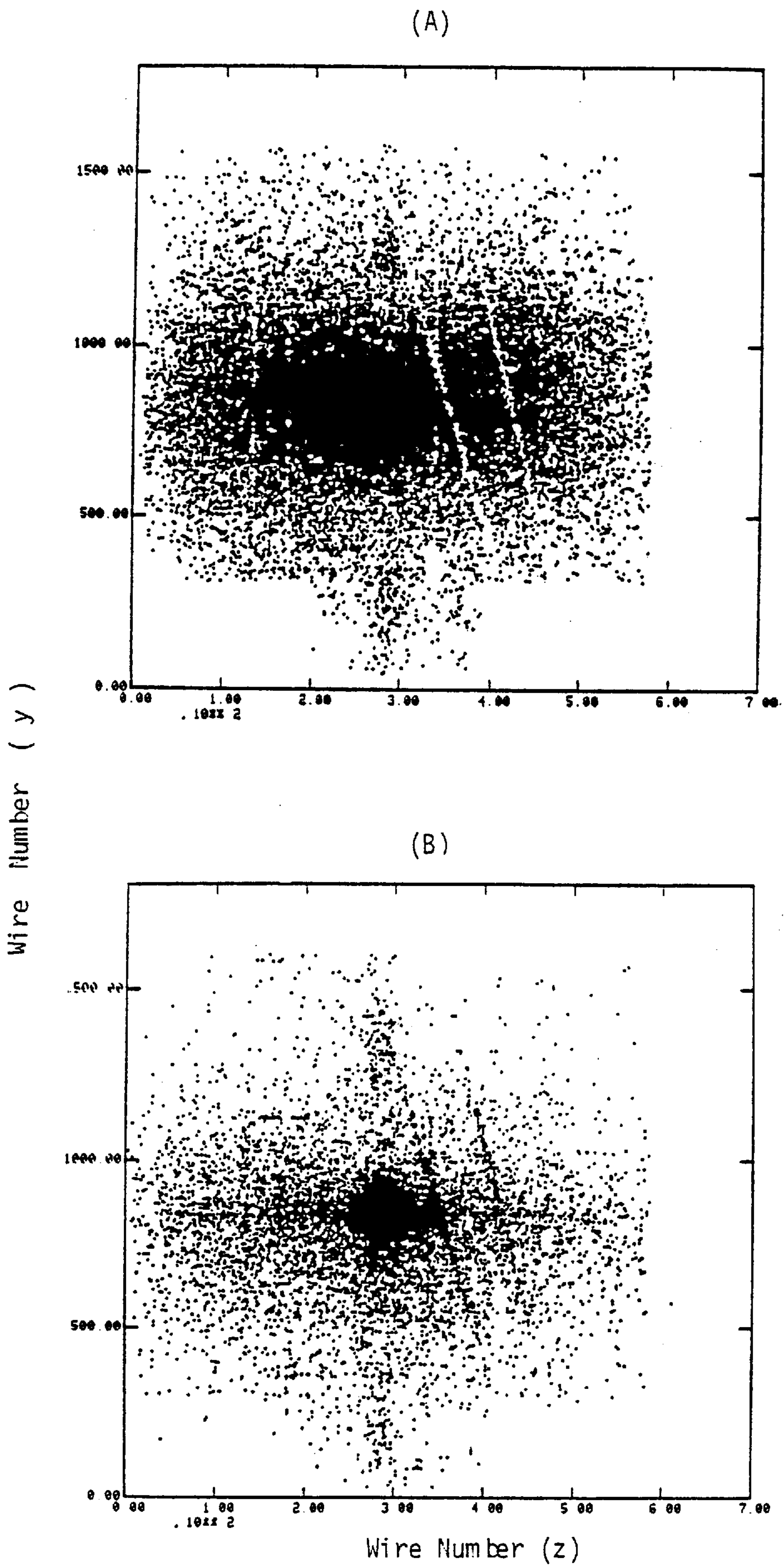

PWC P 5

Fig 2.7 (iii)

CHAPTER 3

Vector Meson Production in Hypercharge Exchange Reactions

3.1 Introduction

Analysis of vector meson production in hypercharge exchange reactions of the type:

$J^P \quad 0^- \quad \tfrac{1}{2}^+ \rightarrow \quad 1^- \quad \tfrac{1}{2}^+$

in:- $\pi^+ p \rightarrow k^{*+}(890) \quad \Sigma^+$ (1)

$k^- p \rightarrow \rho^- \quad \Sigma^+$ (2)

$k^- p \rightarrow \rho^0 \quad \Lambda$ (3)

and $J^P \quad 0^- \quad \tfrac{1}{2}^+ \rightarrow 1^- \quad \tfrac{3}{2}^+$

in:- $\pi^+ \; p \rightarrow k^{*+}(890) \; \Sigma^{*+}(1385)$ (4)

$k^- \; p \rightarrow \rho^- \quad \Sigma^{*+}(1385)$ (5)

at 7 GeV/c is presented. These reactions were studied in conjunction with the S.L.A.C 11.5 GeV/c data.

Total and differential cross-sections, sigma polarization and vector meson decay angular distributions are presented. Energy dependance of a reaction from each of the two types is discussed, low energy results being available for reactions (3) and (5) only. These came from the 4.2 GeV/c k^- p experiment.[17 18] Comparisons are made with corresponding pseudoscalar production reactions.

3.2 Motivation[19]

A prominant feature of inelastic collision processes is the presence and often dominance by quasi-two-body reactions, usually in peripheral interactions involving small momentum transfer,

$$\text{i.e.} \qquad a + b \rightarrow c + d \qquad\qquad (a)$$

c and/or d being mesonic or baryonic resonances.

The relatively small (0 - 1 $(\mathrm{GeV}/c)^2$) momentum transfers indicate that the long range part of the strong interaction force plays a dominant role. This led in the early 1960's to numerous attempts to interpret such peripheral collisions in terms of a model wherein a light particle is exchanged by the participants in the collision. (The one meson exchange model).

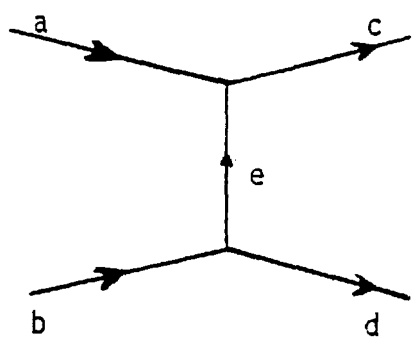

Feynman diagram for one-meson exchange

The reaction amplitude for (a) will therefore contain the propagator, e, and two coupling constants from the two vertices (ace) and (bde). Clearly differential cross section measurements alone will not be enough to distinguish between models which employ different e's that do not differ appreciably in mass. Since besides the flexibility in the vertex coupling constant additional form factor can be introduced for the object e itself. If however either of the production products has spin and is unstable, the decay angular distribution can be used to give further clues about the system e than are attainable from just the differential cross section.

Following the failure of the one-particle exchange model to describe the data adequately the exchanged particle, e, was replaced by Regge trajectory, $\alpha(t)$. However, what ever the model employed to describe the peripheral interaction, the complexity and detailed structure of the exchanged system is not important.

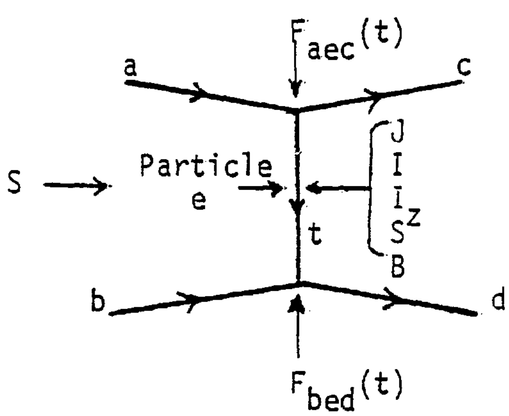

One Particle Exchange

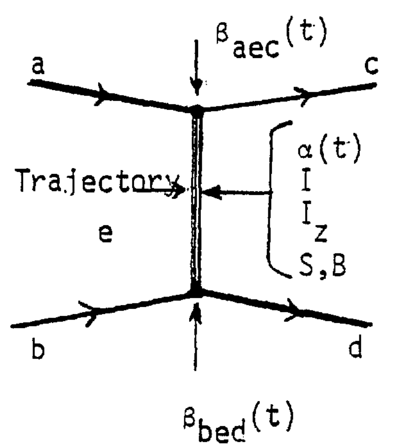

Regge Trajectory Exchange

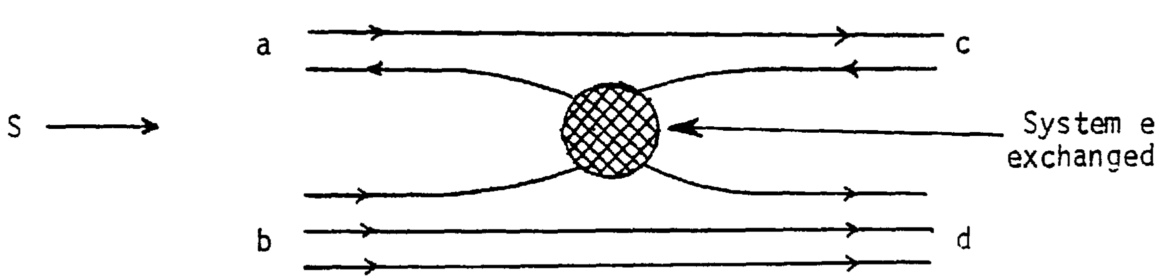

Quark - Quark Interactions

Analogies between the one particle exchange, Regge trajectory exchange and the system e exchange in quark-quark interactions.

In each case above information about the exchanged system will help to give insight into the reaction mechanism. From the decay angular distribution of the vector meson,produced in the reaction to be discussed, it is possible to extract the spin parity relation of the exchanged system.[20]

3.3 Data

The data used for the vector meson study comes from the topology 201 with visible Λ decay, and 210 with visible Σ^+ decay. The reactions studied come from the following channels:-

Channel	Reaction	
$\pi^+ p \rightarrow k^+ \pi^0 \Sigma^+$	$\pi^+ p \rightarrow k^*(890)\ \Sigma^+$	(1)
$k^- p \rightarrow \pi^- \pi^0 \Sigma^+$	$k^- p \rightarrow \rho^- \Sigma^+$	(2)
$k^- p \rightarrow \pi^- \pi^+ \Lambda$	$k^- p \rightarrow \rho^0 \Lambda$	(3)
$\pi^+ p \rightarrow k^+ \pi^0 \pi^+ \Lambda$	$\pi^+ p \rightarrow k^{*+}(890)\ \Sigma^{*+}(1385)$	(4)
$k^- p \rightarrow \pi^- \pi^0 \pi^+ \Lambda$	$k^- p \rightarrow \rho^- \Sigma^{*+}(1385)$	(5)

To increase the purity of the data sample a χ^2 - prubabability cut of>1% for 4C and>5% for 1C - fits was imposed. If an event was still cossistant with more than one fit ambiguities were resolved using the following criteria:-

(1) Highest constraint fit was chosen

(2) Highest probability fit was selected

In addition only events for which a fast outgoing track hybridised downstream were used.

(1) $\pi^+ p \rightarrow k^+ \Sigma^+\pi^0$

As can be seen from the projections of the scatter plot in Fig 3.1 there is a low mass peak in the 1660 Mev region which contribuates substantial background under the $k^*(890)$. A mass cut $M(\Sigma^+\pi^0) > 1.8$ Gev/c^2 removes most of the reflection and gives a very clean $k^*(890)$ signal indicated by the shaded histogram in Fig 3.1.

(2) $k^- p \rightarrow \pi^- \Sigma^+\pi^0$

This channel shows similar characteristics to (1) with a similar 1660 peak in the $\Sigma^+\pi^0$ projection, the reflection of which, under the ρ^- signal, is removed by the mass cut $M(\Sigma^+\pi^0) > 1.8$ Gev/c. This leaves an almost background free ρ^- signal as shown in Fig 3.2.

(3) $k^- p \rightarrow \pi^- \Lambda \pi^+$

From Fig 3.3 it is clear that this channel is dominated by $\Sigma^{*+}(1385)$ and $\Sigma^{*+}(1700)$ bump decaying to $\Lambda\pi^+$. The $\pi^+\pi^-$ mass projection is dominated by reflection from these two resonances. Mass cut $m(\Lambda\pi^+) > 1.8$ Gev/c^2 yields the much cleaner $\pi^+\pi^-$ mass spectrum, shaded in Fig 3.3, which shows the ρ^0 and f^0 signal.

(4) $\pi^+ p \rightarrow k^+ \pi^0 \Lambda \pi^+$

The $M(\Lambda\pi^+)$ / $M(k^+\pi^0)$ scatter plot , shown in Fig 3.4, clearly shows evidence for double resonance production $k^*(890)$-$\Sigma^*(1385)$. The shaded histograms result from k^* and Σ^* selection, defined in table 3.1 . With k^*selection very little background remains under the $\Sigma^*(1385)$. However significant background remains under the $k^*(890)$ after making the $\Sigma^*(1385)$ selection.

(5) $k^- p \rightarrow \pi^- \pi^0 \Lambda\pi^+$

Similar plots to previous channels are shown in Fig 3.5 where

CHANNEL	No. EVTS.	REACTION	APPLIED CUT	No. Evts in Resonance	Resolution $2\delta m$ (MeV)	$\lvert t'\rvert < 1.$ acceptances (%)
$\pi^+ p \to K^+\Sigma^+\pi^0$	569	$\pi^+ p \to K^{*+}\Sigma^+$	$M(\Sigma^+\pi^0) > 1.8$ $0.8 < M(K^+\pi^0) < 1.0$	107	80	65
$K^- p \to \pi^-\Sigma^+\pi^0$	773	$K^- p \to \rho^-\Sigma^+$	$M(\Sigma^+\pi^0) > 1.8$ $0.62 < M(\pi^-\pi^0) < 0.92$	120	95	35
$\pi^+ p \to K^+\pi^+\Lambda\pi^0$	836	$\pi^+ p \to K^{*+} Y^{*+}(1385)$	$1.3 < M(\Lambda\pi^+) < 1.5$ $0.8 < M\ K^+\pi^0 < 1.0$	119	$(K\pi^0)70$ $(\Lambda\pi^+)15$	65
$K^- p \to \pi^-\pi^+\Lambda\pi^0$	1234	$K^- p \to \rho^- Y^{*+}(1385)$	$1.3 < M(\Lambda\pi^+) < 1.5$ $0.62 < M(\pi^-\pi^0) < 0.92$ $M(\pi^-\pi^+\pi^0) > 1.2$ $0.62 > M(\pi^-\pi^+) > 0.92$ $1.3 > M(\Lambda\pi^0) > 1.5$	164	$(\pi^-\pi^0)80$ $(\Lambda\pi^+)15$	30
$K^- p \to \pi^-\pi^+\Lambda$	1492	$K^- p \to \rho^0\Lambda$	$M(\Lambda\pi^+) > 1.8$	76	10	35
					via Cauchy distrns. $2\delta m$ at peak value	

TABLE 3.1

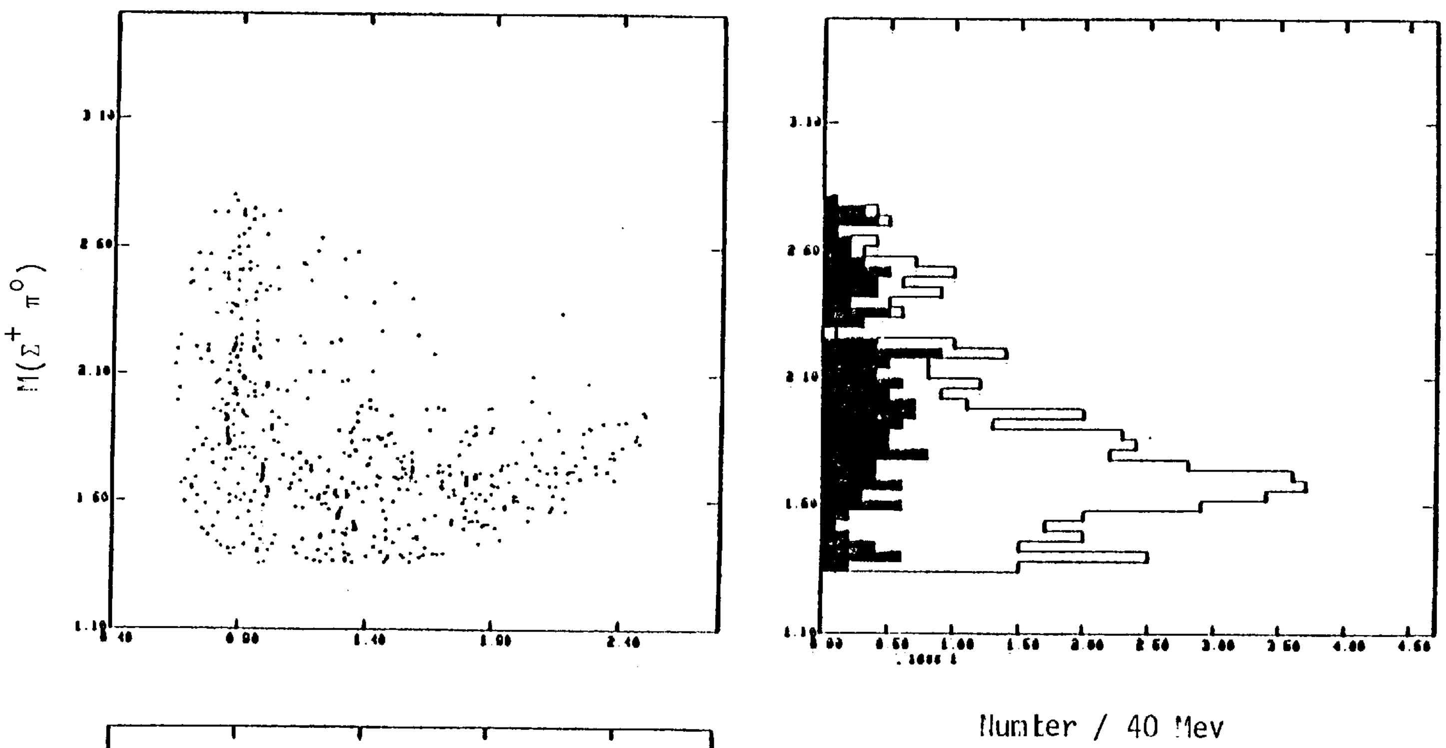

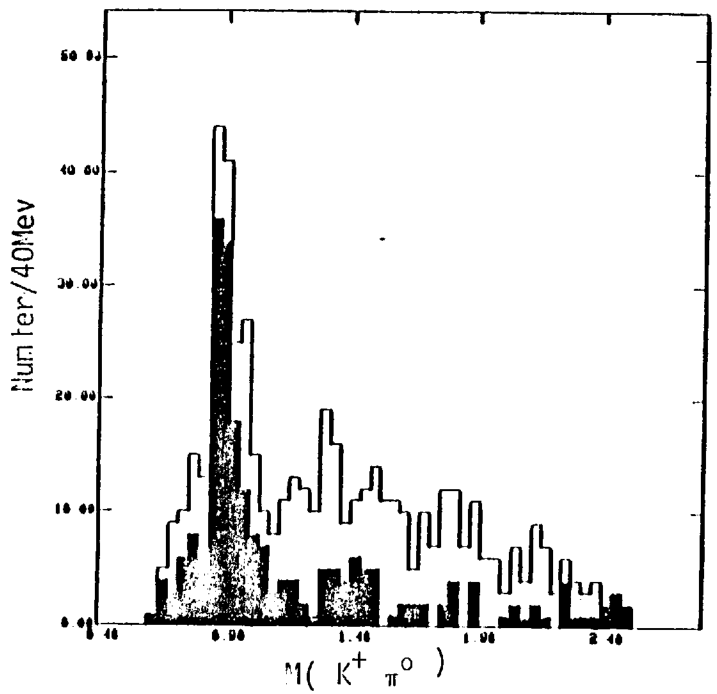

Fig 3.1 Scatter plot for reaction (1)

(shaded histogram indicates vector meson

or hyperon resonance selection)

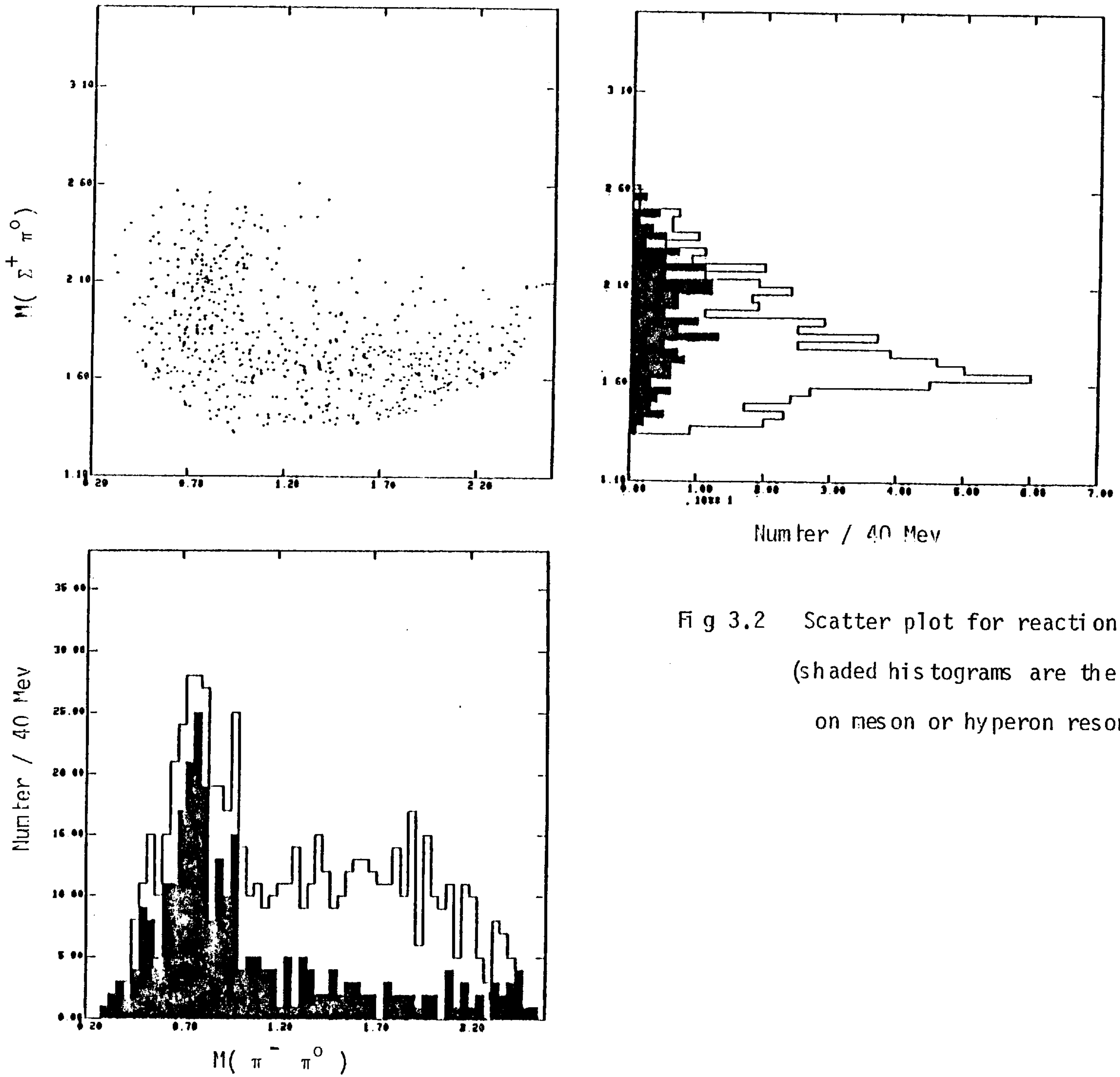

Fig 3.2 Scatter plot for reaction (2)

(shaded histograms are the result of selection on meson or hyperon resonance)

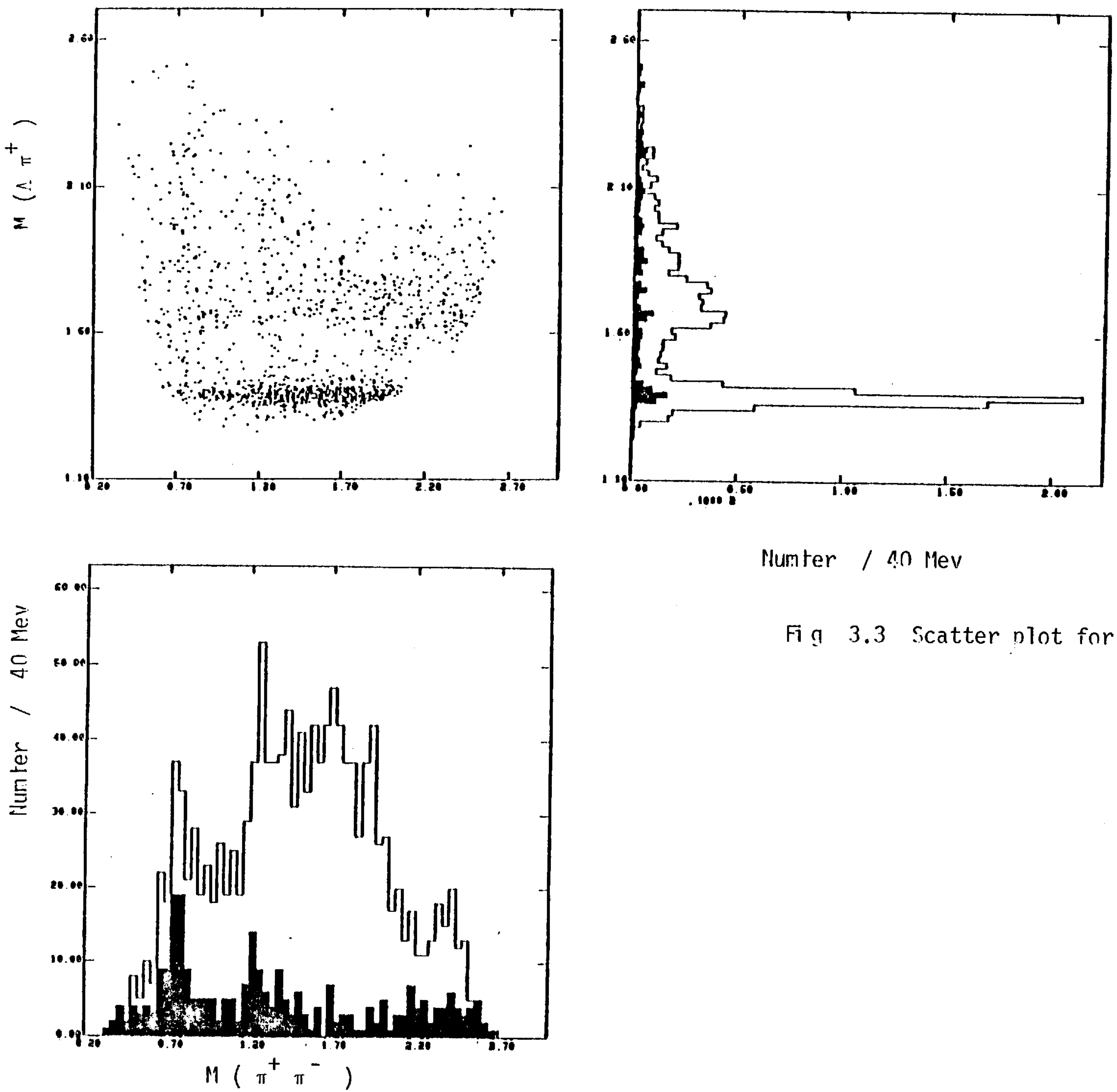

Fig 3.3 Scatter plot for reaction (3)

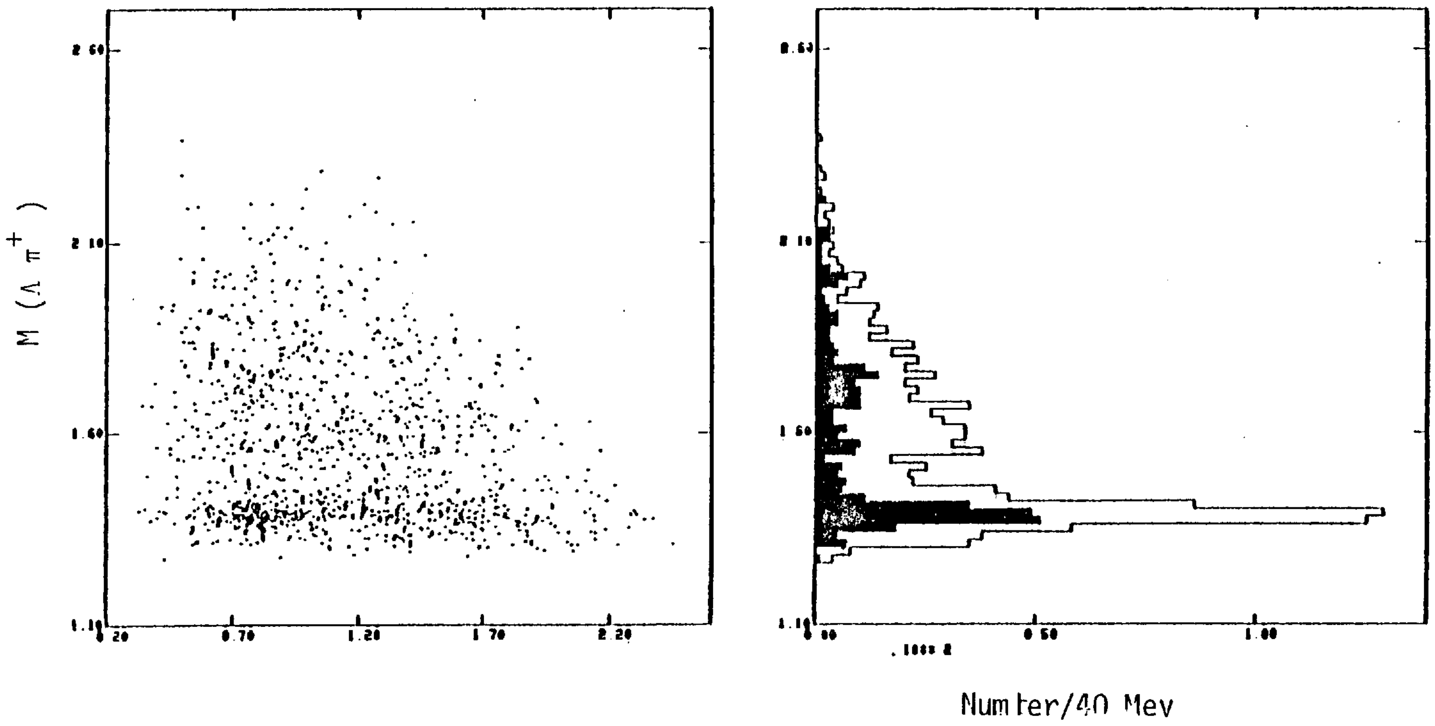

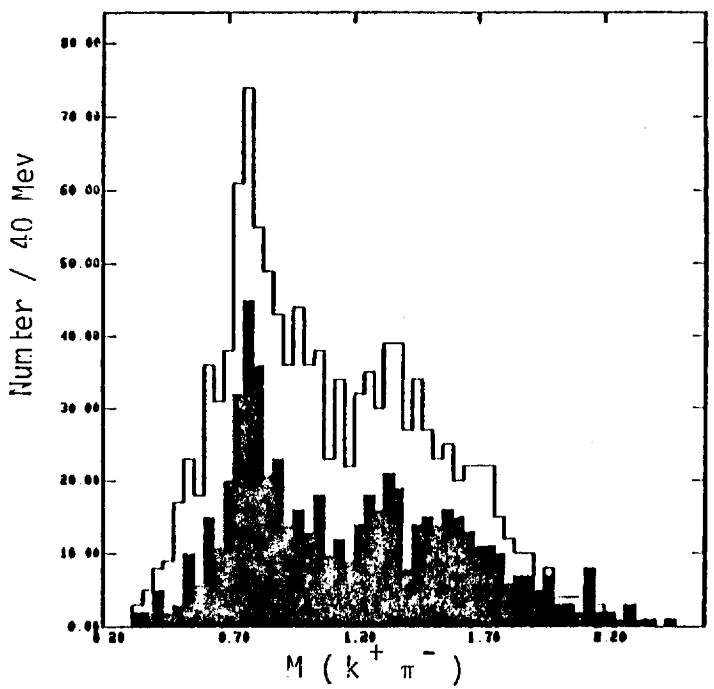

Fig 3.4 Scatter plot for reaction (4)

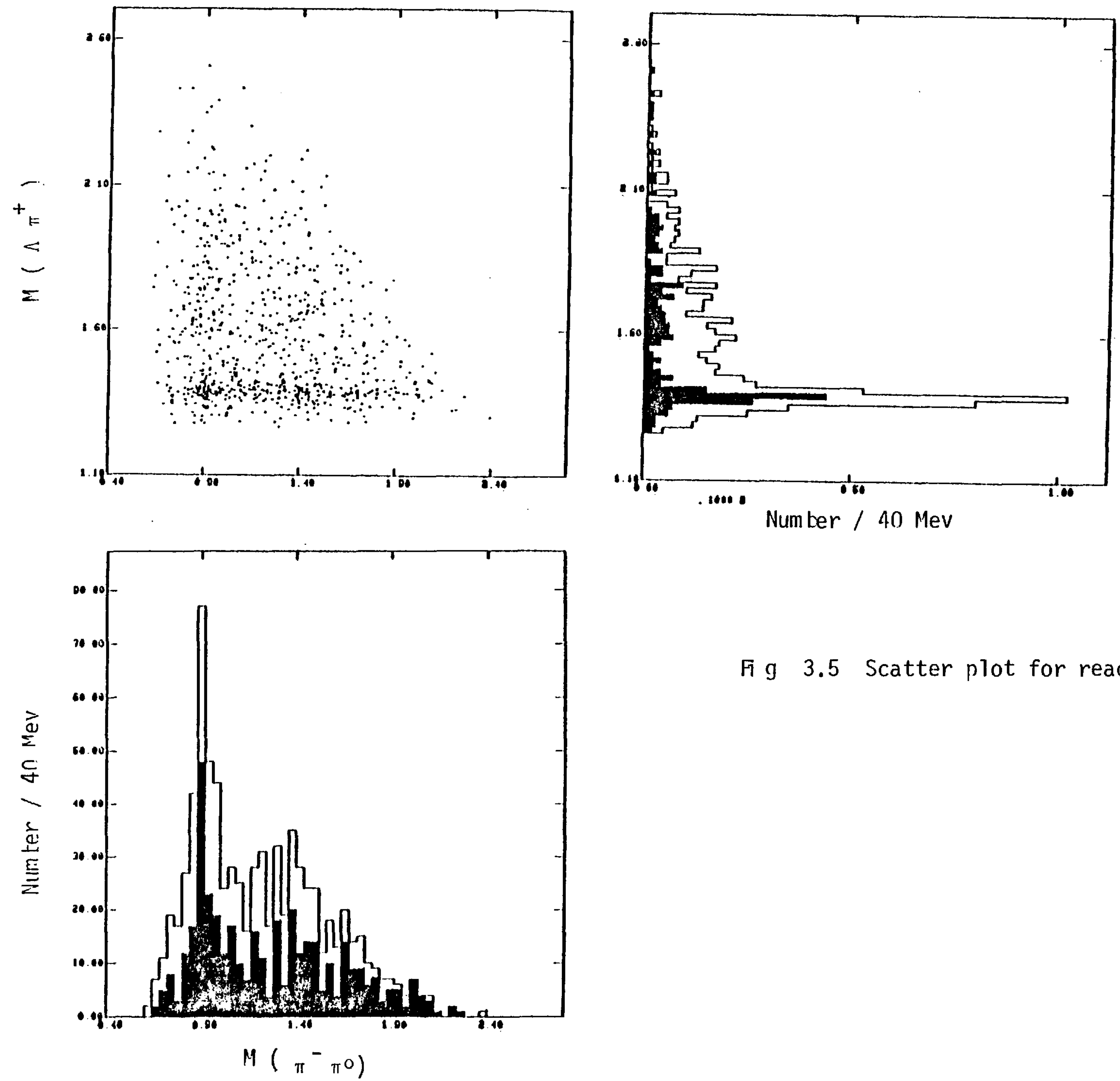

Fi g 3.5 Scatter plot for reacti on for reacti on (5)

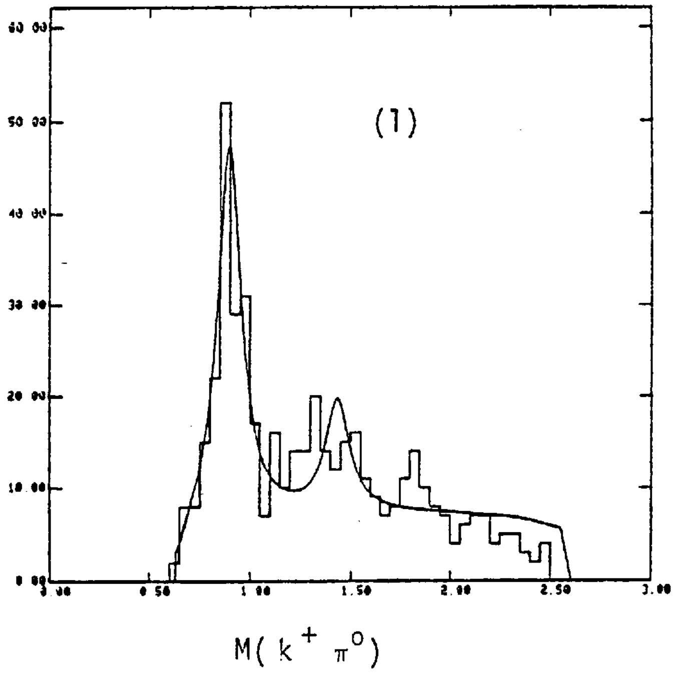

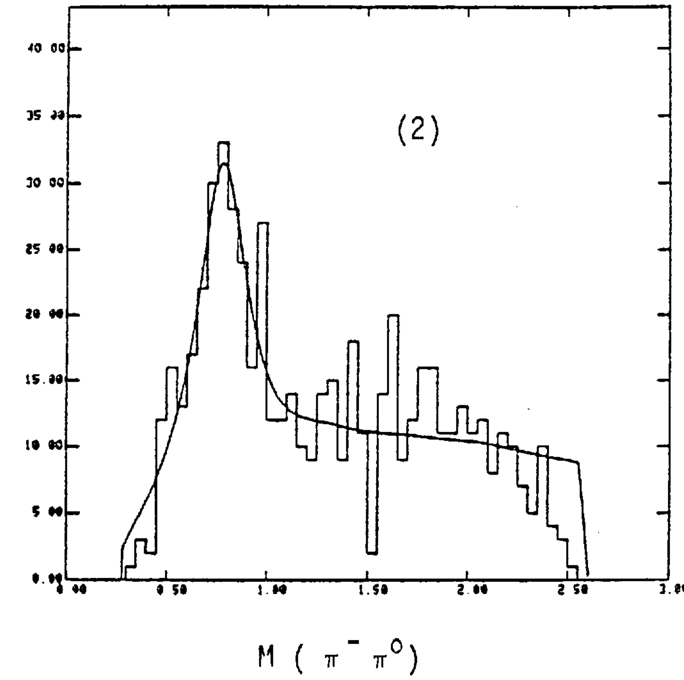

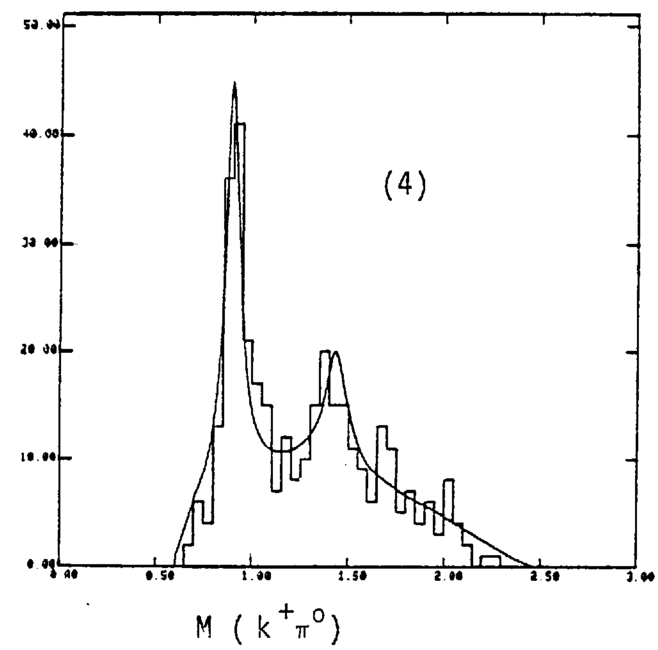

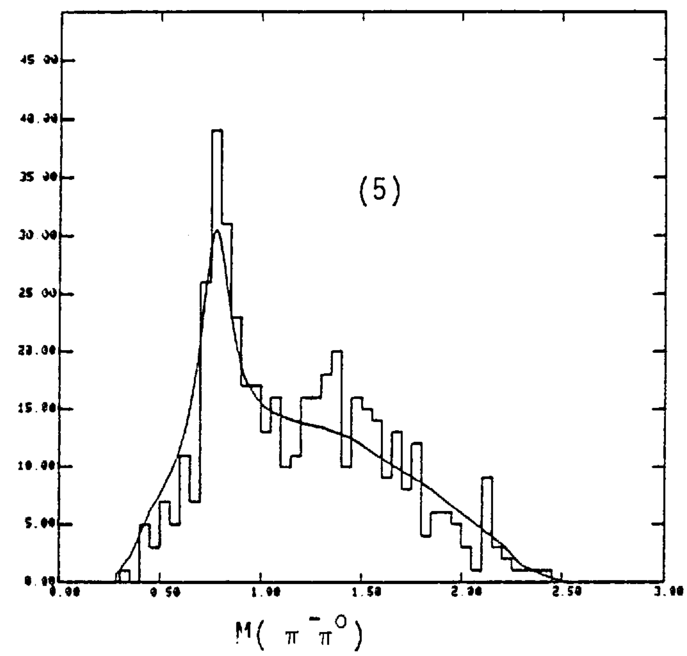

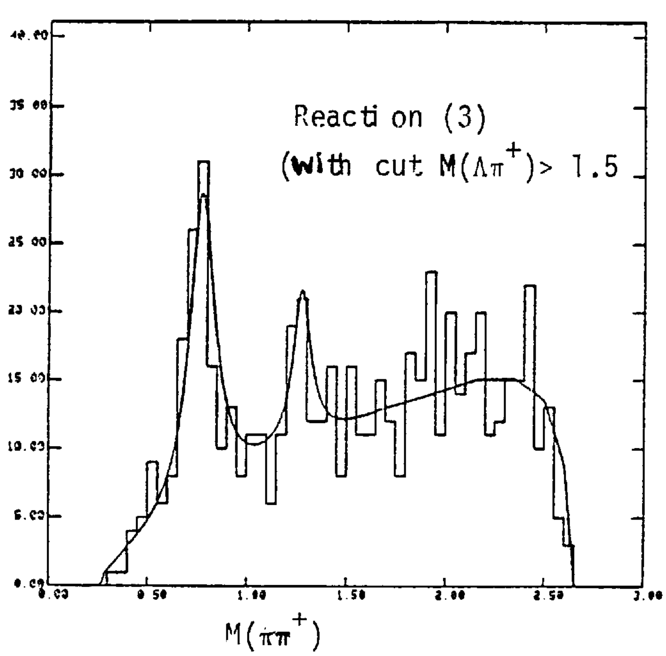

Fig 3.6 Fits to dimeson mass spectrum for reactions (1) - (5).

substantial $\Sigma^*(1385)$ joint production is seen. The main background contribution is under the vector meson after the $\Sigma^*(1385)$ selection. Further selections on $M(\pi^-\pi^+\pi^0)$, $M(\pi^-\pi^+)$ and $M(\Lambda\pi^0)$ were made, as indicated in table 3.1, to reduce contributions from ω, ρ^0 and $\Sigma^{*0}(1385)$ production.

Table 3.1 summarizes our data giving population of each topology. The mass cuts applied for selection of events for each resonance or double resonance reaction are shown in column four. The mass resolution, and for each reaction the average value of the acceptance of the S.H.F. for $-t < 1.(\mathrm{GeV}/c)^2$, where t is the square of the four momentum transfer between the multimeson state and the beam, are shown in columns six and seven respectively.

Determination of the cross sections involves correcting for background under the resonance. To estimate this mass fits to the dimeson effective mass plots for these reactions were used. Maximum likelihood fits to the dimeson mass distribution were made with the likelihood function written as :-

$$\mathrm{Log}\,\mathcal{L} = \sum_i \frac{\alpha_i\ \mathrm{BW}i}{\int \mathrm{BW}i} + \frac{(1 - \sum \alpha_i)\quad \mathrm{B.G.}}{\int \mathrm{B.G.}}$$

BWi: is the Breit-Wigner function. We used the form:

$$\mathrm{BW} = \frac{(\Gamma/2)^2}{(M-Mo)^2 + (\frac{\Gamma}{2})^2}$$

Mo : Mass of resonance

Γ : Width of resonance

M : Mass of the appropriate two particle combination.

BG : Background phasespace.

Experimental acceptance biases are taken into account in order to obtain a realistic background phase space behaviour in the mass fits. Each event generated in the background Monte Carlo was tested for acceptance in the downstream part of the S.H.F. For reaction (3) it was found extremely difficult to fit the $\pi^+\pi^-$ mass spectrum due to the extremely strong reflection. A mass cut $M(\Lambda\ \pi^+)\ >\ 1.5$ GeV/c^2 was imposed in the fit and the corresponding loss of events corrected for. The fits for reactions (1) - (5) are shown in Fig 4.6. The background estimate in the vector meson region, defined by the same cuts as in table 3.1, which were used in the total cross section determination were found to be:-

Reaction	Background Under Vector Meson (%)
$K^* \ \Sigma^+$	15 ± 4
$\rho \ \Sigma^+$	23 ± 6
$\rho \ \Lambda$ $(M(\Lambda\pi^+) > 1.5)$	30 ± 3
$K^* \ \Sigma^{*+}(1385)$	28 ± 5
$\rho \ \Sigma^{*+}(1385)$	47 ± 4

3.4 Exchange Naturality

In a reaction of the general type:

$$\text{Meson} + \text{Nucleon} \longrightarrow \text{(M)eson} + \text{(H)yperon}$$

forward production corresponds to exchange of virtual mesons. When discussing exchange mechanisms it turns out to be only possible to gain information about the spin-parity relation of the exchanged system and not on the spin and parity individually.[20]

One can distinguish between natural-parity exchange and unnatural-parity exchange. The distinction is based on whether the quantity ζ , defined as:

$$\zeta = (-1)^J P$$

is positive or negative respectively. Here J is the spin of the exchanged particle and P its parity.

Table 3.2 shows the combinations of (non exotic) quantum numbers which can be exchanged in reactions of the above type. The names refer to the leading poles of the corresponding Regge trajectries. The C-parity refers to the neutral non-strange members of the corresponding SU(3) nonets.

For hypercharge exchange reactions in which a pseudoscalar meson is produced only natural-parity exchange is allowed by parity conservation at the meson vertex. For other reaction the two types of exchanges can be separated.[21]

	Name	Naturality	J^P	C-Parity
Natural-Parity	K^*	+	1^-	-
Exchange	K^{**}	+	2^+	+
Unatural-Parity	K	-	0^-	+
Exchange	K_B	-	1^+	-
	K_A	-	1^+	+
	K_Z	-	2^-	-

Table 3.2

Production Amplitudes and Spin Density Matrix Elements[21]

The production amplitude for the reaction

$$K^- \; P \longrightarrow M + H$$

can be written as:

$$T^{M}_{HP}\ (s,t) = \langle M\ H \mid T\ (s,t) \mid K^- P \rangle$$

where the spin indices on T denote the spin components along the quantigation axis of the respective particles. The number of independent complex amplitudes is given by total number of combinations of spin indices divided by two. The reduction being due to parity conservation in the production process. For the direction of the quantization axis one of the following frames is generally chosen.

(1) Helicity Frame: y is the production plane normal.
In the s-channel; for each particle quantization axis is along its direction of motion in the O.C.M. frame.
In the t-channel; the meson quantization axis is along the direction of the incoming meson in rest frame of the outgoing meson. Similarly for the baryon vertex. (Gottfried and Jackson frame.)

(2) Transversity Frame: The quantization axis is along the production plane normal.
In the s-channel; y is along the direction of the outgoing meson in the rest frame of the outgoing baryon. (Conversely for the meson vertex.)
In the t-channel; y is the opposite direction to the incoming baryon in the rest frame of the outgoing baryon. (Similarly at the meson vertex.)

In the transversity frame parity conservation implies:

$$T^{M}_{HP} = \eta \; (-1)^{M-H+P} \; T^{M}_{HP}$$

where η is the product of intrinsic parities of the four particles in the reaction. Thus half the transversity amplitudes are zero and the remainder are independent.

The information about the spin orientation of the final state particles is usually expressed in terms of the spin density matrix elements. For the hyperon

$$\rho^{MM'}_{HH'} = \sum_{P} T^{M}_{HP} \; T^{M'*}_{H'P}$$

For mesons where only strong decay distribution is studied

$$\rho_{MM'} = \sum_{HP} T^{M}_{HP} \; T^{M'*}_{HP}$$

In reactions of the type $0^{-}\ \frac{1}{2}^{+} \rightarrow 1^{-}\ \frac{1}{2}^{+}$ there are six non-zero amplitudes:

$$T^{-1}_{-\frac{1}{2}\frac{1}{2}} \quad T^{0}_{\frac{1}{2}\frac{1}{2}} \quad T^{1}_{-\frac{1}{2}\frac{1}{2}} \quad \text{and} \quad T^{-1}_{\frac{1}{2}\frac{1}{2}} \quad T^{0}_{-\frac{1}{2}-\frac{1}{2}} \quad T^{1}_{\frac{1}{2}\frac{1}{2}}$$

i.e. 11 independent parameters + an overall phase.

In reactions of the type $0^{-}\ \frac{1}{2}^{+} \rightarrow 1^{-}\ \frac{3}{2}^{+}$ there are twelve independent amplitues.

$$T^{1}_{\frac{3}{2}\frac{1}{2}} \quad T^{1}_{-\frac{1}{2}\frac{1}{2}} \quad T^{0}_{\frac{1}{2}\frac{1}{2}} \quad T^{0}_{\frac{3}{2}\frac{1}{2}} \quad T^{-1}_{\frac{3}{2}\frac{1}{2}} \quad T^{-1}_{-\frac{1}{2}\frac{1}{2}} \qquad \text{("Proton UP")}$$

$$T^{1}_{\frac{1}{2}-\frac{1}{2}} \quad T^{1}_{-\frac{3}{2}-\frac{1}{2}} \quad T^{0}_{\frac{3}{2}-\frac{1}{2}} \quad T^{0}_{-\frac{1}{2}-\frac{1}{2}} \quad T^{-1}_{\frac{1}{2}-\frac{1}{2}} \quad T^{-1}_{-\frac{3}{2}-\frac{1}{2}} \qquad \text{("Proton Down")}$$

i.e. 23 independent parameters + an overall phase.

The transversity amplitudes with M = 0 correspond to natural parity exchange and the rest to unnatural parity exchange. So that, if only interested in looking at the exchange naturality, the number of amplitudes can be reduced by taking linear combination of the above (- Byers - Yang) amplidudes.

The s-channel helicity density matrix can be determined by rotating the transversity density matrix according to:

$$\rho^{H}_{mn} = \sum_{ij} D_{mi}(-R)\ \rho^{T}_{ij}\ D_{jn}(R)$$

$$R = \left(\frac{\pi}{2}, \frac{\pi}{2}, \frac{\pi}{2}\right)$$

Separation of Cross Section into Natural and Unnatural[22] Parity Exchange

The limited statistics both at 7 and 11.5 GeV/c do not allow a complete amplitude analysis. However, it is possible to extract information on the exchange naturality in the t-channel. The decay distribution of the resonance allows a determination of some density matrix elements of the produced resonance.

Linear combinations of helicity amplitudes can be defined which correspond to a given parity in the t-channel. This is similar procedure to the Byers - Yang type amplitudes which give different naturality contributions from the transversity amplitudes.

For a reaction 1 + 2 → 3 + 4 the new amplitudes in terms of the t-channel helicity amplitudes are:[22]

$$M^{t\pm}_{\lambda_3\lambda_1\lambda_4\lambda_2} = M^{t}_{\lambda_3\lambda_1\lambda_4\lambda_2} \pm \varepsilon\, M^{t}_{-\lambda_3-\lambda_1\lambda_4\lambda_2}$$

$$\varepsilon = \eta_3\eta_1(-1)^{S_3-S_1}(-1)^{\lambda_3-\lambda_1}$$

+ Natural Parity

\- Unnatural Parity

For a vector meson produced form a pseudoscalar then the contribution to the differential cross section when the vector meson is in a helicity state λ_3 is:

$$\frac{d\,\sigma^{\pm}_{\lambda_3}}{d\,t} = \frac{1}{4}\sum_{24}\left|M^{\pm}_{\lambda_3 0\,\lambda_4\lambda_2}\right|^2$$

Relative contribution to the differential cross section being:

$$\sigma^{\pm}_{\lambda_3} = \frac{d\,\sigma^{\pm}_{\lambda_3}}{d\,t} \Big/ \frac{d\,\sigma}{d\,t}$$

with

$$\sum_{\lambda_3} \left(\sigma^{+}_{\lambda_3} + \sigma^{-}_{\lambda_3} \right) = 1$$

In terms of the density matrix elements:

$$\sigma^{\pm}_{\lambda_3} = \tfrac{1}{2}\left(\rho_{\lambda_3\lambda_3} \mp \varepsilon\, \rho_{\lambda_3 -\lambda_3} \right)$$

for $\quad 0^{-} + \tfrac{1}{2}^{+} \rightarrow 1^{-} + \tfrac{1}{2}^{+} \qquad \varepsilon = +1$

when $\lambda_3 = 0$

$$\sigma^{+}_{0} = 0$$

$$\sigma^{-}_{0} = \rho_{00}$$

and for $\lambda_3 = \pm 1$

$$\sigma^{\pm}_{1} = \tfrac{1}{2}\left(\rho_{11} \pm \rho_{1\,-1} \right)$$

Table 3.3 shows the relations between exchange naturality and spin density matrix elements of particle 3 in different quantization frames in the t-channel.

Exchange Naturality	Transversity Density Matrix Elements	Helecity Density Matrix Elements
$\zeta = \eta_1\eta_3$	ρ^{T}_{00}	$\rho^{H}_{11} + \rho^{H}_{1\,-1}$
$\zeta = -\eta_1\eta_3$	$\rho^{T}_{11} + \rho^{T}_{1\,-1}$	ρ^{H}_{00}
	$\mathrm{Re}\ \rho^{T}_{1\,-1}$	$\rho^{H}_{11} - \rho^{H}_{1\,-1}$
	$\mathrm{Im}\ \rho^{T}_{1\,-1}$	$\mathrm{Re}\ \rho^{H}_{10}$

Table 3.3

In the helicity frame natural parity exchange populates only helicities ±1 of the vector meson, whereas unnatural parity exchange populates all helicity states of the vector meson.

The spin density matrix of either reaction product can be expressed in terms of the helicity amplitudes in the crossed t-channel; provided the Gottfried Jackson co-ordinate system is chosen.[20] Diagrammatically this is

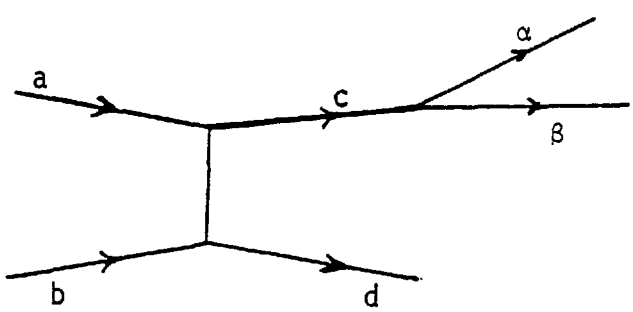

$$\hat{\underline{y}} = \hat{\underline{p}}_a \wedge \hat{\underline{p}}_c = -\hat{\underline{p}}_b \wedge \hat{\underline{p}}_d$$

The production and decay of c being:

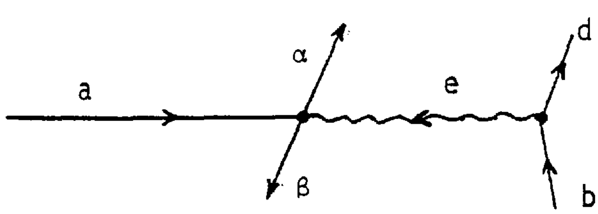

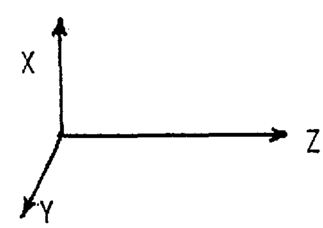

Gottfried and Jackson have shown that the helicity of c in the t-channel equals the spin component along $\hat{\underline{z}}$ as defined above. Measurement of the density matrix with respect to the above quantization axis is therefore related to the t-channel helicity amplitudes.

The resonance, c, with spin J will be produced in a mixed state whose composition is fully described in terms of the density matrix of dimension (2J + 1). Elements $\rho_{mm'}$ label the z-component of the spin.

Diagonal elements represent the probability of finding the resonance with z-components m while off- diagonal elements indicate degree of interference between different spin states $|J, M\rangle$ and $|J, M'\rangle$.

In all these reactions a resonance decays

$$1^- \rightarrow 0^- + 0^-$$

The decay distribution being fully given by the matrix

$$\rho = \begin{bmatrix} \rho_{11} & \rho_{10} & \rho_{1-1} \\ \rho_{o1} & \rho_{oo} & \rho_{o-1} \\ \rho_{-11} & \rho_{-1o} & \rho_{-1-1} \end{bmatrix}$$

and with conditions

$$Tr\,\rho = 1 \qquad\qquad \rho = \rho^\dagger$$

$$\text{and} \qquad \langle m|\rho|m'\rangle = (-1)^{m-m'} \langle -m|\rho|-m'\rangle$$

this reduces to

$$\rho = \begin{bmatrix} \frac{1}{2}(1-\rho_{oo}) & \rho_{1o} & \rho_{1\,1} \\ \rho_{1o} & \rho_{oo} & \rho_{1o} \\ \rho_{1\,1} & \rho_{1o} & \frac{1}{2}(1-\rho_{oo}) \end{bmatrix}$$

The angular distribution of the decay $c \rightarrow \alpha + \beta$ is given by:[23]

$$W(\cos\theta, \phi) = \frac{3}{4\pi}\left[\frac{1}{2}(1-\rho_{oo}) + \frac{1}{2}(3\rho_{oo}-1)\cos^2\theta - \rho_{1-1}\sin^2\theta\cos 2\phi - \sqrt{2}\,\mathrm{Re}\,\rho_{1o}\sin 2\theta\cos\phi\right].$$

θ = Polar angle for α

ϕ = Angle between production plane and plane containing α and z

Parity conservation in the decay of c imposes:

$$W(\theta,\phi) = W(\pi-\theta, \pi+\phi)$$

and parity conservation in production imposes:

$$W(\theta,\phi) = W(\theta, -\phi)$$

Integrating over $\cos\theta$ or ϕ and substituting for :-

$$\rho_+ = \tfrac{1}{2}(\rho_{11} + \rho_{1-1}) \qquad \rho_- = \tfrac{1}{2}(\rho_{11} - \rho_{1-1})$$

$$W(\cos\theta) = \frac{3}{4} \left| \rho_{00}\cos^2\theta + \rho_+ \sin^2\theta + \rho_- \sin^2\theta \right|$$

$$W(\phi) = \frac{1}{2\pi} \left| \rho_{00} + 2\rho_+ \sin^2\phi - 2\rho_- \cos^2\phi \right|$$

By fitting the expressions for $W(\cos\theta)$ and $W(\phi)$ to the data we can obtain the contributions of ρ_+, ρ_- and ρ_{00} to the reaction. This procedure reduces the number of parameters to three from 11, as in the case of vector meson production against Σ^+, and 23, as in the case of vector meson against $\Sigma(1385)$.

Geometric Acceptance

A difficulty in studying the vector meson production mechanism in this experiment is that the downstream trigger biases the decay. At 7 GeV/c (11.5 GeV/c) we trigger on 30% (35%) of the ρ's and 60% (80%) of the K^*'s in the range t_{min} to one $(GeV/c)^2$. In order to estimate the contributions from different exchanges a Monte Carlo study was made giving the expected decay angular behaviour of each exchange contribution. Fig 3.7 shows our acceptance for reactions (4) and (5) for various exchanges.

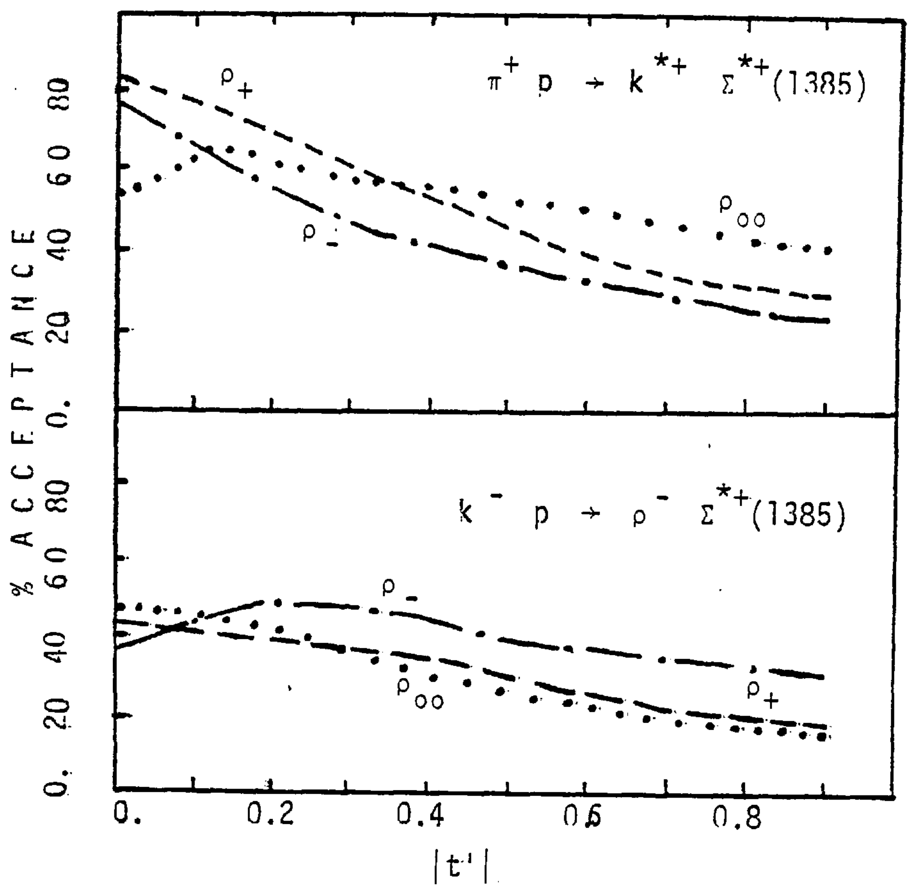

Fig 3.7 S.H.F. acceptance for various exchanges

The Monte Carlo distributions were fitted to the experimental angular distributions by the maximum likelihood method with the likelihood function:

$$\text{Log}\,\mathcal{L} = \frac{\alpha_1\,\rho_+}{I_1} + \frac{\alpha_2\,\rho_-}{I_2} + \frac{\alpha_3\,\rho_{oo}}{I_3} + (1-\alpha_1-\alpha_2-\alpha_3)\,\frac{B.G}{I_{BG}}$$

I_i is the integral over whole of the respective Monte Carlo distribution.

B.G. is the background estimated from regions adjacent to the K^* and ρ. It was only included for reactions (4) and (5).

The Monte Carlo distributions were approximated by smooth curves which were reproduced in the fits by linear interpolation. Fig 3.8 shows our fits to the decay distribution data for reactions (1) to (5). Table 3.4 gives the results of these fits.

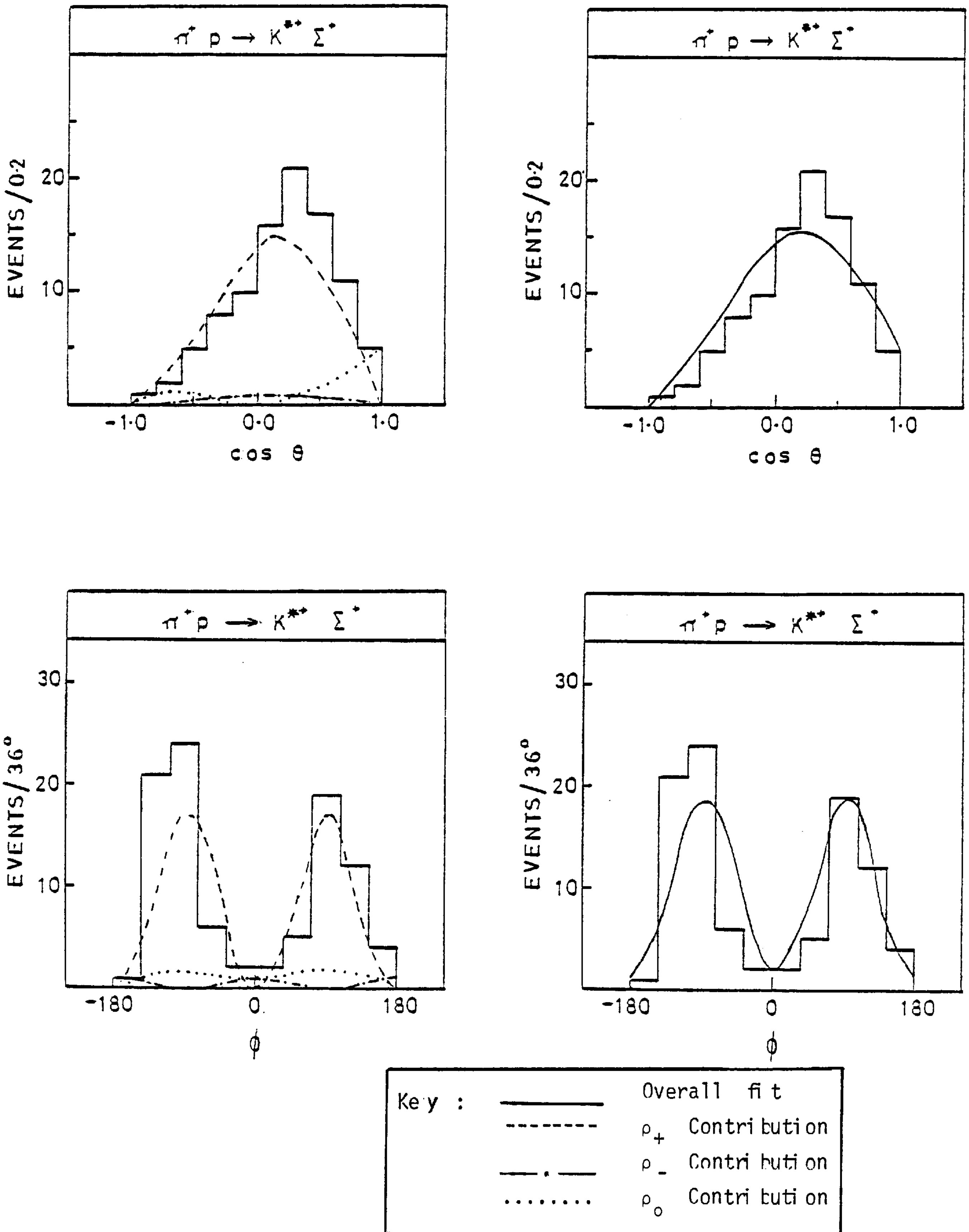

Fig 3.8 Fits to decay distributions of the vector meson for reactions (1) - (5) (Fig 3.8 i - v)

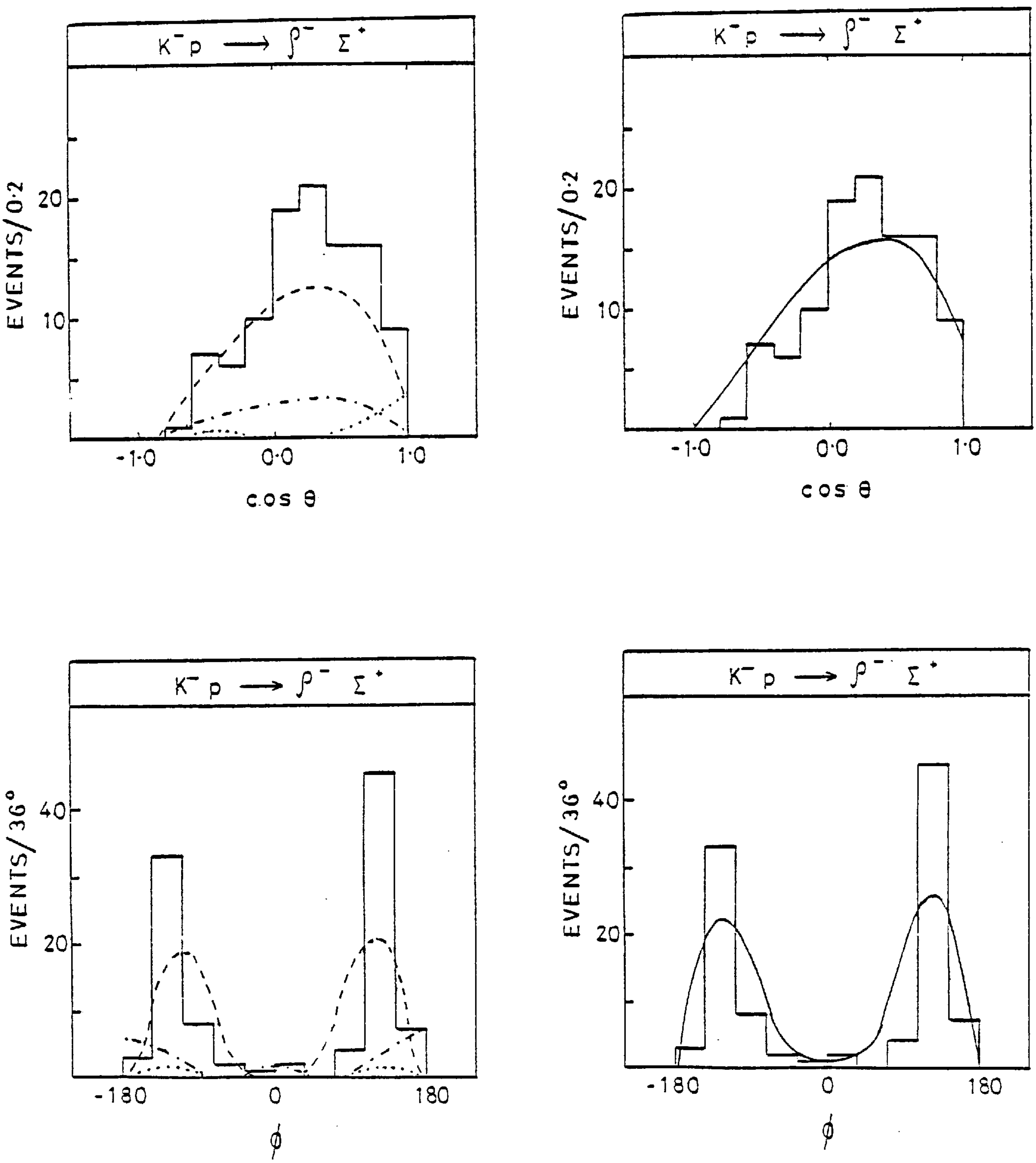

K⁻p ⟶ ρ⁻ Σ⁺
EVENTS/0·2
20
10
-1·0
0·0
1·0
cos θ
K⁻p ⟶ ρ⁻ Σ⁺
EVENTS/0·2
20
10
-1·0
0·0
1·0
cos θ
K⁻p ⟶ ρ⁻ Σ⁺
EVENTS/36°
40
20
-180
0
180
φ
K⁻p ⟶ ρ⁻ Σ⁺
EVENTS/36°
40
20
-180
0
180
φ

Fig 3.8 (ii)

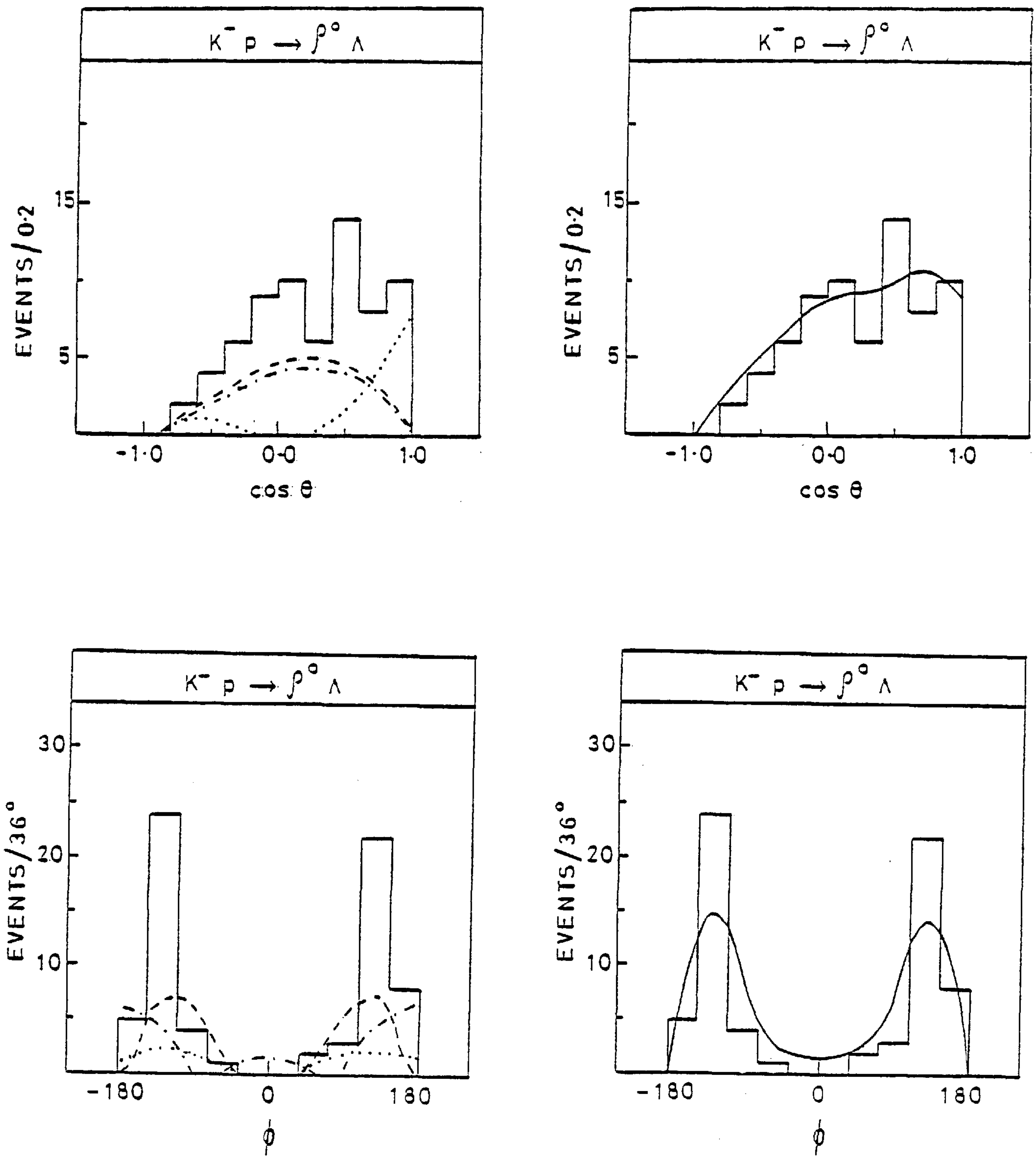
K⁻ p → ρ° Λ
EVENTS/0·2
15
5
-1·0
0·0
1·0
cos θ
K⁻ p → ρ° Λ
EVENTS/0·2
15
5
-1·0
0·0
1·0
cos θ
K⁻ p → ρ° Λ
EVENTS/36°
30
20
10
-180
0
180
φ
K⁻ p → ρ° Λ
EVENTS/36°
30
20
10
-180
0
180
φ

Fig 3.8 (iii)

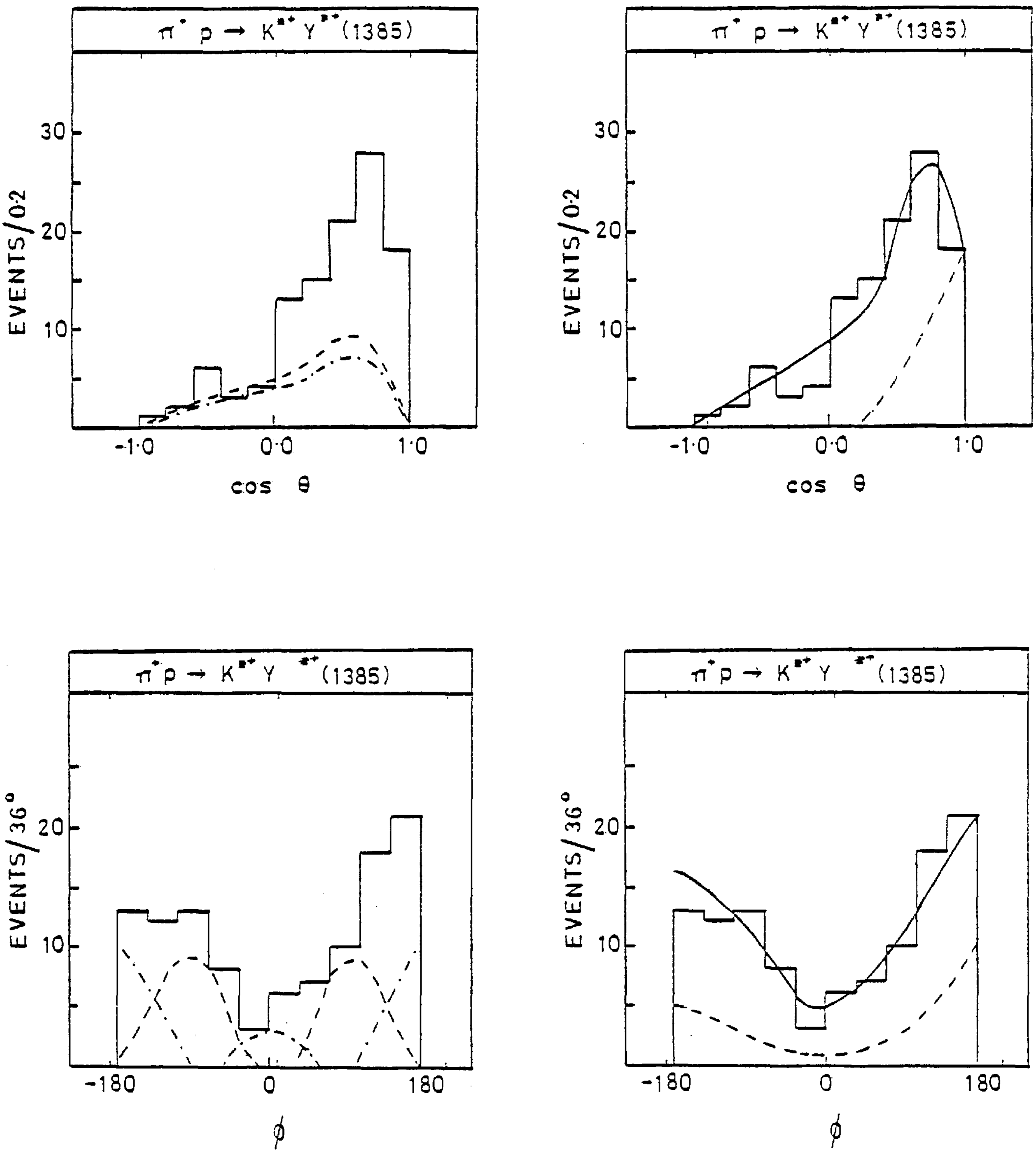

Fig 3.8 (iv) Dashed line below the overall fit is the background

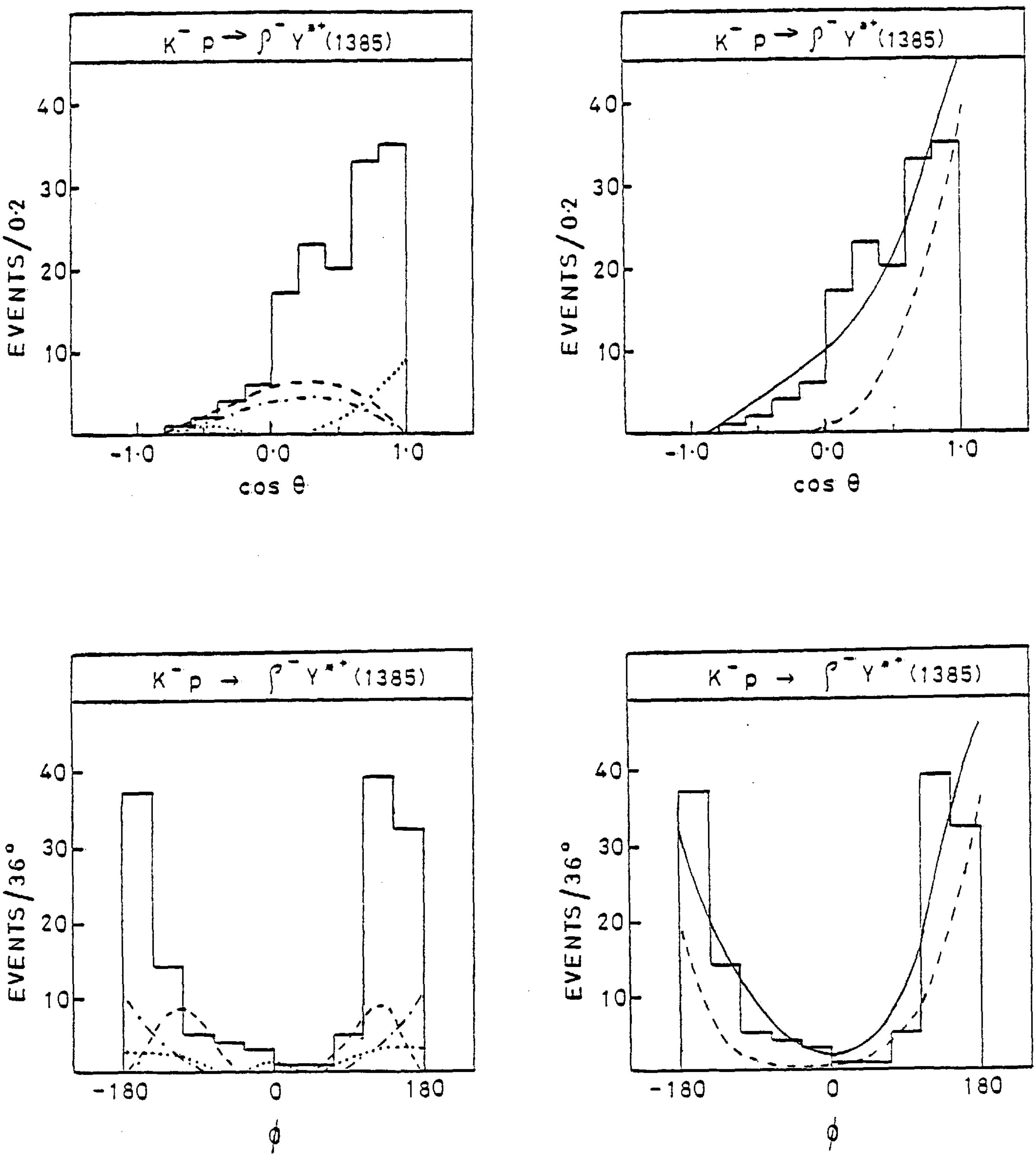

Fig 3.8 (v) Dashed line below the overall fit is the background

REACTION	ρ^{00}	ρ^{-}	ρ^{+}	$\lvert\Delta t'\rvert$ $(GeV/c)^2$
$\pi^{+}p \to K^{*+}\Sigma^{+}$	0.11 ± 0.12	0.04 ± 0.07	0.85 ± 0.09	0. – 0.9
$K^{-}p \to \rho^{-}\Sigma^{+}$	0.05 ± 0.08	0.20 ± 0.06	0.75 ± 0.05	0. – 0.9
$\pi^{+}p \to K^{*+}Y^{*+}1385$	< 0.15	0.44 ± 0.10	0.56 ± 0.10	0. – 1.0
$K^{-}p \to \rho^{-}Y^{*+}1385$	0.19 ± 0.15	0.34 ± 0.10	0.47 ± 0.13	0. – 1.0
$K^{-}p \to \rho\Lambda$	0.19 ± 0.15	0.38 ± 0.10	0.43 ± 0.10	0. – 0.9

(ERRORS ARE STATISTICAL)

TABLE 3. 4

3.5 Cross-sections and Polarizations

To determine the differential and total cross-sections events were weighted for Λ or Σ^+ losses in the bubble chamber. All events used for the cross-sections were also weighted for the geometric acceptance of the S.H.F. (Chapter 2).

The total cross-sections were determined using the expression:

$$\sigma = \frac{N_e \cdot t}{N_b \cdot L}$$

N_e = Corrected number of events (chapter 2)

N_b = Corrected number of beam tracks

t = Thickness of hydrogen (M^3)

L = Fiducial length.

For reactions (1) and (2) both $\Sigma^+ \rightarrow n\pi^+$ and $\Sigma^+ \rightarrow p\pi^0$ decay modes were used. The integrated cross-sections for the t' range $0 < |t'| < 0.9$ $(GeV/c)^2$ are shown in table 3.5.

Differential Cross-sections

All events left with the mass cuts were used in determining the differential cross-sections. The differential cross-sections were obtained using the expression

$$\frac{d\sigma}{dt} = \frac{n'}{N}\frac{\sigma}{\delta t} \ \mu b/(GeV/c)^2$$

n' = Corrected number of events in a bin of width δt.

N = Total number of corrected events corresponding to a total channel cross-section of σ.

The error in the differential cross-section is then

$$\Delta \left(\frac{d\sigma}{dt}\right) = \frac{1}{\sqrt{n}} \left(\frac{d\sigma}{dt}\right)$$

n = Uncorrected number of events.

Fig 3.9 shows the cross-sections for reactions (1) to (5) and the cross-sections are listed in table 3.6. Reactions (1) and (2) both show a simple exponential behaviour. There does not appear to be any evidence of a turnover in the forward direction. Fits to the differential cross-sections for reactions (1) and (2) of the form:

$$\frac{d\sigma}{dt} = A\, e^{-bt'}$$

were made in the $|t'|$ region 0 to 0.9 $(GeV/c)^2$. Results are shown in table 3.5. The differential cross-section for reaction (3) shows a turn-over in the forward direction. However with our statistics it is difficult to make any firm statement. Reaction (4) shows a clear turnover in the forward direction. This differential cross-section was fitted to the parametrization:

$$\frac{d\sigma}{dt} = (A_1 - A_2 t')\; e^{-bt'}$$

parameters of the fit are shown in table 3.5.

Reaction (5) shows no turnover in the forward direction but instead there is an indication of a rise in the forward direction. Differential cross-sections for reactions (3) and (5) were not fitted.

Polarization

In all of the reactions (1) to (5) the hyperon can be spin polarized. Parity conservation in the production process implies polarization is normal to the production plane. In reaciton (1) to (3) the spin analysing power of the weak decay of the hyperon allows its polarization to be determined from its decay distribution. In reactions (4) and (5) however polarization determination is only possible by extracting the production amplitudes.

For Σ and Λ decays the decay distribution of the nucleon with respect to the production plane normal, in hyperon rest frame, is:

$$f(\theta) = \tfrac{1}{2}(1 + \alpha P \cos\theta)$$

α = Decay Asymmetry

P = Polarization degree

The parity violating decay of the hyperon manifests itself as an up - down asymmetry of the nucleon distribution relative to the production plane. The magnitude of the asymmetry being dependent on α whose magnitude reflects the degree of interference between the S and P- wave decay of the Σ^+ (1189) or Λ .

The polarization was determined by the method of moments. The first moment of $\cos\theta$ in $f(\theta)$ gives

$$\langle \cos\theta \rangle = \frac{\alpha P}{3}$$

The error on P is then

$$\Delta P = \frac{1}{\alpha}\sqrt{\frac{1}{n}\left[3 - (\alpha P)^2\right]}$$

n = Number of events used to determine P.

Since α is nearly zero for neutron decays of the Σ^+ only proton decay events could be used to determine the polarization. The decay $\Sigma^+ \rightarrow P\pi^0$ suffers form losses due to small angle decays. These losses are symmetric about zero in $\cos\theta$ in rest frame of the Σ[10]. These losses can be corrected for by taking the second moment of $\cos\theta$.

Since $\langle \cos^2\theta \rangle = \frac{1}{3}$

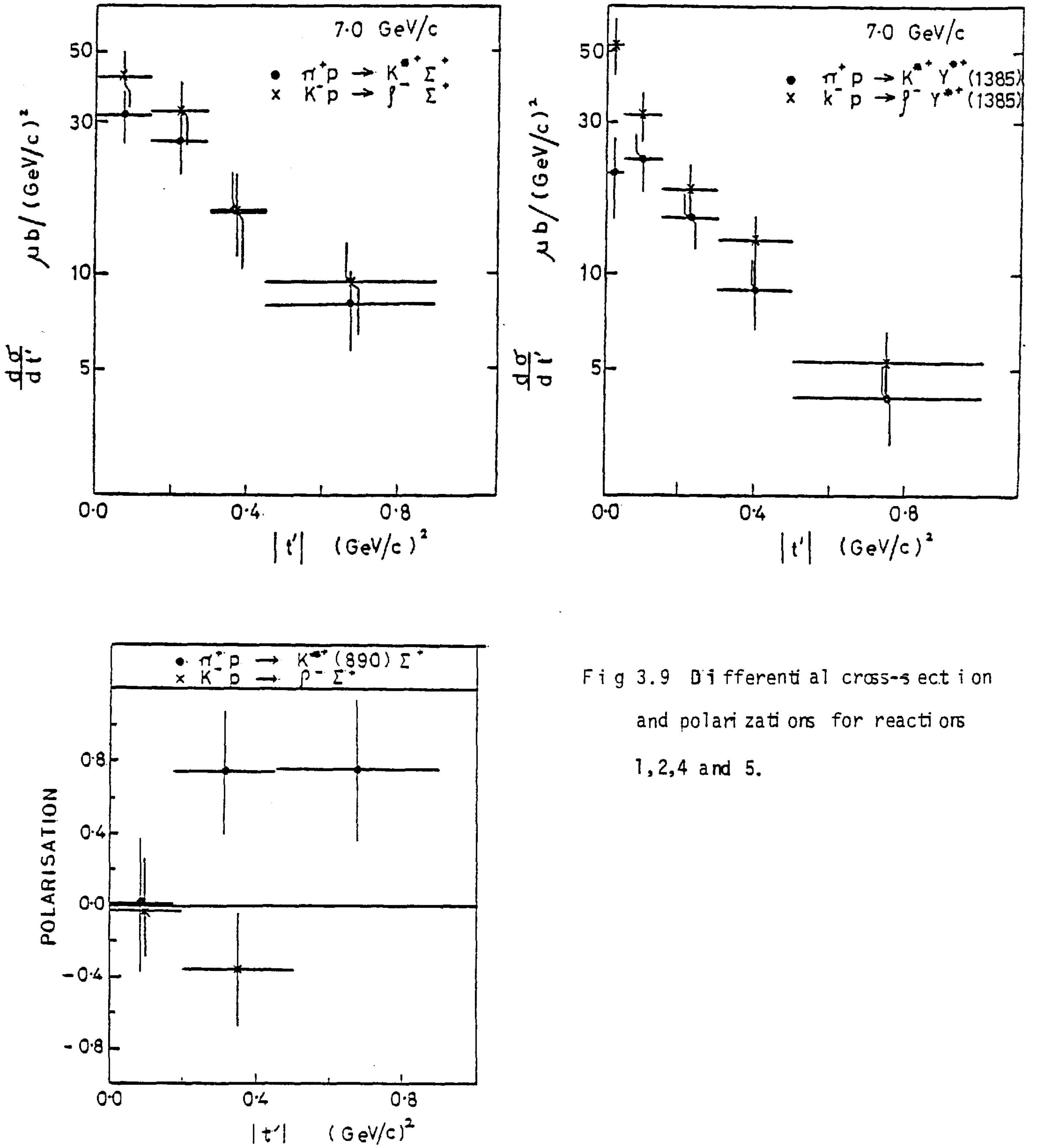

Fig 3.9 Differential cross-section and polarizations for reactions 1,2,4 and 5.

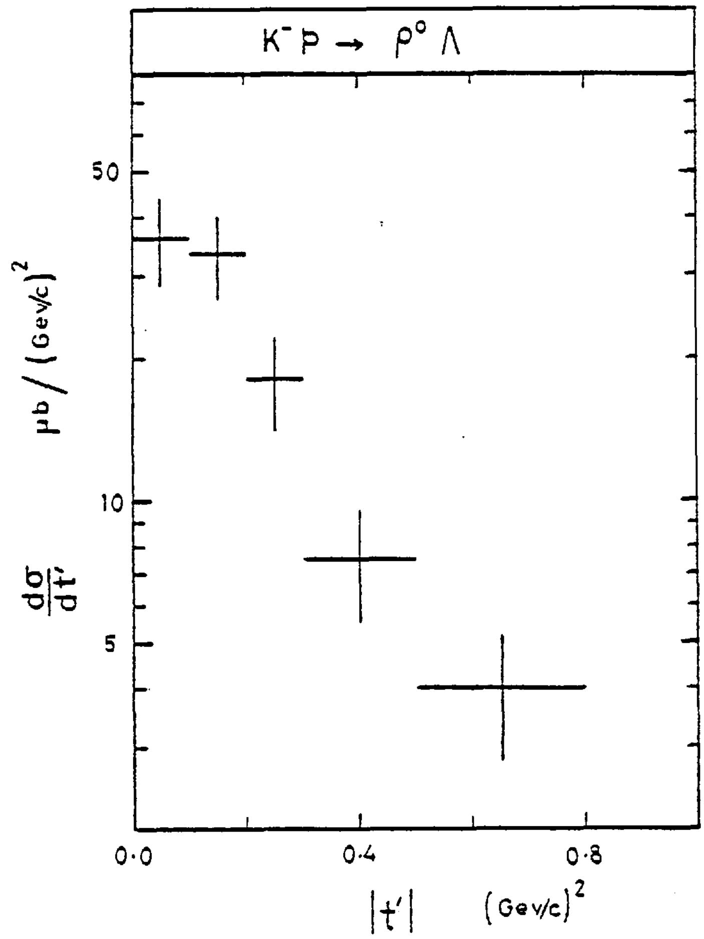

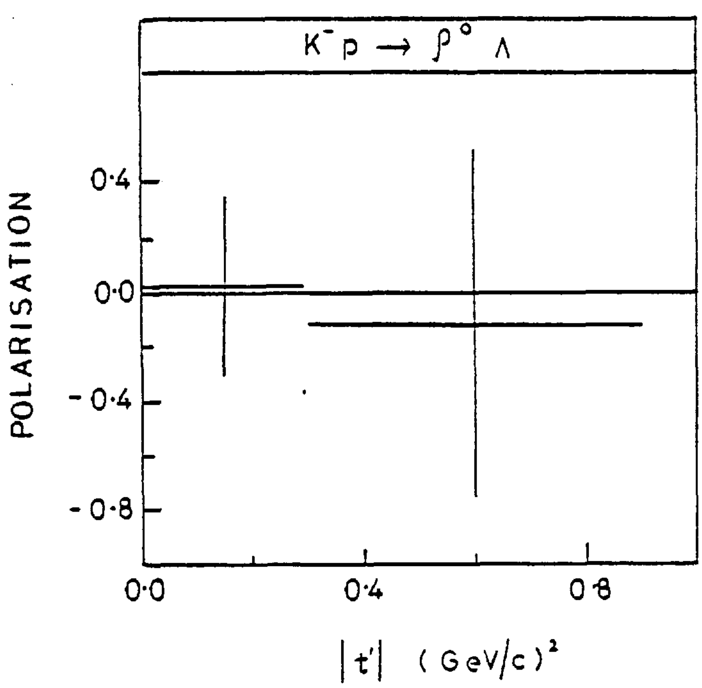

Fig 3.9 Differential cross-section and polarization for reaction (3)

REACTION	A_1	A_2	b	$\sigma_{(\mu b)}$
$\pi^+ p \rightarrow K^{*+} 890\ \Sigma^+$	39.3 ± 7.1	-	2.4 ± 0.5	14.5 ± 2.3
$K^- p \rightarrow \rho^- \Sigma^+$	51.7 ± 10.7	-	2.7 ± 0.7	17.7 ± 3.2
$\pi^+ p \rightarrow K^{*+} 890\ Y^{*+} 1385$	24.2 ± 3.4	48.1 ± 15.2	3.8 ± 0.3	9.4 ± 1.2
$K^- p \rightarrow \rho^- Y^{*+} 1385$				13.6 ± 1.3
$K^- p \rightarrow \rho^o \Lambda$				11.5 ± 1.4

(ERRORS ARE STATISTICAL)

TABLE 3.5

$\lvert t' \rvert$	Number of Events	Number of weighted events	$\frac{d\sigma}{dt}$	$\Delta \frac{d\sigma}{dt}$
	$\pi^+ p \to k^* \Sigma^+$		$\sigma = 14.5 \pm 2.3$ μb	
0. - 0.15	28	94	31.4	5.9
0.15 - 0.3	24	77	25.9	5.3
0.3 - 0.45	12	47	15.8	4.6
0.45 - 0.9	13	71	7.95	2.2
	$k^- p \to \bar{\rho} \Sigma^+$		$\sigma = 17.7 \pm 3.2$ μb	
0. - 0.15	25	193	41.5	8.3
0.15 - 0.3	20	152	32.5	7.3
0.3 - 0.45	9	72	15.4	5.1
0.45 - 0.9	10	132	9.4	3.0
	$k^- p \to \rho^0 \Lambda$		$\sigma = 11.5 \pm 1.4$ μb	
0. - 0.1	23	257	36.	7.5
0.1 - 0.2	24	237	33.2	6.8
0.2 - 0.3	21	129	18.1	3.9
0.3 - 0.5	16	107	7.5	1.9
0.5 - 0.8	12	86	4.0	1.2
	$\pi^+ p \to k^{*+} \Sigma^{*+}(1385)$		$\sigma = 9.4 \pm 1.2$ μb	
0. - 0.05	13	23.2	20.5	5.7
0.05 - 0.15	28	51.9	22.9	4.4
0.15 - 0.3	25	51.0	15.0	3.0
0.3 - 0.5	16	40.4	8.9	2.2
0.5 - 1.0	12	46.4	4.1	1.2
	$k^- p \to \bar{\rho} \Sigma^{*+}(1385)$		$\sigma = 13.6 \pm 1.3$ μb	
0. - 0.05	26	80	52.5	10.5
0.05 - 0.15	32	95	31.3	5.6
0.15 - 0.3	26	83	18.2	3.6
0.3 - 0.5	19	75	12.3	2.8
0.5 - 1.0	16	81	5.3	1.3

Table 3.6 Differential Cross - Sections

(for 7 Gev/c data)

$K^- p \to \rho^0 \Lambda$

$\lvert t' \rvert$	Number of Events	P	ΔP
0.0 - 0.3	67	0.02	0.33
0.3 - 0.9	12	-0.12	0.64

$\pi^+ p \to K^{*+} \Sigma^+$

$\lvert t' \rvert$	Number of Events	P	ΔP
0.0 - 0.175	22	0.01	0.38
0.175 - 0.45	22	0.74	0.34
0.45 - 0.9	12	0.75	0.39

$K^- p \to \rho^- \Sigma^+$

$\lvert t' \rvert$	Number of Events	P	ΔP
0.0 - 0.2	35	-0.03	0.29
0.2 - 0.5	29	-0.36	0.32

Table 3.7 Polarizations

Giving $$P = \frac{< \cos\theta >}{\alpha < \cos^2\theta >}$$

$$\Delta P = \frac{3}{\alpha} \sqrt{\frac{<\cos^2\theta> - <\cos\theta>}{n}}$$

The Σ^+ polarization for reactions (1) and (2) were found to be approximately mirror symmetric with positive polarization for reaction (1). Both polarization being approximately zero at t' = 0 becoming stronger in the higher t - region. The polarization in reaction (3) was found to be consistent with zero. The polarizations are illustrated in fig 3.9 and listed in table 3.7.

3.6 Discussion of Results

3.6.1 Comparisons with Pseudoscalar Production [24 25]

Data from this experiment for reactions where pseudoscalar exchange is forbidden, by parity conservation, indicate support for weak Exchange Degeneracy (W E x D). In the two pairs of

$$\pi^+ p \rightarrow K^+ \Sigma^+ \qquad (1a)$$
$$k^- p \rightarrow \pi^- \Sigma^+ \qquad (2a)$$

$$\pi^+ p \rightarrow K^+ \Sigma^{*+}(1385) \qquad (4a)$$
$$K^- p \rightarrow \pi^- \Sigma^{*+}(1385) \qquad (5a)$$

line reversed reactions (1a), (2a) and (4a), (5a) the differential cross-sections at 11.5 GeV/c are virtually identical and nearly so at 7 GeV/c. The polarization of the Σ^+ shows strong mirror symmetry. Agreement with W E x D improves at the higher energy. It is therefore interesting to consider the implications of E x D in reactions not related by overall line-reversal.

All of the five reactions studied become increasingly dominated by natural parity exchange as incident energy increases (between 7 and 11.5 GeV/c).[26] This implies that pseudoscalar (K) exchange has a stronger energy dependance than vector exchange as one would expect.

A striking result of the present joint investigation at 7 and 11.5 GeV/c is the similarity, with our statictics, of the differential cross-sections for the pairs of reactions:

$$\pi^+ p \rightarrow K^{*+} \Sigma^+ \qquad (1)$$

$$K^- p \rightarrow \rho^- \Sigma^+ \qquad (2)$$

and

$$\pi^+ p \rightarrow K^{*+} \Sigma^{*+}(1385) \qquad (4)$$

$$K^- p \rightarrow \rho^- \Sigma^{*+}(1385) \qquad (5)$$

The similarity being particularly marked at 11.5 GeV/c Fig 3.14. The Σ^+ polarizations in reactions (1) and (2) show mirror symmetry which, within our statistics, is similar to that observed in the pseudoscalar production reactions (1a) and (2a). Fig 3.10.

A significant difference between the cross-sections for Σ^+ production in (1a),(2a) and (1),(2) is the very different intercepts and slope parameters. At 7 Gev/c the slope is 9.25 in (1a) and 7.42(Gev/c)$^{-2}$ in (2a), wheras they are only 2.4 and 2.7 (Gev/c)$^{-2}$ in (1) and (2) respectively. The vector meson production reaction are therefore considerably less peripheral than pseudoscalar meson production against Σ^+.

The similarity of cross-sections of the pairs of reactions (1), (2) and (4), (5) at 11.5 GeV/c can most likely be ascribed to the E x D properties of the vector trajectory, The Su (3) couplings at the meson vertex in both (1) and (2) are equal.

$K^{*o} \rightarrow \pi^- K^{*+}$ $\qquad$ $K^{*o} \rightarrow K^+ \rho^-$

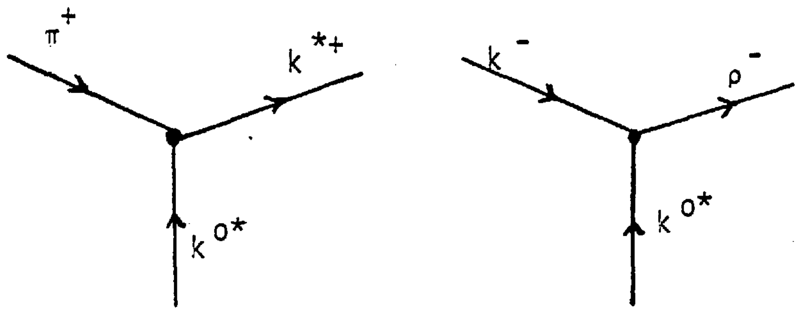

The same arguments apply to pseudoscalar production ($K^{*o} \rightarrow \pi^- K^+$ in (1a) and $K^{*o} \rightarrow \pi^+ K^-$ in (1b)) couplings under Su (3). In this case equality is also insured by invariance under line-reversal.

Additional support for the similarity of psudoscalar and vector meson production characteristics comes from the ideas of the additive quark model. In each of these reactions there is a transition of the type $\bar{d} \rightarrow \bar{s}$ (in π^+) and the quark line reversal process $s \rightarrow d$ (in K^-). The distinction between reaction pairs now involves only spin structure of the final states. Production of the vector mesons requires quark spin flip while pseudoscalar production proceeds with no spin flip.

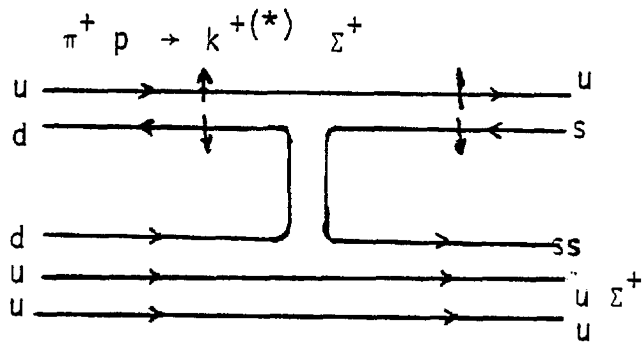

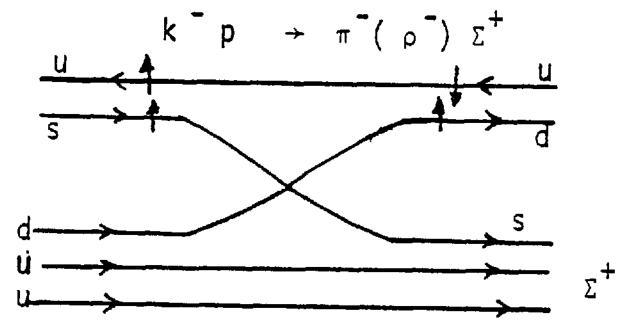

$\bar{d}(\downarrow) \to \bar{s}(\downarrow)$ For k^+

$\bar{d}(\downarrow) \to \bar{s}(\uparrow)$ For k^{+*}

$s(\uparrow) \to d(\uparrow)$ For π^-

$s(\uparrow) \to d(\downarrow)$ For ρ^-

Quark line diagrams for pseudoscalar and vector meson production

Reactions (1a) and (2a) show no evidence for a turnover in the forward direction indicating dominance of the helicity non-flip amplitude, at least at low momentum transfer. Natural parity exchange dominates reactions (1) - (3) at both energies and (4) - (5) at 11.5 GeV/c. This dominance implies helicity flip at the meson vertex. If this is associated with the helicity non-flip amplitude at the baryon vertex then we have overall spin-flip. There must therefore be a dip near $t' = o$ corresponding to the vanishing helicity flip amplitude in that region.

If the baryon vertex has also a helicity flip term the total helicity can be zero and the size of the forward dip would be expected to decrease due to a contribution from the spin non-flip amplitude. For reactions (1) and (2) a dip in low t' region is not observed. The fact that the polarization in these reactions disappears near $t' = o$ indicates only the absence of either the flip or non-flip amplitudes in this region. Further statements about the nature of the amplitudes cannot be made as a t-dependent analysis of the exchange naturalities was not feasible with our statistics.

The differential cross-section for $K^-P \rightarrow \rho^- \Sigma^{*+}(1385)$ shows a rise near $t' = o$. This effect is not seen at 11.5 GeV/c, however it has been seen in the 4.2 GeV/c K^-P experiment where a t- dependant analysis of the exchange naturality was done.[17 18] Their results are illustrated in Fig 3.11. It is seen ρ_{oo} dominates near $t' = o$. The fall of the latter being much steeper with t' than either ρ_+ or ρ_-. The reaction $K^-P \rightarrow \rho^- \Sigma^{*+}(1385)$ therefore shows an energy variation of the exchanged naturality. Table 3.8 shows the energy variation of exchanged naturality for an example of each type of reaction.

The increasing dominance of natural parity exchange with energy is clear. At low energy the dominance of ρ_{oo} near $t' = o$ may give rise to an overall helicity non-flip amplitude in this region.

3.6.2 Energy Dependance of Total Cross-Sections

Total cross-section variation with energy, for reactions (1), (2), (4) and (5), is shown in Fig 3.12. The data is consistant with $P_{Lab}^{-1.8\pm .6}$, a behaviour expected from E x D models if only K^* and K^{**} trajectory were exchanged.[27 28] This is to be compared with $P_{Lab}^{-0.99\pm .05}$ and $P_{lab}^{-1.34\pm .06}$ for the pseudoscalar production reactions (1a) and (2a) respectively.

$$0^- \ \tfrac{1}{2}^+ \longrightarrow 1^- \ \tfrac{1}{2}^+$$
$$K^- \ P \longrightarrow \rho \ \Lambda$$

P_{Lab} GeV/c	ρ_+ %	ρ_- %	ρ_{oo}%	σ_T (μb)
4.2	52 ± 7	35 ± 7	13 ± 4	82 ± 8
7	43 ± 10	38 ± 10	19 ± 15	11.5 ± 1.4
11.5	67 ± 7	33 ± 6	< 4	—

$$0^- \ \tfrac{1}{2}^+ \longrightarrow 1^- \ \tfrac{3}{2}^+$$
$$K^- \ P \longrightarrow \rho^- \ \Sigma^{*+}(1385)$$

P_{Lab} GeV/c	ρ_+ %	ρ_- %	ρ_{oo} %	σ_T (μb)
4.2	14.7 ± 4.4	39.7 ± 4.4	46 ± 6	88 ± 6
7	47 ± 13	34 ± 10	19 ± 15	13.6 ± 1 3
11.5	69 ± 8	30 ± 6	< 5	—

Table 3.8 Energy dependance of Exchange Naturality.

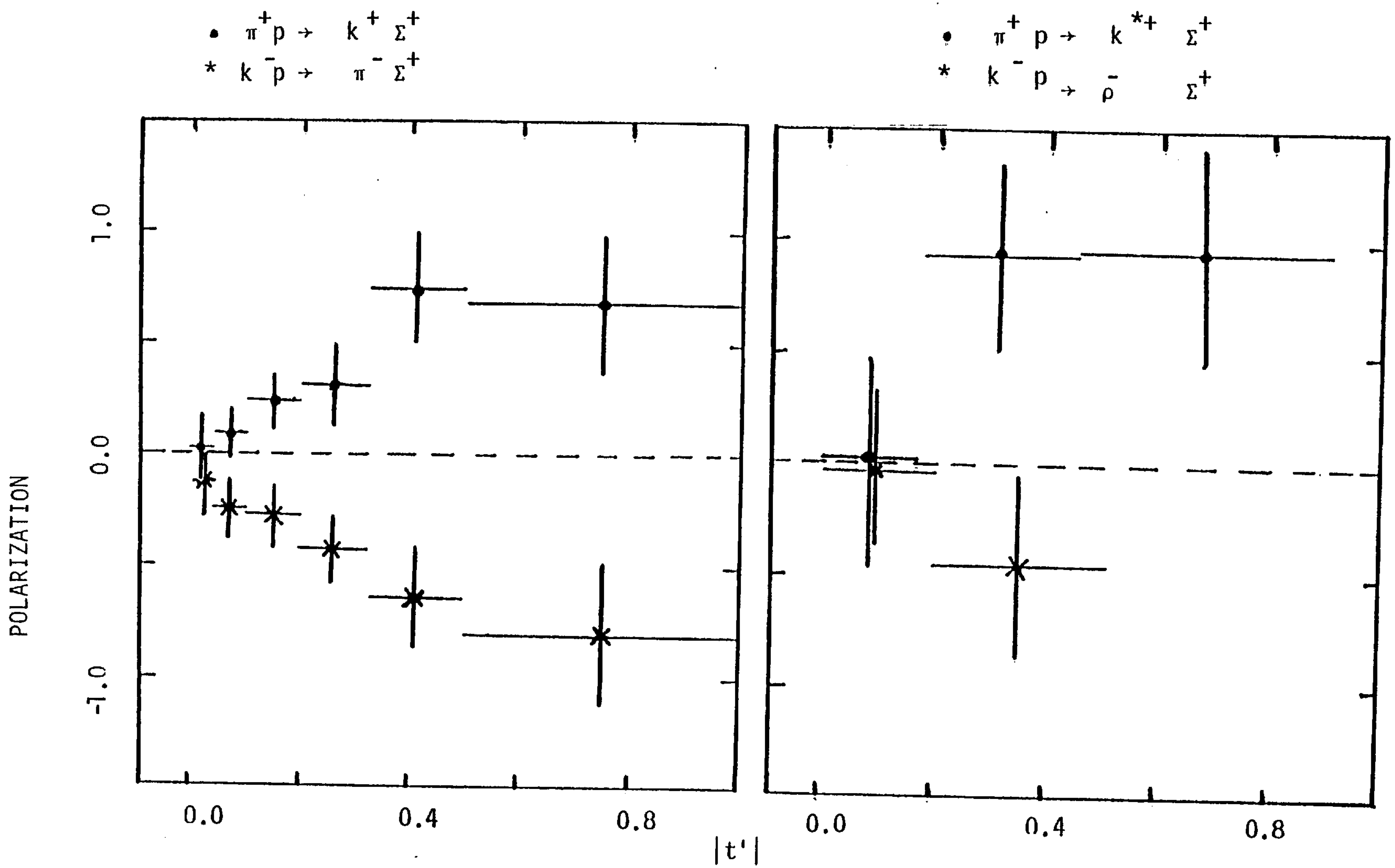

Fig 3.10 Comparisons of Σ^+ polarizations in production against pseudoscalar and vector meson.

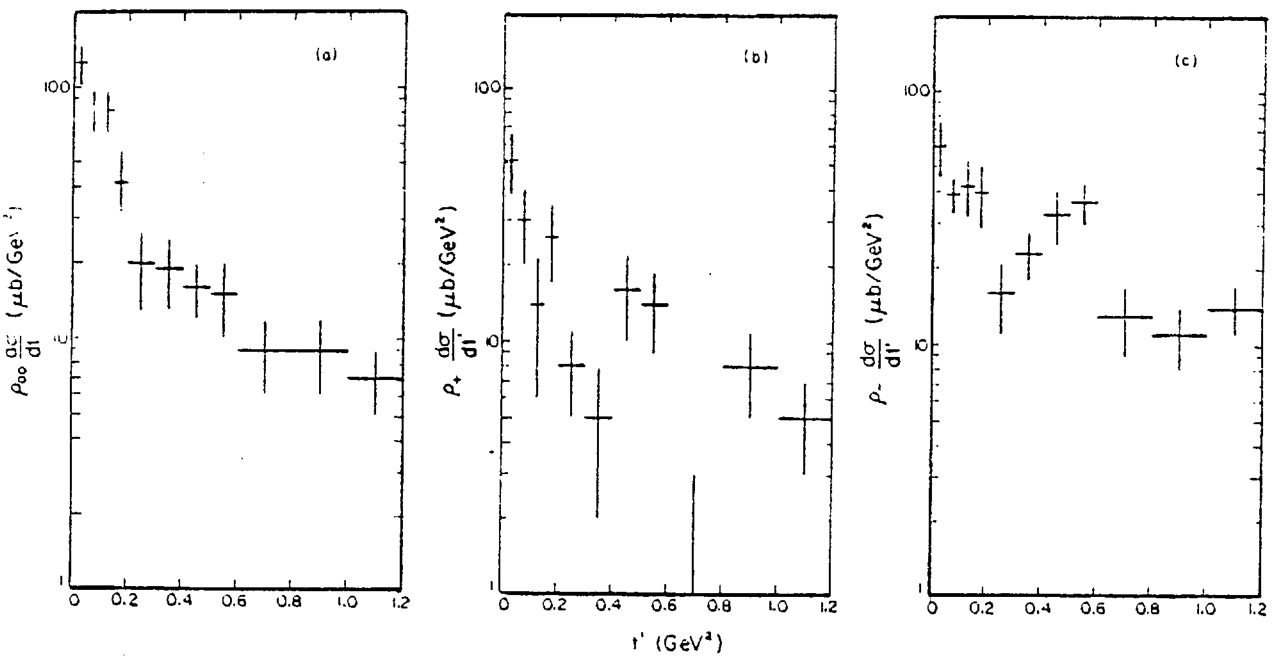

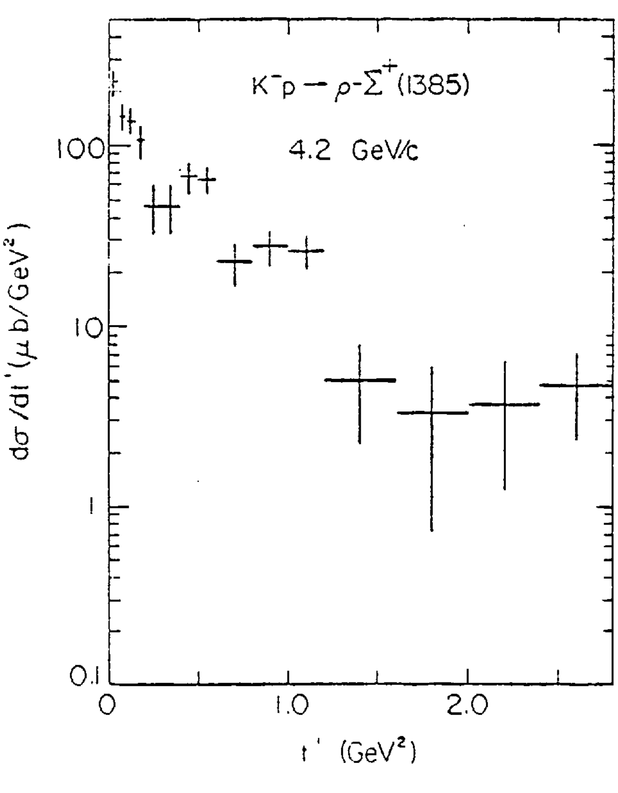

Fig 3.11 t-dependance of the exchange naturality from the 4.2 Gev/c k^-p experiment .

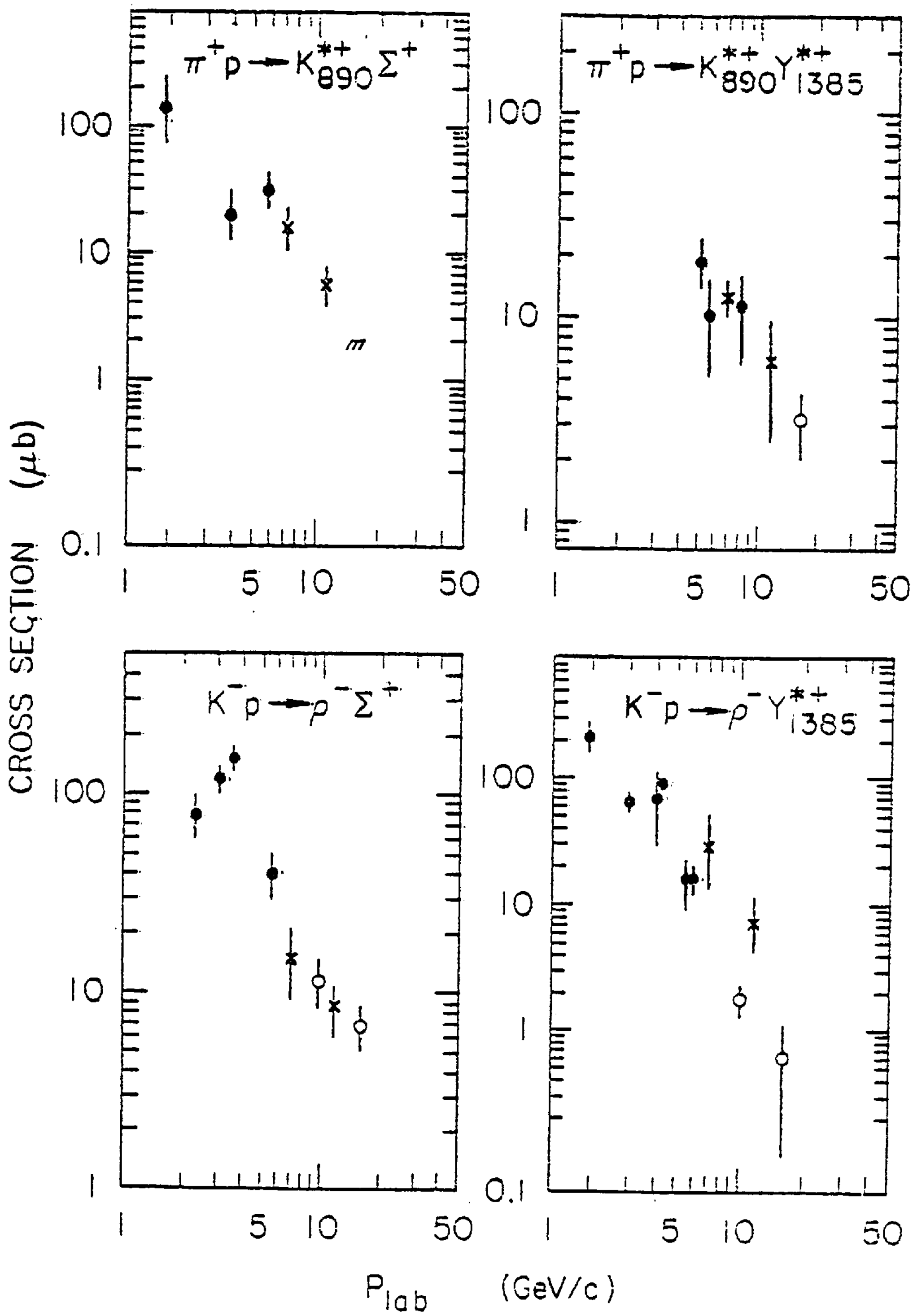

Fig 3.12 Total cross-section variation with P_{lab} .

3.6.3 Decay Distribution of $\Sigma^{*+}(1385)$

For a transition at the baryon vertex of the type:

$$\overline{K}^{*o} + p \longrightarrow \Sigma^{*+}(1385) \rightarrow \Lambda + \pi^+$$

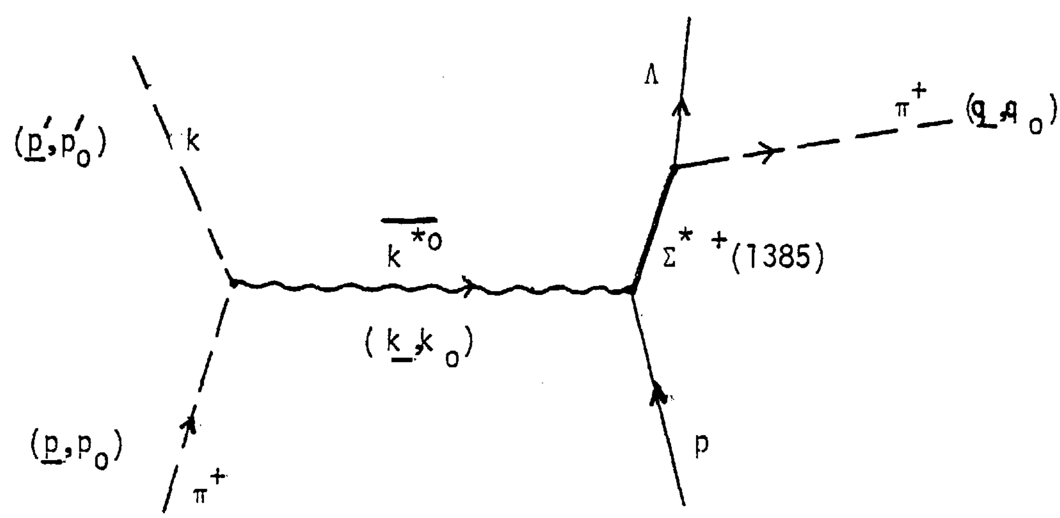

Stodolsky and Sakurai have derived predictions, for the angular distribution of the decay pion, based on the vector meson exchange model for isobar production.[29, 30] For the production of $P_{3/2}$ isobar by the transition $M1 \rightarrow P_{3/2}$ they predict the decay distribution:

$$W(\cos\theta) = 1 + 3\cos^2\theta$$

$$W(\phi) = \text{Constant}$$

| In isobar rest frame |

$$\cos\theta = \hat{q} \cdot \hat{n}$$

$$\hat{n} = \frac{\hat{p} \wedge \hat{p}'}{|p \wedge p'|} \qquad \text{Production plane normal.}$$

The decay distribution of $\Sigma^{*+}(1385)$ for reactions (4), (5) and (4a), (5a) are compared in Fig 3.13. It is clear that the pseudoscalar production reactions (4a) and (5a) are dominated by $M1 \rightarrow P_{3/2}$ transition. However reactions (4) and (5) do not show any preference for a particular type of transition.

$\pi^+ p \rightarrow K^+ Y^{*+}(1385)$

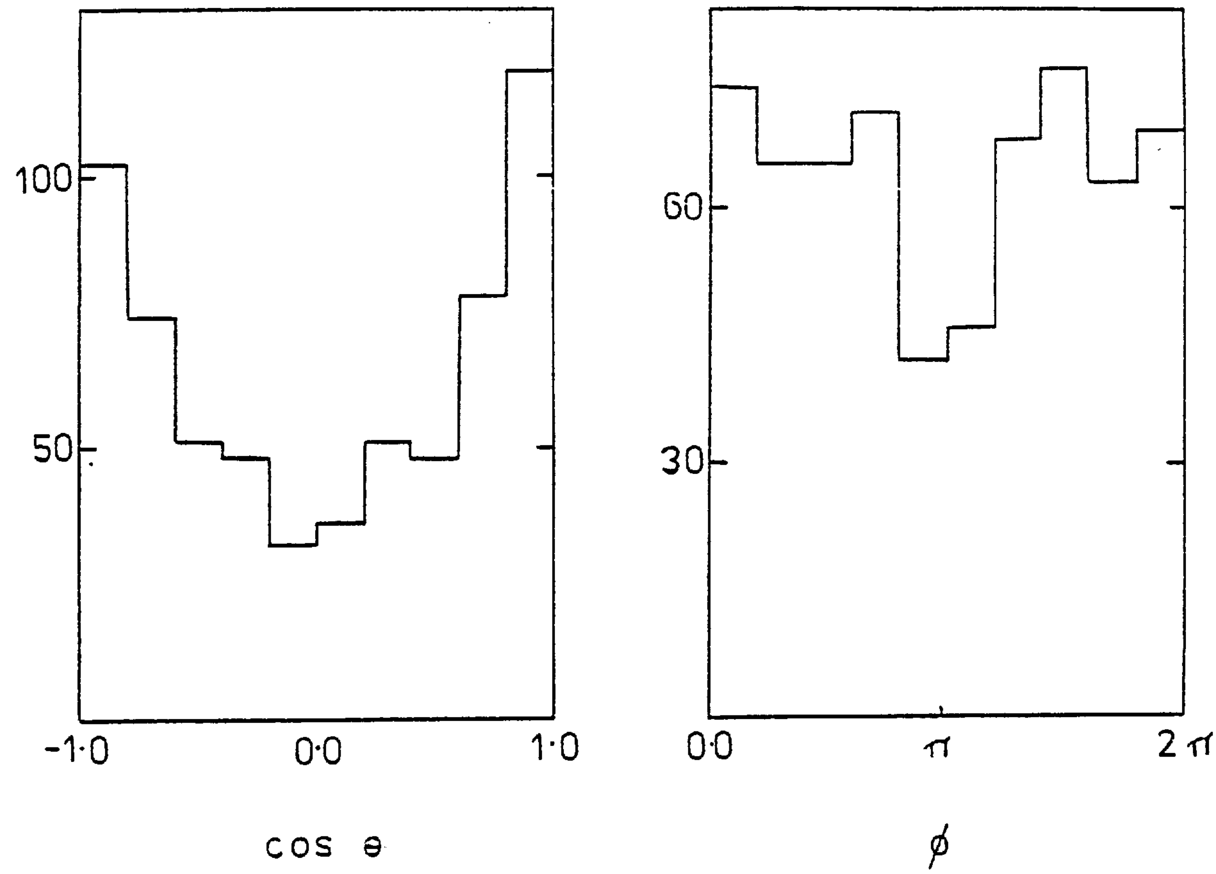

$\pi^+ p \rightarrow K^{*+}(890)\, Y^{*+}(1385)$

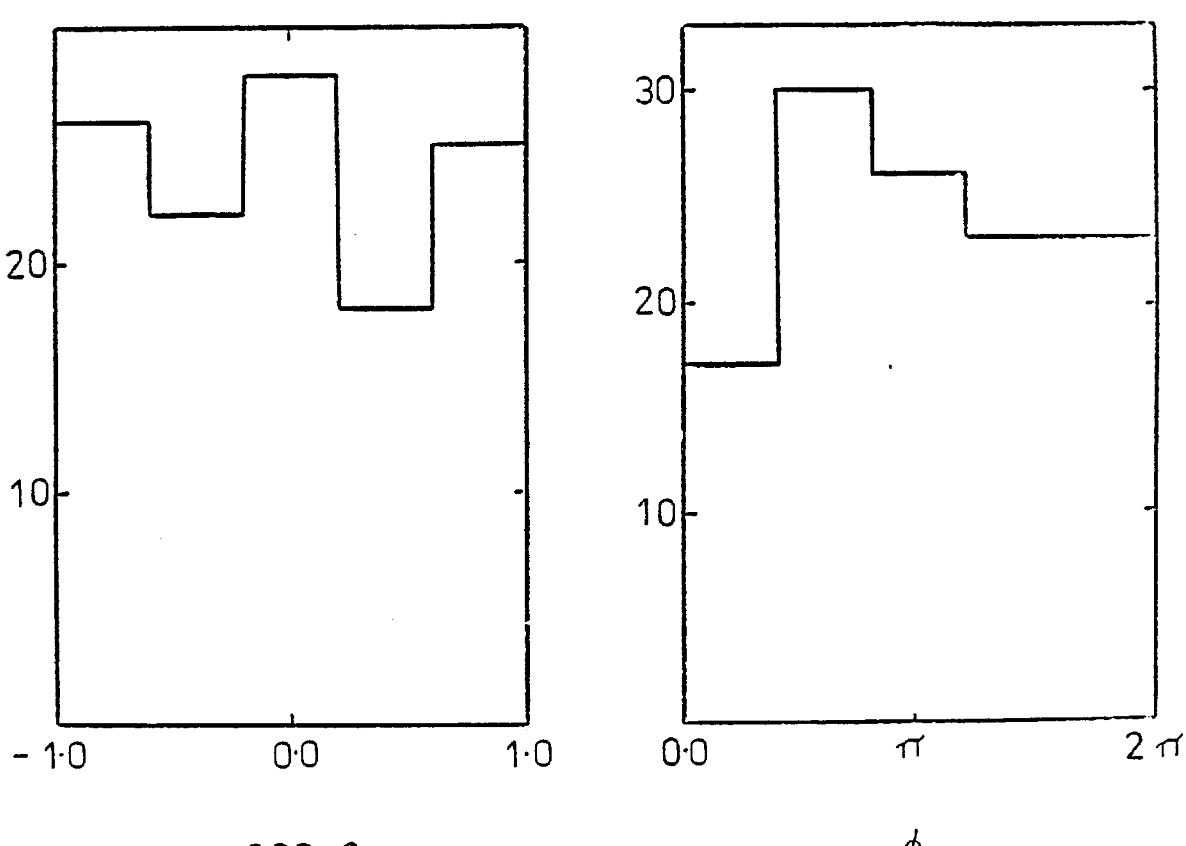

(a)

Fig 3.13 (a)-(b) Decay distribution of $\Sigma^{*+}(1385)$

$K^- p \longrightarrow \pi^- Y^{*+}(1385)$

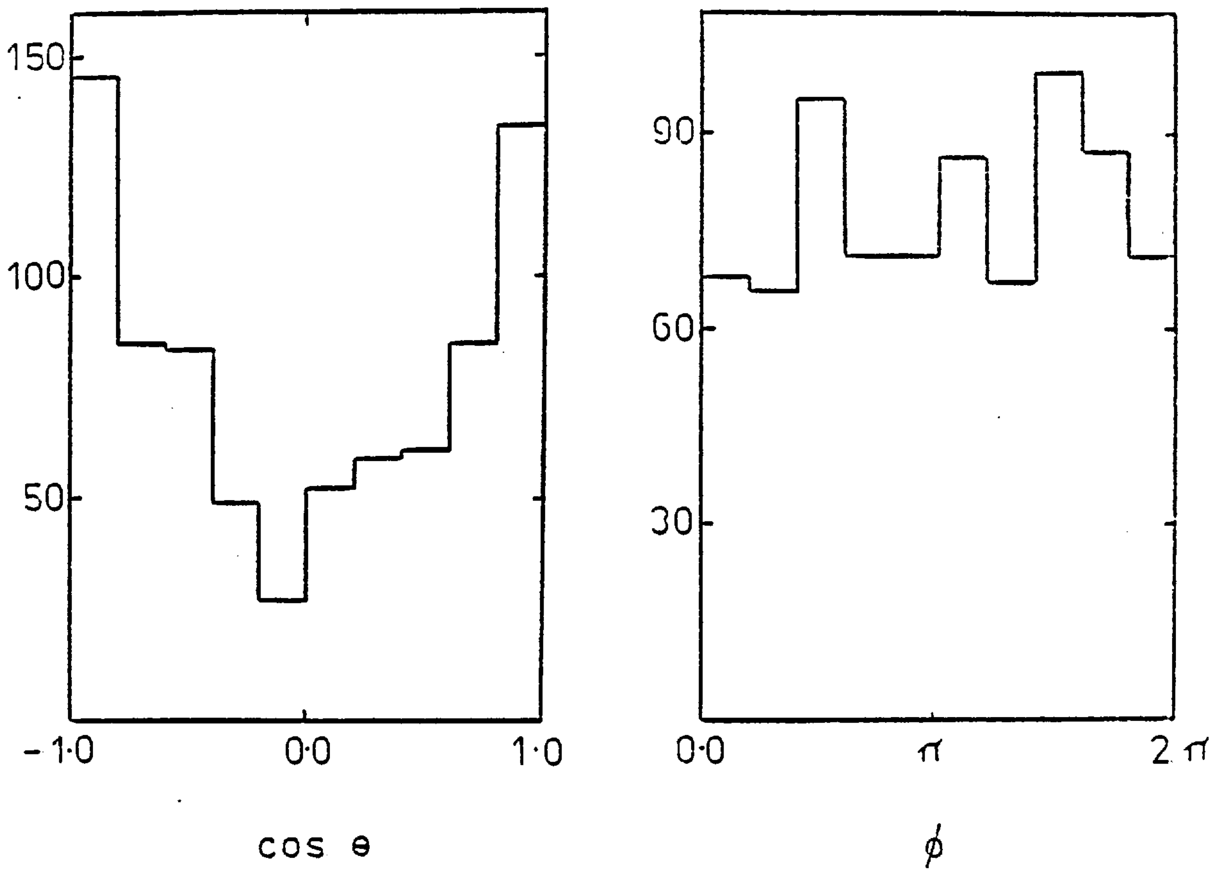

$K^- p \longrightarrow \rho^- Y^{*+}(1385)$

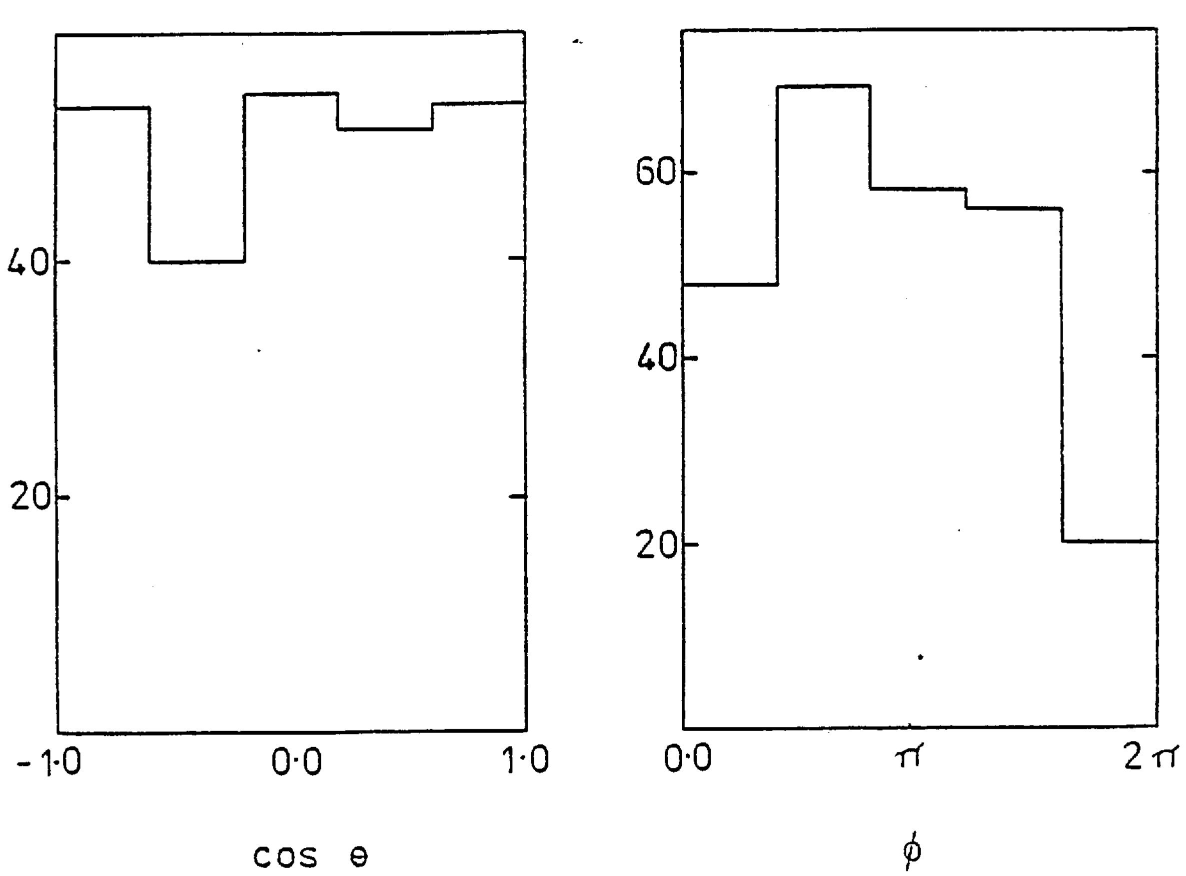

Fig 3.13 (b)

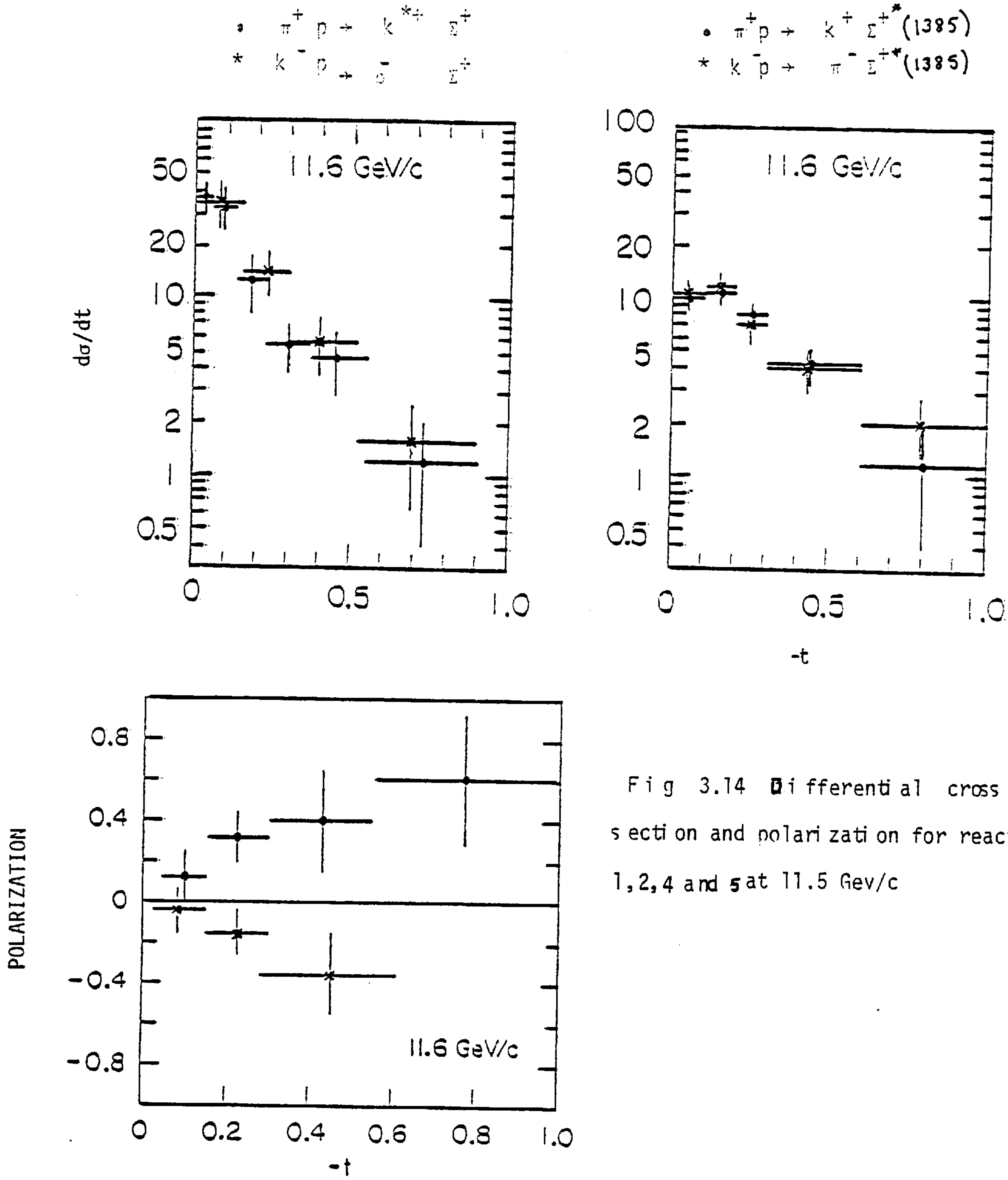

Fig 3.14 Differential cross - section and polarization for reactions 1,2,4 and 5 at 11.5 Gev/c

3.7 Conclusions

Hypercharge exchange reactions producing vector meson against Λ, Σ^+ and $\Sigma^{*+}(1385)$ have been studied at 7 GeV/c in conjunction with the 11.5 GeV/c S.L.A.C. data. Σ^+ reactions are natural parity dominated, which would mainly be K^* and K^{**} exchange, leading to very similar production characteristics in pseudoscalar and vector meson production. Polarization of the Σ^+ shows reflection symmetry between π^+ and K^- in both pseudoscalar and vector meson production. The reactions $K^-P \rightarrow \pi^- \Sigma^{*+}(1385)$ and $K^-P \rightarrow \rho\, \Lambda$ have contribution from ρ_{00} which is decreasing with energy.

CHAPTER 4

Σ Production in the 1700 MeV Region

4.0.1 Introduction

In this chapter results on the $\Sigma(1670)$ region are presented. The final states studied are 201, 210, 401 and 410; the data coming from π^+ and k^- induced reactions at 7 GeV/c.

The present status of the Σ states in the 1700 MeV region, in the Data Card Listing, is tabulated below;[31]

State	PARTIAL WAVE in WHICH SEEN	STATUS	J^P
$\Sigma(1580)$	D_{13}	* *	-
$\Sigma(1620)$	S'_{11}	* *	$\frac{1}{2}^-$
$\Sigma(1660)$	P'_{11}	* * *	$\frac{1}{2}^+$
$\Sigma(1670)$	D_{13}	* * * *	$\frac{3}{2}^-$
$\Sigma(1670)$	--	* *	-
$\Sigma(1690)$	--	* *	-
$\Sigma(1750)$	S''_{11}	* * *	$\frac{1}{2}^-$
$\Sigma(1765)$	D_{15}	* * * *	$\frac{5}{2}^-$

The $\Sigma(1620)$ was first reported ten years ago in the decay mode $\Lambda\pi^+$. Since then there have been conflicting reports about this state (S).[31 32]

The $\Sigma(1660)$ was first reported about 18 years ago, but in spite of a large experimental effort the situation has remained confused. Formation experiments observe two states in this mass region. One of these is the $\Sigma(1670)$ ($J^P = \frac{3}{2}^-$) and has a large $\Sigma\pi/\Sigma\pi\pi$ branching ratio. The other state is the $\Sigma(1660)$ ($J^P = \frac{1}{2}^+$) and its $\Sigma\pi/\Sigma\pi\pi$ branching ratio is unknown.

Production experiments also observe a signal at 1670 MeV. The measured $\Sigma\pi/\Sigma\pi\pi$ branching ratio for the produced $\Sigma(1670)$ is found to be strongly dependent on momentum transfer. This evidence is generally accepted to be suggestive of two Σresonances with the same mass and quantum numbers. One object is produced peripherally with large $\Sigma\pi\pi$ (mainly $\Lambda(1405)\pi$) decay mode, and another one with a large $\Sigma\pi$decay mode produced at larger angles. The quantum numbers for both $\Sigma\pi$ and $\Lambda(1405)\pi$ decay mode are thought to be $\frac{3}{2}^-$.

The state referred to as the $\Sigma(1690)$ in the Data Card Listings has a large $\Lambda\pi/\Sigma\pi$ branching ratio. This is the main justification for its existence as a state different from the $\Sigma(1670)$, since the latter appears to have a dominant $\Sigma\pi, \Sigma\pi\pi$ decay mode. The state has been seen only in production experiments and only in the $\Lambda\pi^+$ mass spectrum. It appears as broad enchancement, earlier low ($\sim$4 GeV/c) energy experiments have quoted $\Gamma\sim$100 MeV while more recent higher (10 GeV/c) energy experiments quote $\Gamma\sim$ 200 MeV.[41 42]

4.0.2 Why Study Resonances?[33_ 37]

Apart from the enumeration of what hadronic states exist and their quantum numbers, the arrangement of states should tell us something about the symmetries of strong interactions. The existance of symmetry groups like SU(2) and SU(3) imply that single particle states fall into multiplet groups. Establishment of such symmetry groups will in turn lead to stronger statements about relations among amplitudes for production and decay of particles.

If hadrons are made of quarks this structure may be reflected in a recognizable way in the spectrum of states. The constituent quark model visualizes hadrons as being built up from basic spin ½ quarks. Excluding charm and higher mass flavours, there are three quarks the quantum number of which are shown in table 4.0.1.

Flavour	J^P	I	I_z	S	Q	B
u	$\frac{1}{2}^+$	½	½	o	2/3	1/3
d	$\frac{1}{2}^+$	½	-½	o	-1/3	1/3
s	$\frac{1}{2}^+$	o	o	-1	-1/3	1/3

Table 4.0.1

Wigner's supermultiplet theory of nuclear structure was transplanted in the early 60's into particle physics. The approximate independence of spin and isospin of forces in nuclear structure lead to the classification of states according to irreducible representations of su(4). Parallel to this in particle physics a supermultiplet theory emerged extending the su(3) multiplets. The baryon states (below charm threshold) are bound states of three types of quarks. The su(3) reduction being:

$$B \sim qqq \sim 3 \times 3 \times 3 = 1 + 8 + \bar{8} + 10$$

baryons are in the 1, 8 and 10 dimensional representation.

The su(6) theory in the context of non relativistic constituent quarks combines Unitary spin, su(3), and spin degree of freedom, su(2), to form a 6 under su(6). The possible quark states now become:

$$q \sim (u\uparrow, u\downarrow, d\uparrow, d\downarrow, s\uparrow, s\downarrow)$$

The possible su(6) content of baryons is given by the reduction:

$$B \sim qqq \sim 6 \times 6 \times 6 = 56 + 70 + 70 + 20$$

with the assumption of independence of spin and unitary spin of the q - q binding force relevent to low lying particles. For higher states - which are orbital excitations of the q - q system within a simple harmonic oscillator type potential - the above assumption about the nature of the confining interaction leads to su(6) X 0(3) hadron multiples, Fig. 4.0.1.

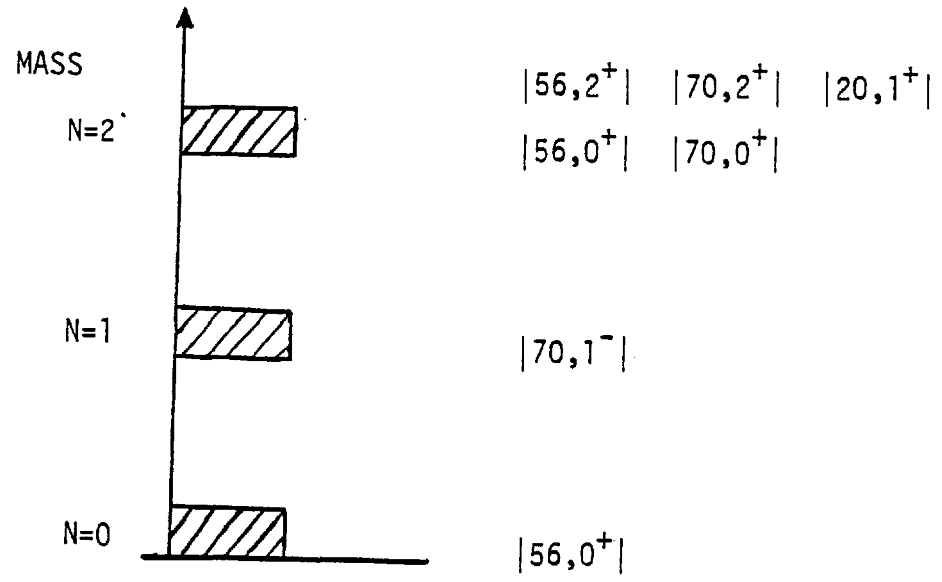

Fig. 4.0.1 Spectrum of allowed su(6) X 0(3) multiplets in the harmonic oscillator quark shell model.

The su(6) baryon multiples with the so far discovered states are shown in Fig. 4.0.2

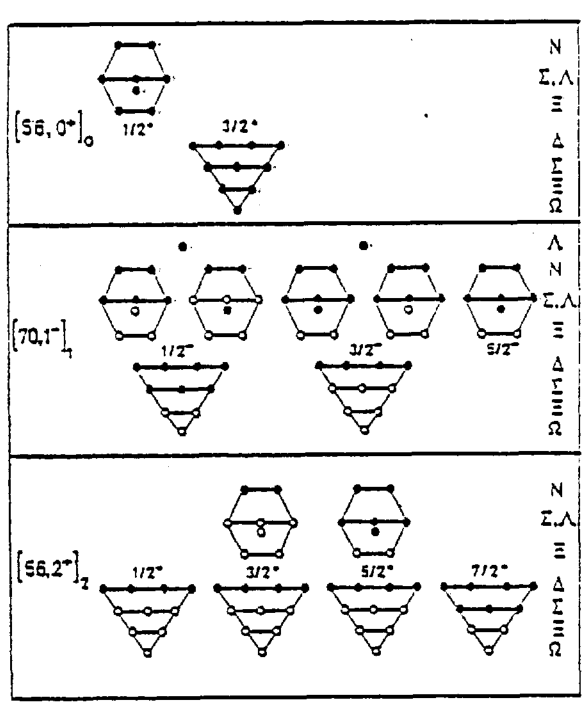

Fig. 4.0.2 Established baryon Multiplets in su(6). (Missing states are in open circles).

As can be seen from this, there are a considerable number of missing sigmas as well as other states. Establishment of these would add greater weight to the su (6) classification.

4.1.1 Results from 201's, 210's in π^+p and k^-p

In this section results from a study of $\Sigma(1670)$ production in the final states

$$\begin{aligned}
\pi^+p \;\rightarrow\; & k^+\,\Sigma^+\,\pi^0 \\
& k^+\,\Sigma^0\,\pi^+ \\
& k^+\,\Lambda\;\;\pi^+\,(\pi^0) \\
& k^+\;\;p\,\overline{k^0}\,(\pi^0) \\
k^+p \;\rightarrow\; & \pi^-\,\Sigma^+\,\pi^0 \\
& \pi^-\,\Sigma^0\,\pi^+ \\
& \pi^-\,\Lambda\;\;\pi^+\,(\pi^0) \\
& \pi^-\;\;p\,k^0\,(\pi^0) \\
& \pi^-\;\;N\,k^0\;\;\pi^+
\end{aligned}$$

are presented . Spin-parity of the Σ state will be discussed,together with the data from 410's,in section 4.3.

4.1.2 Production of $\Sigma(1670) \rightarrow \Sigma^0\,\pi^+$ in:

$$\pi^+\,p \;\rightarrow\; k^+\,\pi^+\,\Sigma^0 \qquad (1)$$

$$k^-\,p \;\rightarrow\; \pi^-\pi^+\,\Sigma^0 \qquad (2)$$

As we trigger on a fast k^+ in reaction (1) and fast π^- in reaction (2) we are sensitive to backward hyperon production. In reaction (1) the meson resonance channel ($k^+\,\pi^+$) is exotic and hence a very clean $\Sigma(1670)$ signal in ($\Sigma^0\,\pi^+$) is produced, Fig. 4.1.1(a).Some $\Sigma(1385)$ is also produced which appears to be split. This is due to events from the 4c channel $\Lambda\pi^+k^+$ being misassigned into the 2c channel $\Sigma^0\,\pi^+\,k^+$ (chapter 2).

The scatter plot, with projections, for reaction (2) is shown in Fig.4. 1.1(b)where it is seen that $\Sigma(1670)$ has a larger background than in reaction (1).

The phase space for the ($\Sigma^0\pi^+$) mass spectrum were generated using the CERN Monte Carlo program FOWL[38]. Fits to the ($\Sigma^0\pi^+$) mass spectrum using the generated phases space plus Briet-Wigner functions were made for both

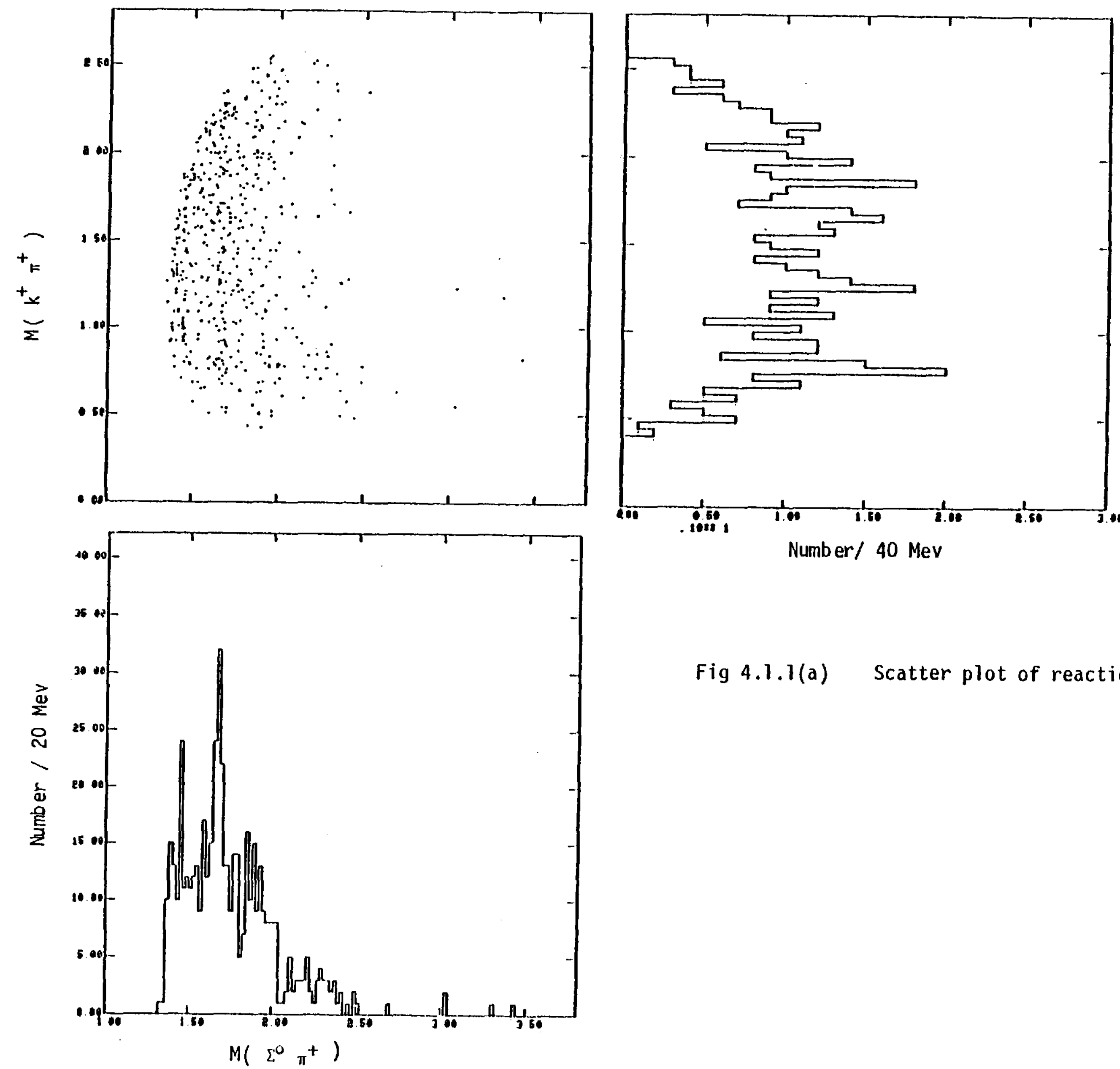

Fig 4.1.1(a)   Scatter plot of reaction (1)

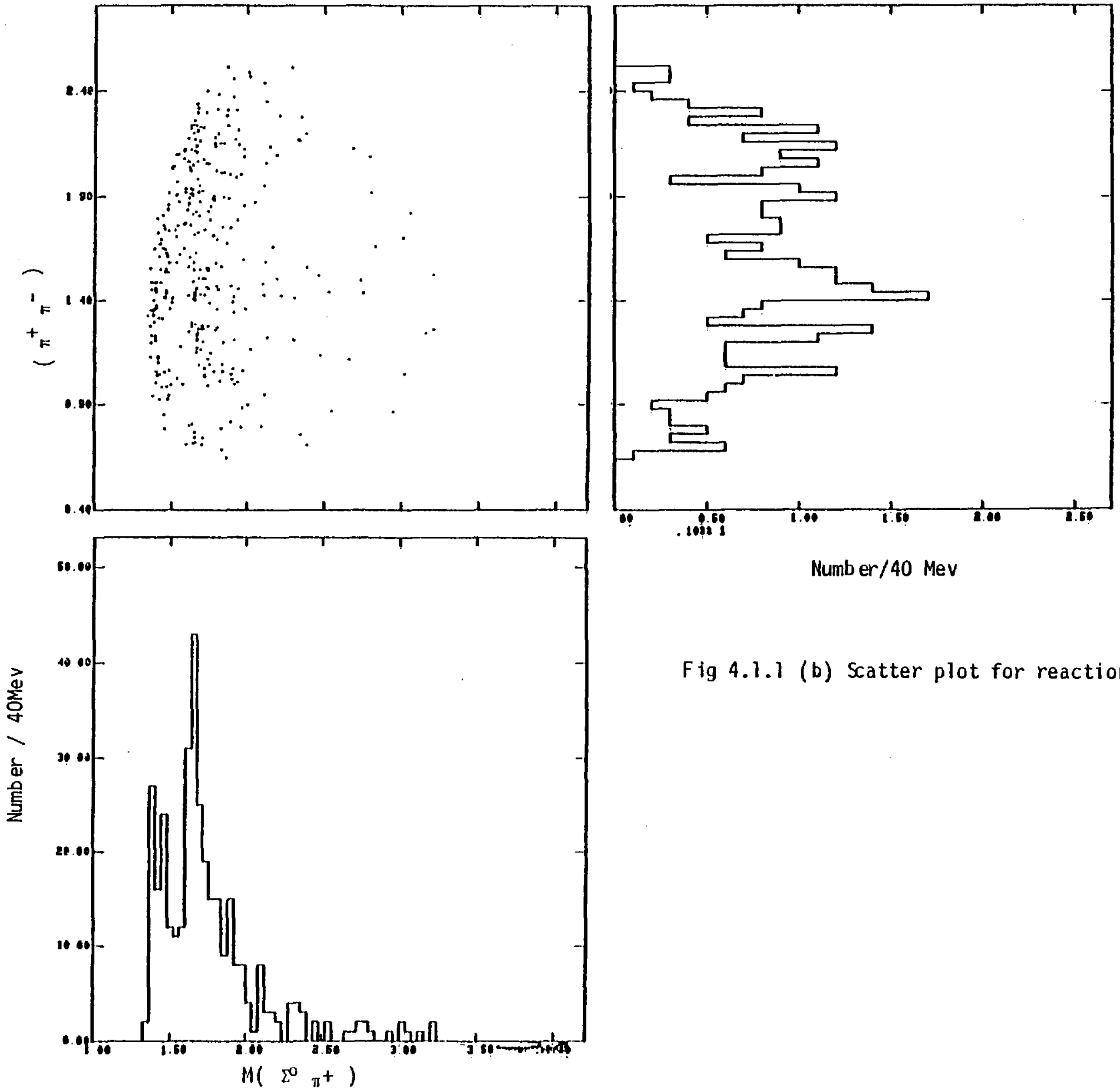

Fig 4.1.1 (b) Scatter plot for reaction (2)

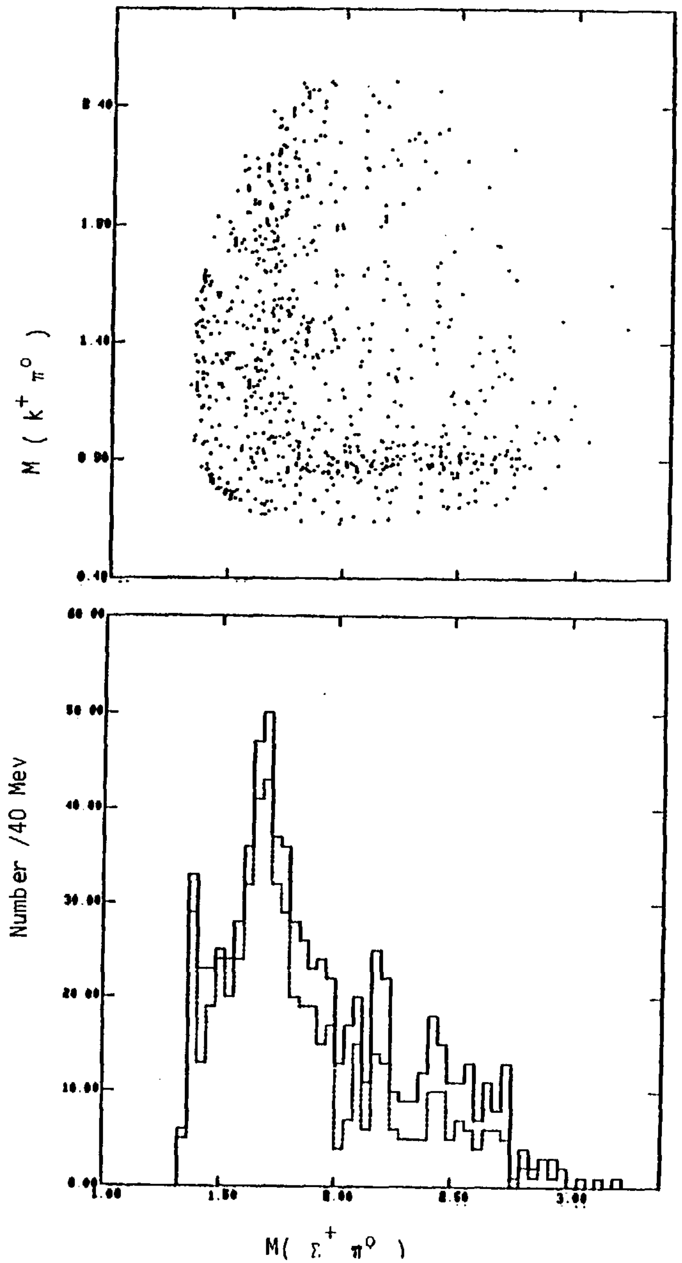

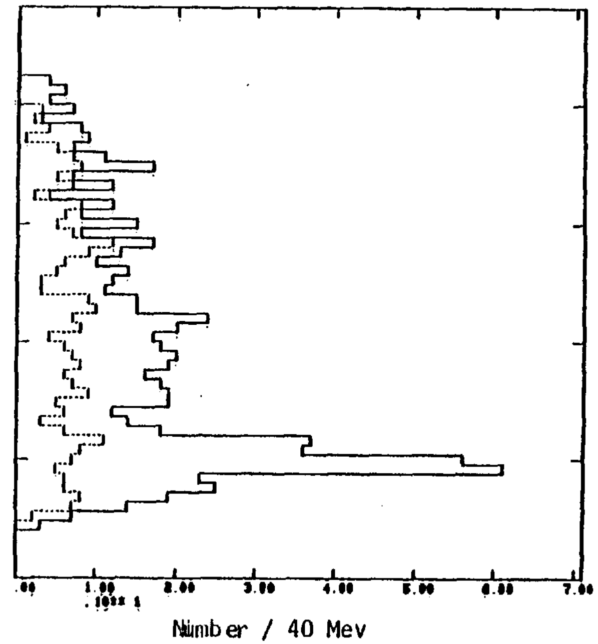

Fig 4.1.2 (a) Scatter plot for reaction (3)

(dashed lines indicate meson or hyperon resonance selection)

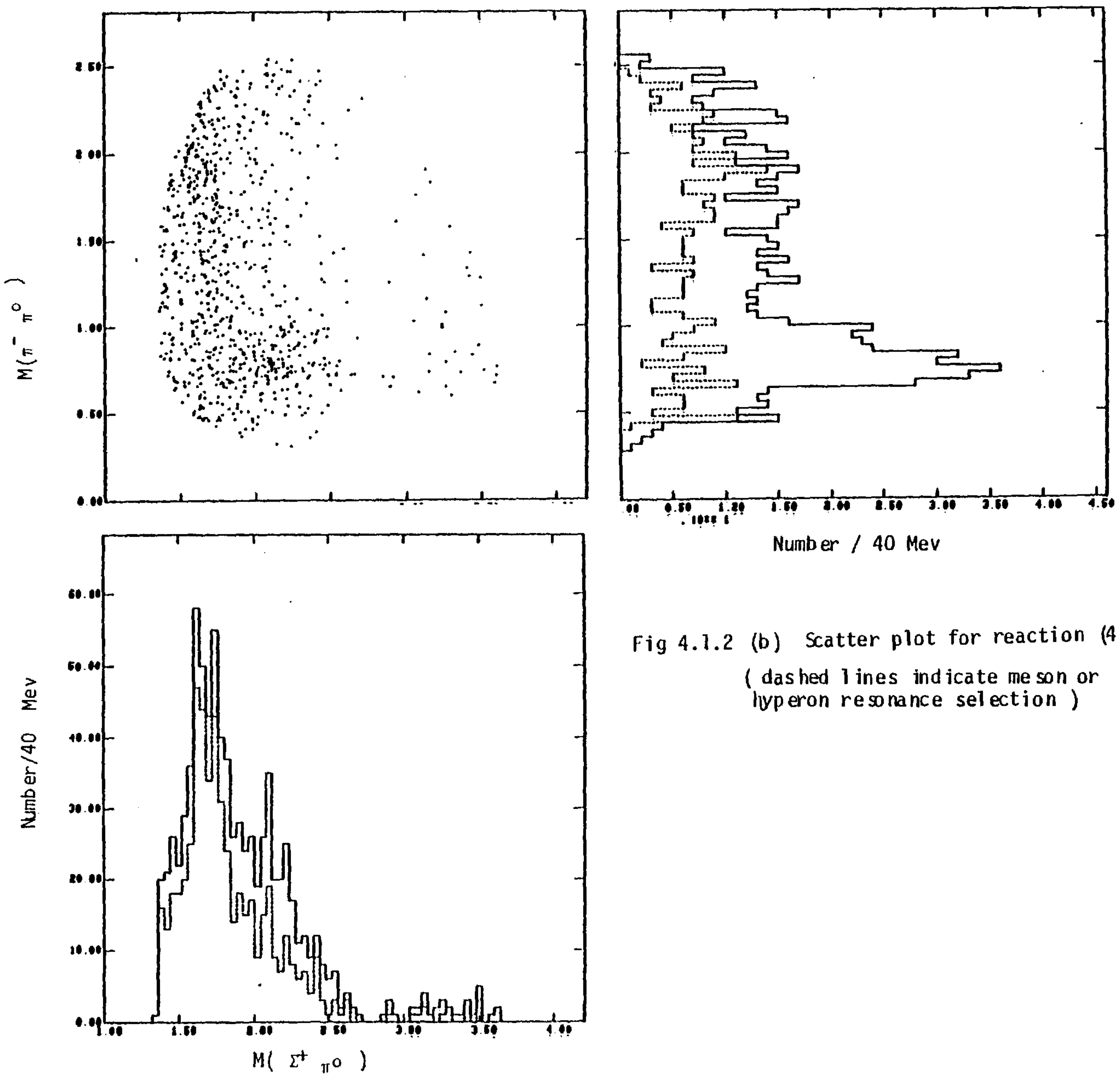

Fig 4.1.2 (b) Scatter plot for reaction (4)

(dashed lines indicate meson or hyperon resonance selection)

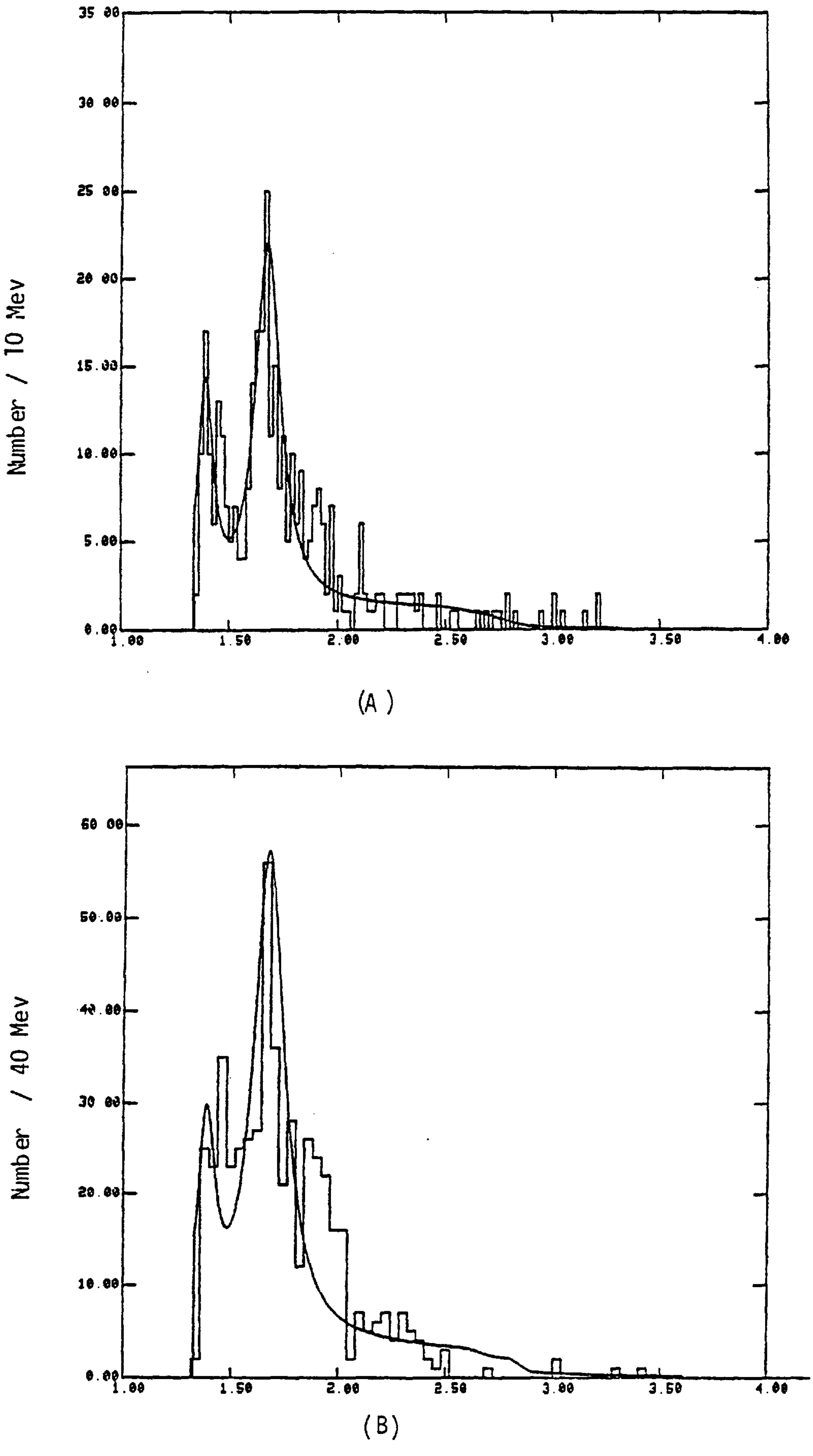

Fig 4.1.3.a Fits to $M(\Sigma^{0}\ \pi^{+})$ for reaction 1, (A), and 2, (B).

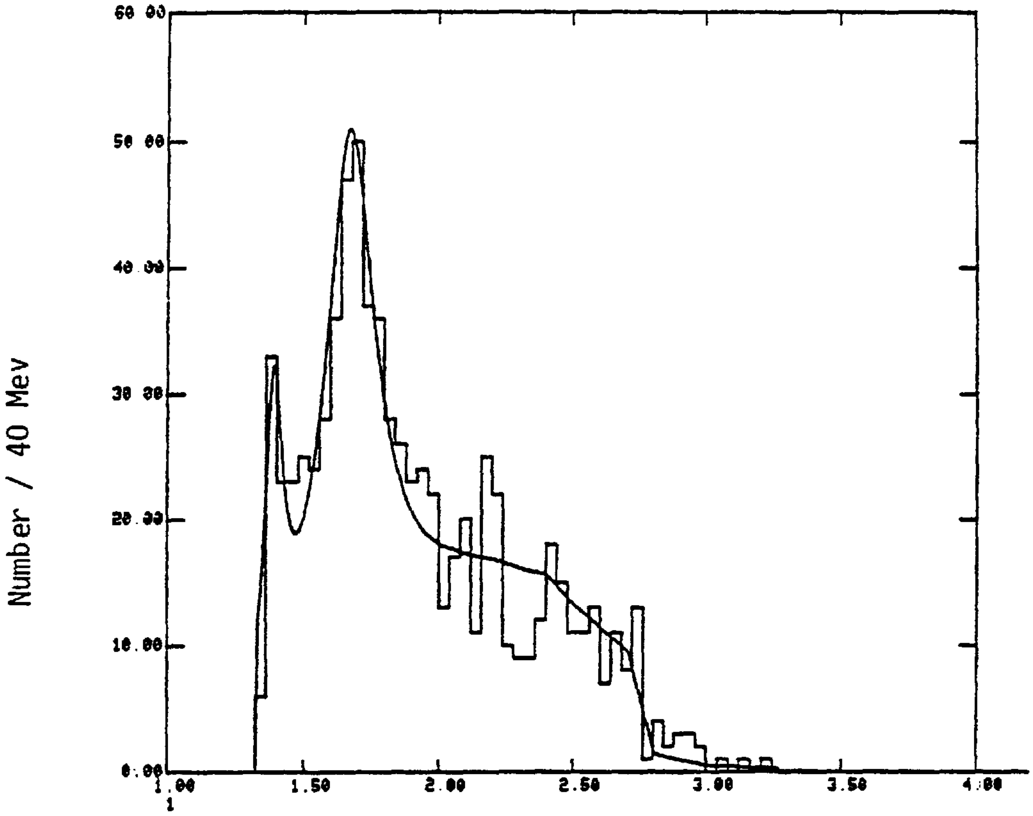

(A)

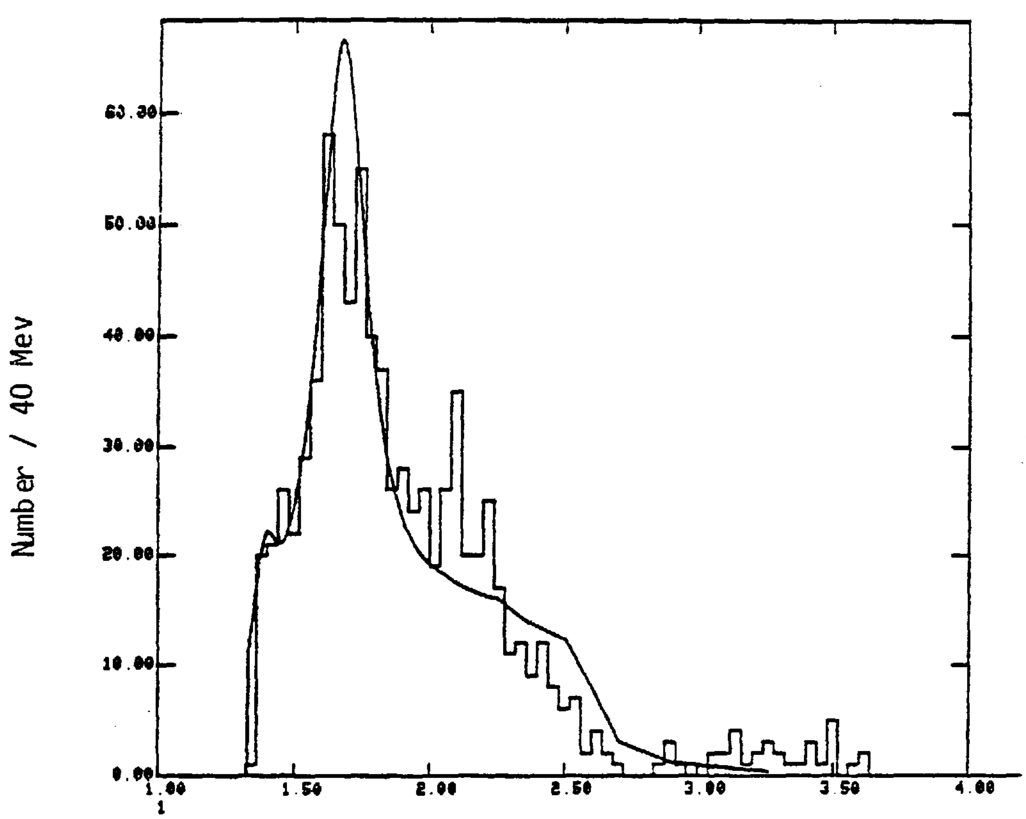

(B)

Fig 4.1.3.(b) Fits to $M(\Sigma^{+} \pi^{o})$ for reaction 3, (A), and 4, (B) .

reactions. Results of these fits are show in Fig 4.1.3. The data and the results of these fits are summarised in table 4.1.1.

Final State	Central Mass (MeV)	Γ(Mev)	No. of EVENTS
$k^+ \Sigma^0 \pi^+$	1673 $\pm$ 12	140 $\pm$ 30	342
$\pi^- \Sigma^0 \pi^+$	FIXED TO ABOVE VALUES		501

Table 4.1.1

Differential and Total Cross-Sections

The cross-sections were determined using the expressions discussed in chapter 2 and 3. The resonance region was defined as $1.6 \leqslant M(\Sigma^0\pi^+) \leqslant 1.72$ GeV/c^2. The total cross-sections have been corrected for background. For the t range $t\ min \leqslant |t| \leqslant 1.\ (GeV/c)^2$ the total cross-section was found to be 1.61 $\pm$ 0.24 μb for reaction (1) and 3.10 $\pm$ 0.37 μb for reaction (2).

Fits to the differential cross-section of the form $\frac{d\sigma}{dt} = A\ e^{-Bt}$ were made, Fig. 4.1.4, and the parameters of the fit are listed in table 4.1.2. The differential cross-sections are listed in table 4.1.3. The slope parameter for the two reactions has a similar value.

Reaction	Number of Events	Weighted Number	SLOPE	INTERCEPT
$\pi^+ p \rightarrow k^+ \Sigma^+(1670)$, $\hookrightarrow \Sigma^0\pi^+$	215	314	4.0 $\pm$ 0.5	6.91 $\pm$ 0.81
$k^- p \longrightarrow \pi^- \Sigma^+(1670)$, $\hookrightarrow \Sigma^0\pi^+$	363	533	3.6 $\pm$ 0.4	11.79 $\pm$ 1.30

Table 4.1.2 Cross-Section Parameters

$\pi^+ p \to k^+ \Sigma(1670)$ $\sigma = 1.61 \pm 0.2o\ \mu b$

$-t\ (GeV/c)^2$	$\frac{d\sigma}{dt}\ (GeV/c)^2$	$\Delta \frac{d\sigma}{dt}$
tmin - 0.2	5.13	0.77
0.2 - 0.4	2.44	0.53
0.4 - 0.6	0.80	0.33
0.6 - 1.0	0.36	0.21
$k^- p \to \pi^- \Sigma^+(1670)$	$\sigma = 3.10 \pm 0.37\ \mu b$	
tmin - 0.2	8.70	1.33
0.2 - 0.4	4.97	0.94
0.4 - 0.6	1.80	0.63
0.6 - 1.0	0.65	0.32

Table 4.1.3 Cross-Sections (Errors are Statistical)

4.1.3 Production of $\Sigma(1670) \to \Sigma^+ \pi^0$ in:

$$\pi^+ p \to k^+ \Sigma^+ \pi^0 \qquad (3)$$

$$k^- p \to \pi^- \Sigma^+ \pi^0 \qquad (4)$$

The scatter plots for reactions (3) and (4) are shown in Fig. 4.1.2 (b - c). The $\Sigma(1670)$ is much broader than in (1) and (2) due to the poorer resolution which is approximately 50 MeV compared to about 15 MeV in (1) and (2). There is also substantial vector meson production compared to reactions (1) and (2). The scatter plot projections also show the vector meson reflection removed ($\Sigma^+ \pi^0$) projections. In both reactions the $\Sigma(1670)$ become somewhat 'cleaner'. The number of events were 766 in reaction (3) and 813 in reaction (4), these were reduced to 551 and 531 respectively with the vector meson cuts. The background in both these reactions is larger than in (1) and (2) being approximately 25% in (3) and 20% in (4). Fits to the $\Sigma^+ \pi^0$ mass spectrum, with the $\Sigma(1670)$ fixed at the value obtained for (1) and (2) are shown in Fig 4.1.3 (b).

Differential and Total Cross-Sections

The resonance region for the pair of reactions (3) and (4) was defined as $1.5 < M(\Sigma^+ \pi^0) \leq 1.8$ GeV/c^2. The vector meson cuts were defined by $0.8 > M(k^+ \pi^0) \geq 1.0$ for (3) and $0.6 > M(\pi^- \pi^0) \geq 1.04$ for (4). The total cross-sections for these two reactions were found to be very dependent on the width taken for the $\Sigma(1670)$ resonance. Hence the total cross-sections of reactions (1) and (2) were used to normalize the differential cross-sections for (3) and (4). Fits to the differential cross-sections as for reactions (1) and (2) are shown in Fig 4.1.4 (b). Results of the fits are listed in table 4.1.4 and the differential cross-sections are listed in table 4.1.5.

Reaction	Number of Events	Weighted Number	Slope	Intercept
$\pi^+ p \rightarrow k^+ \Sigma^+(1670)$, $\hookrightarrow \Sigma^+\pi^0$	292	616	2.91 ± 0.81	5.28 ± 0.92
$k^- p \rightarrow \pi^- \Sigma^+(1670)$, $\hookrightarrow \Sigma^+\pi^0$	240	559	2.77 ± 0.42	10.38 ± 0.92

Table 4.1.4 Cross-Section Parameters

$\pi^+ p \rightarrow k^+ \Sigma^+(1670)$, $\hookrightarrow \Sigma^+\pi^0$ $\quad \sigma = 3.93 \pm 0.59\ \mu b$

$(-t)$ $(\mathrm{GeV}/c)^2$	$(d\sigma/dt)$	$\Delta(d\sigma/dt)$
tmin - 0.2	4.38	0.71
0.2 - 0.4	2.07	0.42
0.4 - 0.6	1.38	0.37
0.6 - 1.0	0.54	0.20

(continued →)

$k^- p \rightarrow \pi^- \; \Sigma^+(1760)$			$\sigma = 7.45 \pm 0.10\ \mu b$
t_{min} - 0.2	8.90	1.26	
0.2 - 0.4	3.93	0.78	
0.4 - 0.6	3.22	0.78	
0.6 - 1.0	0.38	0.22	

Table 4.1.5 Cross-Sections (Errors are Statistical - No Background Subtraction)

The slopes of the differential cross-sections for reactions (3) and (4) are very similar and are consistant with those of reactions (1) and (2).

4.1.4 Branching Ratios and other Channels

Other channels listed at the beginning of this section were studied for $\Sigma(1660)$ production. In the final state with nucleon and $\overline{k^0}$ we had approximately four time and statistics of reaction (1). However, these channels were dominated by A_2 against proton and A_2 against Δ^+ production in the 1c case. In the k^- induced reactions k^* (890) and k^{**} (1430) being produced in place of A_2. Only clear sigma signal seen in $N\overline{k^0}$ was at $\Sigma(1765)$.

Channels with a Λ in the final state usually give broad enhancement in the $\Lambda\pi^+$ mass spectrum in the 1700 MeV region.[41] This mass plot from the 4c channels from both π^+ and k^- induced reactions is shown in Fig. 4.1.5. Available 11.5 GeV/c data has been included in this figure which also shows an enlarged plot of the 1700 MeV region. From this it is clear that the $\Sigma(1695)$ bump is split into two. One is centred on the $\Sigma(1670)$ while the second is centred on the $\Sigma(1765)$. The $\Sigma(1670)$ bump will be discussed further in the spin-parity section.

It appears that the branching ratio of the $\Sigma(1670)$ to $N\bar{k}$ is very much weaker than the 0.3 quoted in the P.D.G. tables. From our data the ratio

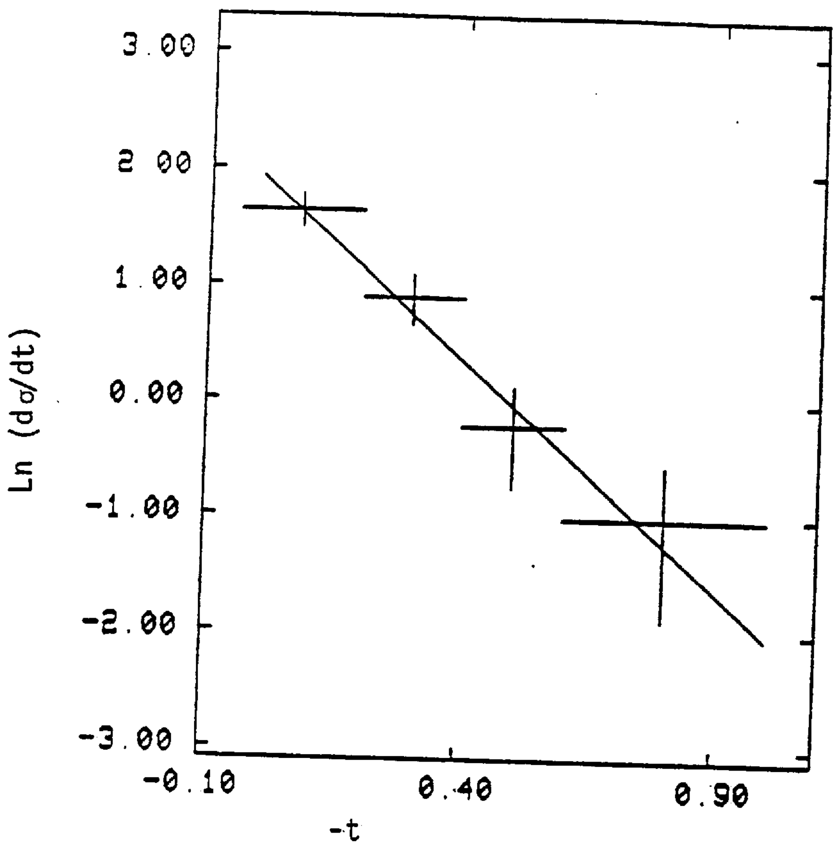

(A)

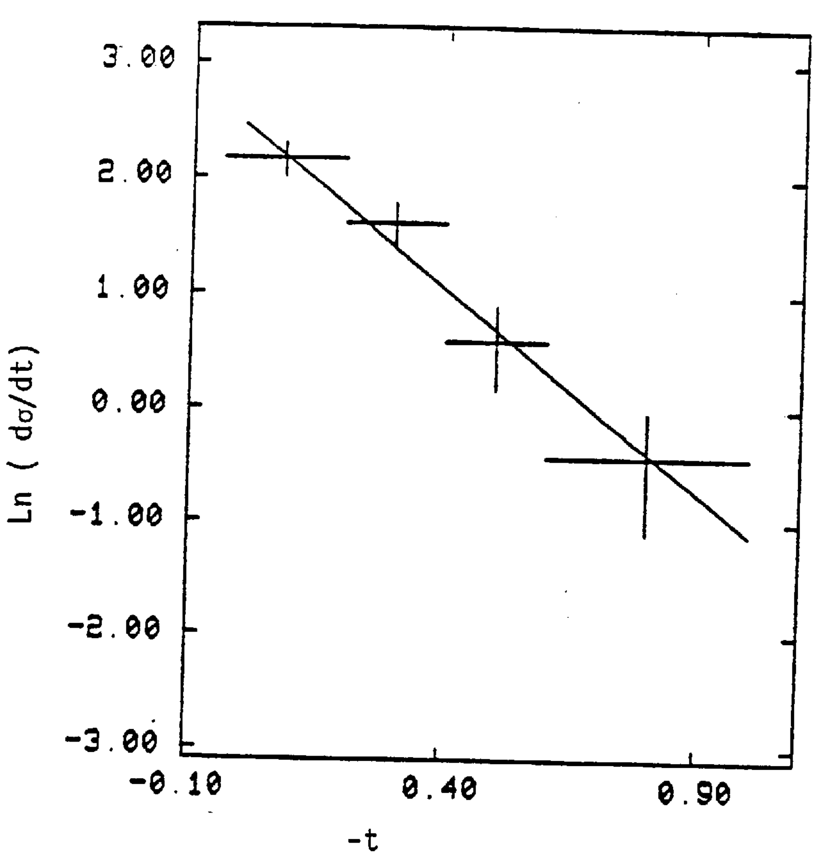

(B)

Fig 4.1.4(a)Fits to differential cross-sections for reaction 1,(A), and 2,(B).

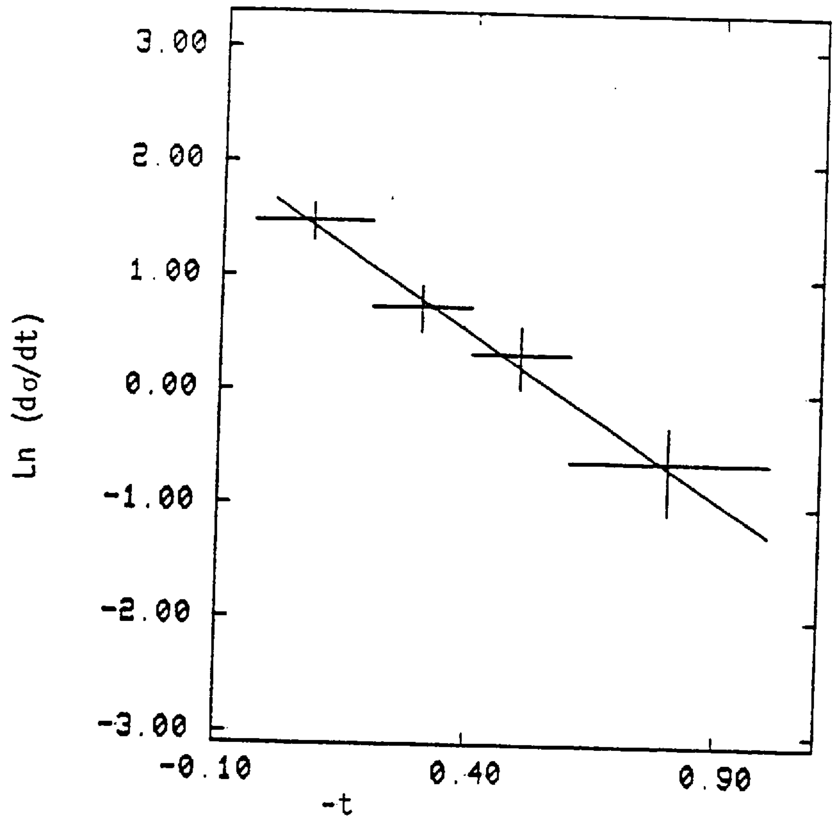

(A)

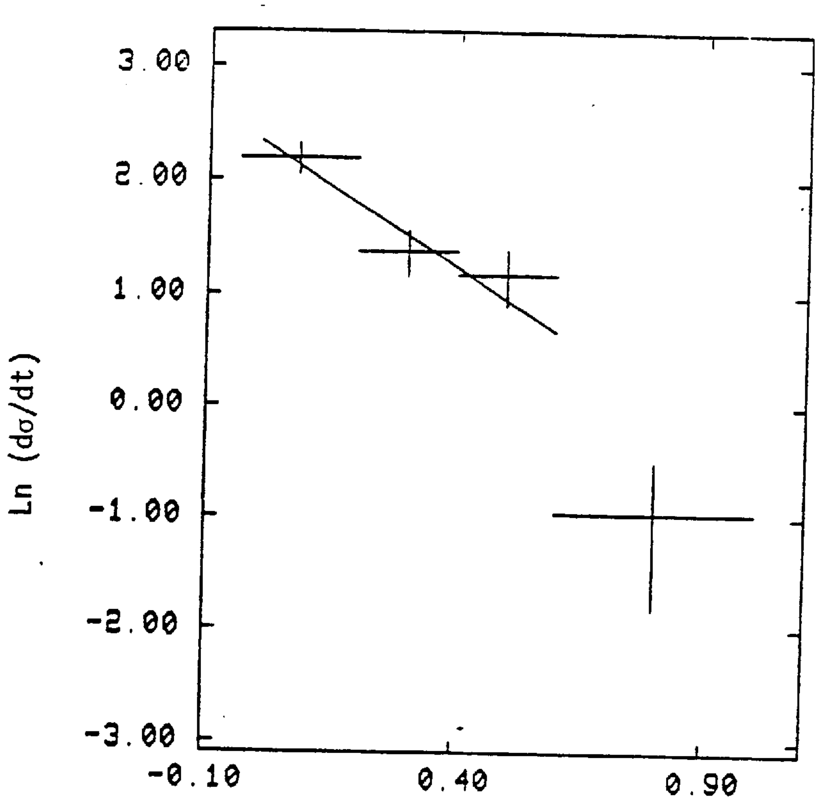

(B)

Fig 4.1.4 (b) Fits to differential cross-sections for reaction 3,(A),and 4,(B).

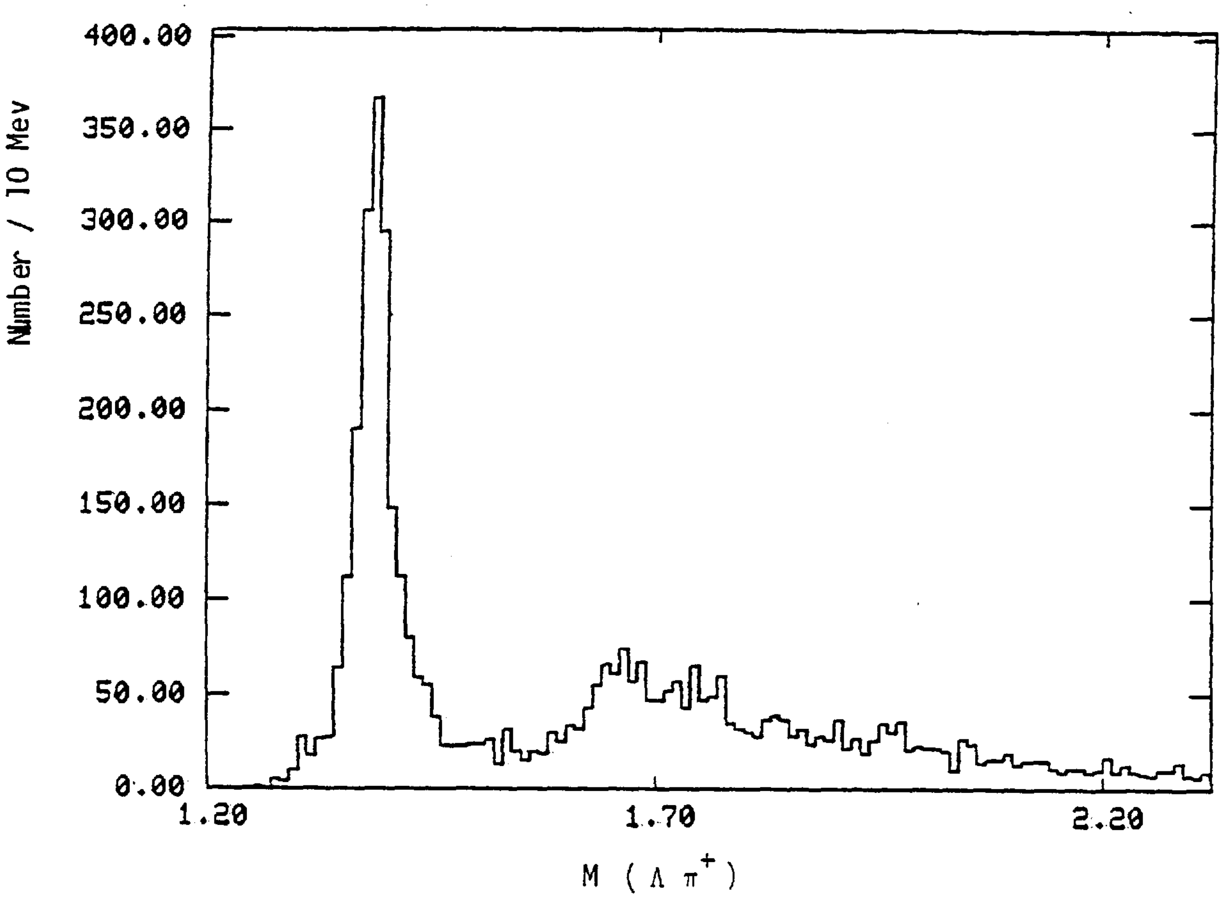

(A)

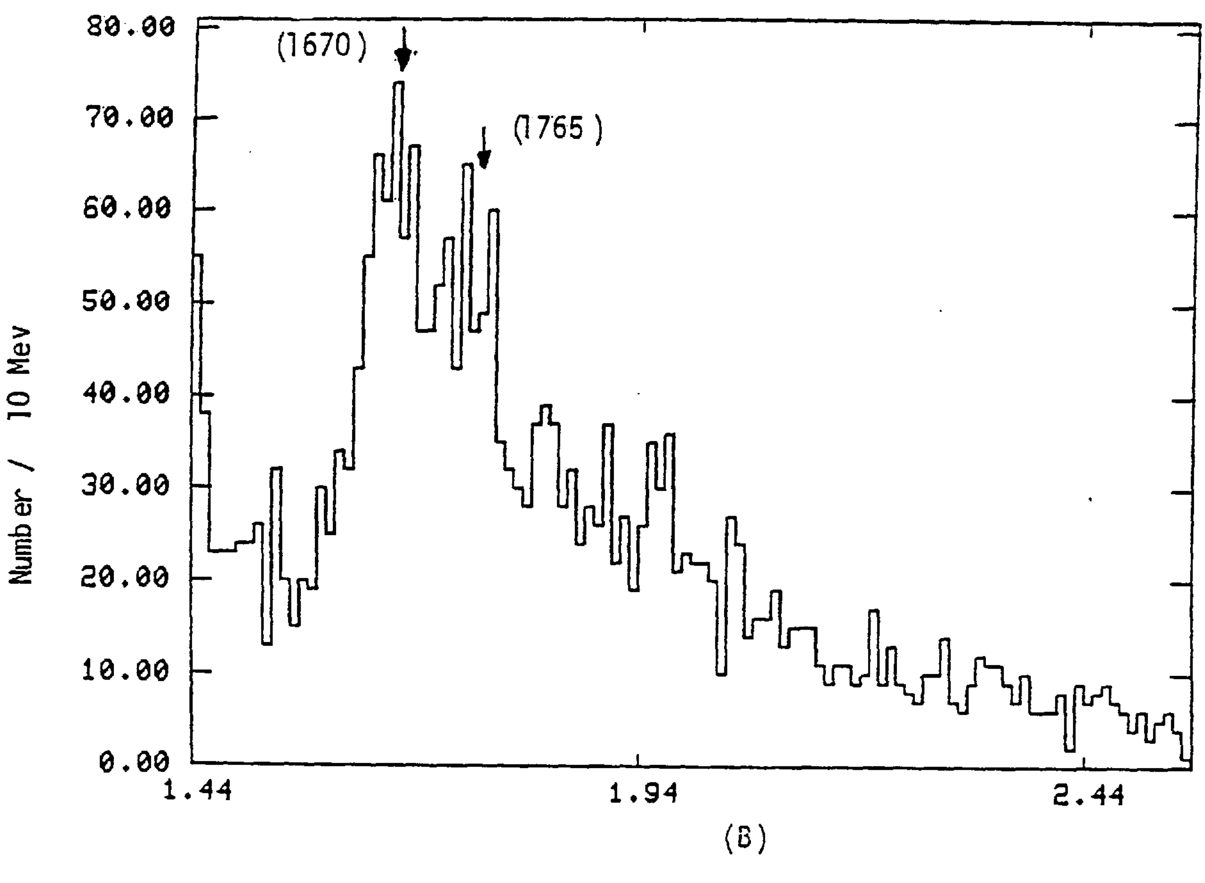

(B)

Fig 4.1.5 $\Lambda\pi^+$ mass spectrum for 7 and 11.5 Gev/c from topology 201 . B

$$\frac{\Sigma(1670) \rightarrow N\bar{k}}{\Sigma(1670) \rightarrow \Sigma\pi}$$

is consistent with zero. We estimate an upper limit of 0.02 for this ratio.

4.2.1 Results from 410's in π^+p and k^-p

In this section results from the channels:

$$\pi^+ p \rightarrow k^+ \Sigma^+ \pi^- \pi^+ \qquad (5a)$$

$$k^+ \Sigma^- \pi^+ \pi^+ \qquad (5b)$$

$$k^- p \rightarrow \pi^- \Sigma^+ \pi^- \pi^+ \qquad (6a)$$

$$\pi^- \Sigma^- \pi^+ \pi^+ \qquad (6b)$$

on Σ^+ (1660) production are presented. Spin-parity of this state together with the state described in the previous section will be discussed in section 4.3. The trigger in (5) and (6) is the same as in (1) and (2) respectively so that hyperon production in (5) and (6) is almost totally backward.

4.2.2 Production Characteristics of $\Sigma(1660)$ in Reaction (5)

In fig. (4.2.1) a $\Sigma(1660)$ signal is clearly seen in the $\Sigma^{\pm} \pi^{\mp} \pi^+$ mass distribution of the final state (5a) and (5b). The resolution in the $\Sigma(1660)$ region is approximately 10 MeV.Fig (4.2.1) also shows the $(\Sigma^+ \pi^-)$ and $(\Sigma^- \pi^+)$ distributions of these final states respectively. In $\Sigma^+ \pi^-$ and $\Sigma^- \pi^+$ signals are evident at $\Lambda(1405)$ and 1520 MeV.

If we select $\Lambda(1405)$ by means of the mass selection $1.34 < M\ (\Sigma^{\mp} \pi^{\pm})$ < 1.44 GeV/c, and plot the resulting $\Lambda(1405)\ \pi^+$ mass distribution (shown in Fig. 4.2.1) the resulting signals in $\Sigma^{\mp} \pi^{\pm} \pi^+$ are almost background free. There was no clear vector meson signal in either final state.

Mass fits were made to the $\Sigma^{\mp}\,\pi^{\pm}\,\pi^{+}$ mass spectrum using a polynomial background which gave the best fit to the off-resonance region, Fig (4.2.2). Table 4.2.1 summarizes our data for reaction 5 and gives results of the mass fits.

Decay Mode	Number of Events	Central Mass (MeV)	Γ (MeV)
$\Sigma^{+}\,\pi^{-}\,\pi^{+}$	387	1657 ± 6	57 ± 4
$\Sigma^{-}\,\pi^{+}\,\pi^{+}$	143		
$\Lambda\,(1405)\;\pi^{+} \rightarrow \Sigma^{+}\,\pi^{-}\,\pi^{+}$	100	1657 ± 6	45 ± 11
$\Lambda\,(1405)\;\pi^{+} \rightarrow \Sigma^{-}\,\pi^{+}\,\pi^{+}$	74		

Table 4.2.1

The ratio of the number of events in the Σ^{+} and Σ^{-} final states in the Σ1660 region defined as $1.6 < M(\Sigma^{\pm}\,\pi^{\mp}\,\pi^{+}) \leqslant 1.72$ GeV/c^2 was found to be 1.1 ± 0.2, consistant with the ratio of 1 expected from isospin. The $\Lambda(1405)$ was defined by the cuts $1.36 < M(\Sigma^{\pm}\,\pi^{\mp}) \leqslant 1.44$.

Cross Sections

Differential cross-sections were determined for the $\Sigma(1660)$ decaying to $\Lambda(1405)\;\pi^{+}$ for the t range tmin - 1.0 (GeV/c)^2 and are shown in Fig. (4.2.3) and listed in table 4.2.2. The differential cross-section has been normalised to unit cross-section. Only π^{+} decay mode events for the Σ^{+} were used.

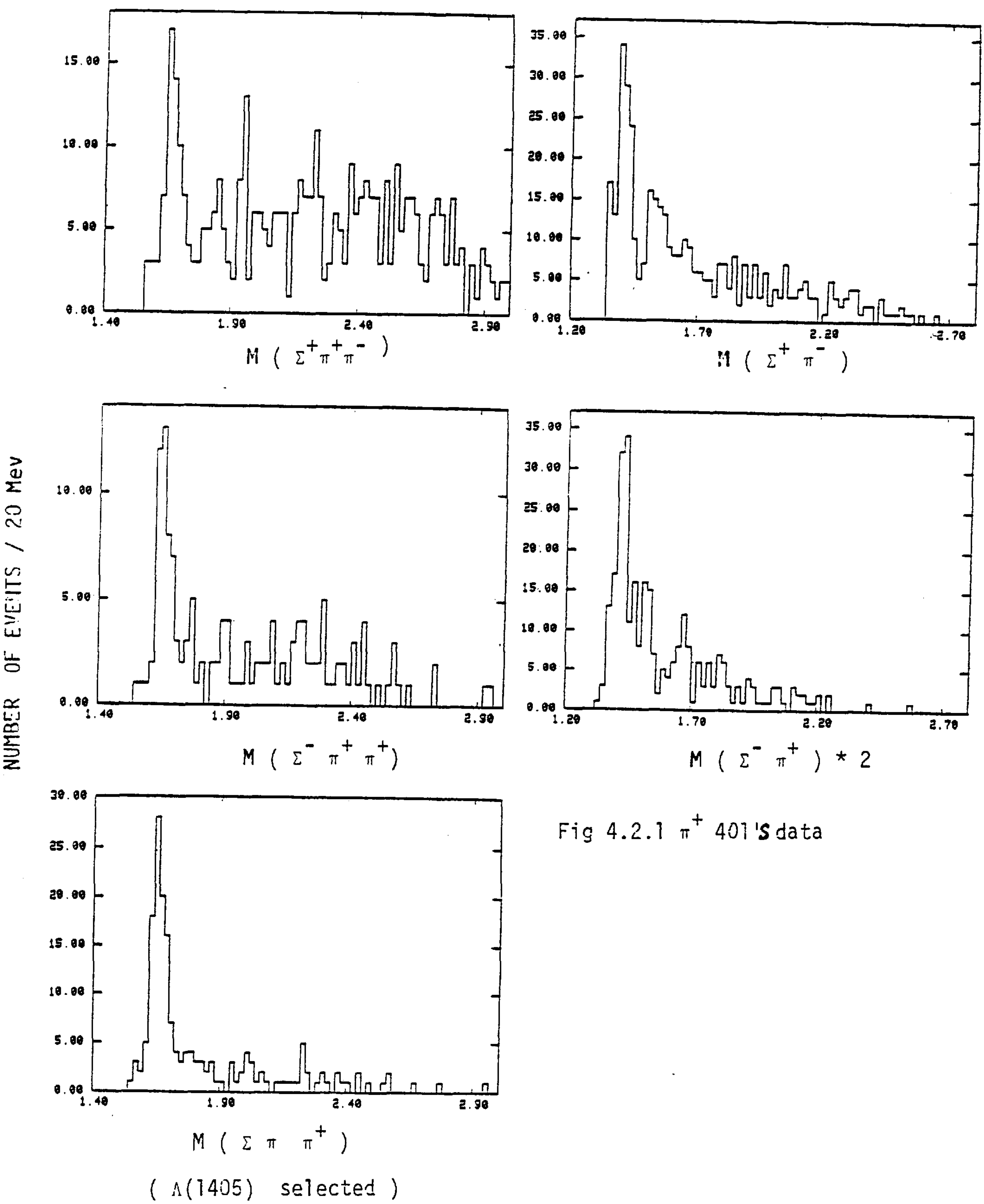

Fig 4.2.1 π^+ 401'S data

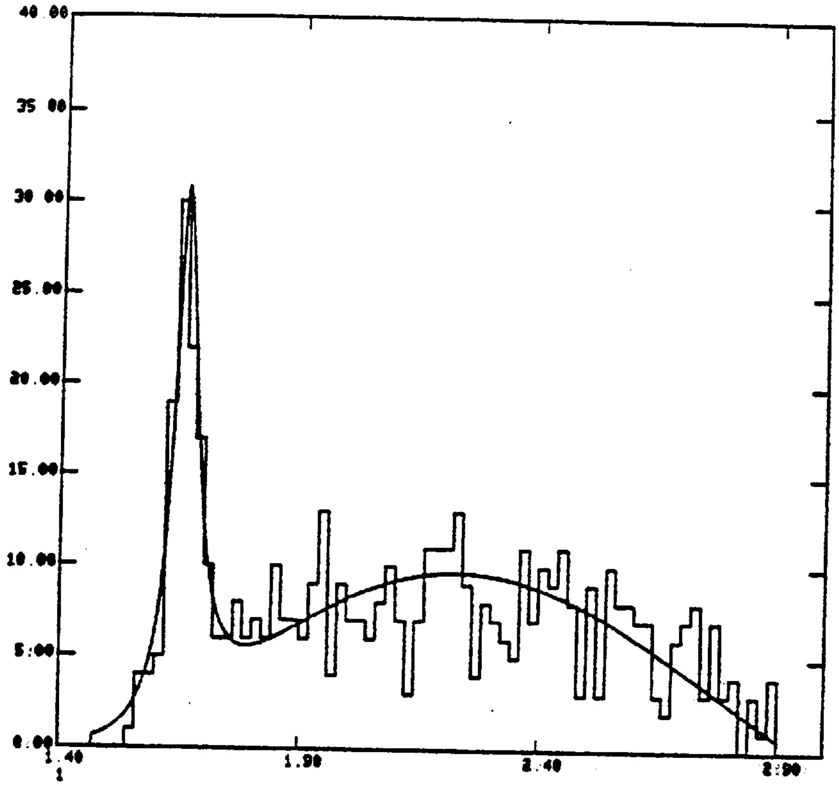

M($\Sigma^{\pm}\pi^{\mp}\pi^{+}$)

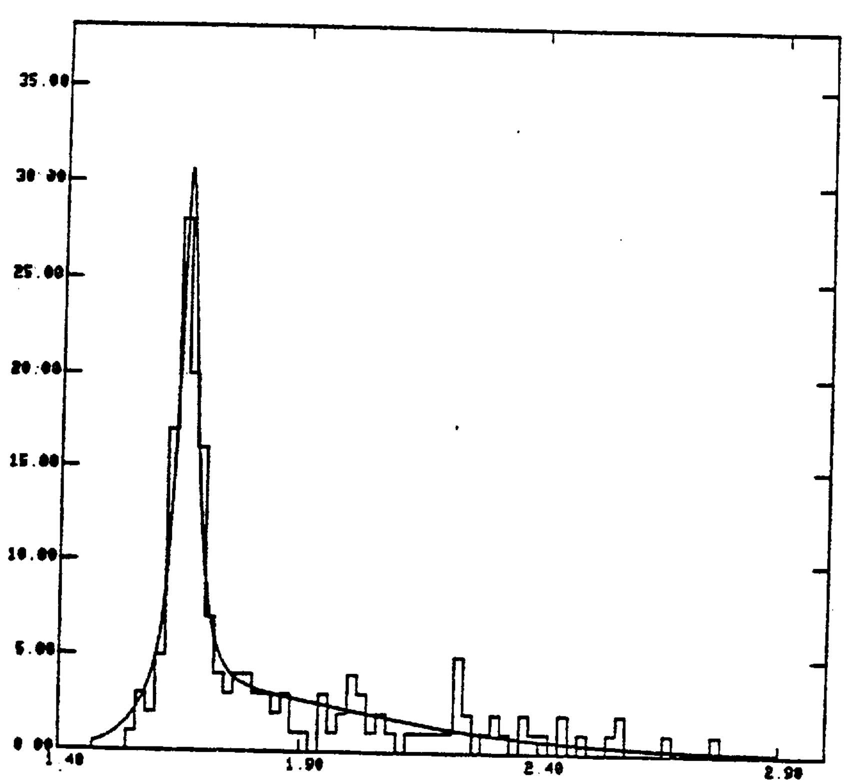

M ($\Sigma^{\pm}\pi^{\mp}\pi^{+}$) Λ(1405) selected

Fig 4.2.2 Mass fits to 401 's π^{+} data

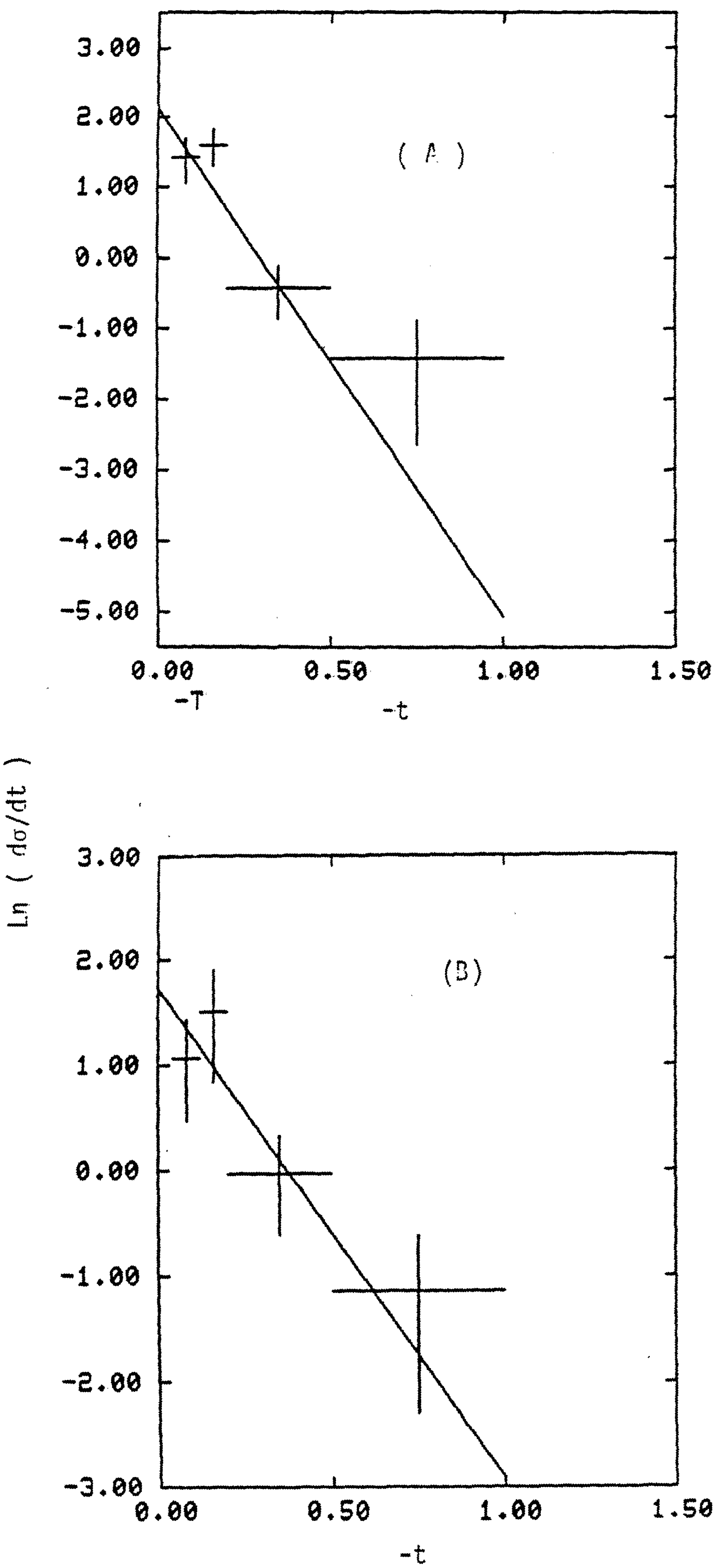

Fig 4.2.3(a) Differential cross-sections for the π^+ 401'S :

(A) Σ^- ,(B) Σ^+ decay of the $\Sigma(1660)$.

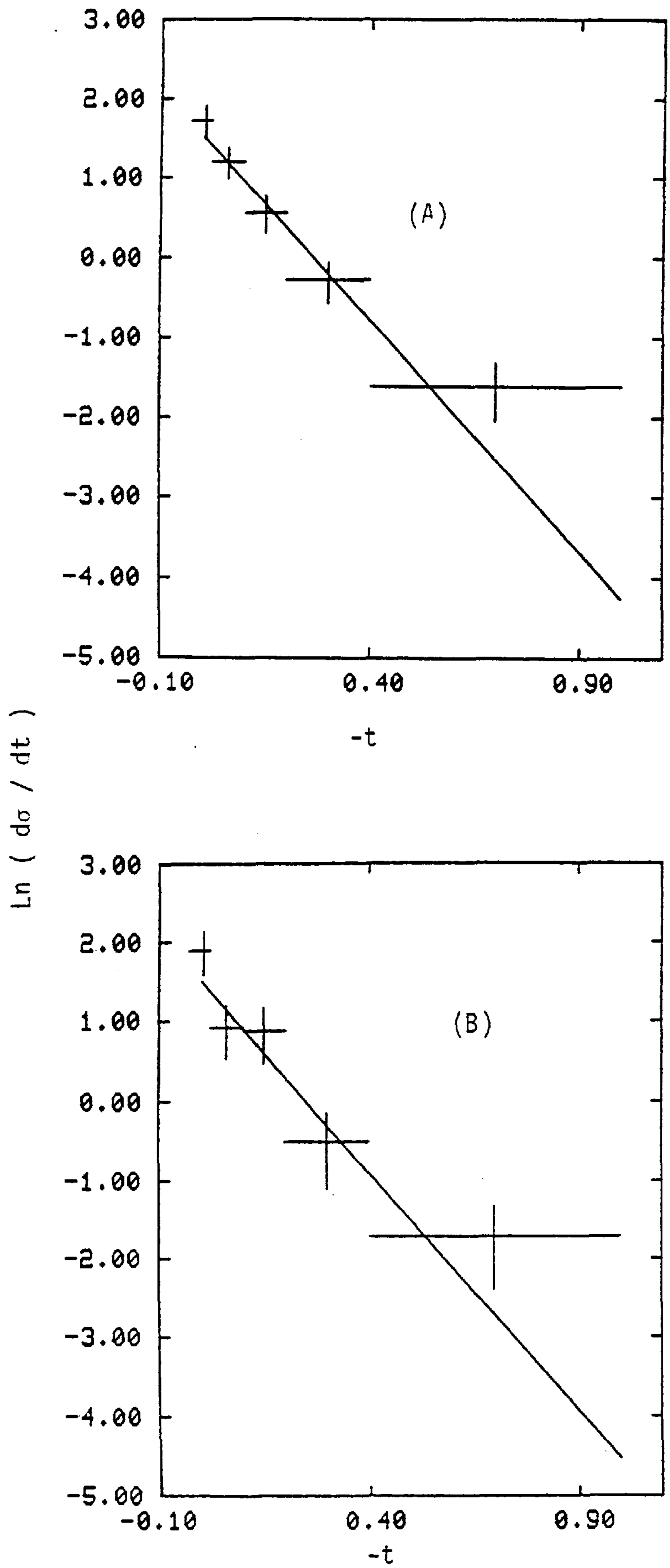

Fig 4.2.3(b) Differential cross-section for the k^- 401's: (A) Σ^- decay,(B) Σ^+ decay of the $\Sigma(1660)$.

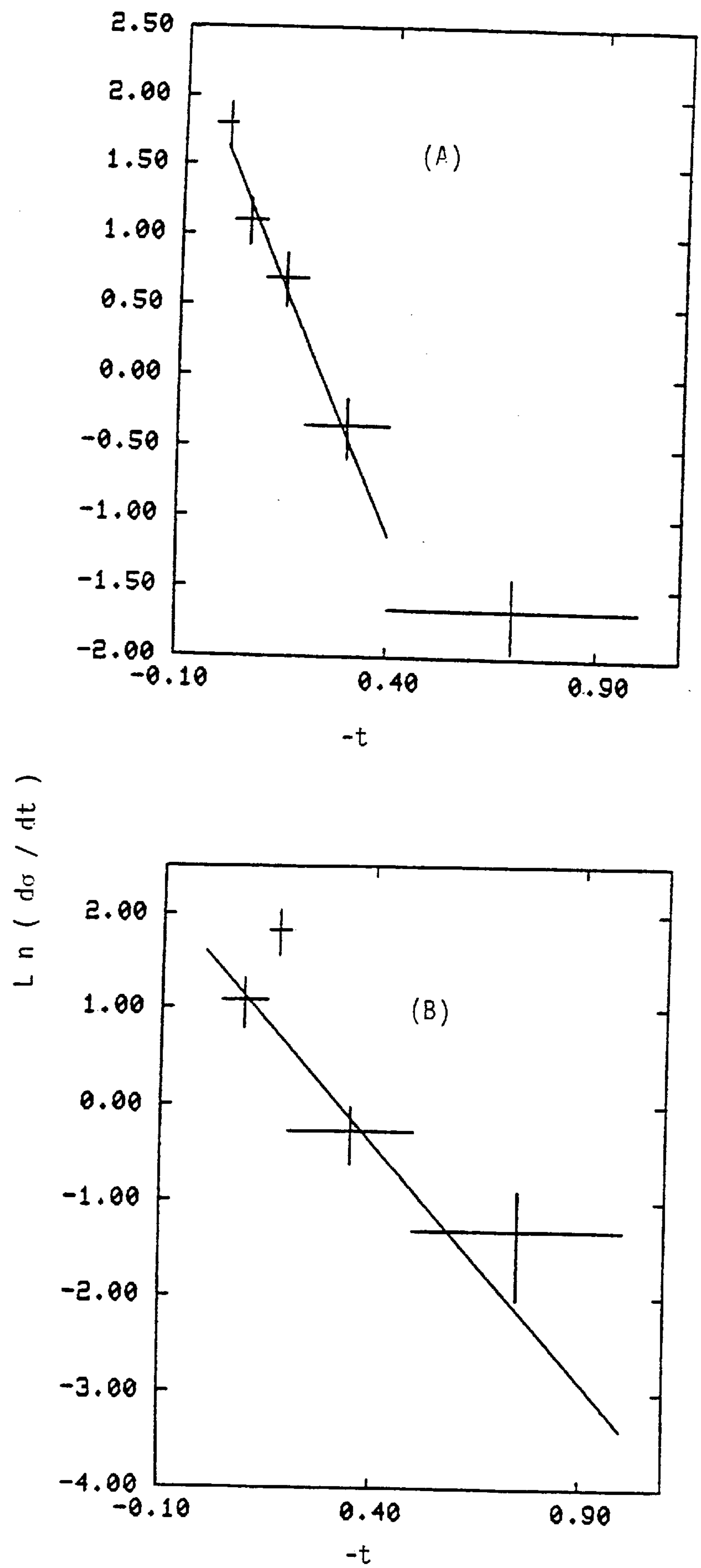

Fig 4.2.3(c) Differential cross-sections for the combined Σ^+ and Σ^- 401'S data :(A) k^- , (B) π^+

$\pi^+ p \rightarrow k^+ \Sigma^+(1660)$

$\lvert\Delta t\rvert$	$(d\sigma/dt)$	$\Delta(d\sigma/dt)$
0.04 - 0.15	2.9	1.3
0.15 - 0.2	4.5	2.2
0.2 - 0.5	0.97	0.43
0.5 - 1.0	0.32	0.22
$\pi^+ p \rightarrow k^+ \Sigma^+ (1660)$		
0.04 - 0.15	4.1	1.3
0.15 - 0.2	4.9	1.3
0.2 - 0.5	0.65	0.24
0.5 - 1.0	0.25	0.17

Table 4.2.2 Differential Cross-Sections for reaction (5)

(Errors are Statistical)

Fits to the differential cross-sections of the form $d\sigma/dt = A\ e^{-Bt}$ gave a slope of 4.6 ± 3.7 for the Σ^+ decay mode and 7.2 ± 1.7 for the Σ^- decay mode, Fig 4.2.3a. Fit to the combined data gave a slope of 4.96 ± 1.66, shown in Fig 4.2.3c. There is an indication of a turnover of the differential cross-section at low $|t|$.

4.2.3 Production Characteristics of $\Sigma(1660)$ in Reaction (6)

The scatter plot for the reactions

$$k^- p \rightarrow \pi^- \Sigma^+ \pi^- \pi^+ \qquad (6a)$$

$$k^- p \rightarrow \pi^- \Sigma^- \pi^+ \pi^+ \qquad (6b)$$

are shown in Fig. (4.2.4) together with their respective projections. Marked feature about these reactions compared to reaction (5) is the substantial forward vecotr and tensor meson production. The ρ^0 and f^0 signals are clearly evident against which there is a strong $\Lambda(1405)$ and

$\Lambda(1520)$ signals. A rough estimate for the Σ^+ reaction indicates an approximate 50% contribution from:

$$k^- p \rightarrow \begin{pmatrix} \rho^o \\ f^o \end{pmatrix} \Sigma^+ \pi^-$$

where the π^- is the non-trigger (slow) . Also shown in Fig. 4.2.4 is the $\Lambda(1405)$ selected $(\pi^+ \pi^-)$ projection where it is clear that there is little ρ^o or f^oproduction against the $\Lambda(1405)$.

Similar production characteristics to the Σ^+ are observed in the Σ^- final state, Fig. 4.2.4(ii) .

The $(\Sigma^{\pm} \pi^{\mp} \pi^+)$ mass spectrums are shown in Fig. 4.2.5a and 5b. The $\Sigma(1660)$ is quite prominent. In addition there is a $\Sigma(2100)$ signal in the $(\Sigma^+ \pi^- \pi^+)$ mass distribution, however there is no equivalent signal in $(\Sigma^- \pi^+ \pi^+)$. The results of selecting $\Lambda(1405)$ and making fits to the mass spectra of $(\Sigma^{\pm} \pi^{\mp} \pi^+)$ are also shown in the same figures. The fits were done in the same way as for reactions 5. Table 4.2.3 summarizes the data for the two reactions together with the results of the mass fits.

Decay Mode	Number of Events	Central Mass (MeV)	Γ(MeV)
$\Sigma^+ \pi^- \pi^+$	553	1655 $\pm$ 4	42 $\pm$ 9
$\Sigma^- \pi^+ \pi^+$	435	1668 $\pm$ 7	73 $\pm$ 6
$\Lambda(1405)\ \pi^+ \rightarrow \Sigma^+ \pi^- \pi^+$	209	1657 $\pm$ 5	53 $\pm$ 12
$\Lambda(1405)\ \pi^+ \rightarrow \Sigma^- \pi^+ \pi^+$	233	1662 $\pm$ 4	58 $\pm$ 12

Fit to the $\Sigma(2100)$ in $\Sigma^+ \pi^- \pi^+$ gave:

$$M = 2106 \pm 17 \text{ MeV}$$

$$\Gamma = 30 \pm 19 \text{ MeV}$$

with significance of approximately 2.5 standareddeviations ("Pessimistic estimate").

Table 4.2.3

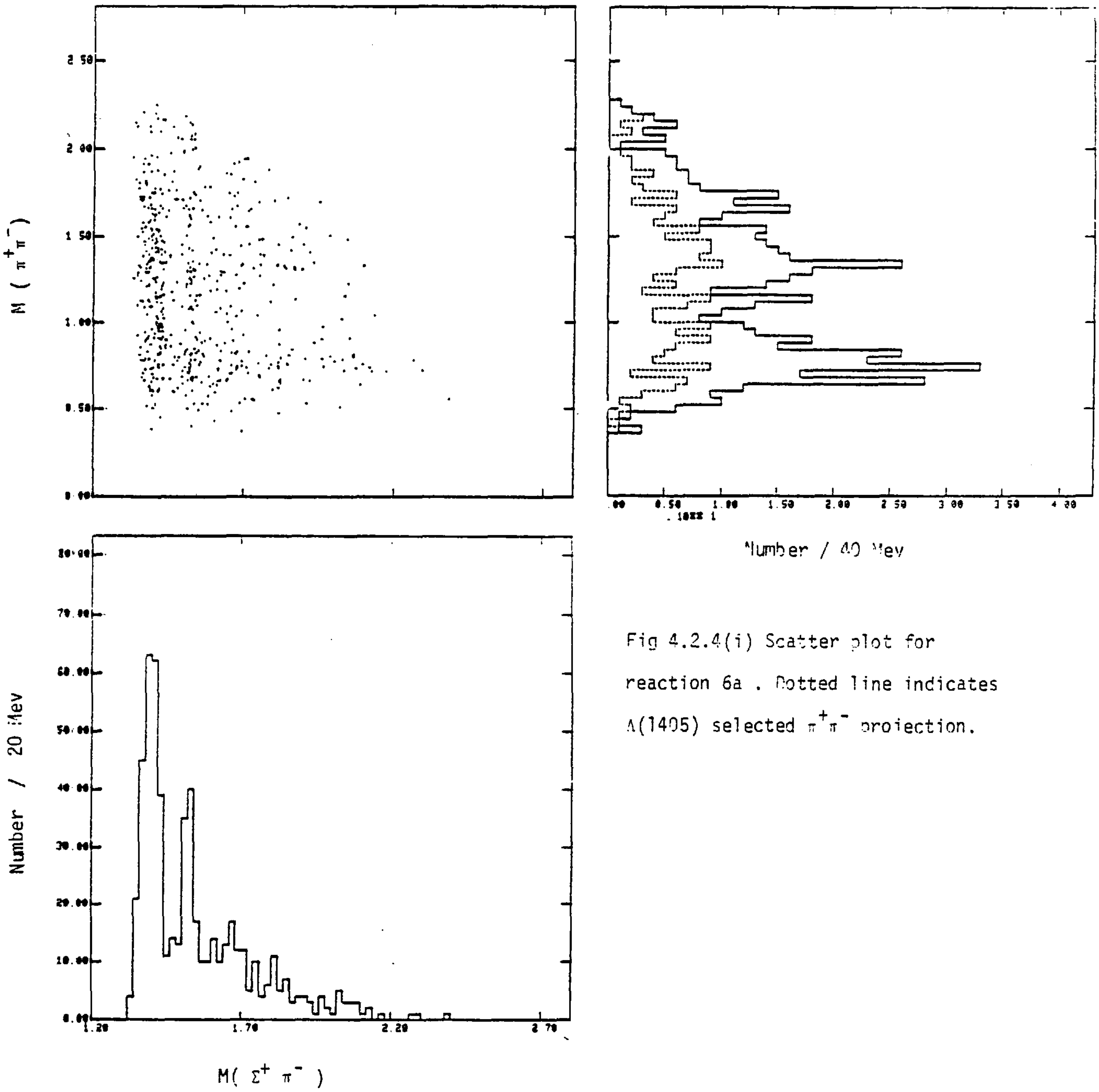

Fig 4.2.4(i) Scatter plot for reaction 6a . Dotted line indicates $\Lambda(1405)$ selected $\pi^+\pi^-$ projection.

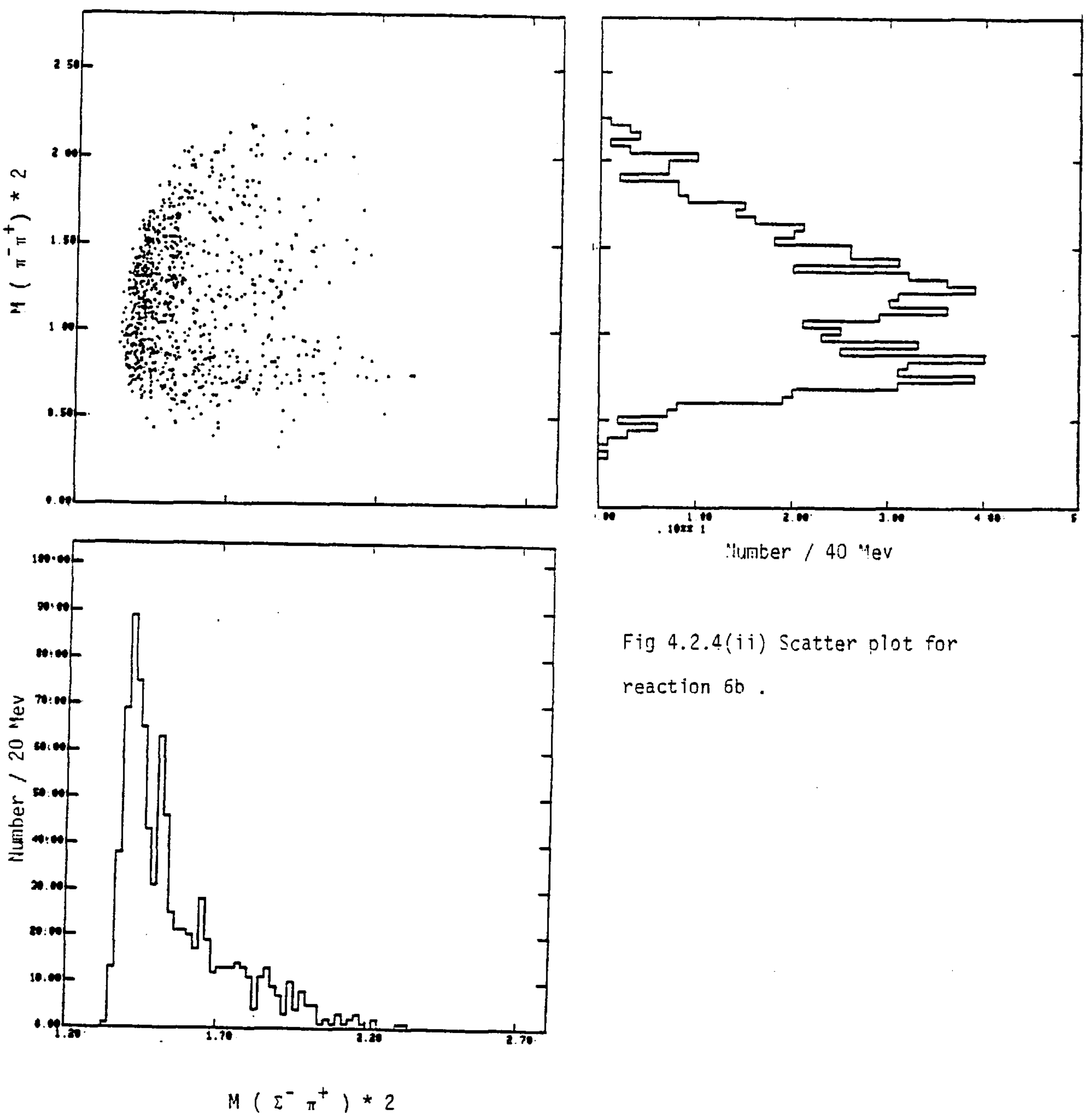

Fig 4.2.4(ii) Scatter plot for reaction 6b .

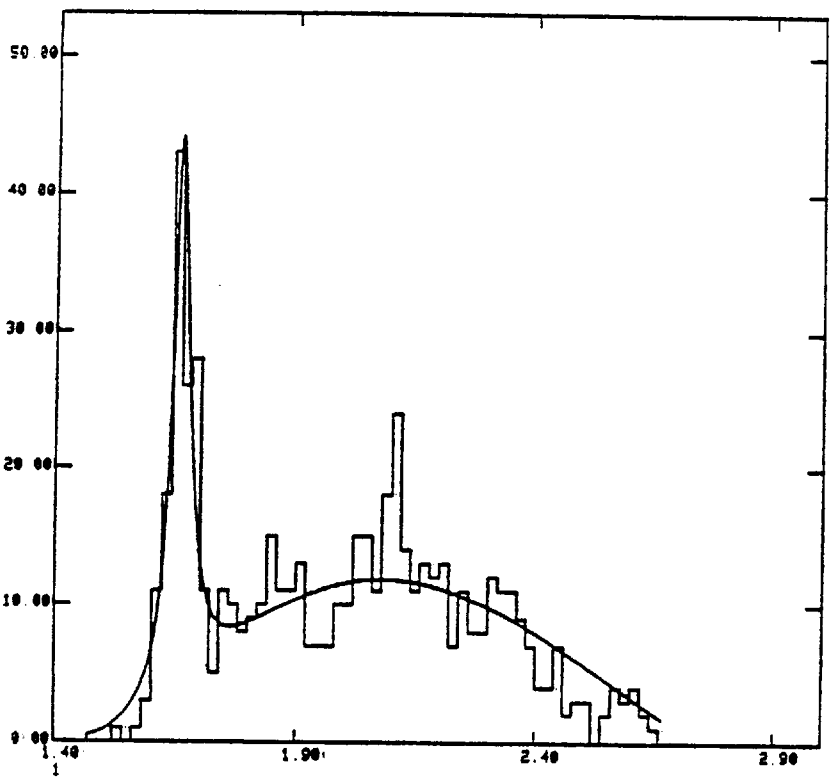

M ($\Sigma^+ \pi^- \pi^+$)

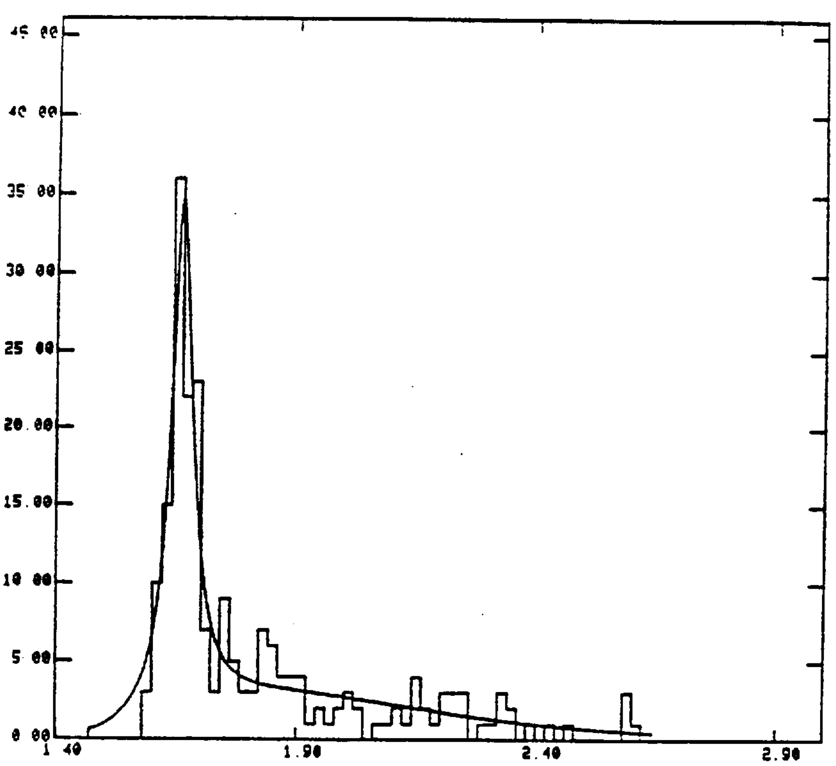

M ($\Sigma^+ \pi^- \pi^+$) $\Lambda(1405)$ selected

Fig 4.2.5(a) Fits to $\Sigma^+\pi^-\pi^+$ mass spectrum from k^-

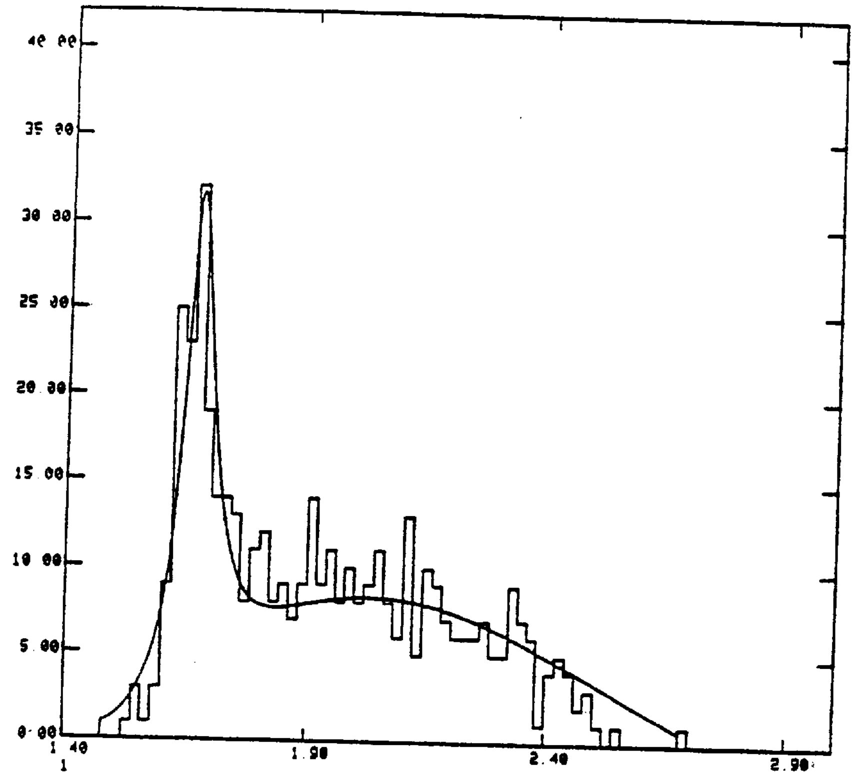

M ($\Sigma^- \pi^+ \pi^+$)

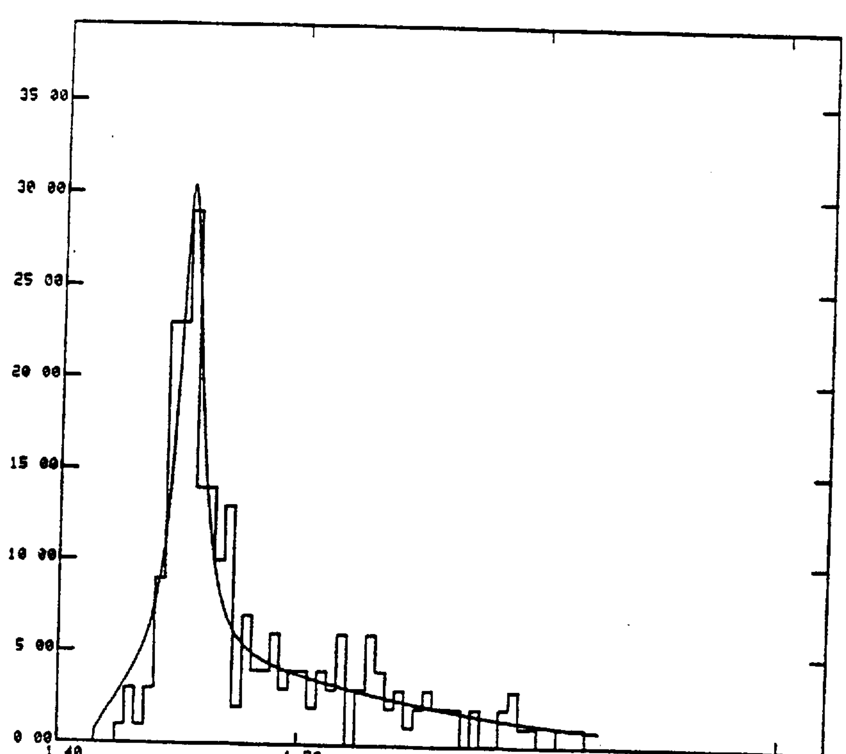

M ($\Sigma^- \pi^+ \pi^+$) $\Lambda(1405)$ selected

Fig 4.2.5(b) Fits to $\Sigma^- \pi^+ \pi^+$ mass spectrum from k^- 410'S .

Cross-Sections

Total and differential cross-sections were determined for the t range tmin - 1.0 $(GeV/c)^2$. The $\Sigma(1660)$ being defined by the cuts $1.6 < M(\Sigma^{\pm}\ \pi^{\mp}\ \pi^{+}) < 1.72$ GeV/c^2. The total cross-section for the Σ^+ mode was found to be $3.16 \pm 0.78\mu b$., and for the Σ^- decay mode $2.33 \pm 0.47\mu b$. The differential cross-sections (normalised to unit cross-section) are listed in table (4.3.4). Only π^+ decay mode was used for the Σ^+ events.

$k^- p \rightarrow \pi^- \Sigma^+ (1660)$ $\sigma = 3.16 \pm 0.78\ \mu b$

$-\Delta t$	$(d\sigma/dt)$	$\Delta(d\sigma/dt)$
-0.03 - 0.02	6.66	1.85
0.02 - 0.1	2.5	0.8
0.1 - 0.2	2.4	0.8
0.2 - 0.4	0.6	0.27
0.4 - 1.0	0.18	0.09

$k^- p \rightarrow \pi^- \Sigma^+ (1660)$ $\sigma = 2.33 \pm 0.47$

-0.03 - 0.02	5.6	1.2
0.02 - 0.1	3.34	0.67
0.1 - 0.2	1.76	0.41
0.2 - 0.4	0.76	0.19
0.4 - 1.0	0.20	0.07

Table 4.2.4 Differential Cross-Sections for Reaction 6

Expontenial fits, of the kind described above, to the differential cross-sections gave the slope 6.03 ± 0.95 for the Σ^+ decay mode and 5.78 ± 0.59 for the Σ^-, Fig. 4.2.3. The combined data (Fig. 4.2.3c) gave a slope of 6.94 ± 0.67.

4.3.1 Spin of $\Sigma(1660)$

In this section results of spin determination of the $\Sigma(1670)$ and $\Sigma(1660)$, described in sections 4.1 and 4.2 respectively, will be presented.

Moments Analysis

To look at the spin of the $\Sigma(1670)$ moments of the spherical harmonics (Appendix 1) were evaluated and plotted as a function of the $\Sigma\pi, \Sigma\pi\pi$ mass. The moments being obtained from:

$$a_L = \langle Y_L^m \rangle = \int I(\cos\Theta, \Phi)\ Y_L^m(\cos\Theta, \Phi)\ d\Omega$$

where $I(\mathrm{Cos}\Theta, \Phi)$ describes the decay distribution of the resonance.

To evaluate the moments the Σ^0 final state data was combined from reactions (1) and (2) as was the Σ^+ data from (3) and (4). Coefficients up to $L = 3$ were plotted, Fig 4.3.1 and 4.3.2, using the angular distribution in the t - channel helicity frame, all moments with $L>3$ showed little structure in the $\Sigma(1670)$ region and are consistant with zero.

In the Σ^0 moments there is no clear indication for a particular spin assignment. The Y_3^0 however shows some structure in the 1670 MeV region. This would indicate the spin is a $3/2$.

The Σ^+ moments show some structure in the Y_3^2 moment, which support the spin $\frac{3}{2}$ indication of the Σ^0 data. However the Y_1^0 moment of the Σ^+ data also shows some structure suggesting the spin could be $\frac{1}{2}$.

Moments of decay:

$$\Sigma(1660) \rightarrow \underset{\substack{\downarrow \\ \Sigma^+ + \pi^-}}{\Lambda(1405)}\ \pi^+$$

in same reference frame as above for the combined π^+ and k^- data were also examined, Fig. 4.3.3. Moments higher than $L = 3$ were consistant with zero.

The Y_2^0 moment shows significant structure in the $\Sigma(1660)$ region. This indicates that the spin is greater than $\frac{1}{2}$. There is also significant structure in the Y_3^2 moment. The moments therefore favour a spin of $\frac{3}{2}$ for the $\Sigma(1660) \rightarrow \Lambda(1405)\,\pi^+$ decay mode.

Adair Analysis

Adair Analysis (Appendix 2) was performed on the $\Sigma(1660)$'s decaying as:

$$\Sigma^+ (1670) \rightarrow \Sigma^0 \pi^+ \qquad (a)$$

$$\Sigma^+ (1660) \rightarrow \Lambda\ (1405)\ \pi^+ \qquad (b)$$

$$\Sigma^+ (1660) \rightarrow \Lambda\pi^+ \qquad (c)$$

(a) The Adair angle was defined as:

$$\mathrm{Cos}\ (A.A) = \hat{\pi}^{+*}_{\Sigma_{c.m.}} \cdot \hat{Beam}_{\sigma .c.m.}$$

Due to low statistics little could be inferred from the 7 GeV/c data alone, we combined the 7 and 11.5 GeV/c data which gave us 434 events, with the cut $\mathrm{Cos}\Theta^* > 0.95$ (see Appendix 2), in the $\Sigma(1670)$ region. Results of fits to various spin assignments are shown in Fig 4.3.4a together with the χ^2 for each hypothesis. A strong preference for spin $\frac{1}{2}$ is evident.

(b) As in (a) the 7 and 11.5 GeV/c data was combined which resulted in 298 events with the cut $\mathrm{Cos}\ \Theta^* > 0.95$. The result is shown in Fig 4.3.4b. The data favours a spin $\frac{3}{2}$ assignment for the $\Sigma(1660)$.

(c) The $\Sigma(1660)$ decaying to $\Lambda\pi^+$ was defined by the mass cuts 1.6 - 1.7 GeV/c^2. The combined 7 and 11.5 GeV/c data gave 470 events. Fig 4.3.4c shows the results. A spin of $\frac{1}{2}$ is favoured although the distribution appears to be that of a $\frac{3}{2}$ state. The figure also shows the result of background substraction defined by $1.5 < M(\Lambda\ \pi^+) \leqslant 1.58$ GeV/c^2.

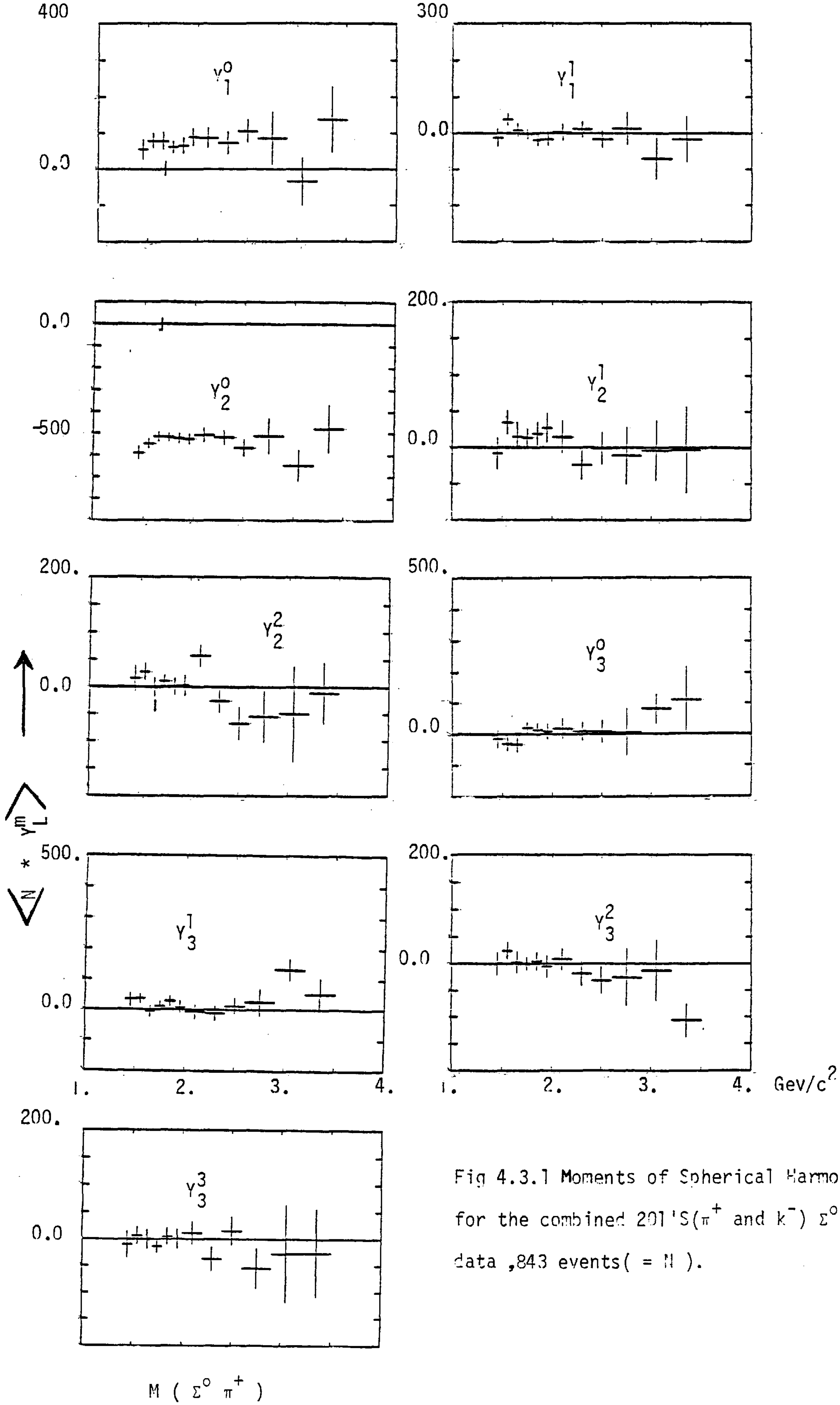

Fig 4.3.1 Moments of Spherical Harmonics for the combined 201'S(π^+ and k^-) Σ^o data ,843 events(= N).

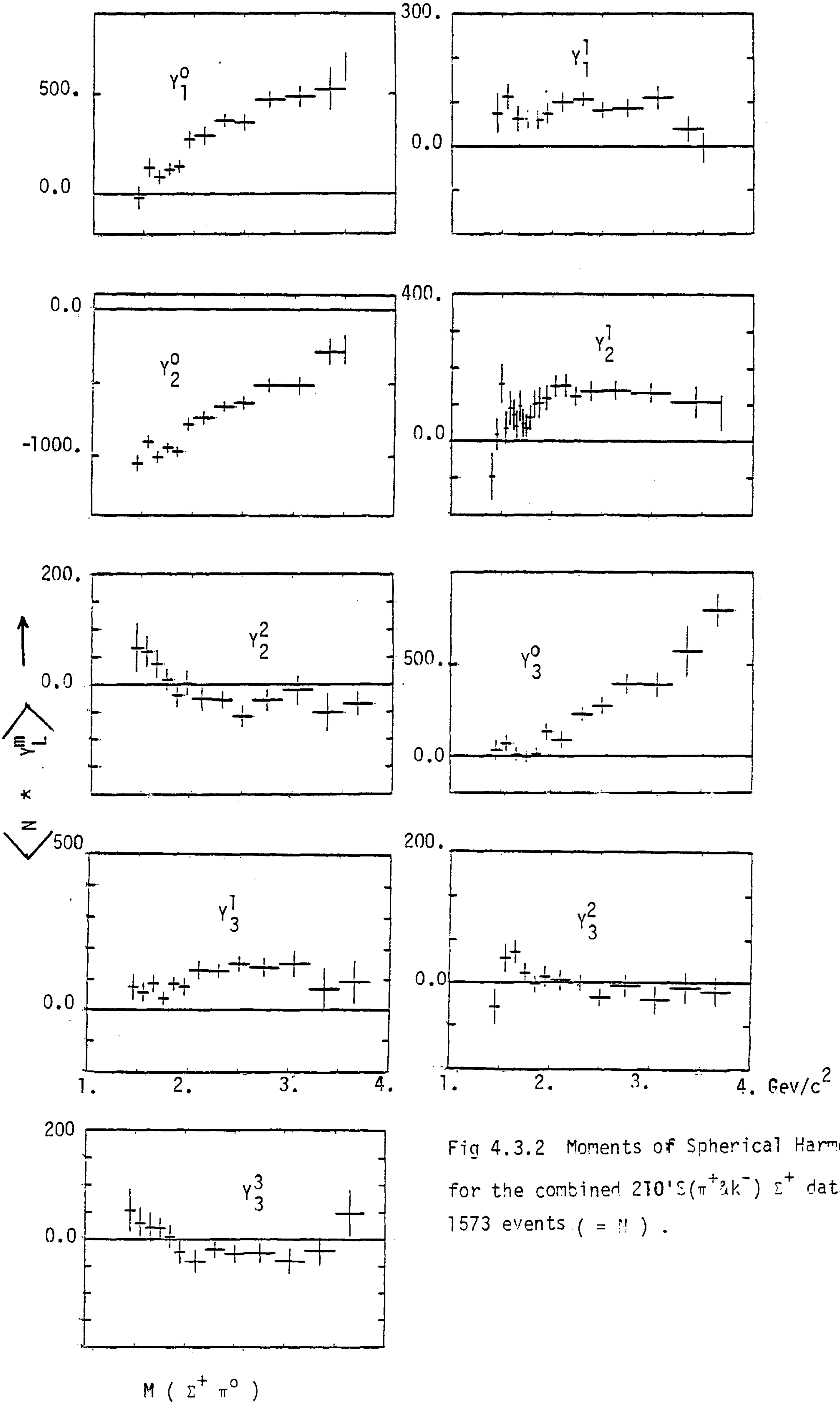

Fig 4.3.2 Moments of Spherical Harmonics for the combined 210'S(π^+&k^-) Σ^+ data, 1573 events (= N) .

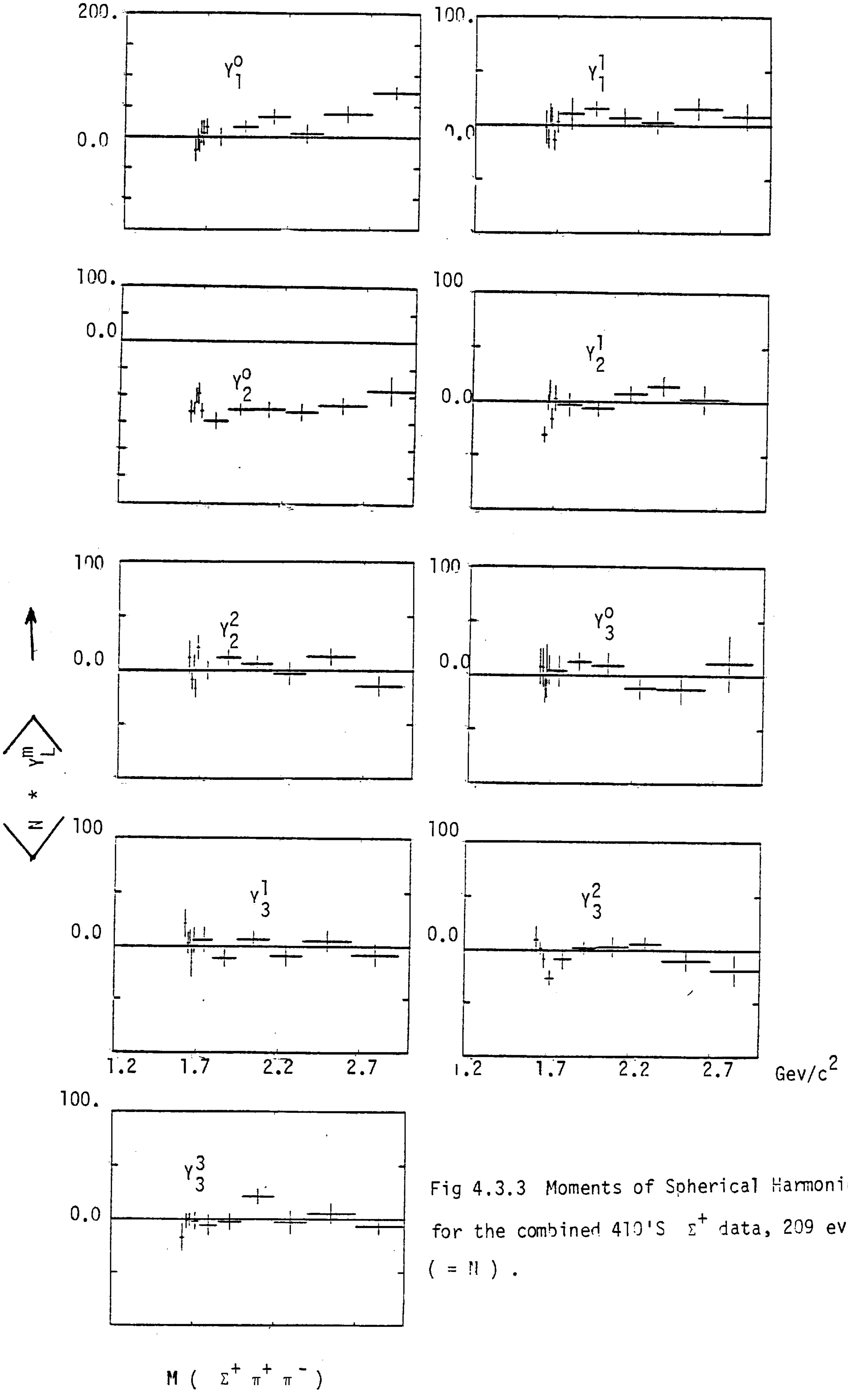

Fig 4.3.3 Moments of Spherical Harmonics for the combined 410'S Σ^+ data, 209 events (= N) .

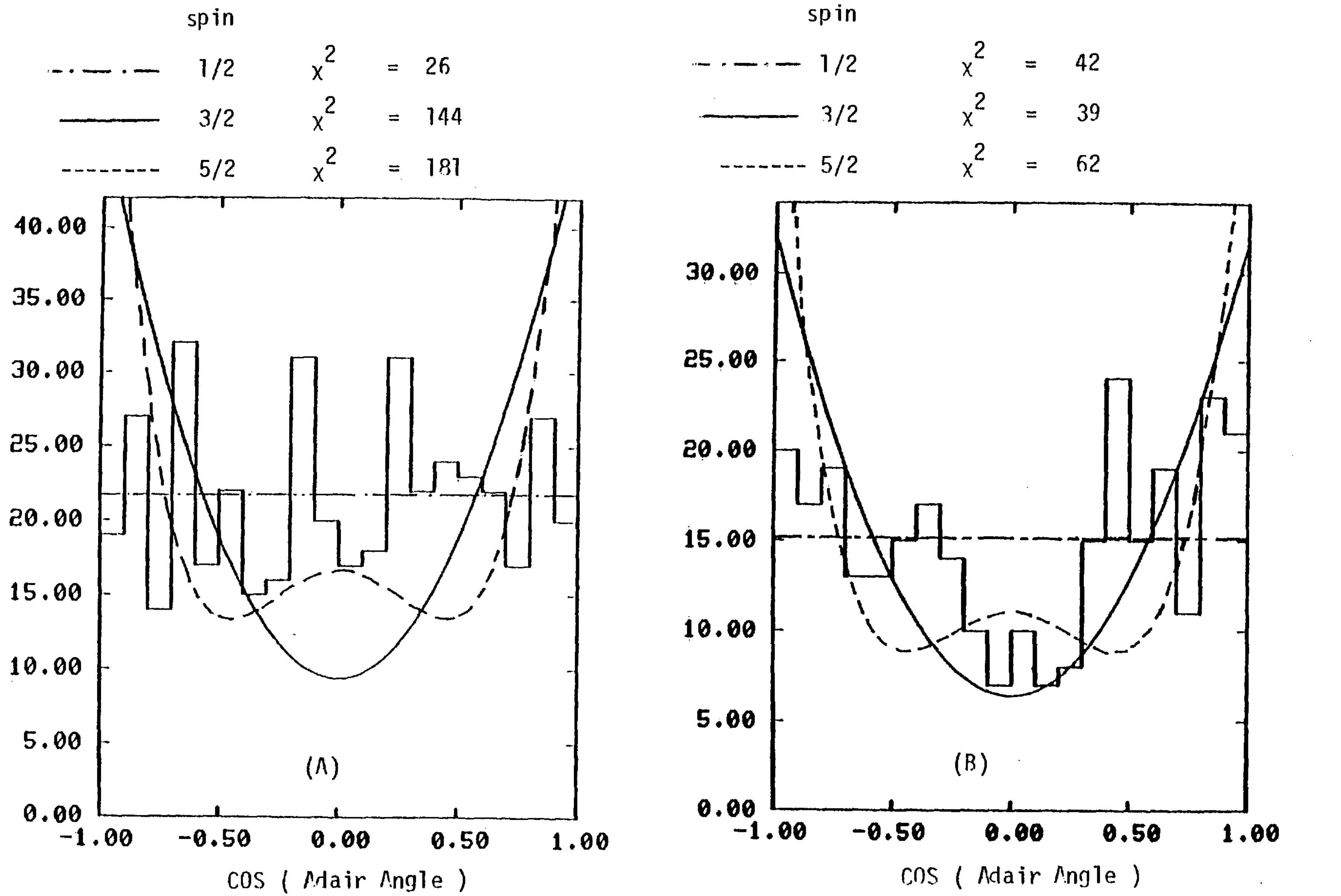

Fig 4.3.4 Adair Analysis for the combined 7 and 11.5 Gev/c data .
(A) 201'S Σ^o data , (B) 410'S Σ^+ data .

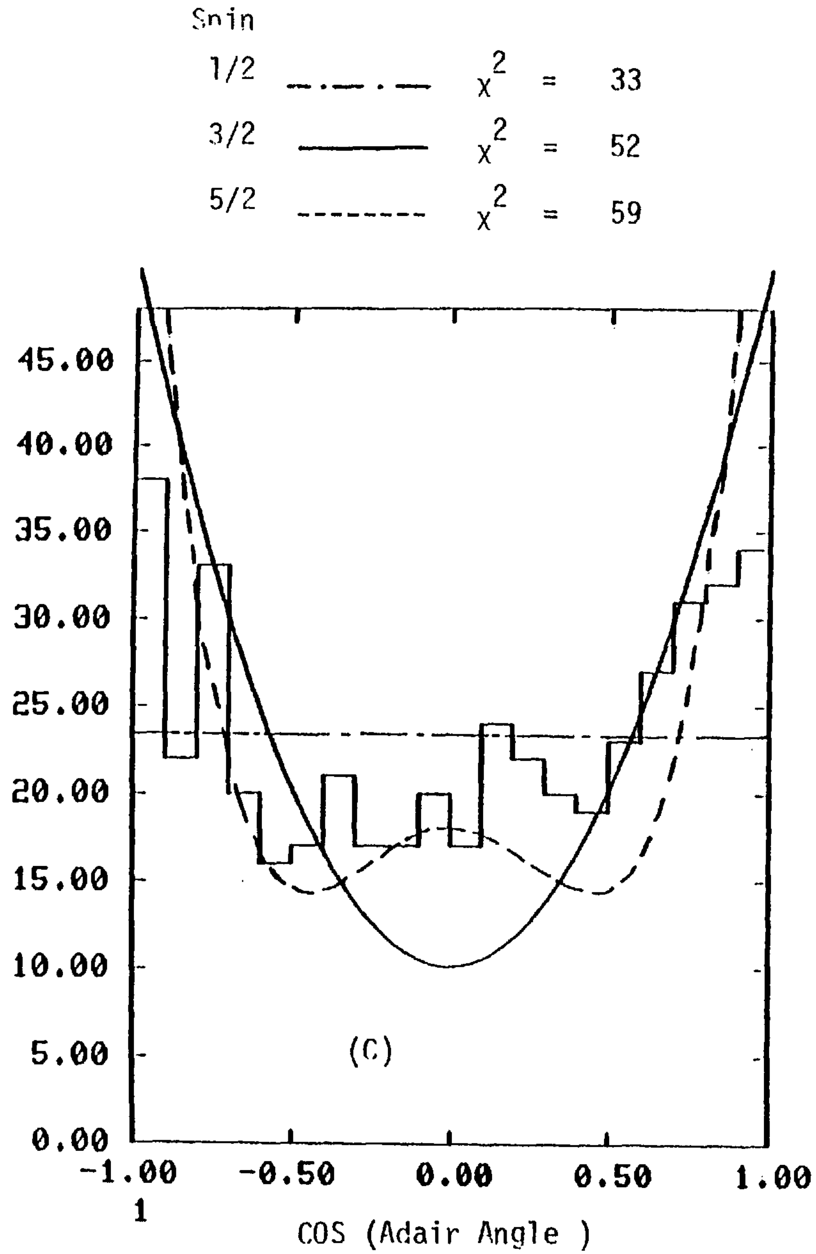

Fig 4.3.4 (C) 201'S Λ data .

(C) with background subtraction (dotted)

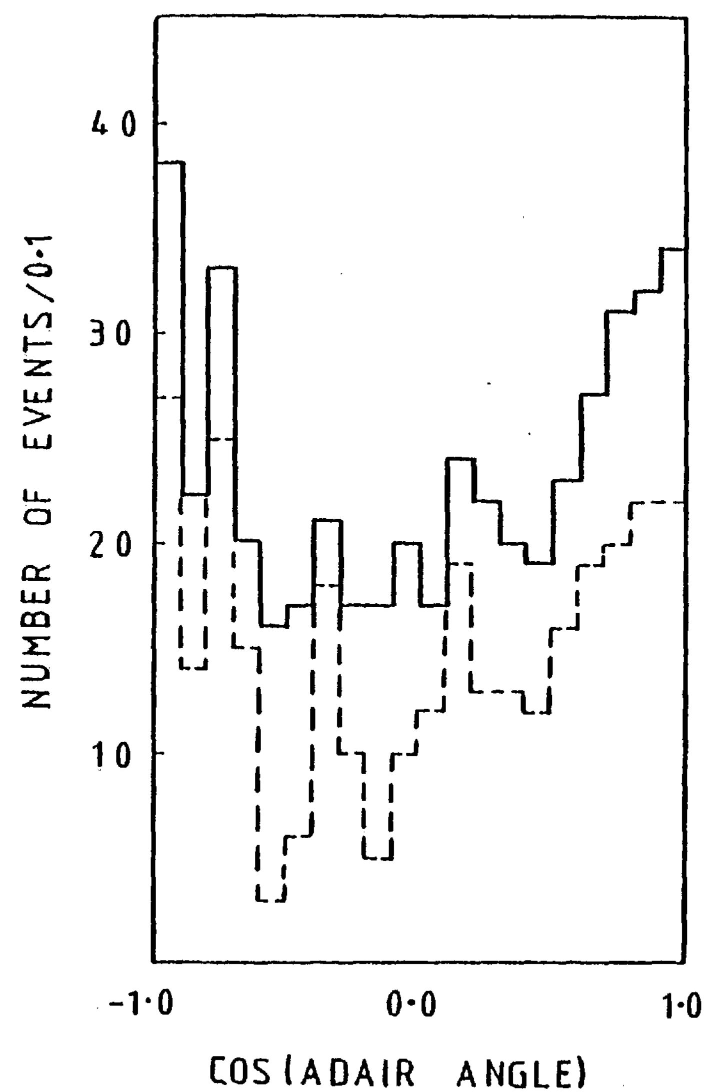

4.4 Conclusion

The $\Sigma(1660)$ found in the 410's has been found to decay dominantly via the $\Lambda(1405)$. The differential cross-section slope was found to be about 7. The $\Sigma(1670)$ in the 210's and 201's decaying to $\Sigma\pi$ was found to have a slope of approximately 3.5. These differences in production characteristics have been observed in earlier experiments and are explained in terms of the existance of two resonances in this region.[37 39-40] Our results support this.

The most sensitive experiment up to the present one was the 4.2 GeV/c k^-p experiment which had approximately 60 events for the Adair analysis of the $\Sigma^0\pi^+$ decay mode of the $\Sigma(1670)$. Results from this experiment indicated a spin of $\frac{3}{2}$ for this resonance. A similar analysis for our data with approximately six time the number of events strongly prefers a spin of $\frac{1}{2}$. While for the $\Lambda(1405)\pi^+$ decay mode a spin of $\frac{3}{2}$ is favoured in agreement with all past experiment studying this resonance.

Due to the triggered nature of the experiment a simple method of parity determination could not be used. Past experiments have indicated negative parity for the $\Lambda(1405)\pi^+$ and the $\Sigma^0\pi^+$ decay mode. If this were the case both resonances could be accommodated in the $|70,1^-|$ multiplet.

For the first time the $\Sigma(1695)$ bump in $\Lambda\pi^+$ appears to be the result of two resonances the $\Sigma(1660)$ and $\Sigma(1765)$. Spin determination of the $\Sigma(1660) \rightarrow \Lambda\pi^+$ was inconclusive . The background in this region is extremely large.

4.5 $\Sigma(1620)$ Production [31]

In this section further evidence is presented for the existance of a $\Sigma(1620)$ resonance,discussed in the introduction to this chapter, decaying to $\Lambda\pi^+$.

The data comes from the 4c - channel:

$$\pi^+ p \rightarrow k^+ \pi^- \Lambda \pi^+ \pi^+$$

at 7 GeV/c, we had 281 events of this type.

A scatter plot of $k^+ \pi^-/\Lambda\pi^+$, shown in Fig 4.5.1, shows substantial k^{o*} and $\Sigma(1385)$ production. In addition there is some indication of structure in the $\Lambda\pi^+$ (1600) and $\Lambda\pi^+$ (2000) region. In the $\Lambda\pi^+$ projection the dominant $\Sigma(1385)$ peak is evident together with a 3 - 4 standard deviation signal in the 1620 region. The $k^+ \pi^-$ projection shows significant k^{o*} (890) production with approximately 20% of the events in the k^{o*} bump. Nothing substantial was seen in $(\Lambda\pi^+ \pi^-)$ mass spectrum with 1385 or 1620 selection on $\Lambda\pi^+$.

It is clear form the scatter plot of $k^+ \pi^-/\Lambda\pi^+$ that the Σ signals can be cleared with k^{o*} selection. The result of this selection is shown in Fig. 4.5.2. Little background under the 1385 and 1620 remains. In addition a broad bump becomes evident around the 1900 MeV region.

The weighted ($\Lambda\pi^+$) * 2 plot, with k^{o*} selection is shown in Fig 4.5.3 where the 1620 is almost as significant as the 1385. The mean weight was 2.3 which resulted in a total of 314 events. The weight was a combination of geometrical and scanning weights described in chapter 2.

Fits to the ($\Lambda\pi^+$)* 2 mass spectrum are show in Fig. 4.5.4. The mass and width parameters of the 1620 were found to be:

$$M = 1628 \pm 10 \text{ MeV}$$

$$\Gamma = 100 \pm 20 \text{ MeV}$$

with k^{o*} selection

$$M = 1619 \pm 15 \text{ MeV}$$

$$\Gamma = 60 \pm 40 \text{ MeV}$$

Production Characteristics

By looking at the C.M.S scattering angle it was found that the $\Lambda\pi^+$ combination which had largest Θ^* gave a cleaner signal.

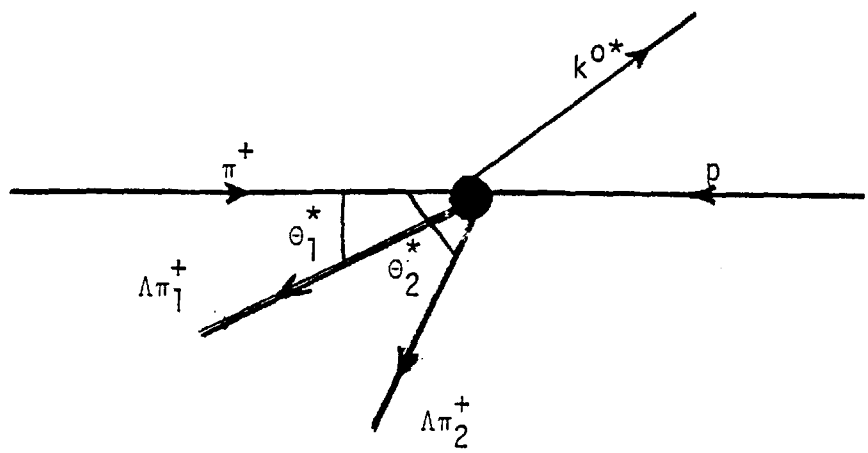

The two combinations of $\Lambda\pi^+$ with lower and higher Θ^* are shown in Fig 4.5.5. Similar results were obtained by choosing $\Lambda\pi^+$ combination with larger (smaller) $|U|$.

Decay Distribution

With the limited statistics available it was diffucult to do any meaningful decay distribution analysis. In order to compare the 1600 region with the 1385 the CosΘ^* distribution, where $\Theta^*$is the angle between Σ direction of flight in the C.M.S and the direction of Λ in Σ restframe. The two distributions are shown in Fig. 4.5.6. Some structure exists in the 1600 region.

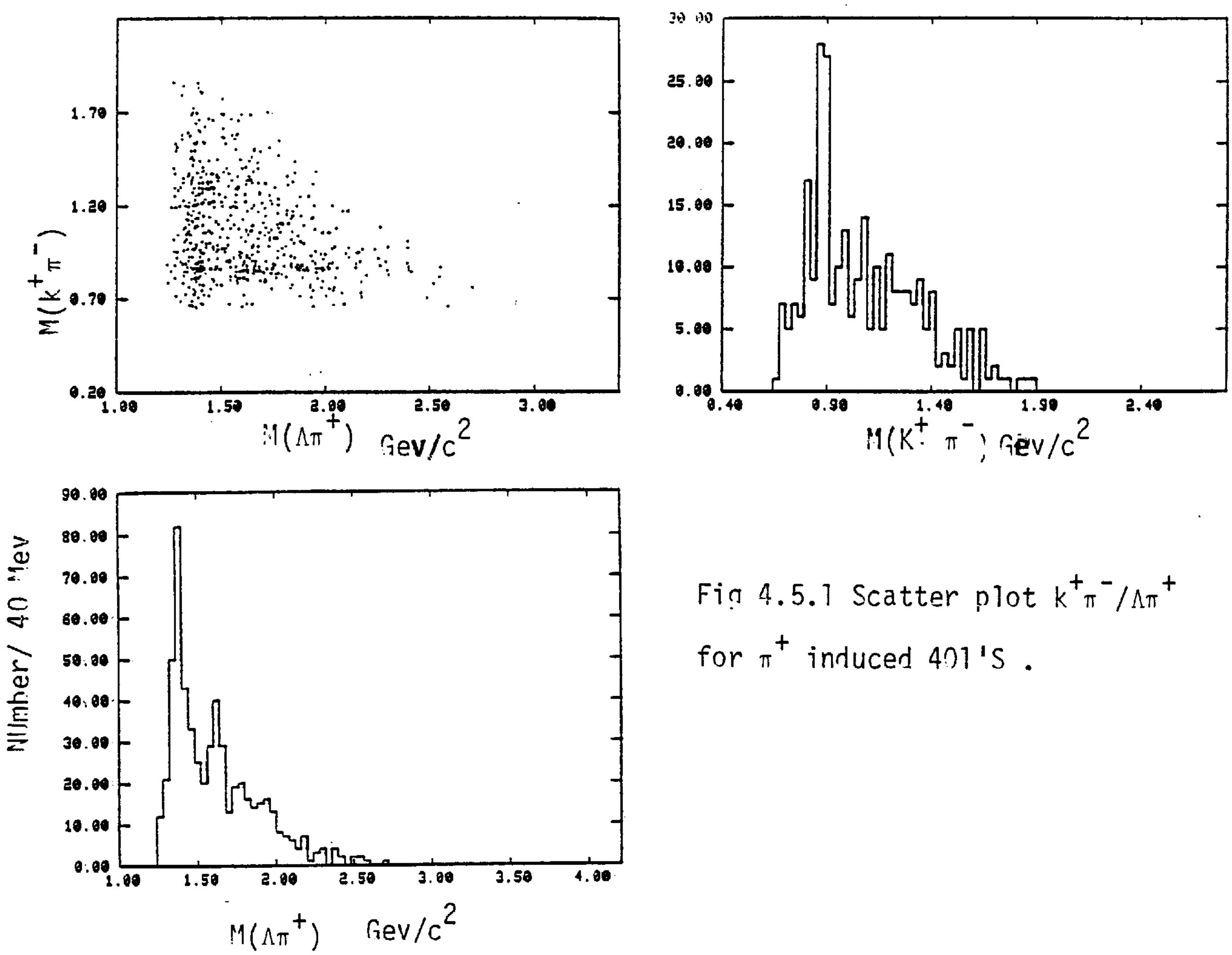

Fig 4.5.1 Scatter plot $k^+\pi^-/\Lambda\pi^+$ for π^+ induced 4OI'S .

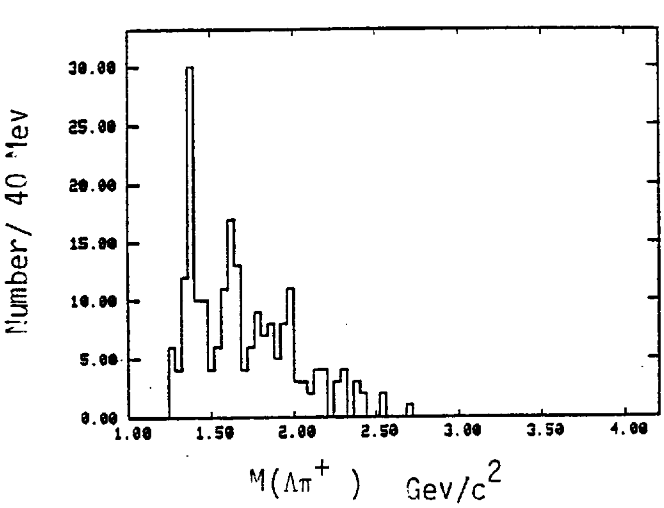

Fig 4.5.2 $\Lambda\pi^+$ mass spectrum with k^{0*} selection .

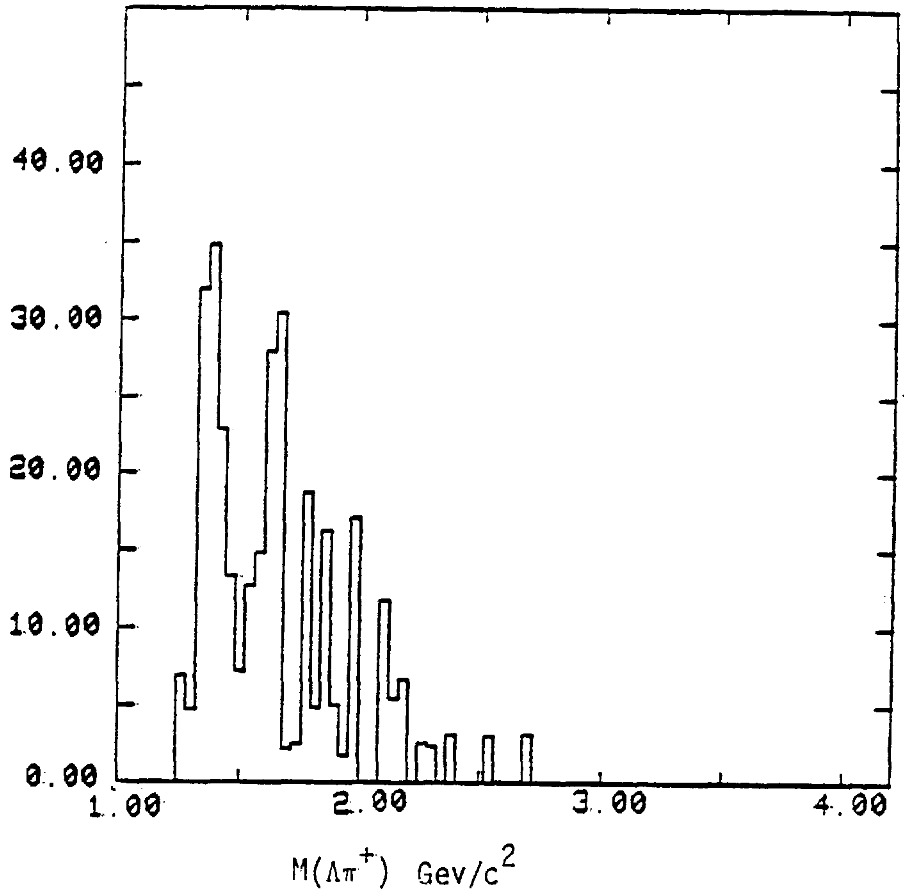

Fig 4.5.3 Weighted $\Lambda\pi^+$ *2 mass spectrum ,with k^{o*} selection .

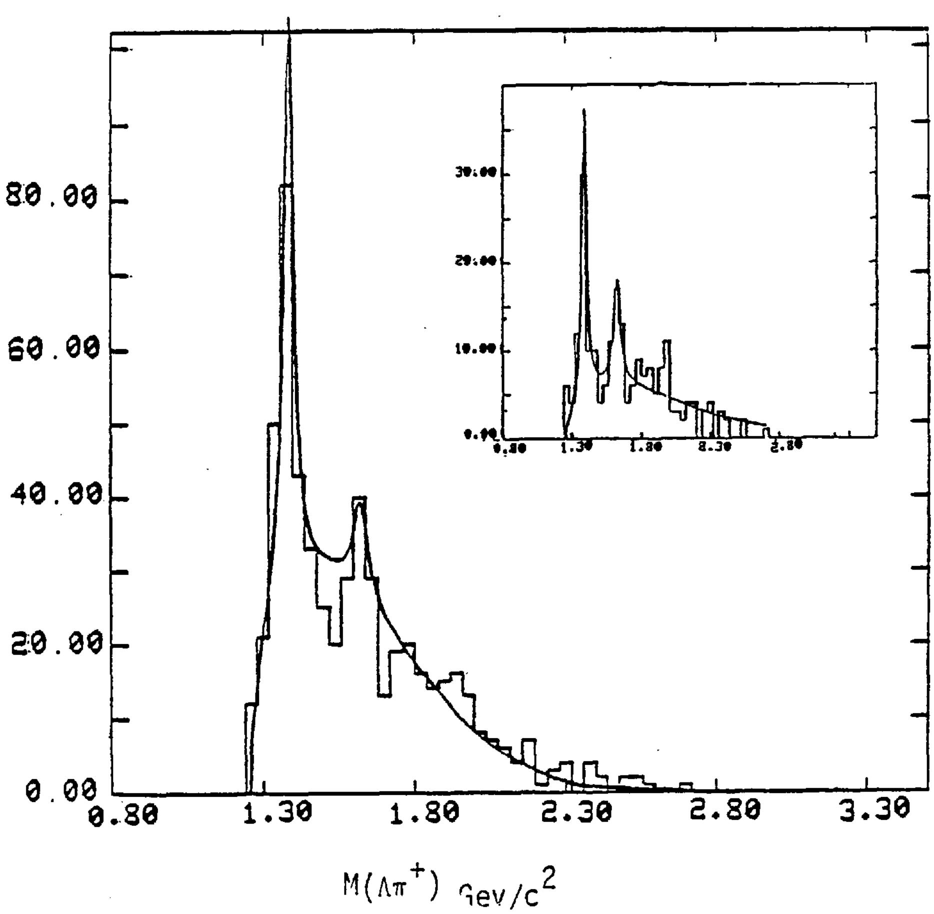

Fig 4.5.4 Mass fit to $\Lambda\pi^+$ mass spectrum .Inset shows the fit with k^{o*} selection .

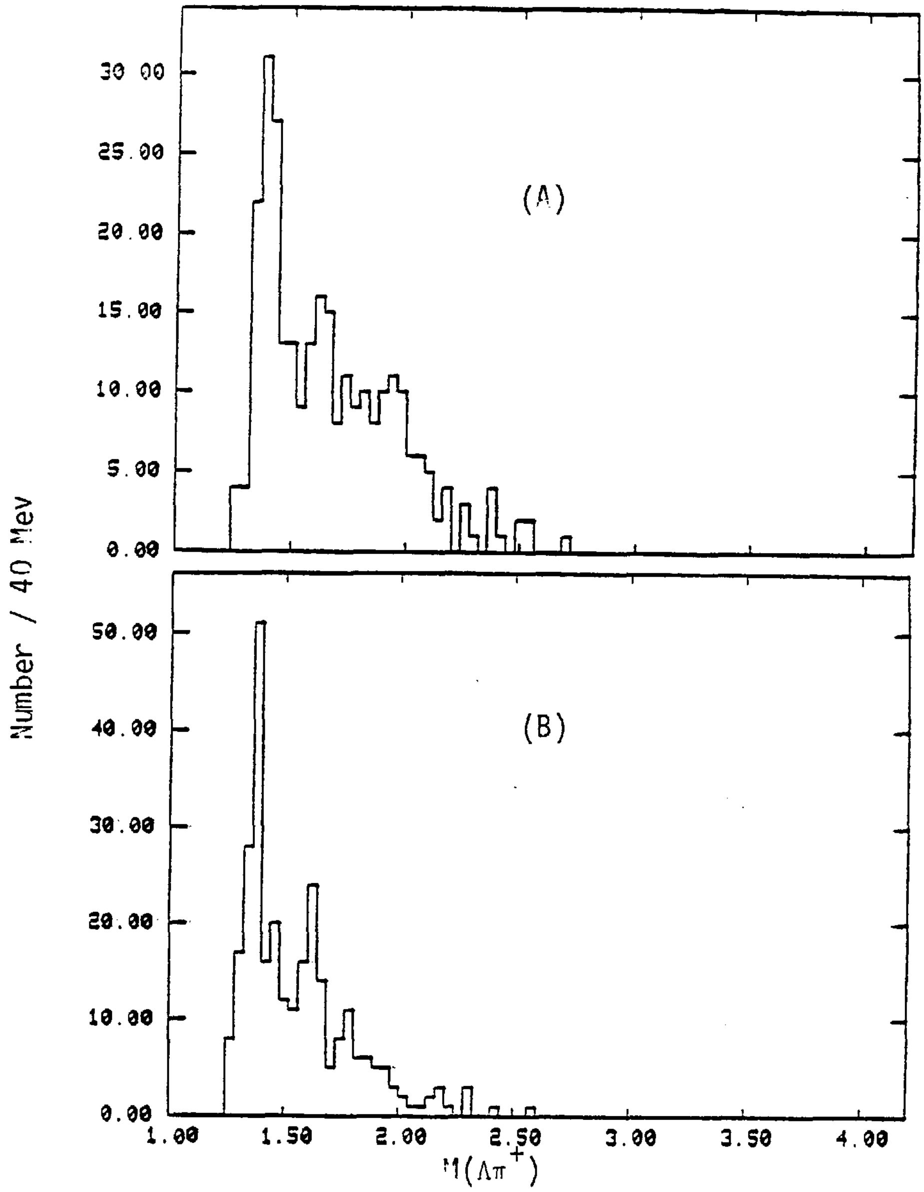

Fig 4.5.5 $\Lambda\pi^+$ mass spectrum with lower,(A), and higher,(B), Θ^* (see text) .

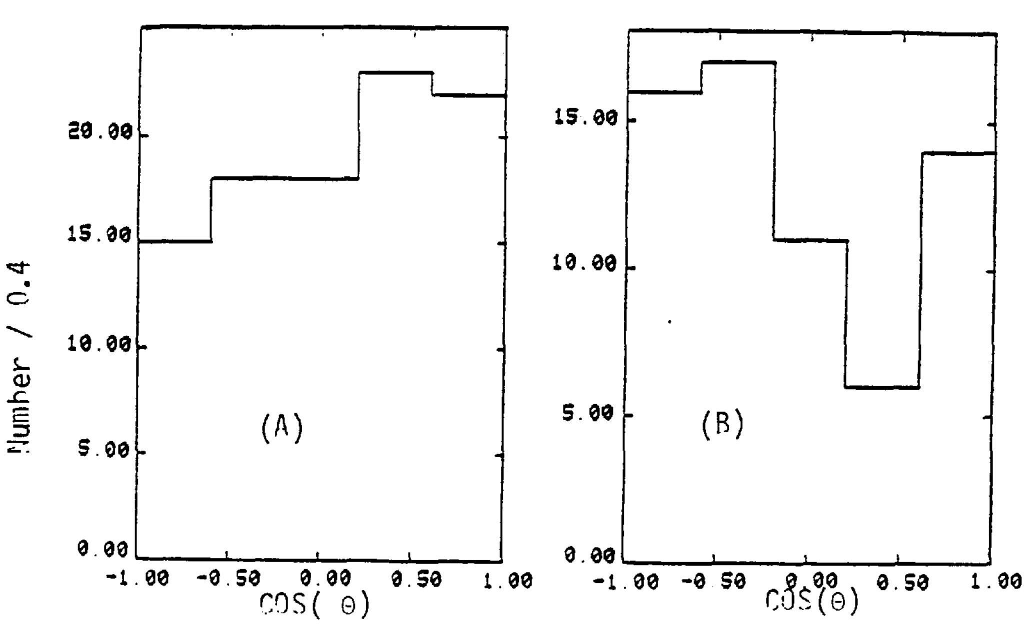

Fig 4.5.6 Decay distributions;(A) 1385 Mev region, (B) 1600 Mev region (see text).

Other Channels

The channel

$$\pi^+ p \rightarrow k^+ p \pi^+ \pi^- \overline{k^0}$$

is dominated by Δ^{++} production, and no clear signal is seen in the 1620 region. The equivalent 4c channel in the k^- induced reaction

$$k^- p \rightarrow \pi^- \pi^- \pi^+ \pi^+ \Lambda$$

contained a strong reflection of a broad ρ^0 in the $\Lambda\pi^+$ mass plot which resulted in a much broader 1385 signal and no clear sign of a 1620 signal was evident.

Conclusions

We have observed a $\Sigma(1620)$ signal of approximately 6 standard deviation significance ('pessimistic estimate') decaying to $\Lambda\pi^+$ in the reaction

$$\pi^+ p \rightarrow k^+ \pi^- \pi^+ \pi^+ \Lambda$$

associated with a strong k^{0*} signal. The mass was found to be 1619 $\pm$ 15 MeV which agrees well with previous claims of a resonance in this region.

CHAPTER 5

Forward Λ Production in $\pi^+ \xrightarrow{p} \Lambda$

5.1 Introduction

In this chapter results will be presented on the baryon exchange process:

$$\pi^+ \; p \longrightarrow \Lambda + X^{++}$$

where X^{++} is two or three particles ($\pi k, \pi\pi k$) and the Λ is a product of beam fragmentation. The SHF was triggered by the proton from the Λ decay. Cross-section, polarization of the Λ, and "inclusive" distributions of the Λ are presented. In these distibutions no distinction will be made between "true" Λ's and Λ's coming from Σ resonances.

The results on this reaction indicates that a large fraction of the forward Λ's result from forward $\Sigma^+(1385)$ and $\Sigma^+(1765)$ production. Some comparisions are presented with the corresponding 11.5 Gec/c SLAC data.

5.2 Experimential Studies Of Baryon Exchange[49]

Detection of baryon exchange is accomplished by studying meson-baryon scattering events in which the baryon is scattered through approximately 180° in the C.M. system. The baryon exchange mechanism gives rise to a "backward peak" in the differential cross-section.

In general backward peaks are much smaller than forward ones and hence gaining information on reaction mechanism in baryon exchange is much more difficult than in meson exchange reactions. Consequently the exchange degeneracy patterns for baryon trajectories are less well established although the baryon resonance spectrum is very well known up to quite high spins (chapter 4).

In order to unambiguously separate baryon exchange from the effects of direct channel resonances the incident energy must be sufficiently high so that direct channel resonances do not play an important role.

The best studied examples of baryon exchange to date are backward π^+p and π^-p elastic scattering.[49] Recently some data has appeared on k^- induced nucleon exchange reactions, but there is practically no data yet on π^+ induced forward hyperon production. Another inelastic reaction for which backward scattering data has been recently collected is $\pi^-p \rightarrow \Lambda k^0$.[49] Striking feature of this data is the nearly maximal polarization of the Λ over the narrow backward angular range studied.

Our analysis is centred around the diagram of Fig 5.1 which involves baryon exchange and has the possibility of an exotic ,doubly charged(K^{++}), meson production at the lower vertex.[50–52]

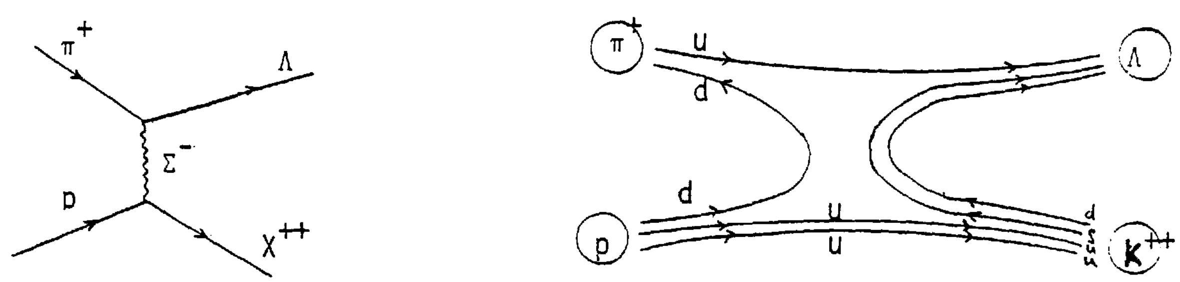

Fig 5.1 Exotic Meson Production by Hyperon Exchange

K^{++}has only one Zweig Rule allowed decay mode into two particles , namely $p\bar{\Sigma}^{+}$, Fig 5.2 .

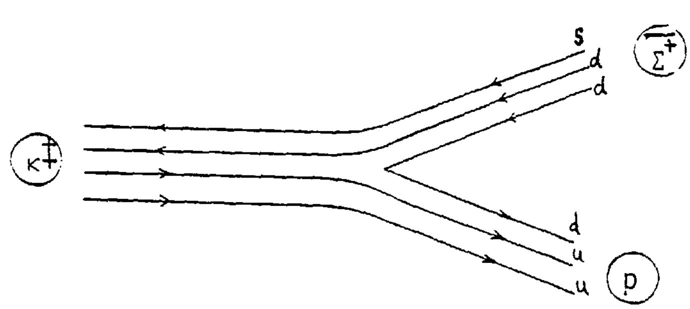

Fig 5.2 Zweig allowed k^{++}decay

The possibility of observing k^{++} decay to $\pi^+ k^+$ mesons relies on the violation of this rule.

5.3 Definition of Variables

In high energy multiparticle reactions it is in general impossible to detect all secondary particles. Most counter experiments at high energies measure only one, or at most a few, of the many outgoing particles. Then two ways of analysing the data can be distinguished. One can try to select those events which originated from quasi-two-body intermediate states and thus analyse these reactions in a "classical" way. This kind of approach has been given the name "exclusive physics". An exclusive reaction can be schematically denoted by: $a+b \rightarrow c+d$ where both outgoing particles are completely measured.

A different approach consists of taking into consideration all measured particles of a certain identity. This "inclusive" way of looking at particle production is usually denoted by $a+b \rightarrow c+x$ where x stands for the set of all other particles. In the inclusive approach one hopes to learn something about the reaction mechanism by studying the momentum spectrum of particle c. Most of the distributions for the reaction $\pi^+p \rightarrow \Lambda+x$ will be represented in this way. The variables used in this kind of description will be defined below.

The momentum of particle c is often decomposed into the transverse momentum P_t and normalised longitudinal momentum, x, as proposed by Feynman. The normalisation can be :

$$X = \frac{P_l^*}{P_{max}^*}$$

where P_l^* is the longitudinal momentum of particle c and P^*_{max} is its maximum(kinematically allowed) momentum, in the overall centre of momentum system (C.M.S.), measured with respect to the axis defined by the incident particles.

Another way of normalising often used is

$$X = \frac{P_l^*}{\sqrt{S}}$$

where S is the total CMS energy squared. In the limit $S \rightarrow \infty$ both definitions coincide. We used the first normalisation. The Mandelstam variables S,t,and u are defined as:-

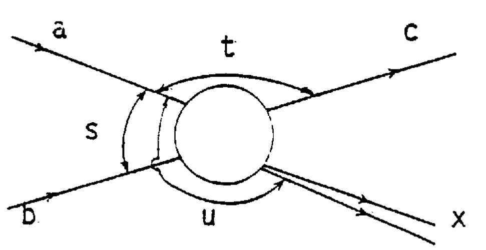

$$S = (P_a + P_b)^2$$
$$t = (P_a - P_c)^2$$
$$u = (P_b - P_c)^2$$
$$M_x^2 = (P_a + P_b - P_c)^2$$

P_i is the four-momentum of particle i. u usually refers to the four-momentum transfer to the baryon,x, a and c are mesons.

Fragmentation Regions

The transition of the proton into the lambda will be called target fragmentation and the transition of the positive pion into the lambda beam fragmentation; denoted by $P \xrightarrow{\pi^+} \Lambda$ and $\pi^+ \xrightarrow{p} \Lambda$ respectively. Both types of fragmentation correspond to strangeness exchange, the beam fragmentation in addition involves baryon exchange. For the 7 Gev/c, and where used the SLAC 11.5 Gev/c, data beam and target fragmentation regions will be defined by the cuts $u > -1.0(\mathrm{Gev/c})^2$ and $t > -1.0(\mathrm{Gev/c})^2$ respectively.

Target and beam fragmentation boundaries in the P_t- P_l plane, at 7 Gev/c, are shown in Fig 5.3 .

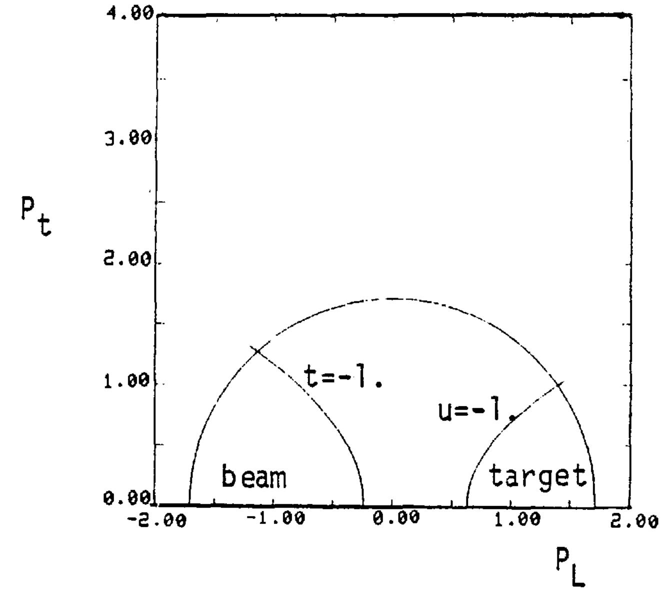

Fig 5.3 Fragmentation Regions

5.4 Experimental Sample

Our total experimental sample in the topology 201 in the 7 Gev/c π^+ induced reactions was 3150 events in the final states:-

$$\pi^+ + p \longrightarrow K^+ \pi^+ \Lambda$$
$$k^+ \pi^+ \Lambda \pi^0$$
$$k^+ \pi^+ \Sigma^0$$
$$\pi^+ \pi^+ \Lambda\ k^0$$

The total data sample is shown in the Peyrou plot of Fig 5.4 . Some 15% of the Λ's are produced in the forward hemisphere,i.e. X> 0. The beam fragmentation selected data is also shown in Fig 5.4 where 270 events remain in the channels:

Channel	Number of Events : U> -1.	U> -2.
$\pi^+ k^+ \Lambda$	66	84
$\pi^+ k^+ \Lambda \pi^0$	112	185
$\pi^+ k^+ \Sigma^0$	36	42
$\pi^+ \pi^+ \Lambda\ k^0$	56	84

80% of these events had a unique fit. Ambiguities in the remainder were resolved on the basis of:

(1) Highest constraint class

(2) Highest probability

5.5 General Features of the Reaction $\pi^+ p \longrightarrow \Lambda + x$

The Feynman x distribution for all our data from the topology 201 together with the SLAC 11.5 Gev/c data is shown in Fig5.5. The considerably stronger backward peaking is evident with the characteristic depression around x=0. The shift of the depression from x=o could be due to resonance production discussed in section 5.7. The fraction of events in the beam fragmentation region halves from 7 to 11.5 Gev/c indicating a strong energy dependance in the baryon exchange cross-section. The 11.5 Gev/c data also gives a much flatter distribution in the positive x region compared to the 7 Gev/c data.

The above feature in the x-distribution is reflected in the u-distribution of the lambda shown in Fig 5.6. The 7Gev/c data shows a fairly clear beam fragmentation signal compared to the much flatter backward distribution at 11.5 Gev/c.

For the remainder of the chapter only the 7 Gev/c data will be discussed.

Momentum Distribution[53]

The invariant inclusive cross-section can be written in terms of the Feynman x variable as :

$$F(x) = \frac{1}{\pi} \int \frac{E}{P_{max}} \frac{d^2\sigma}{dx\, dp_t^2} \quad dp_t^2$$

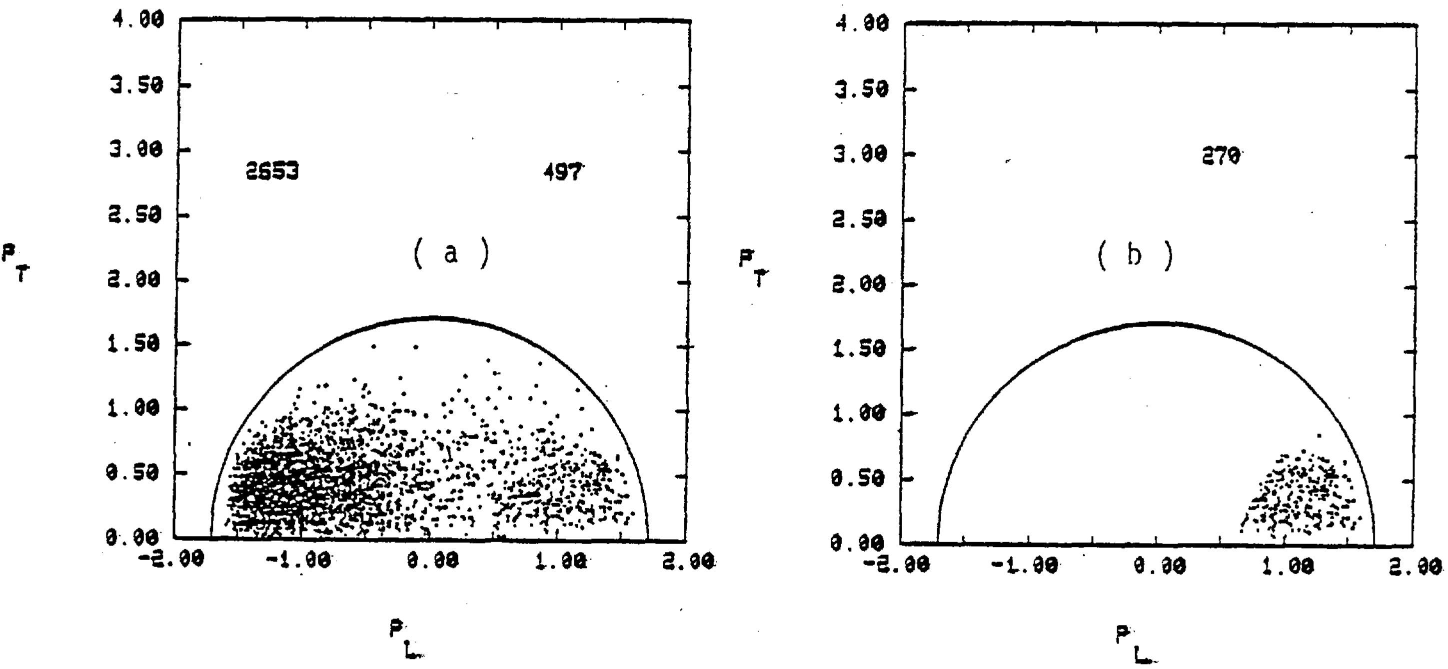

Fig 5.4 (a) P_L / P_t distribution of all the 7 Gev/c data

(b) U >-1 selection

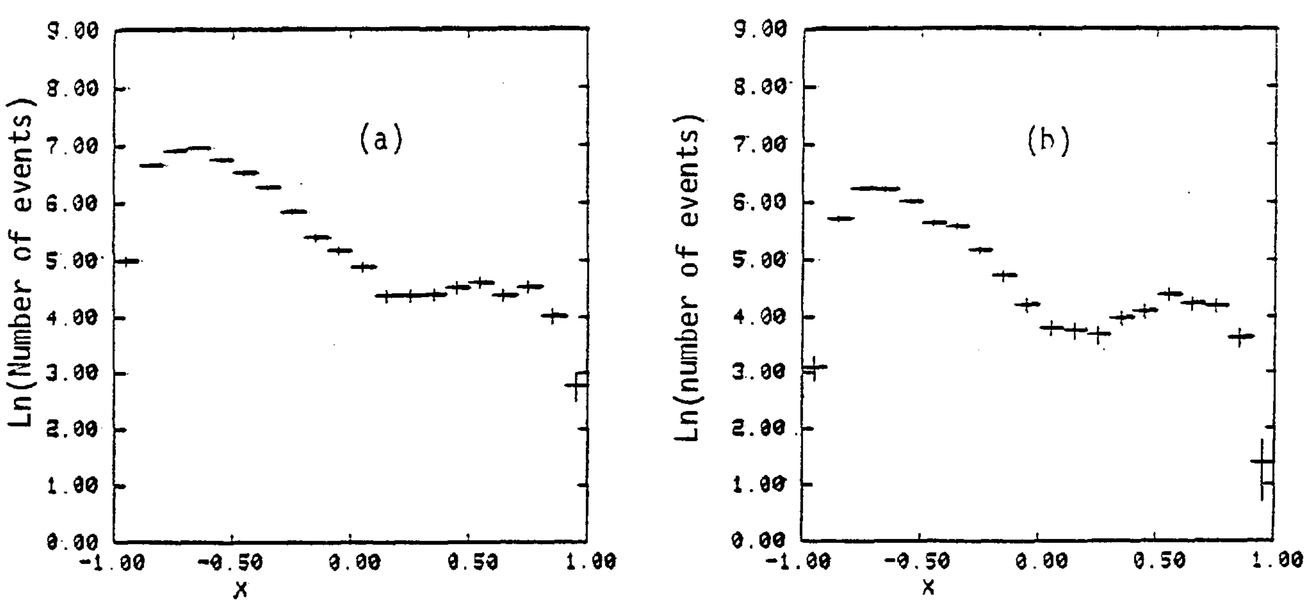

Fig Fig 5.5 (a) X-distribution of the 11.5 Gev/c data

(b) x-distribution of the 7 Gev/c data

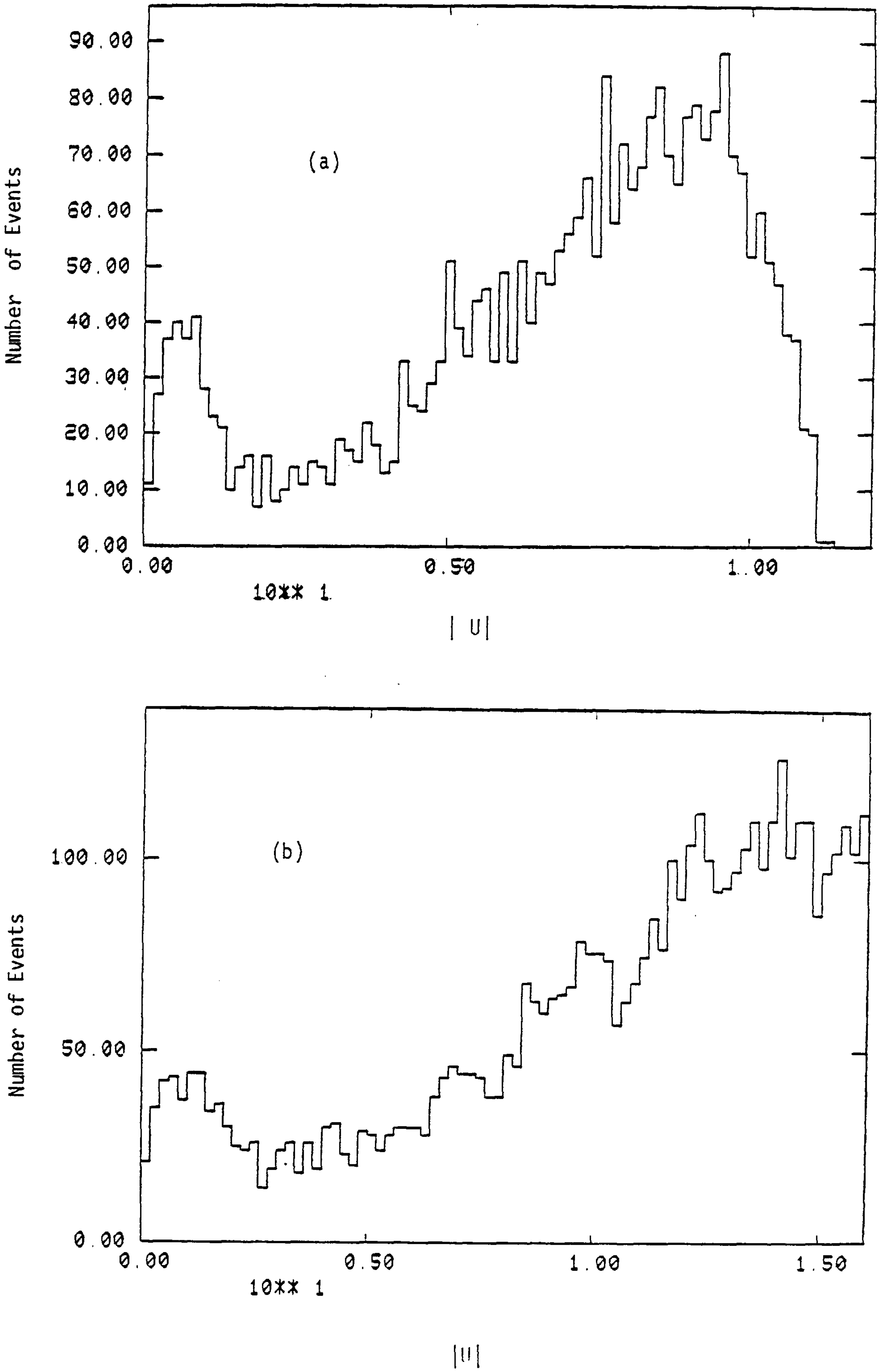

Fig 5.6 U-distribution : (a) 7Gev/c data, (b) 11.5 Gev/c data

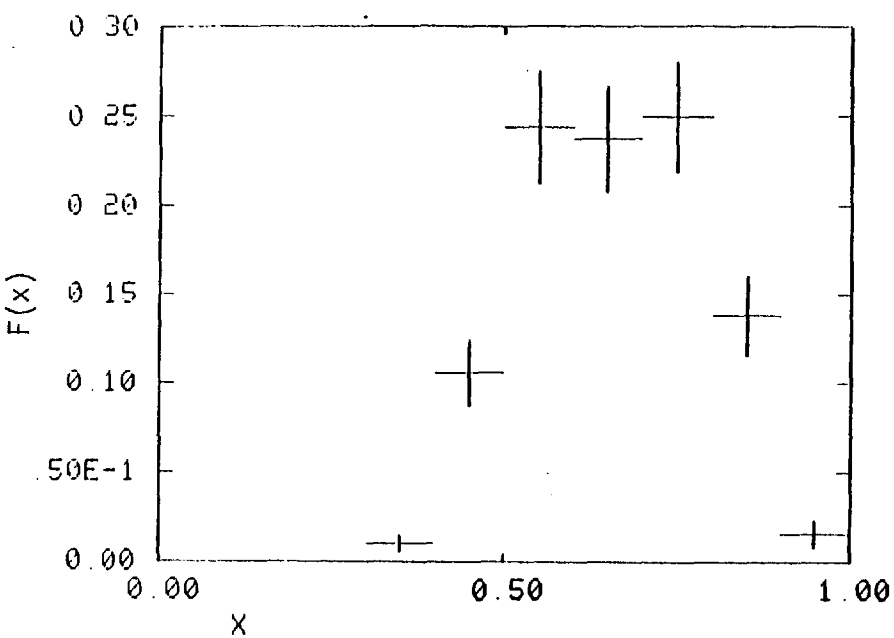

Fiq 5.7 F(x) distribution at 7 Gev/c

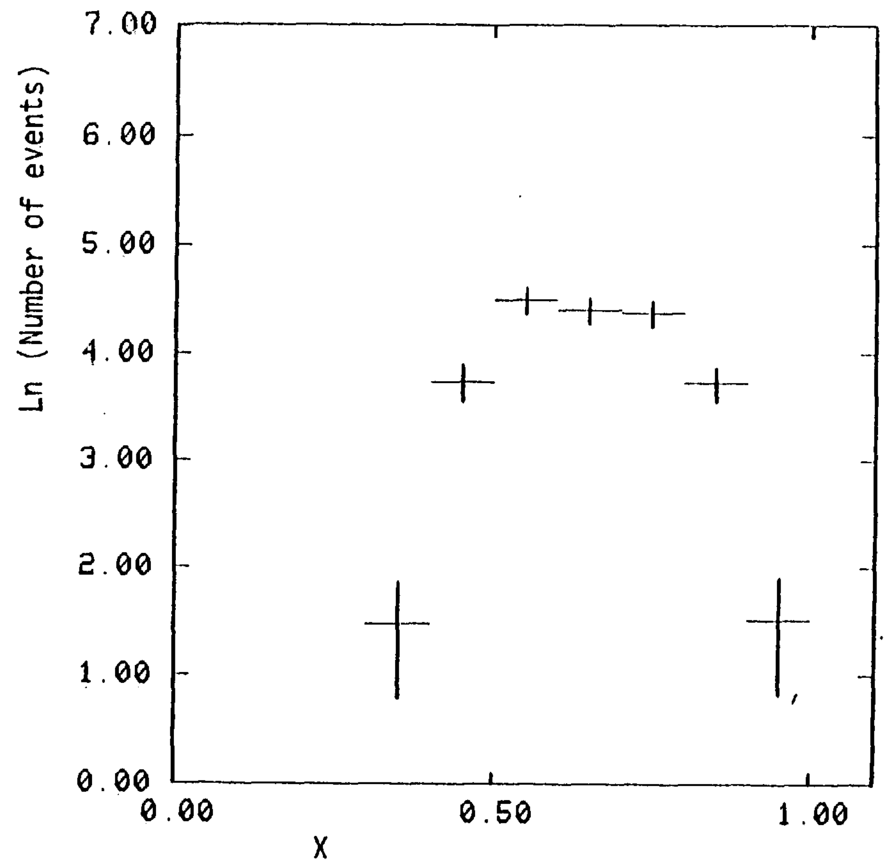

Fiq 5.8 Weighted x distribution at 7 Gev/c

where E, P_{max} and P_t are the energy, the maximum momentum and transverse momentum respectively of the Λ. This distribution is shown in Fig 5.7, the Feynman x distribution is shown in Fig 5.8.

The P_t distribution as a function of x is shown in Fig 5.9. It peaks at approximately x=0.75. The $(d\sigma/dp_t^2)$ distribution follows an exponential distribution in the range 0.0- 0.45$(Gev/c)^2$. Fit to this of the form $(d\sigma/dp_t^2) = A\exp(-Bp_t^2)$ gave the following parameters for A and B:

$$A = 3.8 \pm 0.4$$

$$B = 2.9 \pm 0.5$$

the normalisation is to unity.

The mean p_t and p_t^2 values were found to be:

$$< P_t > = 0.41 \pm 0.01$$

$$< P_t^2 > = 0.17 \pm 0.01$$

while the weighted values were:

$$< P_t >_{wt} = 0.41 \pm 0.01$$

$$< P_t^2 >_{wt} = 0.19 \pm 0.01$$

the weighting procedure is outlined in the next section.

5.6 Weighting Procedure

The trigger in this case is a fast proton with momentum > 2.5 GeV/c coming from the Λ decay and hence the geometrical weighting procedure has to be slightly modified from that described in chapter two. Each event was weighted individually.

For each event random x values were chosen along the fiducial length of the chamber as described in chapter 2. For each such x the Λ - M vector (see diagram below) was rotated in $\emptyset$ about the beam direction.

For each such rotation about the beam direction the triggering proton vector from the Λ decay was then rotated in $\emptyset$ about the A - M vector as shown below. For each of these rotations the proton was swum through the chamber magnetic field and the downstream trigger array. The geometrical weight was then estimated as described in chapter 2.

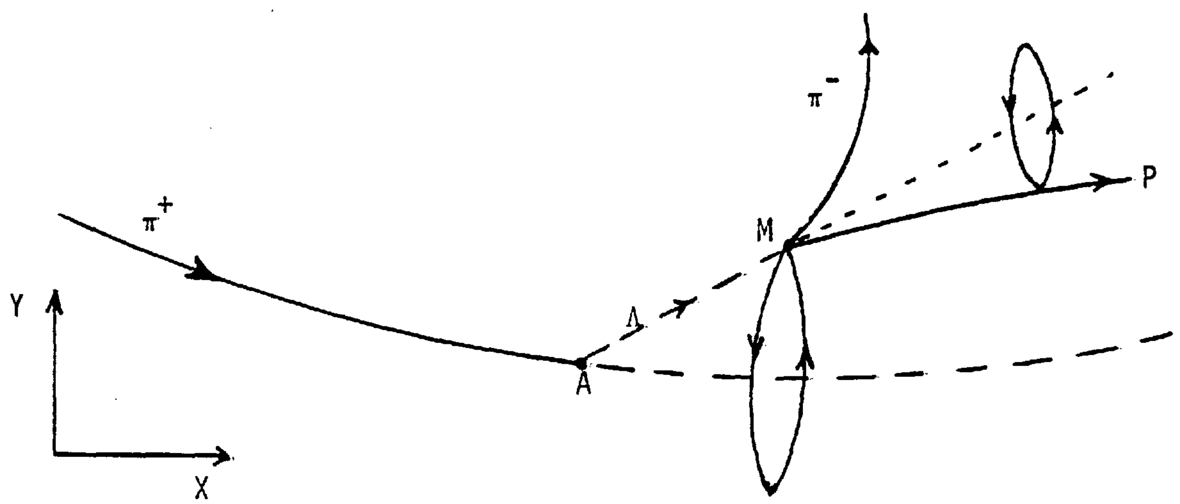

The length weighting (chapter 2) for the fast Λ events was investigated as a function of the upper and lower length cuts. The results are shown in Fig. 5.11. The lower length cut was imposed at 0.8 cm while the upper was at 15 cm. The overall weight distribution as a function of u is shown in Fig. 5.12.

5.7 Resonance Production

Recoiling Mass Spectrum

The mass spectrum, M_X, of the system recoiling against the Λ, in the beam fragmentation region, is shown in Fig. 5.13. There is no

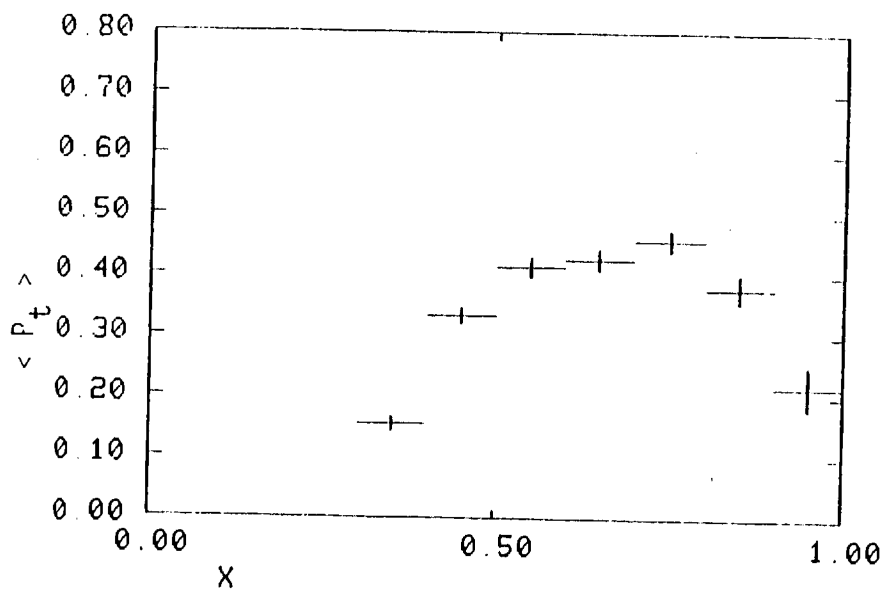

Fig 5.9 P_t distribution at 7 Gev/c

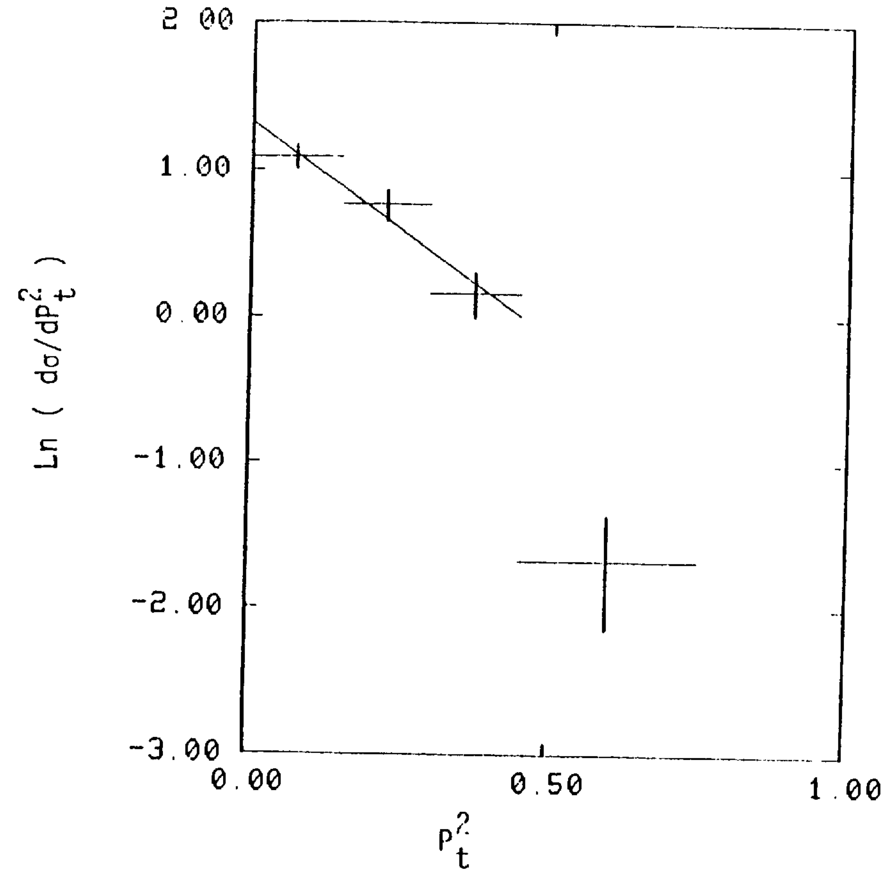

Fig 5.10 $d\sigma/dp_t^2$ distribution at 7Gev/c

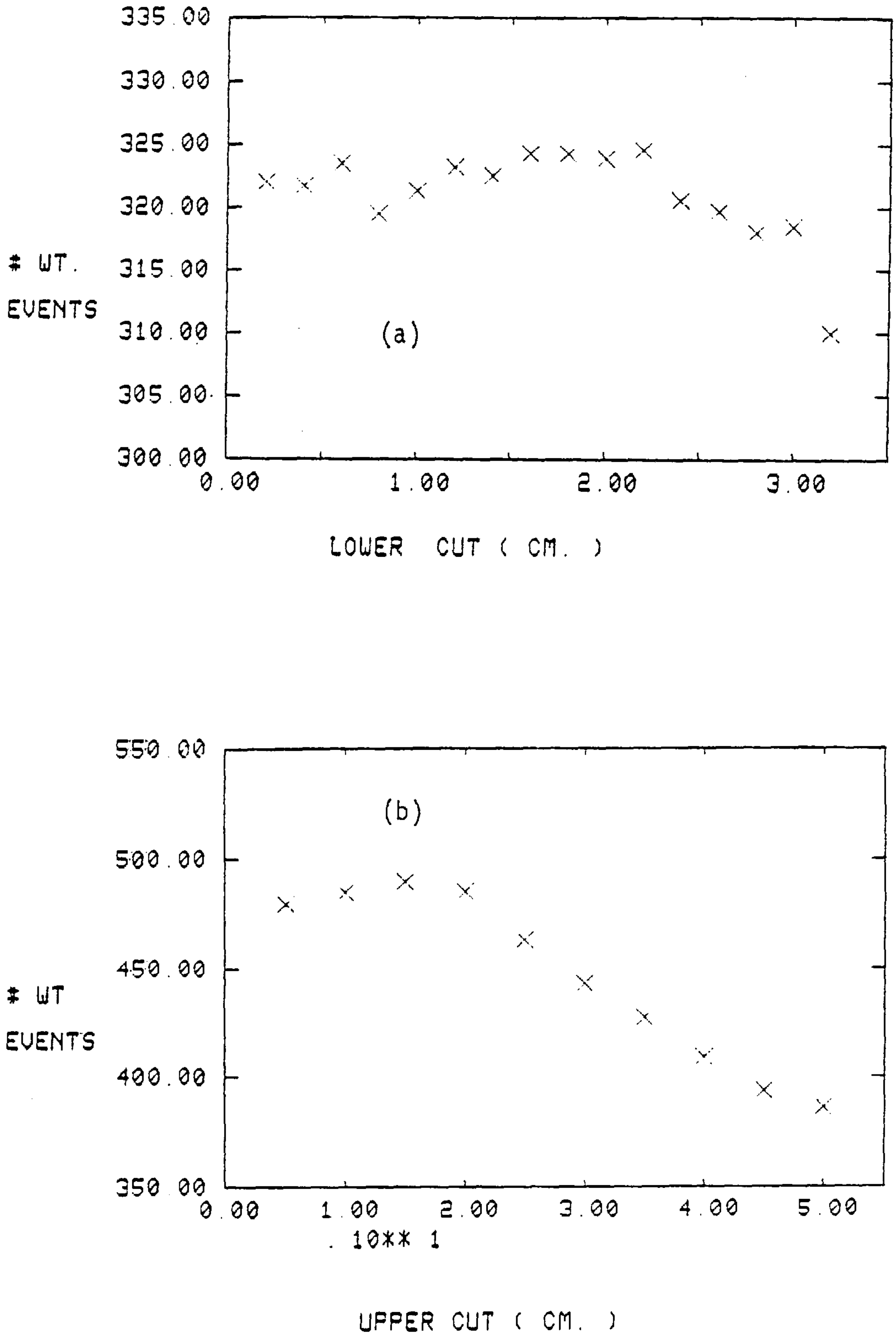

Fig 5.11 Number of weighted events as a function of lower (a) and upper (b) length cuts.

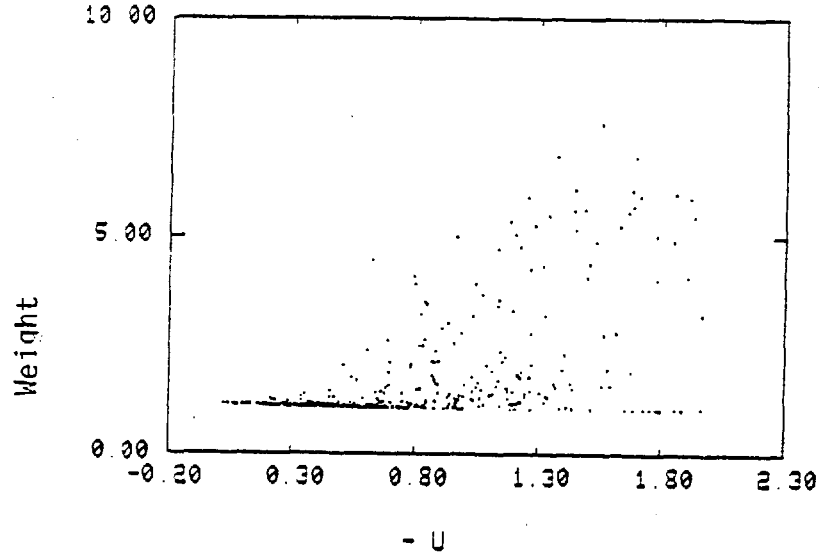

(a)

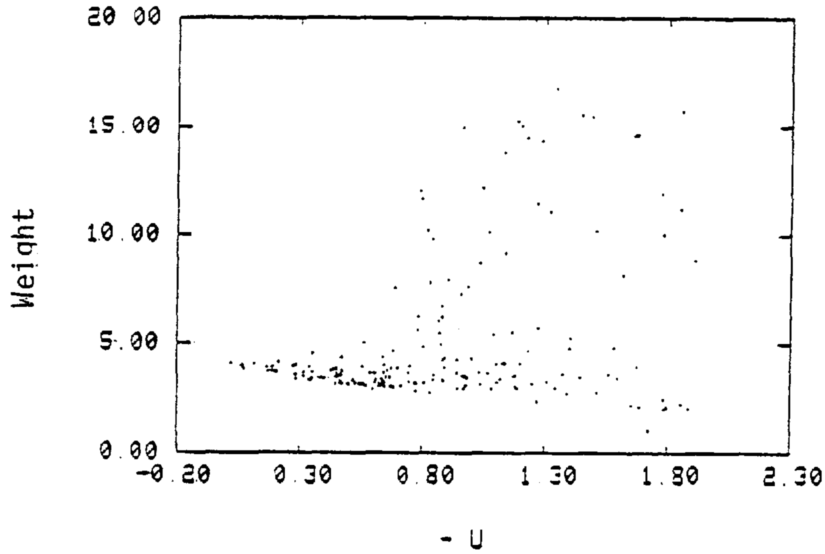

(b)

Fig 5.12 (a) Geometric weight distribution as a function of u
(b) Overall weight distribution as a function of u

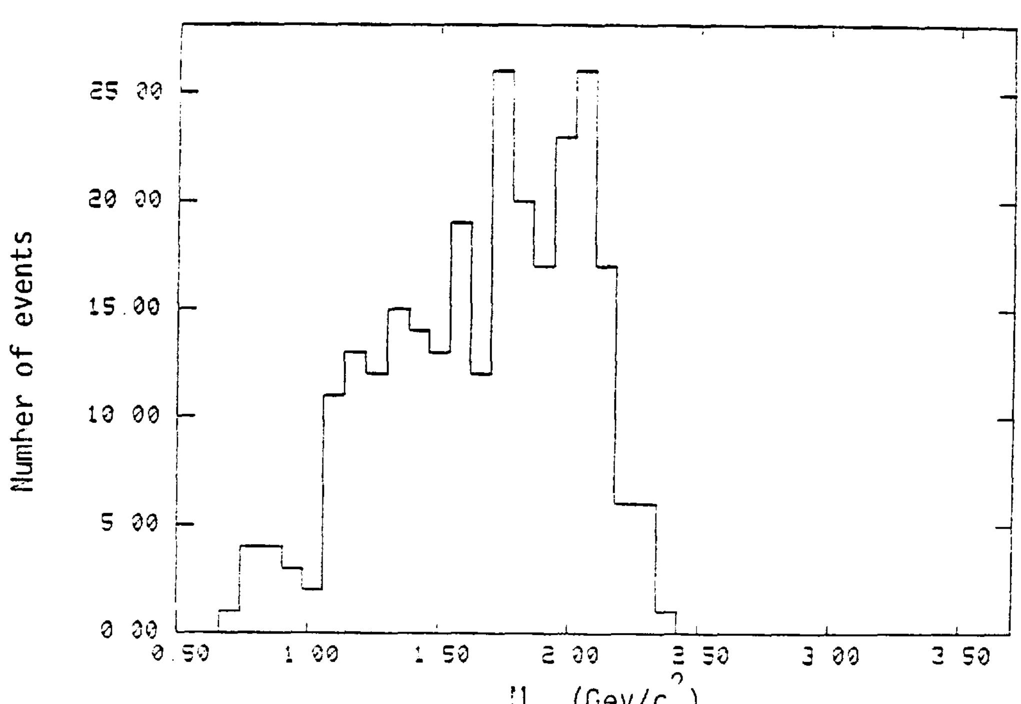

Fig 5.13 Missing massagainst lambda.

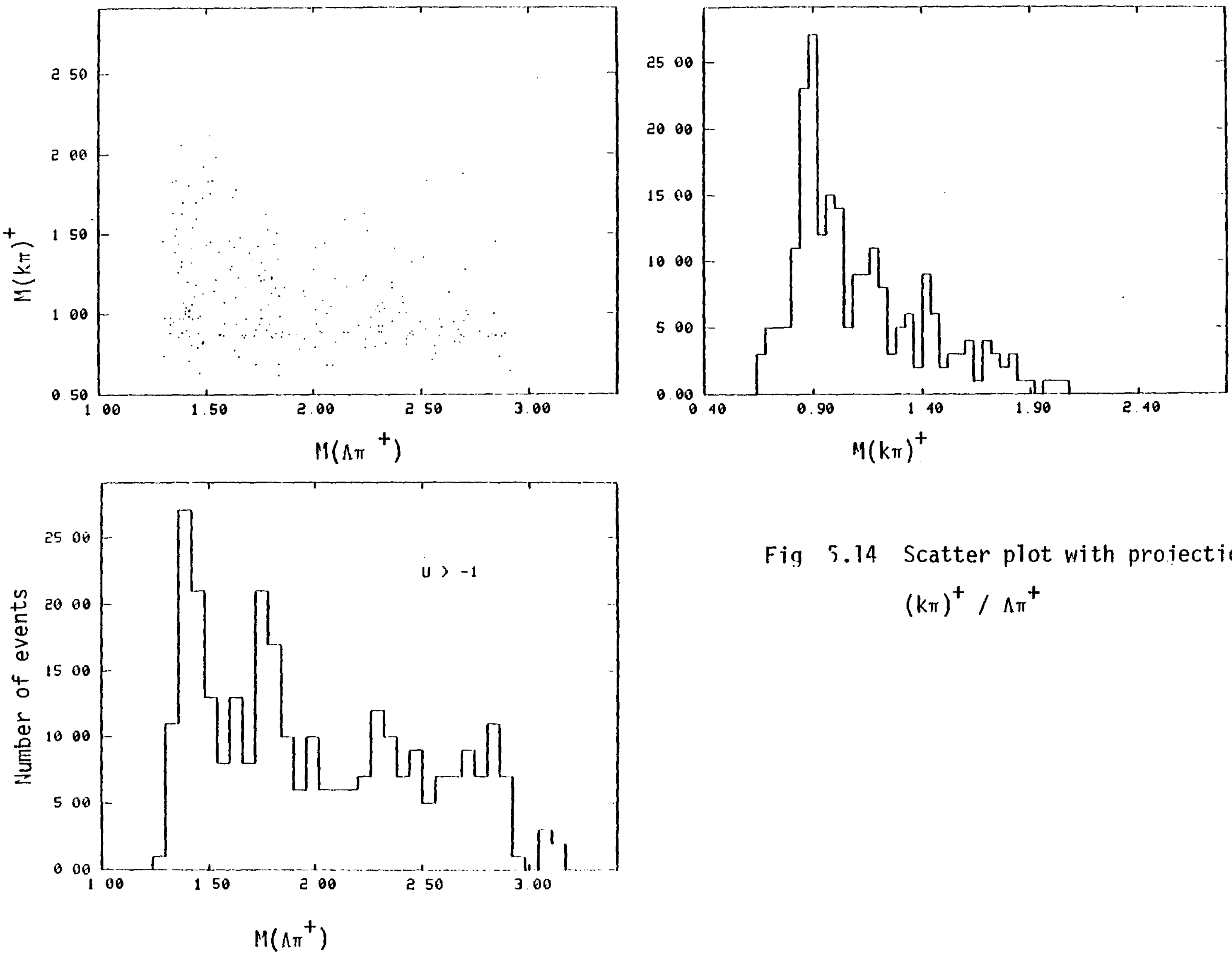

Fig 5.14 Scatter plot with projections of $(k\pi)^+$ / $\Lambda\pi^+$

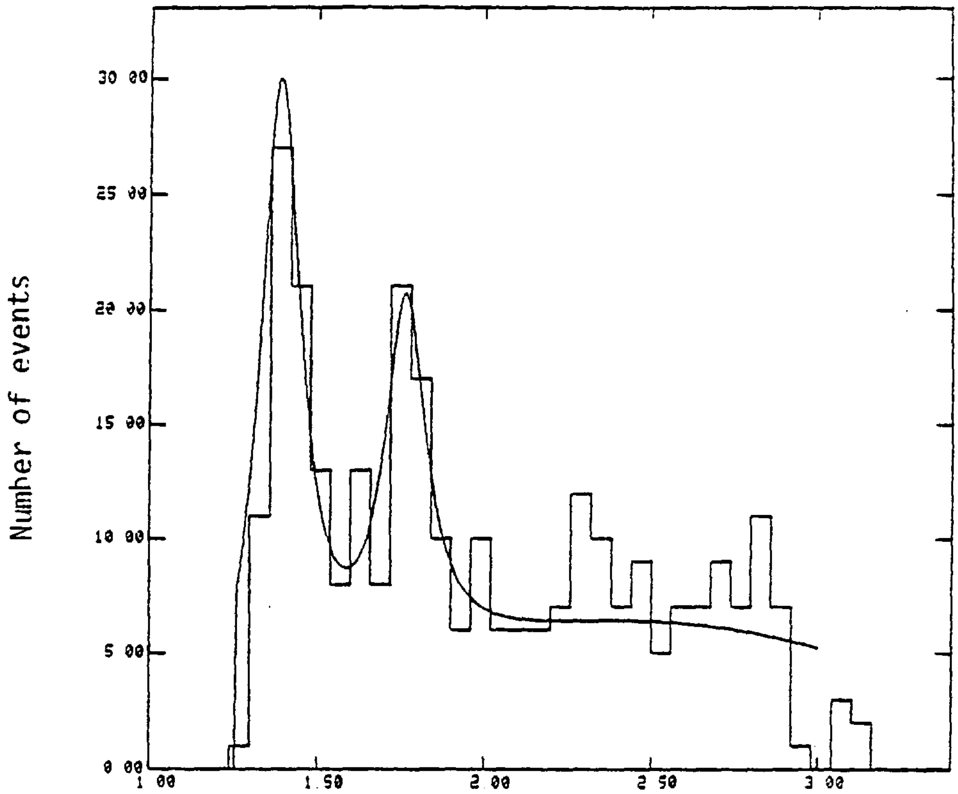

Fig 5.15 Mass Fit to $\Lambda\pi^+$

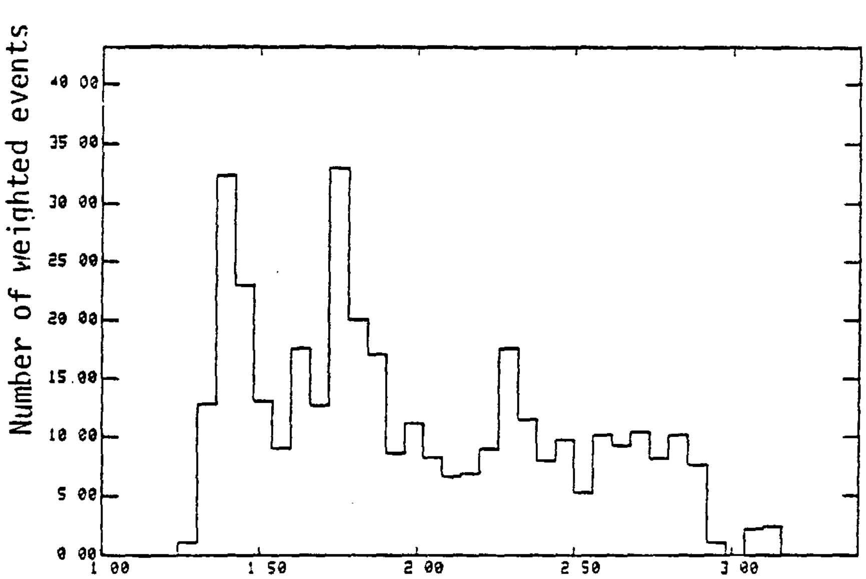

Fig 5.16 Weighted $(\Lambda\pi^+)$ mass spectrum .

(Geometric weight used only)

indication of meson resonance production.

Resonance Production

Due to the very small number of events in the Σ^0 channel only $\Lambda\,\pi^+\;\pi^+\,k^0$, $\Lambda\pi^+\,k^+$ and $\Lambda\pi^+\,k^+\,\pi^0$ final states were used to look at Σ and meson resonance production. Scatter plot for these final states of $\Lambda\,\pi^+/k\pi$ is shown in Fig. 5.14. Accumulation of events in the $\Sigma(1385)$, $\Sigma(1700)$ and k^* (890) region in evident. The associated histograms are also shown in Fig. 5.14 where the broad k^* (890) signal is present in the $k\pi$ projection. In the $\Lambda\pi$ projection $\Sigma(1385)$ and $\Sigma(1700)$ are present. The mass spectrum has been fitted to Briet-Wigner functions and a polynomial background. The 1700 MeV bump is centred at 1760 MeV with Γ = 150 MeV.

The weighted $\Lambda\pi^+$ mass plot is shown in Fig. 5.16 where it is seen that the $\Sigma(1760)$ is as prominent as the $\Sigma(1385)$ signal. There were only a few events in the reaction involving joint resonance production $\Sigma(1385)$/ $k^*(890)$. So that a study of forward $\Sigma(1385)$ production against k^* to complement the study of chapter 3 of backward $\Sigma(1385)$ production against k^* was not feasable.

5.8 Cross-Sections and Λ Polarization

The total cross-section for the process $\pi^+p \rightarrow \Lambda + X^{++}$ in the beam fragmentation region was found to be:

$$\sigma = 3.6 \pm 1.2\ \mu b$$

The differential cross-section, normalised to unit cross-section, are listed in table 5.1. Also listed is the differential cross-section with respect to u' where

$$u' = u - u_{min}$$

The differential cross-section was fitted to the form $d\sigma/du = A\, e^{-Bu}$. The fits are shown in Fig 5.17 with the fit parameters:

For $d\sigma/du$:- $A = 0.46 \pm 0.13$

$B = -1.4 \pm 0.4$

For $d\sigma/du'$:- $A = 1.25 \pm 0.14$

$B = 0.5 \pm 0.3$

The dip in $d\sigma/du$ at low $|u|$ is due to the u_{min} effect where by the kinematics of the reaction depopulate the low $|u|$ region. This effect becomes particularly important above a missing mass of 1.5 Gev/c^2 against the Λ. The $d\sigma/du'$ distribution shows no significant dip at low $|u'|$. In the range $|u'|$ = 0.0 to 0.6 $(\text{gev/c})^2$ this distribution is essentially flat.

Upper Limit On Single Forward Λ Production

The total cross-section for forward Λ production is $3.6 \pm 1.2\ \mu b$. We estimated the number of forward Λ's coming from forward $\Sigma^+(1385)$ and $\Sigma^+(1765)$ production from the mass fit to the $\Lambda\pi^+$ mass spectrum. The cross-section for single Λ production was estimated to be:

$$\sigma_\Lambda = 1.57 \pm 0.52\ \mu b$$

Hence the upper limit on X^{++} production decaying to mesons is σ_Λ .

Λ Polarization

In this section polarization of the Λ(inclusive) will be presented. The polarization, P_Λ , of the Λ is given by :-

$$P_\Lambda = \frac{3}{\alpha} \sum_{i=1}^{N} w_i \cdot q_i \cdot n_i \Big/ \sum_{i=1}^{N} w_i$$

where q is the unit vector along direction of the proton in the Λ rest

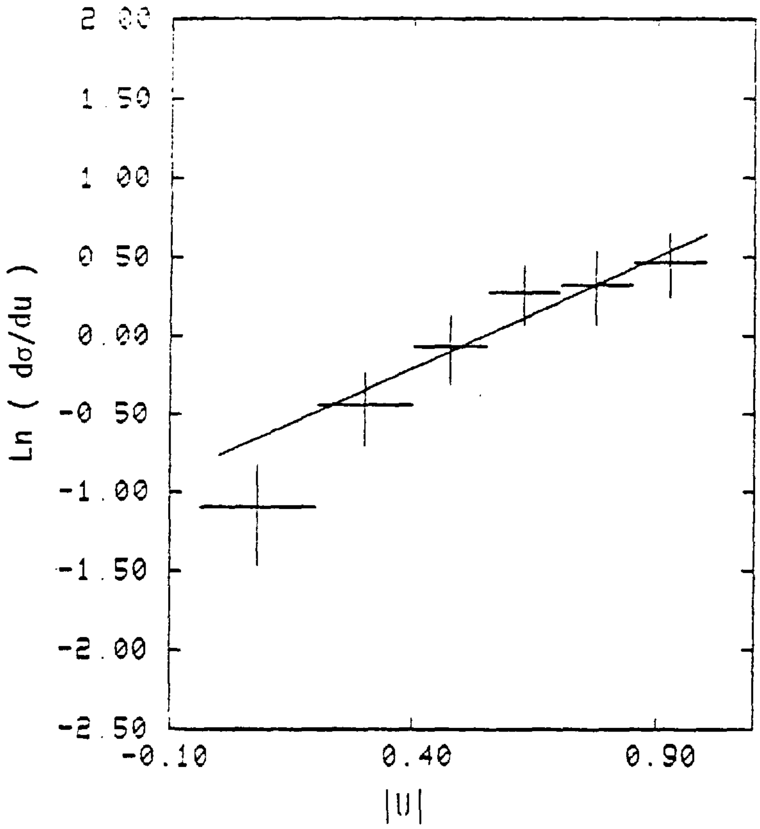

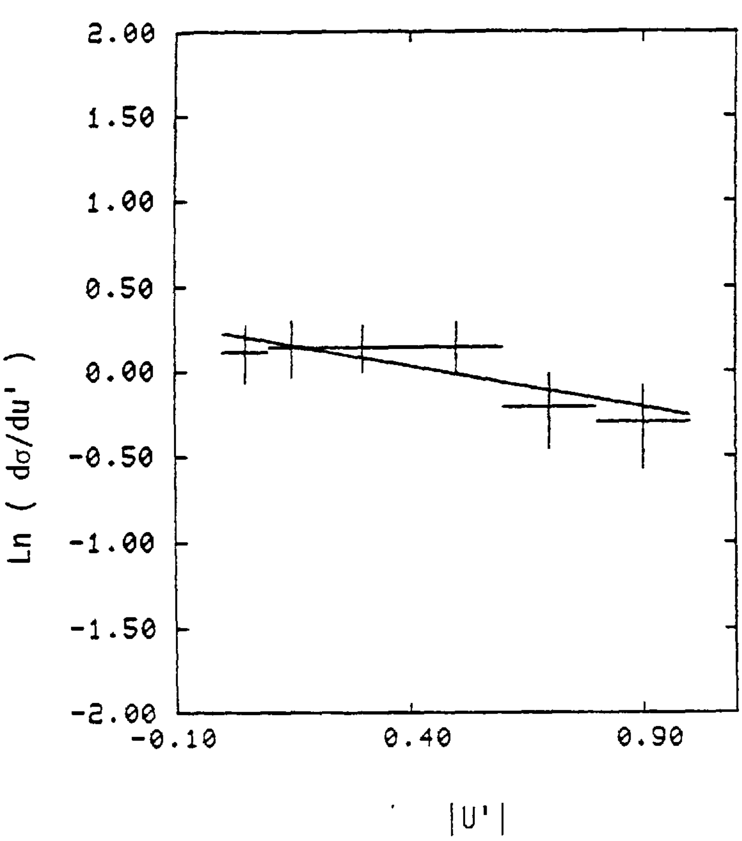

Fig 5.17 Fit to differential cross-section

$\lvert \Delta U \rvert$			$d\sigma/du$ $(\mu b/(Gev/c)^2)$	$\Delta(d\sigma/du)$
U_{min}	-	0.2	0.33	0.1o
0.2	-	0.4	0.64	0.15
0.4	-	0.55	0.94	0.21
0.55	-	0.7	1.32	0.25
0.7	-	0.85	1.38	0.32
0.85	-	1.0	1.59	0.33

$\lvert \Delta U' \rvert$			$d\sigma/du'$	$\Delta(d\sigma/du')$
0.o	-	0.1	1.12	0.19
0.1	-	0.2	1.15	0.19
0.2	-	0.4	1.15	0.16
0.4	--	0.6	1.15	0.18
0.6	-	0.8	0.81	0.18
0.8	-	1.0	0.74	0.18

Table 5.1 Differential Cross-Section

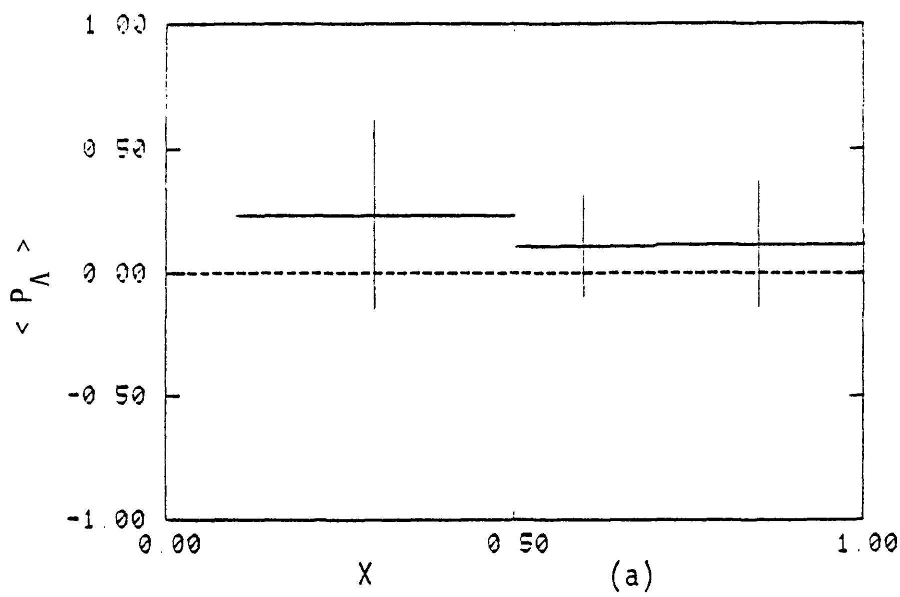

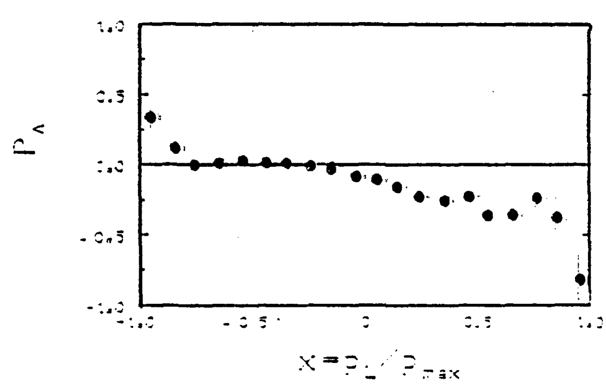

(b)

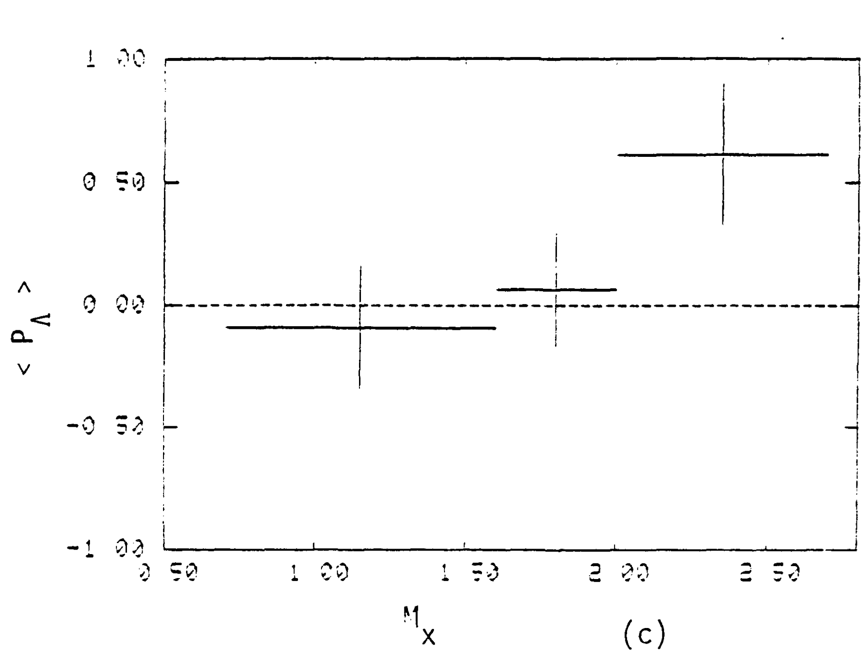

Fig 5.18 Λ Polarization: (a) As a function of x (b) From k^-(8.25) Gev/c experiment (c) As a function of the missing mass

frame, n is the unit vector normal to the Λ production plane and w is the weight for the event: α is the decay asymmetry parameter (taken as 0.647) and N is the number of observed events.

Fig 5.18a shows the polarization as a function of x, and is consistent with zero. There is hardily any data on π fragmentation into a Λ . However data is available in k^- fragmentation into a Λ. The general trend of this is very similar at various beam momenta. Results from k^-(8.25 Gev/c)[53] are shown in Fig 5.18b. The Λ is unpolarized when produced backwards. However significant negative polarization is found in the forward region ; and in particular in the extreme forward region ($x \sim 1$) which is dominated by baryon exchange. In our data however the polarization is consistant with zero in this region. The mean polarization in the region $0 < x < 1$ with $U > -1$ is:

$$< P_\Lambda > \; = \; 0.25 \pm 0.17$$

$$< P_\Lambda >_{wt.} = \; 0.13 \pm 0.15 \qquad \text{(WEIGHTED)}$$

Polarization of the Λ as a function of the missing mass against it is shown in Fig 5.18c. There seems to be a systematic increase in polarization with increasing missing mass.

Conclusions

The reaction $\pi^+ P \rightarrow \Lambda + X^{++}$ was studied where Λ is a product of the beam fragmentation. Results indicate approximately 45% of the forward Λ's are the result of forward $\Sigma^+(1385)$ and $\Sigma^+(1765)$ production. We have estimated an upper limit of 1.57 ± 0.52 μb for single Λ production.

The polarization was found to be consistent with zero in the forward direction which is at variance with data from k^- induced reactions where the forward Λ's have a negative polarization.

APPENDIX I[43-45]

This appendix briefly describes the method of moments used in chapter four to look at the spin of a particle.

To look at the spin of a resonance X decaying as

$$X \rightarrow a + b$$

the angular distribution information can be utilised. The decay distribution can be expanded in terms of the spherical harmonics:

$$I(\cos\theta,\phi) = \sum_{L} a_L Y_L^m(\cos\theta, \phi)$$

where the resonance X has spin j decaying with relative orbital angular momentum L between a and b. If one of a or b has a spin 1/2 and the other zero then

$$L = j \pm 1/2$$

The multiple parameters t_{Lm} describing the resonance X can also be written in terms of the moments of the decay distribution:

$$\int I(\theta, \ ) \, Y_L^m(\theta, \ ) \, d\Omega = \frac{1}{2} (-1)^{j-1/2} \sqrt{\frac{2j+1}{4\pi}} < jj,-1/2 \ \ L,0 > |1+(-1)^L| \ t_{Lm}$$

Clebsch-Gordan coefficients ensure that moments with L> 2j vanish. So the observation of a statistically significant non-vanishing average value of Y_L^m means that the spin of X is at least 1/2 L.

i.e. $j \geqslant \frac{1}{2} L$

APPENDIX II [44 – 48]

In this appendix the Adair argument for determining the spin of a hyperon is described.

In a reaction of the type

$$\pi^+ + p \rightarrow k^+ + H^+$$

with H^+ produced in the backward direction in the initial state we have:-

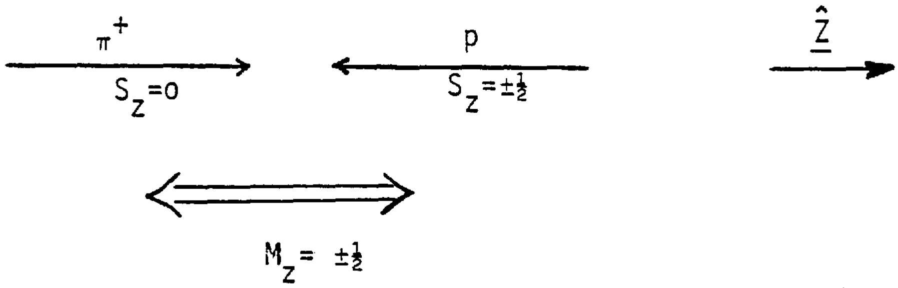

Choosing the axis of quantization in the incident π^+ direction. In the final state we have:

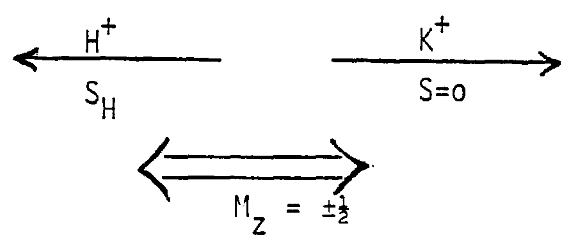

In the initial state, where m_1=o , the proton spin must be oriented to give

$$m_z = \pm \frac{1}{2}$$

and by momentum conservation m_z of H^+ must also be $\pm 1/2$.

Now defining the decay angle, θ, in H^+ restframe for the decay:

$$H^+ \rightarrow \pi^+ + H^o$$

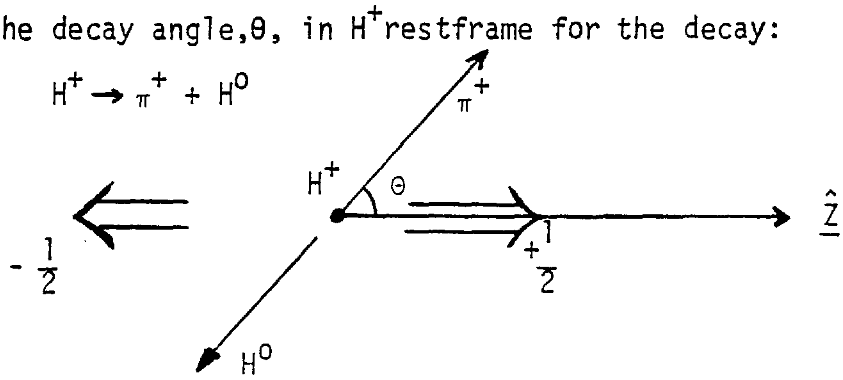

If the spin of H^+ is J ($J_z = \pm 1/2$); if J=1/2 then the decay distribution will be isotropic in cosθ, θ being the angle Of emission of the π^+, since the states with $J_z = \pm 1/2$ are equally populated.

When J= 3/2 for H^+ the states with $J_z = \pm 3/2$ are unpopulated.Hence angular correlations will arise in the decay of H^+.

For a $P_{3/2}$ final state J=L+S the π^+p eigenfaction in terms of the space and spin states is

$$X_{3/2}^{\pm 1/2} = \sqrt{\frac{2}{3}}\ Y_1^0\ \Psi_{\frac{1}{2}}^{\pm\frac{1}{2}} + \sqrt{\frac{1}{3}}\ Y_1^{\pm 1}\ \Psi_{\frac{1}{2}}^{\pm\frac{1}{2}}$$

which gives the decay distribution:-

$$\frac{d\sigma}{d\Omega} \equiv \frac{1}{8\pi} (1 + 3 \cos^2 \theta)$$

The distributions for various spins are listed below.

SPIN	ANGULAR DISTRIBUTION
1/2	1
3/2	$1/2 + 3/2 \cos^2 \theta$
5/2	$3/4 - 3/2 \cos^2\theta + 15/4 \cos^4\theta$
7/2	$9/16 + 45/16 \cos^2\theta - 165/16 \cos^4\theta$ $+ 175/16 \cos^6\theta$

In practice one has to use events in which the H^+ is not produced in the direction of the beam. This will lead to $m_L \neq 0$. Adair[47] has shown the argument is unaffected if centre of momentum scattering angle θ^* satisfies the condation:-

$$\theta^* < \frac{1}{L_{max}} \text{ rad.}$$

where L_{max} is the maximum important angular momentum. θ is known as the Adair Angle.

REFERENCES

1 The Proposal, Imperial College Ic/HENP/74/01
S L A C Proposal No. BC 59

2 J Ballam and R D Watt, Hybrid Bubble Chamber Systems, An, Rev. Nucl. Sci. 27
R C Field , The SLAC 1M Bubble Chamber Hybrid Facility , S H F Memo 67 (1977)

3 T H Fieguth and R A Gearhart, R F separators and separated beams at SLAC, SLAC-Pub-1552 (1975)

4 The software algorithm was developed by P J Dornan and A P White of Imperial College.

5 The HPD mark 2 Flying-spot digitizer at CERN ,Report 68-4

6 B Penny Ph.D. Thesis Imperial College (1971)

7 The beam following package was written by R Campbell of Imperial College

8 'Hydra Geometry' ,CERN Program Library

9 G Hall , Fast Track fitting in SLAC hybrid experiment, Imperial College Internal Memo Ic/HENP/Pn/27 (1975)

10 T S Virdee Ph.d. Thesis Imperial College (1979)

11 Program 'Grind', CERN T C Program Library long write-up

12 P M Heinen Ph. D. Thesis Nijmegen (1976)

13 Program 'Autogrind', CERN T C Program Library

14 J B GAY , Weighting of V^0 and kink events, CERN/D.Ph II/ X42

15 A J de Groot Ph.D. Thesis Zeeman Lab., Amsterdam (1975)

16 R A Lewis, Normalisation, SLAC internal report SHF memo 46 (1976)

17 Study of Hypercharge Exchange reactions of the type $k^-p \to 1^- \ 3^+/2$ at 4.2 Gev/c , CERN/D.Ph.II/ Phys. 75-23

18 Non-strange vector meson production in k^-p interactions at 4.2 Gev/c CERN/ EP/ Phys 77-45

19 M Pearl, High Energy Hadron Interactions

20 K Gottfried and J D Jackson , On connection between production mechanism and decay of Resonances at High Energy, Nuovo Cimento Vol xxxiii No 2

21 G G G Massaro Ph.D. Thesis Zeeman Lab. Amsterdam (1978)

22 J P Ader and M Capdeville, Nouovo Cimento Vol LVlA No.4

23 Proceedings of the 1965 Easter School for Physicists CERN 65-24

24 P A Baker et.al. P R L Vol. 40 No. 11

25 P A Baker et. al. Imperial College Preprint Ic/HENP/79/8

26 Vector Meson Production in Hypercharge Exchange Reactions at 7 & 11.5 Gev/c. SLAC-Pub.- 2403

27 A C Irving and R P Worden , Physics Reports, Vol 34 No. 3 (1977) & Ref therein

Two Body Collisions , 7 th Rencontre de Moriond (1972)

28 Jackson & Pilkuhn , On the Production of Vector Mesons and Isobars in Peripheral Production , Nuovo Cimento Vol xxxiii No3

29 Stodolsky and Sakurai , Vector Meson Exchange Model for Isobar Production, P R L Vol 11 No.2 (1963)(& ref 30)

30 P R L Vol 134 No. 5B (1964)

31 CERN P D G Review of Particle Properties

32 Proceedings of the 1976 Oxford Baryon Conference

New Directions in Hadron Spectroscopy ANL-HEP-CP-75-58

33 O W Greenberg , Quarks, Ann Rev. Nucl.Part. Sci. 1978

34 Proceedings of the School for Young High Energy Physicists, R.L. 1977

35 Hendry and Lichtenberg, The Quark Model, Reports on Progress in Physics

36 A J G Hey ,Particle Systematics, CERN Preprint Thep. 78/9-17

37 R H Dalitz, Baryon Spectroscopy with the Quark Model,Proceedings of the A N L Conference July 1975

38 'FOWL' , CERN Program Library

39 Aspell et. al. Phy. Rev. D Vol 10 No. 5 1974

40 Nucl. Phy. B112 (1976) 77-106 & ref therein

41 $Y^* k$ & $Y^* K^*$ Production in $\pi^+ p$ interactions at 10.3 Gev/c BNL 24719 and Ref therein

42 Primer et.al. P R L Vol 20 No12 1968

43 Spin Formalism Cern report CERN 71-8

44 Byers and Fenster P R L Vol 11 No. 1 (1963)

45 N Byers , Determination of spin, CERN 67-20

46 Eberhard et. al. P R Vol 63 No 5 (1967)

47 R K Adair P R L (pp 1540-) (1955)

48 R Levi Setti, Elementary Particles, Chicago Lectures in Physics

49 Barger and Cline, Phenomenological theries of high energy scattering, Benjamin 1969

50 D Faiman, A Quark-eye view of Exotics, CEREN Preprint

51 B French, Mesons- 1975

52 C Baltay et. al., Paper No.F1-30, Mesons -1975

53 A study of inclusive Λ, Σ^0 and $\Sigma(1385)$ production in $k^- p$ interactions at 8.25 Gev/c , CEREN /EP/PHYS 78-36

54 The off-line " PWC program" used for efficiency calculation was written by D R Freytag of SLAC

55 The normalisation was done by P J Dornan of Imperial College

ACKNOWLEDGEMENTS

A large number of people have contributed to the completion of this experiment. I would like to thank everybody working in this group at present and also those who participated in the experiment in various ways.

I thank Prof. I Butterworth for affording me the opportunity of working in the field of H E N P , and the S R C for financial support.

I am grateful to Dr. P J Dornan for acting as my supervisor.

Thanks are due to Niander for the excellent typing of this thesis.

Finally I am grateful to my wife, Jaswinder, for encourgement during the last year.